

NASA CONTRACTOR REPORT 159363

Analytical Prediction of the Interior Noise for Cylindrical Models of Aircraft Fuselages for Prescribed Exterior Noise Fields

**PHASE I : DEVELOPMENT AND VALIDATION OF
PRELIMINARY ANALYTICAL MODELS**

L. D. POPE
D. C. RENNISON
E. G. WILBY

BOLT BERANEK AND NEWMAN INC.
CANOGA PARK, CA. 91303

CONTRACT NAS1-15782
OCTOBER 1980



National Aeronautics and
Space Administration

Langley Research Center
Hampton, Virginia 23665

TABLE OF CONTENTS

	<u>Page</u>
1.0 SUMMARY	1
2.0 INTRODUCTION.	4
2.1 Candidate Approaches for Analytical Model.	5
2.2 Report Organization.	8
3.0 ANALYTICAL MODELS	10
3.1 Generalized Power Flow Approach	10
3.2 Solution of a General Sound Transmission Problem.	12
3.3 General Results for the Noise Reduction	17
3.4 Cylinder Noise Reduction.	21
3.5 Transmission of a Discrete Tone	33
3.6 Response to Point Input Harmonic Mechanical Excitation	52
3.7 Interior Response for Progressive Wave Field Excitation	64
3.8 Modifications for the Non-ideal Cylinder.	66
3.8.1 Cylinder Lap Joint Effect	69
3.8.2 Effects of End Caps and Longitudinal Flexibility.	74
4.0 EXPERIMENTAL INVESTIGATIONS	79
4.1 Phase I Test Article.	80
4.1.1 Resonance Frequencies	81
4.1.2 Damping	86
4.2 Noise Reduction Measurements.	95
4.3 Plane-Wave Tonal Excitation	98
4.4 Point Mechanical Excitation	108
4.5 Progressive Wave Excitation	118
5.0 COMPARISONS AND VALIDATION OF ANALYTICAL MODELS	134
5.1 Basics of Computer Program.	136
5.2 Noise Reduction of the Test Article	137

TABLE OF CONTENTS (Contd).

	<u>Page</u>
5.2.1 Calculated Results.	137
5.2.2 Statistical Analysis of Cylinder Noise Reduction Data	150
5.3 Tone Transmission Comparison.	159
5.4 Mechanical Excitation	164
5.5 Excitation by a Random Progressive Wave Field . .	164
5.6 Noise Reduction for Increased Interior Absorption	170
REFERENCES	172
APPENDICES:	
A: Plane Wave Tonal Transmission Data	
B: Mechanical Excitation Data	
C: Progressive Wave Field Data	

LIST OF FIGURES

<u>Figure No.</u>	<u>Page</u>
1. Cylinder Coordinates and Nomenclature.	23
2. Cylinder/Cavity Configurations	27
3. Tone Transmission: Incident Plane Wave at $\theta = \pi$. . .	35
4. Phase I Test Article: Unpressurized, Unstiffened Cylinder.	67
5. Cylinder Lap Joint Detail.	68
6. Low Frequency Model.	75
7. Interior Acoustic Response to Acoustic Source Inside.	82
8. Cylinder Acceleration Response to Interior Acoustic Excitation	83
9. Cylinder Structure Resonance Frequencies	87
10. Cylinder Acoustic Resonance Frequencies.	88
11. Typical Instrumentation for Loss Factor Measurement.	90
12. Acoustic Loss Factors of Bare Cylinder	91
13. Measured Structural Loss Factors for Bare Cylinder .	94
14. Instrumentation Diagram for Cylinder Noise Reduction Measurements with Reverberant Field Excitation. . .	96
15. BBN Measured Noise Reduction (Bare Cylinder)	99
16. LaRC Measured Noise Reduction (Bare Cylinder). . . .	100
17. Test Layout for Plane Wave Excitation of Cylinder. .	102
18. Equipment Schematic for Tonal Plane Wave Excitation.	103
19. Measurement Locations for Tonal Plane-Wave Excitation.	104
20. (a) Ratio of Incident Pressure to Interior Pressure, Tonal Plane Wave Excitation, $\phi = 15^\circ$	105
20. (b) Ratio of Incident Pressure to Interior Pressure, Tonal Plane Wave Excitation, $\phi = 45^\circ$	106
21. Experimental Configuration for Point Mechanical Excitation of Test Cylinder, Showing Shaker and Measurement Locations	110
22. Instrumentation for Cylinder Inertance and Transfer Function Measurements	111

LIST OF FIGURES

<u>Figure No.</u>	<u>Page</u>
23. Force Output Signal for Fixed Driving Voltage to Unloaded Shaker, Showing Effect of Mass Cancellation Circuit	112
24. Inertance Function, $H(f)$, For Point Mechanical Excitation.	114
25. Sound Level-to-Force Input Transfer Function, $H_s(f)$, for Point Mechanical Excitation	115
26. Experimental Configuration for Progressive Wave Excitation of Cylinder.	119
27. Instrumentation Schematic for Progressive Wave Excitation.	120
28. Variation of Mean Circumferential Level Along Cylinder Length	124
29. Microphone Locations for Measurement of Coherence and Phase of Progressive Wave Field	126
30. Typical Axial Coherence and Phase Data for Progressive Wave Test	128
31. Typical Circumferential Coherence and Phase Data for Progressive Wave Test	129
32. Ratio of Exterior Pressure to Average Interior Pressure, Progressive Wave Excitation	133
33. Initial Noise Reduction Predictions with Analytical Model	139
34. Comparison of Predicted and Measured Noise Reductions.	146
35. Modal Contributions to Interior Sound Levels	151
36. Structure Response Contributions to Resonant Acoustic Response Only.	152
37. Measured and Predicted Noise Reduction for Cylinder.	158
38. Predicted Tone Transmission, 15° Angle of Incidence.	160
39. Predicted Tone Transmission, 45° Angle of Incidence.	161
40. Comparison of Predicted and Measured Acceleration, Point Mechanical Excitation	165
41. Comparison of Predicted and Measured Acceleration, Point Mechanical Excitation	166

LIST OF FIGURES

<u>Figure No.</u>	<u>Page</u>
42. Comparison of Predicted and Measured Interior Pressure, Point Mechanical Excitation	167
43. Comparison of Predicted and Measured Interior Pressure, Point Mechanical Excitation	168
44. Predictions Versus Measurements, Band-Limited Ratio of Exterior Pressure to Average Interior Pressure, Progressive Wave Excitation	169
45. Cylinder Noise Reduction With a 0.00635 Meter (0.25 Inch) Layer of Acoustical Foam.	171

LIST OF TABLES

<u>Table No.</u>	<u>Page</u>
1. Acoustic Resonance Frequencies of LaRC Cylinder. . . .	84
2. Structural Resonance Frequencies of LaRC Cylinder. . .	85
3. Band Average Loss Factors--Undamped LaRC Cylinder. . .	93
4. Details of Interior Microphone Locations for Tone Transmission Measurements.	107
5. Summary of Measurement Information for Point Mechanical Excitation	116
6. Exterior Sound Levels for Progressive Wave Excitation.	121
7. Summary of Coherence and Phase Measurements.	127
8. Data for Progressive Wave Field Excitation	132
9. Noise Reduction Estimates from LaRC Experiments. . . .	154
10. Noise Reduction Estimates from BBN Experiments	155
11. Estimated Mean Value of Noise Reduction and 99% Confidence Intervals.	157
12. Most Significant Contributions to $\langle p_i^2 \rangle / \langle p_{inc}^2 \rangle$, Plane Wave Excitation, $\phi = 45^\circ$	162

1.0 SUMMARY

During recent years there has been a growing interest in new aircraft propulsion systems such as powered-lift devices and high-speed propellers (propfans) for both commercial and military applications. Studies of the systems have indicated that they will generate high noise levels, particularly at low frequencies, in the fuselage interiors. At the same time there has been an increasing demand on the National Aeronautics and Space Administration to provide technical support to the general aviation industry, and one problem identified in this field is the reduction of cabin noise levels. In an attempt to solve some of the complicated problems involved in the control of airplane interior noise, NASA Langley Research Center embarked on an extensive program to identify the important parameters associated with acoustic transmission (airborne and structureborne) into airplane interiors and to determine appropriate noise control methods which are acceptable with regards to weight and space. As a part of this program, an aircraft interior noise prediction model is being developed by Bolt Beranek and Newman Inc. (BBN), the purpose being to undertake the required analyses and integrate the technologies and information needed to understand sound transmission through a fuselage wall into an aircraft cabin, both for future development studies and for the immediate need of accurate prediction of interior levels (more properly stated, for prediction of the noise isolation characteristics of the fuselage structures). The effort has been divided into three phases. These are:

Phase I.

Analytical modeling of the transmission problem (interaction of the structures with the exterior and interior acoustic fields) and preliminary verification studies using, as a test article, an unpressurized unstiffened cylinder.

Phase II.

Development of the general aircraft interior noise model and basic master computer program with application to advanced test articles (for instance, a stiffened cylinder with interior partitions and simulated trim).

Phase III.

Completion of the analytical models and software with application to an actual aircraft fuselage, verification tests, comparisons, refinements, and documentation of the finalized model and software.

This report presents the results of the Phase I studies. The basic theoretical work required to understand sound transmission into an enclosed space (that is, one closed by the transmitting structure) is developed for random pressure fields and for harmonic (tonal) excitation. The analysis is used to predict the noise reduction of the test article (i.e., the unpressurized unstiffened cylinder) and, also, the interior response of the cylinder given a tonal (plane wave) excitation. Comparisons of predictions and measurements are made and a detailed analysis of

the transmission is presented. This latter study is perhaps the most informative aspect of the exercise undertaken in Phase I. In addition to the above, results for tonal (harmonic) mechanical excitation are considered.

The work was accomplished as a joint effort by BBN/Los Angeles and NASA Langley Research Center. L. D. Pope served as BBN program manager and William H. Mayes was LaRC technical monitor. The authors wish to thank Mr. Mayes and Conrad Willis of NASA LaRC for their contributions to the experimental program; also Allan G. Piersol of BBN who performed the statistical analysis of the noise reduction data, and John F. Wilby of BBN for general assistance.

2.0 INTRODUCTION

The present study has the specific goal of developing an analytical model which can be used to predict the sound levels in a cylinder for several excitation inputs and interior configurations. However, this objective has to be viewed in terms of the overall objective of the program of which this present study forms only the first phase. The complete program has the objective of developing an analytical model to describe the sound field inside an airplane cabin. Consequently, the analytical model resulting from the present study must not only predict the sound levels in the unstiffened and unpressurized test cylinder (which is an idealized fuselage structure), but it must be adaptable to the more complicated situation present in a realistic airplane fuselage. Only then can this study be viewed as a first phase in the larger program.

The two main efforts of Phase I are the construction of the analytical models and the experimental validation of those models on an unstiffened cylinder. The work effort under Phase I and envisaged for Phases II and III of the present program can be considered in terms of the interior noise research and development program underway at Langley Research Center. This overall program is concentrating on two areas: (1) the accumulation of experimental data which can be incorporated into a prediction methodology, and (2) development of the prediction methodology itself. The work has a bias towards general aviation aircraft.

Interior noise levels have been measured by Catherines and Mayes [1] in single- and twin-engined propeller-driven light aircraft. These studies define to a large extent the nature of

the acoustic environment in light aircraft and establish the need for analytical prediction methods which will eventually be useful in the design of quiet interiors. Sound levels in the cabins of the aircraft were found to be dominated by propeller and engine exhaust noise, the spectra being essentially tonal in nature. In [2] the measured exterior spatial distributions of the acoustic pressures showed the dominance of propeller noise over the forward part of the fuselage, and exhaust noise over the aft part. Reduction of interior noise is clearly desirable since levels in light aircraft range from 85 to 105 dBA. Barton [3] developed a method for predicting interior noise in STOL aircraft and, utilizing a sidewall noise reduction model which likely is conservative, predicted levels of 90 - 105 dBA and 88 - 92 dBA in aircraft with USBF and EBF systems respectively.

Howlett et al., [4] measured the noise reduction of a light aircraft in a reverberant room. Using the Cockburn and Jolly model [5], a comparison of predicted and measured noise reduction was made. Agreement was not very satisfactory.

In addition to the above studies, a series of progressively more complicated analysis and data reduction investigations has been completed under LaRC sponsorship. These include studies by Koval [6, 7, 8], Vaicaitis [9] and Rennison and Wilby [10,11] among others.

2.1 Candidate Approaches for Analytical Model

Before developing an analytical model for the present study, it is useful to review the technology available and to consider its applicability to the Phase I studies, and to subsequent Phase II and Phase III work. In general, it can be stated that much of the technological base required for the prediction of

the test cylinder response and acoustic radiation is available already. Potential analytical techniques which could be used for the present predictions may be generally grouped into two categories, each of which may be broken down further, basically in terms of computational schemes. When making predictions, such as required here, with potentially high acoustic and structure modal densities, it is important to keep in mind that the choice of computational scheme is significant in the overall problem solving procedure. The two types of analyses are:

1. Basic Normal Mode Approach

(Pure tone and noise formulations; simple structures and geometrically simple cavities are specified).

- (a) Computations performed by straightforward summation over acoustic and structure modes.
- (b) Calculations performed by selecting the most likely responsive modes and by applying a convergence criterion to limit the number of summations.

2. Power Balance Approach

- (a) Statistical energy analysis (high frequency band average predictions for noise).
- (b) Generalized power flow formulation (harmonics or noise, complex structures and geometrically complex cavities).

Each of the above techniques has been used at one time or another in studies similar to that of the present Phase I.

The Type 1(a) analysis and computation scheme might best be described as the brute force method. In principle, the exact dynamics of the structure have been developed by Pope [12]. Cockburn and Jolly [5] and Pope [12] have solved the finite closed

cylinder problem for the case of a reverberant field (and in general for any homogeneous stationary random pressure field). The computer software procedures used in those studies are limited because the computation time requirements can be large, since summations over large numbers of acoustic and structure modes can be required.

The analytical method of Type 1(b) is identical to Type 1(a) and might be typified by work such as that of Plotkin et al., [13]. The significant difference in this approach and 1(a) is the calculation procedure, which reduces computational times. The work in [13] represents an advance in the computational scheme for high modal density systems. Nevertheless, in general, the normal mode approach alone leaves much to be desired because it does not create a substantial understanding of the transmission phenomenon. That is, it gives answers but does not provide much auxiliary physical information to discern why certain results are computed.

Type 2 analyses are significantly different from Type 1 in that net inflowing acoustic power is calculated and equated to net internal dissipation to obtain the interior levels. Early applications of this approach utilized statistical energy analysis, the Type 2(a) procedure. Analyses by Lyon [14], White [15], Scharton [16], and Eichler [17] have great utility but they all have the severe handicap that they are not applicable to low frequencies.

Type 2(b) is a technical approach developed recently at BBN by Pope and Wilby [18, 19, 20], for the acoustic environment in the payload bay of the space shuttle orbiter vehicle, that enables the use of power flow concepts at both low and high frequencies,

thereby overcoming a major disadvantage of the statistical energy analysis method. Essentially, beginning with modal analysis, a system of power flow and dissipation expressions has been developed which encompasses the normal mode approach at low frequencies and a modified form of statistical energy analysis at high frequencies. The technique considers power transmission by resonant and nonresonant structure modes into resonant and nonresonant acoustic modes. It can handle random and pure tone excitations at low or high frequencies, provide band-limited or harmonic predictions, and be converted into computer software which performs calculations over the entire frequency range of concern faster than can the method of [5]. It also provides auxiliary information, such as radiation efficiencies of structures, band-averaged joint acceptances, etc., and can utilize modal data generated by different methods such as closed form equations or finite-element analyses. The method is not limited to simple structural models and it can handle complex receiving spaces. Moreover, its usefulness and accuracy have been demonstrated already in application to a structure as complex as the mid-fuselage of the space shuttle orbiter vehicle [21]. It is this latter technique which has been selected for the present study.

2.2 Report Organization

With these preliminaries behind, a brief overview of the organization of this report may be useful. Basically this report presents results of (1) analytical derivations, (2) experimental tests, and (3) verification studies (comparisons).

In the analytical development, there are always two fundamental requirements. The models have to have the capacity for application to a realistic fuselage, and, for the immediate needs of the

Phase I study, they must be specialized for application to the test article. Because of the first requirement, there is, of necessity, a certain abstractness in the fundamental developments. Every attempt has been made to allow the reader to follow the mathematics without excessive difficulty. Application of the general results to the case of the test cylinder will, hopefully, then reveal considerable insight into the meaning and usage of the models. It is important to understand this application because there will be a similarity involved when the models are used in reference to an actual fuselage.

The parts of the report concerned with the presentation of the experimental work describe the purpose of the tests, data acquisition and reduction techniques, and give results usually as raw data, and in format as required for the comparison studies.

Comparisons are of different types ranging from the "weak" qualitative type such as visual comparisons of graphs of data versus predictions, to the "strong" statistical type of comparison deemed useful and necessary for verification purposes.

3.0 ANALYTICAL MODELS

3.1 Generalized Power Flow Approach

In the preceding section, a broad review of the general analysis techniques and calculation methods which are available to undertake Phase I, II, and III studies was given. In the review, the generalized power flow approach (Type 2(b)) was identified as the method most suitable to all three phases of the overall program. Thus it is appropriate to consider this approach in detail so that the component parameters can be identified. For purposes of discussion, it is assumed that the excitation is broadband acoustic noise, but the approach is not restricted to this excitation, as will be shown.

The power balance method of analysis can be basically described with the equation

$$W_{in} = W_{diss}. \quad (1)$$

This equation simply states that the net time-averaged power, W_{in} , flowing into the interior of the cylinder must equal the net time-averaged power, W_{diss} , dissipated on the interior walls. By expressing the inflowing power in terms of the exterior exciting pressure and the dissipated power in terms of the interior response pressure and equating the expressions according to Eq. (1), one can solve for the interior pressure. Thus, if these expressions are available, one can write down the solution to most sound transmission problems immediately.

A primary feature of the generalized power flow approach adopted here is that integration of spectral components has been performed

analytically to achieve band-limited levels, i.e.,

$$W_{in} = \int_{\Delta\omega} \text{Re}[W_{rad}^{int}(\omega)] d\omega \quad (2a)$$

$$W_{diss} = \int_{\Delta\omega} \text{Re}[W_{abs}^{int}(\omega)] d\omega \quad (2b)$$

In the above expressions $W_{rad}^{int}(\omega)$ is the complex spectral density of the power radiated by the structure into the interior acoustic space and $W_{abs}^{int}(\omega)$ is the spectral density of power absorbed on the inner wall of the space from the interior acoustic field. Note here the similarity to statistical energy analysis (SEA has a band-limited power basis). However, Eqs. (2) have applicability at all frequencies and can be applied even when there are no acoustic or structure modes in the band $\Delta\omega$.

Power flow into each individual acoustic mode is computed, whether the mode is resonant in the band or not. If the mode is resonant in the band, one can speak of the "resonant response" of the mode; if the mode is resonant outside the band, the "nonresonant response" of the mode *in the band* $\Delta\omega$. Similarly power flowing out of the acoustic field to the inside wall is computed mode-by-mode. By equating the power into a mode to the power out, the space average mean square modal pressure for mode n , limited to band $\Delta\omega$, is obtained, i.e., $\langle p_n^2 \rangle_{s,t}$. The band-limited, space-average mean-square pressure in the interior is the sum

$$\langle p_i^2 \rangle_{s,t} = \sum_n \langle p_n^2 \rangle_{s,t} \quad (3)$$

Here n is the complete set of acoustic modes, i.e., those resonant inside $\Delta\omega$ (denoted by the symbolism, $n \in \Delta\omega$), as well as those resonant above and below $\Delta\omega$ ($n \notin \Delta\omega$). At this point it should be noted that the letter "n" always denotes acoustic modes and the letter "r" structure modes, usually being used as subscripts, superscripts, or indexes.

3.2 Solution of a General Sound Transmission Problem

As previously stated, much of the technological base for the predictions of interest here has been developed [19,20]. Rather than repeat the derivations given in these two papers, the purpose of this section is to summarize and use the results. It is not absolutely necessary (but it will be helpful) for the reader to go through the papers before continuing with this section. The highlights of the developments are discussed below.

The concern is with a closed volume V , into which sound energy is propagating. The excitation of the space occurs at its boundary with the enclosing structure which vibrates due to an exterior source. For the present, the excitation can be considered to be a broadband random acoustic field. For the specific case where the noise reduction is desired, the exterior field is taken to be diffuse (reverberant).

Consider first the spectral density of the power that flows into the cavity. This quantity is obtained by integrating, over the transmitting area, the cross-power spectral density of interior pressure on the wall with the wall velocity at that position.

$$W_{\text{rad}}^{\text{int}}(\omega) = \int_A \text{Sp}_i v(\bar{x}, \omega) d\bar{x} \quad (4)$$

The development of this expression into the desired form is presented in Sections II and III of Reference [19], resulting in Eq. (13) of Section III of [19], which is Eq. (5) below.

$$\begin{aligned} \operatorname{Re}\left[W_{\text{rad}}^{\text{int}}(\omega)\right] &= \frac{2\rho\omega^3 A^4 S_{\text{pbl}}(\omega)}{V} \sum_n \frac{\epsilon_n \lambda_n \Lambda_n}{|\bar{\lambda}_n^2 - k^2|^2} \\ &\times \sum_r \frac{f'^2(n,r) j_r^2(\omega)}{|M_r Y_r - \rho\omega^2 (J^{rr} + I^{rr})|^2} \quad . \end{aligned} \quad (5)$$

Nomenclature here is consistent with that in References [19,20]. This result is substituted into Eq. (2a), to obtain

$$\begin{aligned} W_{\text{in}} &= \frac{\rho c^2 A^4 S_{\text{pbl}}(\omega)}{V} \sum_r \frac{j_r^2(\omega)}{M_r^2 \omega_r^4} \\ &\times \sum_n \frac{\epsilon_n \eta_n f'^2(n,r)}{\omega_n^2} \\ &\times \int_{\Delta\omega} \frac{\omega^3 d\omega}{\{[1 - (\omega^2/\omega_n^2)]^2 + \eta_n^2\} \{[1 - (\omega^2/\omega_r^2)]^2 + \eta_r^2\}} \quad . \end{aligned} \quad (6)$$

Eq. (6) is the fundamental result for the input power. All that remains to obtain the desired left-hand side of Eq. (1) is to integrate the expression (Eq. (6) is the same as Eq. (3) of Section I of [20]).

Different forms for the inflowing power, W_{in} , are obtained in References [19] and [20]; e.g., compare Eq. (19) of Section III of [19] to Eq. (5) of Section II of [20]. This difference has to do with how the integration is performed, i.e., with or without restrictions being placed upon the locations of the resonance frequencies of the modes (either inside or outside the band $\Delta\omega$). In Reference [20], the integration has been performed without restriction on mode locations. Thus Eq. (5) of Section II of [20] is the general result. The restriction $n \notin \Delta\omega$ (i.e., that ω_n lie outside $\Delta\omega$) can be lifted since it is artificial. Therefore, the required form of the left-hand side of Eq. (1) is

$$\begin{aligned}
 W_{in} = & \frac{\langle p_{bl}^2 \rangle}{c_\omega \omega} \frac{2\pi A^2 \left(\frac{mA}{4}\right)^2}{\rho V} \tau_{ML} \sum_n \epsilon_n \eta_n \sum_r \frac{j_r^2(\omega) f'^2(n, r)}{M_r^2} \left\{ \frac{2}{\pi} \frac{\omega^2 \omega_n^2}{D_{nr}} \left[\left(\frac{c_r - c_n}{4} \right) \ln_n \right. \right. \\
 & + \left(\frac{2c_n(b_r - b_n) - b_n(c_r - c_n)}{4\eta_n \omega_n^2} \right) \arctan_n + \left(\frac{c_n - c_r}{4} \right) \ln_r \\
 & \left. \left. + \left(\frac{2c_r(b_n - b_r) - b_r(c_n - c_r)}{4\eta_r \omega_r^2} \right) \arctan_r \right] \right\}, \quad (7)
 \end{aligned}$$

where

$$D_{nr} = (c_r - c_n)^2 + (b_n - b_r)(b_n c_r - b_r c_n)$$

with

$$b_n = -2\omega_n^2, \quad b_r = -2\omega_r^2,$$

$$c_n = \omega_n^4(1 + \eta_n^2), \quad c_r = \omega_r^4(1 + \eta_r^2),$$

and for n or $r = j$,

$$\ln_j = \ln \left(\frac{|(1+c_\omega/2)^4 \omega^4 + b_j (1+c_\omega/2)^2 \omega^2 + c_j|}{|(1-c_\omega/2)^4 \omega^4 + b_j (1-c_\omega/2)^2 \omega^2 + c_j|} \right),$$

$$\begin{aligned} \arctan_j &= \tan^{-1} \{ [(2+c_\omega)^2 \omega^2 - 4\omega_j^2] / 4\eta_j \omega_j^2 \} \\ &\quad - \tan^{-1} \{ [(2-c_\omega)^2 \omega^2 - 4\omega_j^2] / 4\eta_j \omega_j^2 \} . \end{aligned}$$

Consider now the interpretation of Eq. (7). W_{in} represents the band-limited time averaged power which is being accepted by the acoustic field inside the enclosure, that is, the power received over frequencies lying in band $\Delta\omega$. The band has a width $\Delta\omega = c_\omega \omega$ where ω is the center frequency of the band. c_ω is a constant percentage which defines the bandwidth ($c_\omega = 0.232$ for one-third octaves). The quantity $\langle p_{bl}^2 \rangle / c_\omega \omega$ is the same quantity as $S_{pbl}(\omega)$, that is, it is the power spectral density of the average exciting blocked pressure which acts on the transmitting structure. $\langle p_{bl}^2 \rangle$ is the average mean square blocked pressure as would be measured in band $\Delta\omega$ obtained with a microphone sampling the surface pressures on the (hypothetical) blocked structure. As stated the transmitting structure has an area A exposed to volume V . The average surface mass of the structure is m . The structure has a mass law transmission coefficient $\tau_{ML} = (2\rho c_o / \omega m)^2$, where ρ and c_o are the density and sound speed of air. The normalization of structure modes is taken such that, generally, the modal mass is

$$M_r = \int_A m(\bar{x}) \psi^2(\bar{x}) d\bar{x} = \frac{mA}{4} ,$$

if the structure is unrestrained. The normalization of the acoustic modes is such that

$$\int_V \phi_n^2 d\bar{v} = \frac{V}{\epsilon_n} \quad .$$

The coupling of the exterior field to the r th mode of the transmitting structure is given in terms of the joint acceptance, $j_r^2(\omega)$. It is assumed that $j_r^2(\omega)$ changes little across $\Delta\omega$, i.e., that by evaluating $j_r^2(\omega)$ at the center frequency of the band, a good approximation is obtained all across $\Delta\omega$. For this reason $\Delta\omega$ must not be too wide, typically one-third octave or less. If the exterior field is reverberant, $j_r^2(\omega)$ takes the appropriate form for that field. The same is true for a progressive wave field.

The coupling of a structure mode to an acoustic mode of the volume is given by the term

$$f'(n,r) = \frac{1}{A} \int_A \phi_n(\bar{x}) \psi^r(\bar{x}) d\bar{x} \quad .$$

In the above \bar{x} represents a point on the surface of the transmitting structure. Note that $f'(n,r)$ is non-dimensional (hence the prime as a reminder) and that $f'(n,r)$ is always squared. $f'^2(n,r)$ is a positive number less than unity.

The term in the braces { } determines the coupling in frequency of the acoustic and structure modes (n and r respectively). The power flow depends on the locations of the resonance frequencies ω_n and ω_r , i.e., relative to each other and to the band $\Delta\omega$, and upon the acoustic and structural loss factors η_n and η_r .

Consider now the right-hand side of Eq.(1). W_{diss} is the band-limited, time-averaged power that flows out of the interior

acoustic field to the inner wall of the enclosure. This power flow is given by Eqs. (6) and (8) of Section III of [20] which reduce to

$$W_{\text{diss}} = \frac{V}{\rho c_0^2} \sum_n \frac{\eta_n \omega_n^2}{\omega} \langle p_n^2 \rangle_{s,t} \quad , \quad (8)$$

where $\langle p_n^2 \rangle_{s,t}$ is the interior space average mean square pressure in band $\Delta\omega$ attributable to the n th acoustic mode. The development of Eq. (8) is presented in the appendix of [20].

The solution of a sound transmission problem is obtained by setting the n th term of Eq. (7) equal to the n th term of Eq. (8), solving for the individual modal pressures, $\langle p_n^2 \rangle_{s,t}$, one-by-one, and by adding the results according to Eq. (3), to obtain the interior level.

3.3 General Results for the Noise Reduction

The noise reduction of an enclosure is defined by

$$NR = -10 \log_{10} \frac{\langle p_i^2 \rangle_{s,t}}{\langle p_e^2 \rangle_{s,t}} \quad (9)$$

where $\langle p_e^2 \rangle_{s,t}$ is the average mean square pressure over that space which will be occupied by the enclosure, and $\langle p_i^2 \rangle_{s,t}$ is the space average mean square pressure over that same volume when enclosed. Following the instructions given above for the solution of a sound transmission problem and letting, $\langle p_e^2 \rangle_{s,t} = \langle p_{bl}^2 \rangle / 2$, it is found that for reverberant field excitation, i.e., with $j_r^2(\omega) \rightarrow j_r^{2\text{rev}}(\omega)$,

$$\begin{aligned}
\frac{\langle p_i^2 \rangle_{s,t}}{\langle p_e^2 \rangle_{s,t}} &= \frac{8}{c_\omega} \frac{A^2}{V^2} \left(\frac{mA}{4} \right)^2 \tau_{ML} c_o^2 \omega^3 \\
&\times \sum_n \epsilon_n \sum_r \frac{j_r^{2, rev.}(\omega) f'^2(n,r)}{M_{rnr}^2 D} \\
&\times \left\{ \left(\frac{c_r - c_n}{4} \right) \ln_n + \left[\frac{2c_n(b_r - b_n) - b_n(c_r - c_n)}{4\eta_n \omega_n^2} \right] \arctan_n \right. \\
&+ \left. \left(\frac{c_n - c_r}{4} \right) \ln_r + \left[\frac{2c_r(b_n - b_r) - b_r(c_n - c_r)}{4\eta_r \omega_r^2} \right] \arctan_r \right\} \quad (10)
\end{aligned}$$

Eq. (10) is used in the present study to predict the noise reduction of the cylinder in one-third octave bands at those frequencies where it is necessary to account for the individual modal response and transmission contributions. At high frequencies, the summation over acoustic modes can be limited to those in the band $(n\epsilon\Delta\omega)$. Eventually at sufficiently high frequencies, the acoustic modal density will become so large that Eq. (10) will require an excessive amount of computer time. To avoid this problem, Eq. (5) can be substituted into Eq. (2a) and evaluated according to the technique discussed in Section IV of Reference [19]. The reader is again referred to the paper for details. At these high frequencies, the net in-flowing power in band $\Delta\omega$ is given by the expression

$$W_{in} = \left\{ \frac{A\tau_R}{4\rho c_o} + \frac{8}{\pi} \frac{A^2}{m^2} \frac{\rho}{c_o} \sum_{r < \Delta\omega} \left[j_r^2(\omega) \right]^2 \right\} \langle p_e^2 \rangle_{s,t}$$

$$- \left\{ \frac{\bar{\eta}_r}{\eta_{rad}^{ext}} \frac{A\tau_R}{4\rho c_o} + \frac{8}{\pi} \frac{A^2}{m^2} \frac{\rho}{c_o} \sum_{r < \Delta\omega} \left[j_r^2(\omega) \right]^2 \right\} \langle p_i^2 \rangle_{s,t} \quad , \quad (11)$$

which corresponds to Eq. (30), Section IV of [19].

In this expression τ_R is the resonant transmission coefficient

$$\tau_R = \left(2n_r \pi^2 c_o \eta_{rad}^{ext} \eta_{rad}^{int} / \rho \omega^2 m A \bar{\eta}_r \right) (4\rho c_o / A),$$

where n_r is the structural modal density (modes/rad/sec) near frequency ω , and $\bar{\eta}_r$ is the sum of the average external radiation loss factor, i.e., η_{rad}^{ext} , and the average structural loss factor, η_r , over $\Delta\omega$. Calculation of these quantities will be discussed later.

The power absorbed on the wall is as before

$$W_{diss} = \frac{V}{\rho c_o^2} \sum_n \frac{\eta_n \omega_n^2}{\omega} \langle p_n^2 \rangle_{s,t} \quad .$$

Since the response is resonant acoustic, ω_n lies in $\Delta\omega$ and the above reduces to

$$W_{diss} = \frac{V}{\rho c_o^2} \sum_{n \in \Delta\omega} \frac{\eta_n \omega_n^2}{\omega} \langle p_n^2 \rangle_{s,t} \quad .$$

Further, noting that $\omega_n \approx \omega$ for any n , and letting the group of acoustic modes have an average loss factor $\bar{\eta}_n$, this reduces to

$$\begin{aligned}
W_{\text{diss}} &= \frac{V}{\rho c_o^2} \omega \bar{\eta}_n \sum_{n \in \Delta\omega} \langle p_n^2 \rangle_{s,t} \\
&= \frac{V}{\rho c_o^2} \omega \bar{\eta}_n \langle p_i^2 \rangle_{s,t} , \tag{12}
\end{aligned}$$

which is Eq. 7, Section III of [20]. Finally, setting

$$\bar{\eta}_n = \frac{\bar{\alpha}_o S}{4\omega V} , \tag{13}$$

where $\bar{\alpha}$ is the band average absorption coefficient and S the absorbing surface area, Eq. (12) reduces to the familiar form

$$W_{\text{diss}} = \frac{\bar{\alpha} S}{4\rho c_o} \langle p_i^2 \rangle_{s,t} . \tag{14}$$

The high frequency form of Eq. (10) is obtained by equating the results given in Eqs. (11) and (14).

$$\frac{\langle p_e^2 \rangle_{s,t}}{\langle p_i^2 \rangle_{s,t}} = \frac{\bar{\alpha} S + \left[\left(\bar{\eta}_r / \eta_{\text{rad}}^{\text{ext}} \right) \tau_R + \tau_f \right] A}{\left(\tau_R + \tau_f \right) A} , \tag{15}$$

where τ_f is defined to be the field incidence transmission coefficient for mass controlled panel transmission, and is given by

$$\tau_f = \frac{32}{\pi} \frac{A^2}{m^2} \rho^2 \sum_{r < \Delta\omega} \left[j_r^{\text{rev}}(\omega) \right]^2 . \tag{16}$$

Letting $\tau_R + \tau_f = \tau$, which is denoted as the total transmission coefficient, gives the form

$$\frac{\langle p_e^2 \rangle_{s,t}}{\langle p_i^2 \rangle_{s,t}} = \frac{\bar{\alpha}S + \left[\tau_f + \left(\frac{\bar{n}_r}{n_{rad}} \right) \tau_R \right] A}{\tau A} . \quad (17)$$

The noise reduction of the cylinder of concern in this study is computed using Eqs. (10) and (17). The frequencies over which the use of Eq. (10) is limited will be considered in a subsequent section of this report.

3.4 Cylinder Noise Reduction

Eqs. (10) and (17) are now specialized for the case of the test article, i.e., the unpressurized, unstiffened cylinder. Consider first the acoustic and structure modes, which can be ordered according to the occurrence of their resonance frequencies. For $n = 1$, ω_n can be taken as the acoustic mode with lowest resonance frequency; for $n = 2$, the mode of second lowest frequency, etc. ω_r can be similarly ordered. Corresponding to each acoustic mode is a trio of indices (q,n,s) and to each structure mode a duo of indices (M, N). These are used in the definition of the characteristic functions corresponding to each resonance frequency or eigenvalue. For the case of cylinder acoustics, the modal functions obey the Helmholtz equation

$$\nabla^2 \phi_n + \bar{\lambda}_n^2 \phi_n = 0 \quad ,$$

subject to the requirement that the particle and surface velocities be equal along the surface normal

$$\frac{\partial \phi_n}{\partial v} - ik\beta \phi_n = 0 \quad ,$$

where β is the inner wall surface admittance (i.e., the ratio of surface velocity to surface pressure). The solutions for the mode shapes, $\phi_n(\bar{\xi}) \equiv \phi_{qns}(r, \theta, z)$, and eigenvalues, $\bar{\lambda}_n = \bar{\lambda}_{qns}$, for uniform surface admittance $\beta \ll 1$, are approximately the following:

$$\begin{aligned}\phi_{qns} &= J_n(m_{ns}r) \cos [n(\theta - \theta')] \cos \frac{q\pi z}{L} \\ \bar{\lambda}_{qns} &= \lambda_{qns} - i\Lambda_{qns} \\ \lambda_{qns} &= \frac{\omega_{qns}}{c_o} = \sqrt{m_{ns}^2 + (q\pi/L)^2} \\ \Lambda_{qns} &= \frac{\omega_{qns}\eta_{qns}}{2c_o} = \frac{k}{2\lambda_{qns}} \frac{\epsilon_{qns}}{V} \operatorname{Re}[\beta] \int_A \phi_{qns}^2(\bar{x}) d\bar{x} \quad , \quad (18)\end{aligned}$$

where q represents the number of axial half-waves, n gives the number of circumferential waves, and s counts within the sequence n of zeros of $J'_n(ma) = 0$. The geometry is as shown in Figure 1.

The mode normalization obeys the relation

$$\epsilon_n \rightarrow \epsilon_{qns} = V / \iiint_V \phi_{qns}^2(\bar{\xi}) dV \quad (19)$$

For the cylinder

$$\iiint_V \phi_{qns}^2(\bar{\xi}) dV = \left[\frac{m_{ns}^2 a^2 - n^2}{2m_{ns}^2} \right] J_n^2(m_{ns}a) \frac{\pi L}{2} \epsilon_q \epsilon_n \quad (20)$$

where

$$\epsilon_q, \epsilon_n = \begin{cases} 2 & q, n = 0 \\ 1 & q, n > 0 \end{cases} .$$

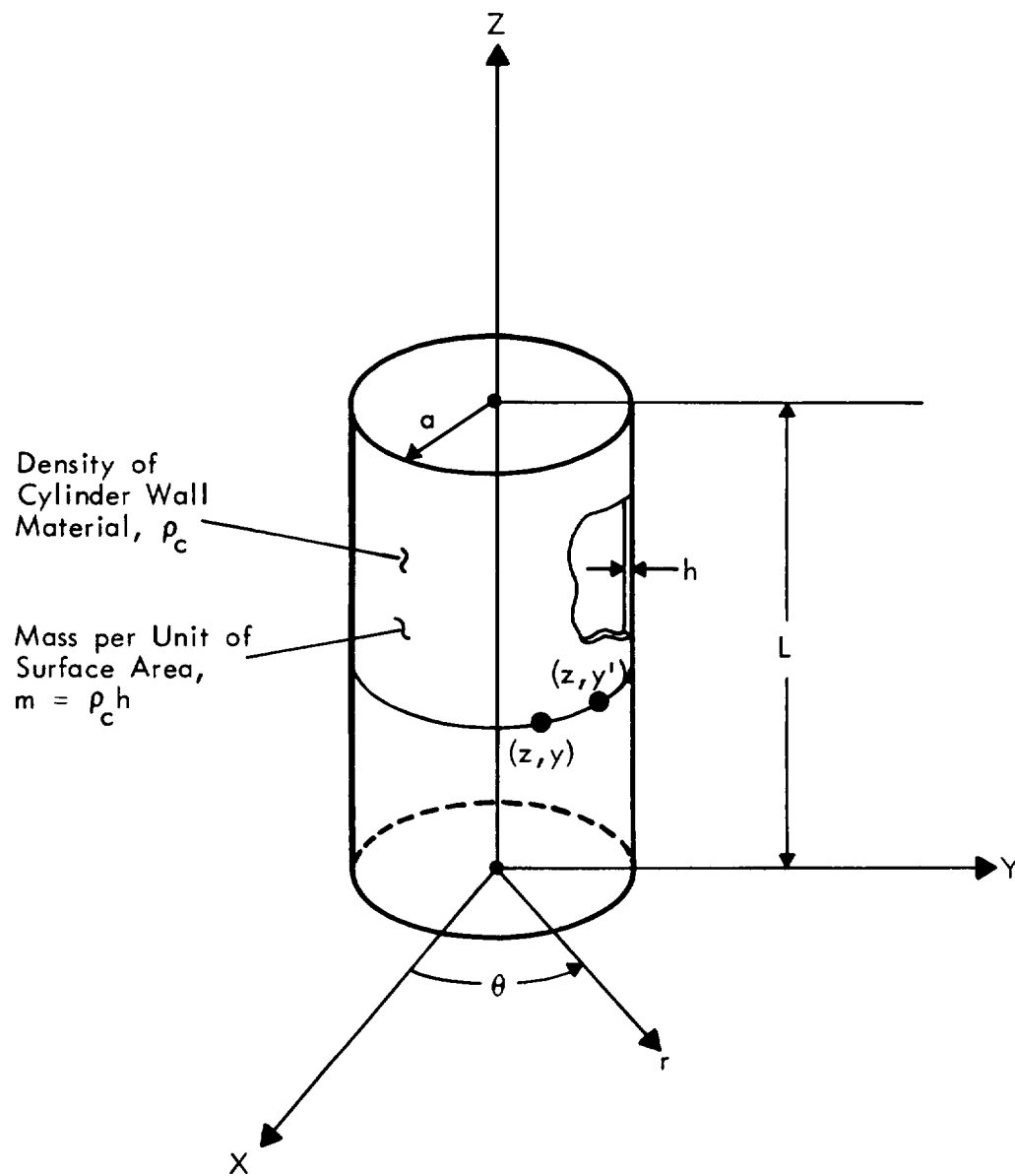


FIGURE 1. CYLINDER COORDINATES AND NOMENCLATURE

The nomenclature here may be confusing so to review, consider the meaning of Eq. (19). This states that the mode whose resonance frequency is ω_n has a normalization such that the integral over the volume of the square of the mode shape is equal to the volume divided by a factor called ϵ_n which depends on the trio (q,n,s), and takes the value ϵ_{qns} which is given by the results in Eqs. (19) and (20). Do not confuse n as a counter within the sequence ω_n with the n in the trio of indices which defines the number of circumferential waves. The range of values for q,n,s is as follows:

$$\begin{aligned} q &= 0, 1, 2, \dots \\ n &= 0, 1, 2, \dots \\ s &= 1, 2, 3, \dots \end{aligned}$$

When values for q, n, and s are selected, the resonance frequency of the acoustic mode may be found using the relation

$$\omega_{qns} = c_o \lambda_{qns} \quad (\text{rad/sec}) .$$

The remaining factors which are required for the cylinder calculations using Eq.10 are the following: (1) the modal mass M_r , (2) the coupling factor $f'(n,r)$, (3) the joint acceptance $j_r^{rev}(\omega)$, and (4) the acoustic and structural resonance frequencies and loss factors.

The structure mode shapes for a freely supported (ideal) cylinder are:

$$\psi^r(\bar{x}) = \psi^{MN}(z, \theta) = \sin \frac{M\pi z}{L} \begin{Bmatrix} \cos N \theta \\ \sin N \theta \end{Bmatrix} \quad (21)$$

The corresponding resonance frequencies are computed with the following characteristic equation [22]

$$\Omega^6 - (K_2 + k\Delta K_2) \Omega^4 + (K_1 + k\Delta K_1) \Omega^2 - (K_0 + k\Delta K_0) = 0, \quad (22)$$

where

$$\Omega = \frac{\rho_c (1-\mu^2)}{E} a^2 \omega_{III}^2, \quad k = h^2/12a^2$$

ρ_c is the mass density of the material of which the cylinder is constructed; E is the elastic modulus and μ Poisson's ratio. Also

$$K_2 = 1 + \frac{1}{2} (3-\mu)(N^2 + \lambda^2) + k(N^2 + \lambda^2)^2$$

$$K_1 = \frac{1}{2} (1-\mu) \left[(3+2\mu)\lambda^2 + N^2 + (N^2 + \lambda^2)^2 + \left(\frac{3-\mu}{1-\mu}\right)k (N^2 + \lambda^2)^2 \right]$$

$$K_0 = \frac{1}{2} (1-\mu) \left[(1-\mu^2)\lambda^4 + k (N^2 + \lambda^2)^4 \right]$$

with

$$\lambda = M\pi a/L.$$

Constants K_0 , K_1 , and K_2 are from the Donnell-Mushtari shell theory; ΔK_0 , ΔK_1 , ΔK_2 are modifying constants for the theory of Arnold and Warburton [22].

$$\Delta K_2 = 2(1-\mu) \lambda^2 + N^2$$

$$\Delta K_1 = 2(1-\mu) \lambda^2 + N^2 + 2(1-\mu) \lambda^4$$

$$-(2-\mu) \lambda^2 N^2 - \frac{1}{2} (3 + \mu) N^4$$

$$\Delta K_0 = \frac{1}{2}(1-\mu) \left[4(1-\mu^2) \lambda^4 + 4\lambda^2 N^2 + N^4 - 2(2-\mu)(2+\mu) \lambda^4 N^2 - 8\lambda^2 N^4 - 2N^6 \right]$$

Only resonances associated with flexure of the cylinder wall are retained. Using this cylinder model, it is found that

$$M_r \rightarrow M_{MN} = \frac{m(2\pi aL)\epsilon_N}{4} = \frac{mA}{4} \epsilon_N \quad (23)$$

where

$$\epsilon_N = \begin{cases} 2 & N = 0 \\ 1 & N > 0 \end{cases}.$$

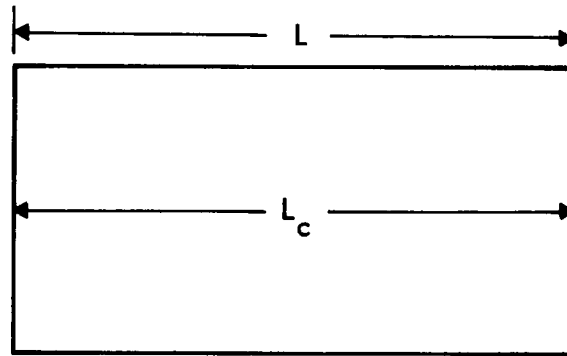
The interior coupling factor is

$$\begin{aligned} f'(n,r) &\rightarrow f'(qns,MN) \\ &= \frac{1}{A'} \int_{A'} \phi_{qns}(\bar{x}) \psi^{MN}(\bar{x}) d\bar{x} \end{aligned}$$

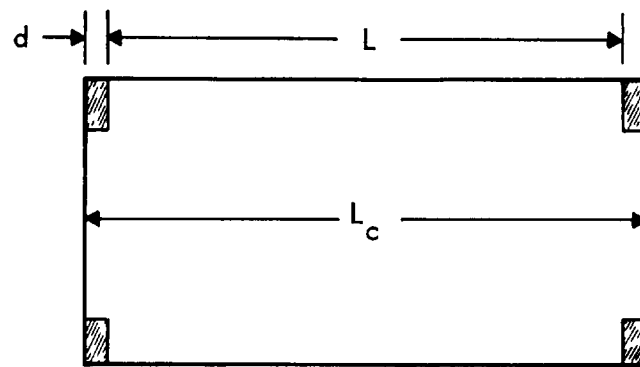
where A' is the transmitting area.

Two cases are considered, and are shown in Figure 2. In one case the cylinder and cavity lengths are identical; in the other the cylinder is taken shorter than the cavity. These cases were chosen after consideration of the application to the test article (the test cylinder configuration will be discussed in Section 4). For the case of Figure 2(a),

$$\begin{aligned} f'(qns,MN) &= \frac{1}{A} \int_0^L \int_0^{2\pi} J_n(m_{ns}a) \cos n(\theta - \theta') \cos \frac{q\pi z}{L} \sin \frac{M\pi z}{L} \left\{ \frac{\cos N\theta}{\sin N\theta} \right\} a d\theta dz \\ &\quad \theta' = 0 \\ &= \begin{cases} f_{qM} f_{Ns} & ; \quad n = N, \quad M \neq q \\ f_{qM} f_{Ns} & ; \quad n = N, \quad M = q \\ 0 & ; \quad n \neq N \end{cases} \quad (24) \end{aligned}$$



(a) Cavity Length, $L_c =$ Cylinder Length, L



(b) Cavity Length, $L_c >$ Cylinder Length, L

FIGURE 2. CYLINDER/CAVITY CONFIGURATIONS

where

$$f_{Ns} = \frac{J_N(m_{Ns}a)}{2} \epsilon_N$$

and

$$f_{qM} = \frac{1}{2\pi} \left\{ \frac{1 - \cos[(M+q)\pi]}{M+q} + \frac{1 - \cos[(M-q)\pi]}{M-q} \right\}; \quad M \neq q$$

$$f^{qM} = 0; \quad M = q$$

Note here that

$$f'(qns, MN) \rightarrow f'(qNs, MN),$$

i.e., unless the circumferential waves are of the same order, the acoustic and structure modes are not coupled. This is true only for the case of an ideal cylinder, one in which there is uniform surface density. The actual test article has a lap joint running axially whose effect is considered in a later section. Note that it is possible to write Eq. (24) in the form

$$f'(qns, MN) = \begin{cases} \frac{J_N(m_{Ns}a)}{2L} \frac{\epsilon_N k_M [1 - (-1)^{M+q}]}{[k_m^2 - k_q^2]} & ; n = N, \text{ and } M \neq q \\ 0 & ; n \neq N, \text{ or } M = q \end{cases}$$

where $k_m = M\pi/L$, and $k_q = q\pi/L_c$. It can be seen that for Case (a) of Figure 2, $f'(qns, MN)$ is zero if $(M+q)/2$ is an integer.

Consider now the case of Figure 2(b). It is found that

$$f'(qns, MN) = \begin{cases} f_{qM} f_{Ns} & n = N, M \neq q \\ f^{qM} f_{Ns} & n = N, M = q \\ 0 & n \neq N \end{cases}$$

where

$$\begin{aligned}
f_{qM} = \cos \pi c_d M & \left[\frac{\cos \pi c_d (M-\kappa) - \cos \pi (1 + c_d)(M-\kappa)}{2\pi(M-\kappa)} \right. \\
& \left. + \frac{\cos \pi c_d (M+\kappa) - \cos \pi (1 + c_d)(M+\kappa)}{2\pi(M+\kappa)} \right] \\
& - \sin \pi c_d M \left[\frac{\sin \pi (1 + c_d)(M-\kappa) - \sin \pi c_d (M-\kappa)}{2\pi(M-\kappa)} \right. \\
& \left. + \frac{\sin \pi (1 + c_d)(M+\kappa) - \sin \pi c_d (M+\kappa)}{2\pi(M+\kappa)} \right], \quad (25) \\
f^{qM} = \cos \pi c_d \kappa & \left[\frac{\sin^2 \pi (1 + c_d) \kappa - \sin^2 \pi c_d \kappa}{2\pi \kappa} \right] \\
& - \sin \pi c_d \kappa \left[\frac{1}{2} \left(1 + \frac{\sin 2\pi (1 + c_d) \kappa - \sin 2\pi c_d \kappa}{2\pi \kappa} \right) \right],
\end{aligned}$$

with

$$\kappa = k_q L / \pi \text{ and } c_d = d/L.$$

For the particular case where $L_c = L$, $c_d = 0$, and

$$\begin{aligned}
f_{qM} &= \frac{1}{2\pi} \left[\frac{1 - \cos \pi (M - \kappa)}{(M - \kappa)} + \frac{1 - \cos \pi (M + \kappa)}{(M + \kappa)} \right] \\
f^{qM} &= 0,
\end{aligned}$$

which is the same as Eq. (24).

The joint acceptance function describes the coupling between the excitation field and the structure, and is defined by the relation

$$j_{MN}^2(\omega) = \frac{1}{A^2 S_{pbl}(\omega)} \iint S_{pbl}(\bar{x}|\bar{x}', \omega) \psi^{MN}(\bar{x}) \psi^{MN}(\bar{x}') d\bar{x} d\bar{x}' ,$$

where A is the structure area, $S_{pbl}(\omega)$ is the blocked pressure power spectral density, and $S_{pbl}(\bar{x}|\bar{x}', \omega)$ is the blocked pressure cross power spectral density. To evaluate the joint acceptance it is necessary to have representations for the excitation field and the structure mode shapes.

Consider first the representation of the excitation field. It has been general practice, when representing random pressure fields with spatially decaying correlation, to use a correlation function of the form

$$\rho(\bar{x}|\bar{x}', \omega) = \frac{\text{Re}\{S_p(\bar{x}|\bar{x}', \omega)\}}{S_p(\omega)} .$$

It is assumed in the present analysis that this function is separable in the longitudinal and transverse directions, i.e.,

$$\rho(\bar{\xi}, \omega) = \rho_x(\xi, \omega) \rho_y(\zeta, \omega)$$

where $\xi = x' - x$ and $\zeta = y' - y$.

The representation for a diffuse excitation field is well established and is given by

$$\rho_x(\xi, \omega) = \frac{\sin(k\xi)}{k\xi}$$

$$\rho_y(\zeta, \omega) = \frac{\sin(k\zeta)}{k\zeta}$$

For the case of the reverberant field, the joint acceptance functions for the cylinder must consider both sines and cosines of the circumferential wavenumber. One can write $j_{MN}^{2rev}(\omega)$ in the form

$$j_{MN}^{2rev}(\omega) = j_{MN}^{2rev}(\omega, \psi) + j_{MN}^{2rev}(\omega, \phi) = j_M^{2rev}(\omega) \left[j_N^{2rev}(\omega, \psi) + j_N^{2rev}(\omega, \phi) \right] ,$$

where ψ represents the cosine and ϕ the sine of the wavenumber.

The joint acceptance for the axial cylinder modes, $j_M^{2rev}(\omega)$, is given by Eq.(26) [23] :

$$j_M^{2rev}(\omega) = I_1(M) + I_2(M) + I_3(M) \quad (26)$$

where

$$I_1(M) = \frac{1}{2\pi M k L_x} \{ \text{Cin}(k L_x + M\pi) - \text{Cin}|M\pi - k L_x| \}$$

$$I_2(M) = \frac{1}{2k L_x} \{ \text{Si}(k L_x + M\pi) - \text{Si}(M\pi - k L_x) \}$$

$$I_3(M) = \frac{1 - (-1)^M \cos k L_x}{(M\pi)^2 - (k L_x)^2}$$

Si and Cin are the sine and cosine integrals [24].

The joint acceptances for the circumferential modes are [23],

$$j_N^{2rev}(\omega, \psi) = \int_0^1 \int_0^1 \frac{\sin 2\pi k a (y_1 - y_2)}{2\pi k a (y_1 - y_2)} \cos 2N\pi y_1 \cos 2N\pi y_2 dy_1 dy_2$$

$$j_N^{2rev}(\omega, \phi) = \int_0^1 \int_0^1 \frac{\sin 2\pi k a (y_1 - y_2)}{2\pi k a (y_1 - y_2)} \sin 2N\pi y_1 \sin 2N\pi y_2 dy_1 dy_2 ,$$

where $y_1 = y/2\pi a$, $y_2 = y'/2\pi a$, y and y' being circumferential coordinates of the two correlated points, and k the acoustic wavenumber. It follows that

$$j_N^2(\omega) \equiv j_N^2(\omega, \psi) + j_N^2(\omega, \phi)$$

$$= \int_0^1 \int_0^1 \frac{\sin 2\pi k a (y_1 - y_2)}{2\pi k a (y_1 - y_2)} \cos 2N\pi (y_1 - y_2) dy_1 dy_2 \quad .$$

This reduces to

$$j_N^2(\omega) = 2 \int_0^1 \frac{\sin 2\pi k a \bar{\eta}}{2\pi k a \bar{\eta}} (1 - \bar{\eta}) \cos 2N\pi \bar{\eta} d\bar{\eta} \quad ,$$

and

$$j_0^2(\omega) = \int_0^1 \frac{\sin 2\pi k a \bar{\eta}}{2\pi k a \bar{\eta}} (1 - \bar{\eta}) d\bar{\eta} \quad ,$$

where $\bar{\eta} = y_1 - y_2$. Performing the integration results in

$$j_N^2(\omega) = \frac{1}{2\pi k a} \left[\text{Si}[2\pi(N+ka)] - \text{Si}[2\pi(N-ka)] \right]$$

$$+ \frac{1}{2(N\pi)^2} \frac{1 - \cos(2\pi k a)}{1 - \left(\frac{k a}{N}\right)^2} \quad , \quad (27)$$

and

$$j_0^2(\omega) = \left[\frac{\text{Si}(2\pi k a)}{\pi k a} - \frac{1 - \cos(2\pi k a)}{2\pi^2 (k a)^2} \right]. \quad (28)$$

With this, all that remains to be determined are the acoustic and structure loss factors. These data are obtained experimentally and considered in Section 4.

3.5 Transmission of a Discrete Tone

Previously, it has been shown that for a noise field, the band-limited power flowing inwardly is

$$\begin{aligned}
 W_{in} = & \frac{2\pi}{\rho V} \left(\frac{mA}{4}\right)^2 \tau_{ML} \frac{2}{\pi} \omega^2 \sum_n \frac{\epsilon_n \eta_n}{\omega_n^2} \\
 & \times \sum_r \frac{f_{(n,r)}^2}{M_r^2 \omega_r^4} \int_{\Delta\omega} \int_{\bar{x}} \int_{\bar{x}'} C_{p_{bl}}(\bar{x}|\bar{x}';\omega) \psi^r(\bar{x}) \psi^r(\bar{x}') d\bar{x} d\bar{x}' \\
 & \times \frac{\omega^3 d\omega}{\left[\left(1 - \frac{\omega^2}{\omega_n^2}\right)^2 + \eta_n^2\right] \left[\left(1 - \frac{\omega^2}{\omega_r^2}\right)^2 + \eta_r^2\right]} . \quad (29)
 \end{aligned}$$

This result is the same as Eq. (6), except $j_r^2(\omega)$ has been replaced by its defining relation. Note that only the cospectral density $C_{p_{bl}}(\bar{x}|\bar{x}';\omega)$, i.e., the real part of the cross spectral density of the exterior blocked pressure field, is used.

For the present case, the external field is a propagating wave with a component along the z axis of the cylinder, with a discrete frequency ω_0 .

Consider the cross power spectral density function

$$\begin{aligned} S_{pbl}(\bar{x}|\bar{x}';\omega) &= \lim_{T \rightarrow \infty} \frac{2}{T} \left(\frac{1}{2\pi} \right) P_{bl_T}(\bar{x};\omega) P_{bl_T}^*(\bar{x}';\omega) \\ &= \frac{1}{\pi} \int_{-\infty}^{\infty} R_{pbl}(\bar{x}|\bar{x}';\tau) e^{i\omega\tau} d\tau \quad . \end{aligned}$$

$R_{pbl}(\bar{x}|\bar{x}';\tau)$ is the average cross correlation of the blocked pressure over the exterior, i.e.,

$$R_{pbl}(\bar{x},\bar{x}';\tau) = \lim_{T \rightarrow \infty} \frac{1}{T} \int_{-T/2}^{T/2} \text{Re}[p_{bl}(\bar{x},t)] \text{Re}[p_{bl}(\bar{x}',t+\tau)] dt \quad .$$

Note here that the real part of $p_{bl}(\bar{x},t)$ is required. Consider the form of the blocked pressure field for the case of a cylinder with an incoming plane wave at angle ϕ with $\theta = \pi$, as shown in Figure 3. The incident plane wave has amplitude P_i and is given by

$$p_i = P_i \exp \left[-i\omega_o t + i(k_x x + k_z z) \right] \quad ,$$

where $k_x = k \sin \phi$, $k_z = k \cos \phi$, k being the acoustic wavenumber ω_o/c_o . According to the geometry, $x = r \cos \theta$, which gives

$$p_i = P_i \exp \left[-i(\omega_o t - k_z z) + i k_x r \cos \theta \right] \quad .$$

This can be expanded in cylindrical harmonics using [25]

$$\exp \left[+i k_x r \cos \theta \right] = \sum_{m=0}^{\infty} \epsilon_m i^m J_m(k_x r) \cos m\theta \quad ,$$

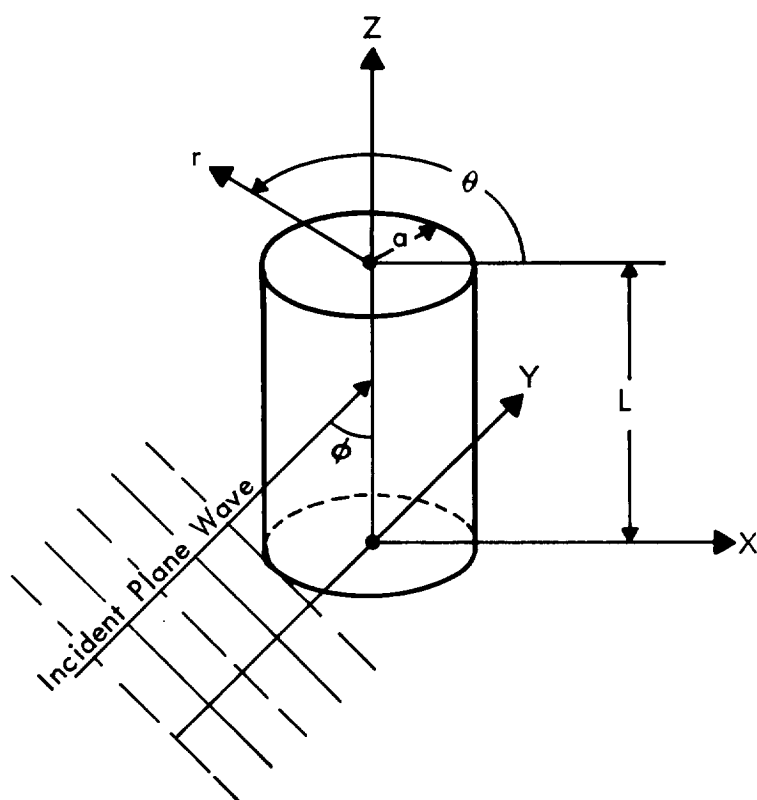


FIGURE 3. TONE TRANSMISSION: INCIDENT
PLANE WAVE AT $\theta = \pi$

where

$$\epsilon_m = \begin{cases} 1 & m = 0 \\ 2 & m \geq 1 \end{cases} .$$

This gives the incident pressure wave as

$$p_i = P_i \exp \left[-i(\omega_o t - k_z z) \right] \sum_{m=0}^{\infty} \epsilon_m i^m J_m(k_x r) \cos m\theta .$$

The reflected (or scattered) wave can be written in the form

$$p_s = \exp \left[-i(\omega_o t - k_z z) \right] \sum_{m=0}^{\infty} A_m H_m^{(1)}(k_x r) \cos m\theta ,$$

where $H_m^{(1)}(k_x r)$ is the Hankel function of the first kind of integer order m , which represents an outward traveling wave for the assumed $e^{-i\omega_o t}$ dependence. A_m are unknown coefficients which remain to be determined. At the cylinder surface, the blocked pressure is

$$p_{bl} = p_i + p_s ,$$

where p_{bl} satisfies the boundary condition associated with a rigid (blocked) surface, i.e.,

$$\frac{\partial p_{bl}}{\partial r} = 0 \quad \text{at } r = a ,$$

which is equivalent to

$$\frac{\partial(p_i + p_s)}{\partial r} = 0 , \quad \text{at } r = a .$$

Thus

$$\left. \frac{\partial p_i}{\partial r} \right)_a = - \left. \frac{\partial p_s}{\partial r} \right)_a .$$

Substituting and canceling out the t and z dependence gives

$$\begin{aligned} P_i &= \sum_{m=0}^{\infty} \epsilon_m i^m J'_m(k_x a) \cos m\theta \\ &= - \sum_{m=0}^{\infty} A_m H_m^{(1)'}(k_x a) \cos m\theta . \end{aligned}$$

On a term-by-term basis, this reduces to

$$A_m = \frac{-\epsilon_m i^m J'_m(k_x a) P_i}{H_m^{(1)'}(k_x a)} ,$$

where

$$J'_m(k_x a) = \left. \frac{d}{dr} J_m(k_x r) \right]_{r=a}$$

$$H_m^{(1)'}(k_x a) = \left. \frac{d}{dr} H_m^{(1)}(k_x r) \right]_{r=a}$$

The blocked pressure is therefore

$$\begin{aligned}
 p_{bl}(z, r, \theta, t) = & P_i \exp \left[-i(\omega_o t - k_z z) \right] \\
 & \times \sum_{m=0} \epsilon_m i^m \cos m\theta \left\{ J_m(k_x r) \right. \\
 & \left. - \frac{J'_m(k_x a)}{H_m^{(1)'}(k_x a)} H_m^{(1)}(k_x r) \right\} . \quad (30)
 \end{aligned}$$

At the surface $\bar{x} = (a, \theta, z)$,

$$\begin{aligned}
 p_{bl}(\bar{x}, t) = & P_i \exp \left[-i(\omega_o t - k_z z) \right] \\
 & \times \sum_{m=0} \epsilon_m i^m \cos m\theta \left\{ J_m(k_x a) \right. \\
 & \left. - \frac{J'_m(k_x a)}{H_m^{(1)'}(k_x a)} H_m^{(1)}(k_x a) \right\} . \quad (31)
 \end{aligned}$$

Consider the term in the braces $\{ \}$, i.e.,

$$\begin{aligned}
 & J_m(k_x a) - \frac{J'_m(k_x a)}{H_m^{(1)'}(k_x a)} H_m^{(1)}(k_x a) \\
 = & \frac{H_m^{(1)'}(k_x a) J_m(k_x a) - J'_m(k_x a) H_m^{(1)}(k_x a)}{H_m^{(1)'}(k_x a)} .
 \end{aligned}$$

Now

$$H_m^{(1)}(k_x a) = J_m(k_x a) + iY_m(k_x a)$$

$$H_m^{(1)'}(k_x a) = J_m'(k_x a) + iY_m'(k_x a)$$

$$= k_x J_{m-1} - \frac{m}{a} J_m + i \left[k_x Y_{m-1} - \frac{m}{a} Y_m \right]$$

Therefore the numerator of the term in the braces is

$$J_m \left[k_x J_{m-1} - \frac{m}{a} J_m + i \left(k_x Y_{m-1} - \frac{m}{a} Y_m \right) \right]$$

$$- \left[k_x J_{m-1} - \frac{m}{a} J_m \right] \left[J_m + iY_m \right]$$

$$= i k_x \left[Y_{m-1} J_m - J_{m-1} Y_m \right]$$

$$= i k_x \left(\frac{2}{\pi k_x a} \right) = \frac{2i}{\pi a} \quad .$$

Here use has been made of an identity given in Morse and Ingard [26]. The term in braces becomes

$$\left\{ \right\} = \frac{2i}{\pi a H_m^{(1)'}(k_x a)} \quad .$$

Again

$$\begin{aligned} H_m^{(1)'}(k_x a) &= k_x [J_{m-1} + iY_{m-1}] - \frac{m}{a} [J_m + iY_m] \\ &= k_x H_{m-1}^{(1)}(k_x a) - \frac{m}{a} H_m^{(1)}(k_x a) \end{aligned}$$

At the surface, the blocked pressure is therefore

$$\begin{aligned} p_{bl}(\bar{x}, t) &= \frac{2P_i}{\pi a} \exp [-i(\omega_o t - k_z z)] \\ &\times \sum_{m=0} \epsilon_m i^{m+1} \cos m\theta / H_m^{(1)'}(k_x a) \end{aligned} \quad (32)$$

Consider the limiting forms of the Hankel function and its derivative for $k_x a \gg m + 1/2$

$$H_m^{(1)}(k_x r) \approx \sqrt{\frac{2}{\pi k_x r}} \exp \left[ik_x r - i\frac{\pi}{2}(m + \frac{1}{2}) \right],$$

so

$$H_m^{(1)'}(k_x a) \approx ik_x \sqrt{\frac{2}{\pi k_x a}} \exp \left[ik_x a - \frac{i\pi}{2} (m + \frac{1}{2}) \right].$$

Substituting this last result into Eq.(32) gives

$$\begin{aligned} p_{bl}(\bar{x}, t) &= \frac{2}{\pi a} P_i \exp [-i(\omega_o t - k_z z)] \\ &\times \sum_{m=0} \frac{\epsilon_m i^{m+1} \cos m\theta}{ik_x \sqrt{\frac{2}{\pi k_x a}} \exp \left[ik_x a - i\frac{\pi}{2} (m + \frac{1}{2}) \right]} \end{aligned}$$

Let

$$k_x a - \frac{\pi}{2} \left(m + \frac{1}{2}\right) = \gamma_m$$

$$\sqrt{\frac{2}{\pi k_x a}} = E_m ; \quad m > 0$$

$$\sqrt{\frac{8}{\pi k_x a}} = E_0$$

Then the above can be written in the form

$$p_{bl}(\bar{x}, t) = \frac{2 P_1}{\pi k_x a} \exp \left[-i(\omega_0 t - k_z z) \right] \\ \times \left\{ \frac{2}{E_0} e^{-i\gamma_0} + \sum_{m=1}^{\infty} \frac{\epsilon_m i^m \cos m\theta e^{-i\gamma_m}}{E_m} \right\} .$$

Since $\epsilon_m = 2$ for $m > 1$,

$$p_{bl}(\bar{x}, t) = \frac{4 P_1}{\pi k_x a} \exp \left[-i(\omega_0 t - k_z z) \right] \\ \times \sum_{m=0}^{\infty} \frac{\cos m\theta}{E_m} e^{-i\gamma_m(i^m)} .$$

But

$$i^m = e^{i\pi m/2} ,$$

so for the case $k_x a \gg m + \frac{1}{2}$

$$p_{bl}(\bar{x}, t) = \frac{4P_i}{\pi k_x a} \exp \left[-i(\omega_o t - k_z z) \right] \\ \times \sum_{m=0}^{\infty} \frac{\cos m\theta}{E_m} e^{+i[-\gamma_m + \pi m/2]} \quad .$$

This result is consistent with Eq.(8.1.6) of [26], which is just a check of the results to this point.

Consider now the average cross correlation of the blocked pressure over the surface

$$R_{p_{bl}}(\bar{x}|\bar{x}'; \tau) = \lim_{T \rightarrow \infty} \frac{1}{T} \int_{-T/2}^{T/2} \text{Re}[p_{bl}(\bar{x}, t)] \text{Re}[p_{bl}(\bar{x}', t+\tau)] dt$$

The general result for the blocked pressure required here is given by Eq.(32).

$$p_{bl}(\bar{x}, t) = \frac{2P_i}{\pi a} \exp \left[-i(\omega_o t - k_z z) \right] \\ \times \sum_{m=0}^{\infty} \epsilon_m i^{m+1} \cos m\theta / H_m^{(1)'}(k_x a) \quad .$$

The lagged pressure is:

$$p_{bl}(\bar{x}', t+\tau) = \frac{2P_i}{\pi a} \exp \left[-i(\omega_o t + \omega_o \tau - k_z z') \right] \\ \times \sum_{n=0}^{\infty} \epsilon_n i^{n+1} \cos n\theta' / H_n^{(1)'}(k_x a) \quad .$$

Since $p_{bl}(x,t)$ is periodic of the form $e^{-i\omega_0 t}$, the time average can be performed over one period, $T_0 = 2\pi/\omega_0$, giving

$$R_{p_{bl}}(\bar{x}|\bar{x}';\tau) = \frac{1}{T_0} \int_{-T_0/2}^{T_0/2} \text{Re}[p_{bl}(\bar{x},t)] \text{Re}[p_{bl}(\bar{x}',t+\tau)] dt .$$

Consider now the following theorem. If

$$a = \bar{A}e^{-i\omega t}; \quad b = \bar{B}e^{-i\omega t}; \quad T = \frac{2\pi}{\omega} ,$$

where \bar{A} and \bar{B} are complex numbers, then

$$\frac{1}{T} \int_{t'}^{t'+T} \text{Re}[a] \text{Re}[b] dt = \frac{1}{2} \text{Re}[\bar{A} \cdot \bar{B}^*] .$$

Let

$$p_{bl}(\bar{x},t) = P_{bl}(\bar{x})e^{-i\omega_0 t}$$

$$p_{bl}(\bar{x}',t+\tau) = P_{bl}(\bar{x}',\tau) e^{-i\omega_0 t} .$$

Then

$$\begin{aligned} R_{p_{bl}}(\bar{x}|\bar{x}';\tau) &= \frac{1}{2} \text{Re} [P_{bl}(\bar{x}) P_{bl}^*(\bar{x}',\tau)] \\ &= \frac{1}{2} \text{Re} \left\{ \frac{4P_1^2}{\pi^2 a^2} e^{i\omega_0 \tau} e^{ik_z(z-z')} \right. \\ &\quad \cdot \sum_{m,n=0}^{\infty} \frac{\epsilon_m \epsilon_n^{m+1} (-i)^{n+1} \cos m\theta \cos n\theta'}{H_m^{(1)'}(k_x a) H_n^{(1)'}(k_x a)^*} \left. \right\} . \end{aligned}$$

This can be rewritten in the form

$$R_{p_{bl}}(\bar{x}|\bar{x}';\tau) = \frac{1}{2} \operatorname{Re} \left\{ \frac{4P^2}{\pi^2 a^2} e^{i[\omega_0 \tau + k_z(z-z')]}\right. \\ \cdot \left[\sum_{m=0}^{\infty} \frac{\epsilon_m^2 \cos m\theta \cos m\theta'}{|H_m^{(1)'}(k_x a)|^2} \right. \\ \left. + \sum_{m \neq n=0}^{\infty} \frac{\epsilon_m \epsilon_n i^{m+1} (-i)^{n+1} \cos m\theta \cos n\theta'}{H_m^{(1)'}(k_x a) H_n^{(1)'}(k_x a)^*} \right] \left. \right\} .$$

The last term involving the summation of terms for which $m \neq n$ is complex. Now note that the cospectral density, $C_{p_{bl}}(\bar{x}|\bar{x}';\omega)$, required in Eq.(29) is to be integrated upon multiplication by the product $\psi^r(\bar{x})\psi^r(\bar{x}')$, where

$$\psi^r(\bar{x}) = \psi_{(\bar{x})}^{MN} = \sin \frac{M\pi z}{L} \cos N\theta \\ \psi^r(\bar{x}') = \psi_{(\bar{x}')}^{MN} = \sin \frac{M\pi z'}{L} \cos N\theta' .$$

Terms of the form $\cos m\theta \cos n\theta'$ will appear in $C_{p_{bl}}(\bar{x}|\bar{x}';\omega)$ after $R_{p_{bl}}(\bar{x}|\bar{x}';\tau)$ has been transformed to obtain it. Since

$$\int_0^{2\pi} \cos N\theta \cos m\theta \, d\theta = \begin{cases} 0; m \neq N \\ \pi; m = N \\ 2\pi; m = N = 0 \end{cases} ,$$

it follows that all terms for which $m \neq n$ vanish when the integral

$$\int_{\bar{x}} \int_{\bar{x}'} C_{p_{bl}}(\bar{x}|\bar{x}';\omega) \psi^r(\bar{x}) \psi^r(\bar{x}') \, d\bar{x} d\bar{x}'$$

is evaluated. Thus, only terms for which $m = n$ need be of concern and $R_{pb1}(\bar{x}|\bar{x}';\tau)$ can be taken in the reduced form

$$R_{pb1}(\bar{x}|\bar{x}';\tau) = \frac{2P_1^2}{\pi^2 a^2} \cos[\omega_0 \tau + k_z(z-z')] \\ \times \sum_{m=0}^{\infty} \frac{\epsilon_m^2 \cos m\theta \cos m\theta'}{|H_m^{(1)'}(k_x a)|^2} .$$

Transforming gives the two sided cross spectrum

$$\bar{S}_{pb1}(\bar{x}|\bar{x}';\omega) = \frac{1}{2\pi} \int_{-\infty}^{\infty} R_{pb1}(\bar{x}|\bar{x}';\tau) e^{i\omega\tau} d\tau \\ = \frac{1}{2\pi} \left(\frac{2P_1^2}{\pi^2 a^2} \right) \sum_{m=0}^{\infty} \frac{\epsilon_m^2 \cos m\theta \cos m\theta'}{|H_m^{(1)'}(k_x a)|^2} \\ \times \int_{-\infty}^{\infty} \cos[\omega_0 \tau + k_z(z-z')] e^{i\omega\tau} d\tau .$$

Now

$$\int_{-\infty}^{\infty} \cos[\omega_0 \tau + k_z(z-z')] e^{i\omega\tau} d\tau \\ = \int_{-\infty}^{\infty} \left\{ \frac{e^{i[\omega_0 \tau + k_z(z-z')]} + e^{-i[\omega_0 \tau + k_z(z-z')]} }{2} \right\} e^{i\omega\tau} d\tau \\ = \frac{1}{2} \left[e^{ik_z(z-z')} 2\pi\delta(\omega+\omega_0) + e^{-ik_z(z-z')} 2\pi\delta(\omega-\omega_0) \right] \\ = \pi \left[\delta(\omega+\omega_0) e^{ik_z(z-z')} + \delta(\omega-\omega_0) e^{-ik_z(z-z')} \right] .$$

This gives

$$\begin{aligned} \bar{S}_{pb1}(\bar{x}|\bar{x}';\omega) &= \frac{P_1^2}{\pi^2 a^2} \sum_{m=0}^{\infty} \frac{\epsilon_m^2 \cos m\theta \cos m\theta'}{|H_m^{(1)'}(k_x a)|^2} \\ &\times \left[\delta(\omega+\omega_0) e^{ik_z(z-z')} + \delta(\omega-\omega_0) e^{-ik_z(z-z')} \right] . \end{aligned}$$

The one-sided cross spectrum is defined by

$$S_{pb1}(\bar{x}|\bar{x}';\omega) = 2 \bar{S}_{pb1}(\bar{x}|\bar{x}';\omega); \quad 0 \leq \omega < \infty$$

$$\begin{aligned} &= \frac{2P_1^2}{\pi^2 a^2} \sum_{m=0}^{\infty} \frac{\epsilon_m^2 \cos m\theta \cos m\theta'}{|H_m^{(1)'}(k_x a)|^2} \\ &\times e^{-ik_z(z-z')} \delta(\omega-\omega_0) . \end{aligned}$$

Note that

$$S_{pb1}(\bar{x}|\bar{x}';\omega) = S_{pb1}^*(\bar{x}'|\bar{x};\omega) .$$

Therefore, the integral

$$\int_{\bar{x}} \int_{\bar{x}'} S_{pb1}(\bar{x}|\bar{x}';\omega) \psi^r(\bar{x}) \psi^r(\bar{x}') d\bar{x} d\bar{x}' ,$$

is also equal to

$$\int_{\bar{x}'} \int_{\bar{x}} S_{pb1}^*(\bar{x}|\bar{x}';\omega) \psi^r(\bar{x}) \psi^r(\bar{x}') d\bar{x} d\bar{x}' .$$

Letting

$$S_{pbl}(\bar{x}|\bar{x}';\omega) = C_{pbl}(\bar{x}|\bar{x}';\omega) - iQ_{pbl}(\bar{x}|\bar{x}';\omega) \quad ,$$

it follows that

$$\int_{\bar{x}} \int_{\bar{x}'} Q_{pbl}(\bar{x}|\bar{x}';\omega) \psi^r(\bar{x}) \psi^r(\bar{x}') d\bar{x} d\bar{x}' = 0 \quad ,$$

i.e., the imaginary part of $S_{pbl}(\bar{x}|\bar{x}';\omega)$ vanishes from the solution (Q_{pbl} = quadrature). Therefore, the only part of the cross spectrum to be used in Eq. (29) is the cospectrum

$$C_{pbl}(\bar{x}|\bar{x}';\omega) = \frac{2P_1^2}{\pi^2 a^2} \sum_{m=0}^{\infty} \frac{\epsilon_m^2 \cos m\theta \cos m\theta'}{|H_m^{(1)'}(k_x a)|^2} \cos k_z(z-z') \delta(\omega-\omega_0) \quad .$$

Substituting into Eq.(29) and integrating with respect to ω gives

$$\begin{aligned} W_{in} &= \frac{2\pi}{\rho V} \left(\frac{mA}{4}\right)^2 \tau_{ML}^0 \frac{2}{\pi} \omega_0^2 \sum_n \frac{\epsilon_n \eta_n}{\omega_n^2} \\ &\times \sum_r \frac{f_{n,r}^2}{M_r^2 \omega_r^4} \left\{ \int_{\bar{x}} \int_{\bar{x}'} C_{pbl}(\bar{x}|\bar{x}') \psi^r(\bar{x}) \psi^r(\bar{x}') d\bar{x} d\bar{x}' \right\} \\ &\times \frac{\omega_0^3}{\left[\left(1 - \frac{\omega_0^2}{\omega_n^2}\right)^2 + \eta_n^2 \right] \left[\left(1 - \frac{\omega_0^2}{\omega_r^2}\right)^2 + \eta_r^2 \right]} \quad , \end{aligned} \quad (33)$$

where

$$C_{pbl}(\bar{x}|\bar{x}') = \frac{2P_1^2}{\pi^2 a^2} \sum_{m=0}^{\infty} \frac{\epsilon_m^2 \cos m\theta \cos m\theta'}{|H_m^{(1)'}(k_x^0 a)|^2} \cos k_z^0(z-z') \quad ,$$

with

$$k_z^o = k^o \cos \phi = (\omega_o/c_o) \cos \phi ; \tau_{ML}^o = \left(\frac{2\rho c_o}{\omega_o m} \right)^2$$

$$k_x^o = k^o \sin \phi = (\omega_o/c_o) \sin \phi .$$

The superscript o on k_x and k_z is to remind that the wavenumbers are evaluated at the excitation frequency ω_o . Performing the integration, and noting that with $r = (M, N)$, all cases $m \neq N$ appearing in the summation $m = 0$ to ∞ vanish, it is found that

$$\begin{aligned} & \int_{\bar{x}} \int_{\bar{x}'} C_{pbl}(\bar{x}|\bar{x}') \psi^r(\bar{x}) \psi^r(\bar{x}') d\bar{x} d\bar{x}' \\ &= \int_0^L \int_0^{2\pi} \int_0^L \int_0^{2\pi} \frac{2P_1^2}{\pi^2 a^2} \frac{\epsilon_N^2 \cos N\theta \cos N\theta'}{|H_N^{(1)'}(k_x^o a)|^2} \cos k_z^o (z-z') \\ & \quad \times \sin \frac{M\pi z}{L} \cos N\theta \sin \frac{M\pi z'}{L} \cos N\theta' a^2 d\theta d\theta' dz dz' \\ &= \frac{2P_1^2}{\pi^2 a^2} \frac{4\pi^2 a^2}{|H_N^{(1)'}(k_x^o a)|^2} \int_0^L \int_0^L \cos k_z^o (z-z') \sin \frac{M\pi z}{L} \sin \frac{M\pi z'}{L} dz dz' \\ &= \frac{8P_1^2 L^2}{|H_N^{(1)'}(k_x^o a)|^2} \int_0^1 \int_0^1 \cos \bar{k}_z^o (\bar{z}-\bar{z}') \sin M\pi \bar{z} \sin M\pi \bar{z}' d\bar{z} d\bar{z}' , \end{aligned} \tag{34}$$

where

$$\bar{k}_z^o = k_z^o L ; \bar{z} = z/L ; \bar{z}' = z'/L .$$

The integral is just the joint acceptance for a non-decaying progressive wave field, i.e.,

$$j_M^2(\omega_o) = \int_0^1 \int_0^1 \cos \bar{k}_Z^O(\bar{z}-\bar{z}') \sin M\pi\bar{z} \sin M\pi\bar{z}' d\bar{z} d\bar{z}' \quad .$$

In general, a progressive wave field with decaying correlation has the form

$$j_M^2(\omega_c) = \int_0^1 \int_0^1 \exp \left[-\frac{k_Z^O |\bar{z}-\bar{z}'|}{a_Z} \right] \cos \bar{k}_Z^O(\bar{z}-\bar{z}') \sin M\pi\bar{z} \sin M\pi\bar{z}' d\bar{z} d\bar{z}' .$$

For $a_Z = \infty$, this reduces to the non-decaying progressive wave field. This is denoted by $j_M^2(\omega_o, a_Z = \infty)$. Eq.(33) therefore becomes

$$W_{in} = \frac{32P_1^2 L^2}{\rho V} \left(\frac{mA}{4} \right)^2 \tau_{ML}^O \omega_o^5 \sum_n \frac{\epsilon_n \eta_n}{\omega_n^2} \left[\left(1 - \frac{\omega_o^2}{\omega_n^2} \right)^2 + \eta_n^2 \right]^{-1} \\ \times \sum_{r=MN} \frac{f_r'^2(n,r)}{M_r^2 \omega_r^4} \frac{j_M^2(\omega_o, a_Z = \infty)}{|H_N^{(1)'}(k_X^O a)|^2} \left[\left(1 - \frac{\omega_o^2}{\omega_r^2} \right)^2 + \eta_r^2 \right]^{-1} \quad . \quad (35)$$

This is the fundamental result for the inflowing power.

The power absorbed by the wall is

$$W_{abs} = \frac{V}{\rho c_o^2} \sum_n \frac{\eta_n \omega_n^2}{\omega_o} \langle p_n^2 \rangle_{s,t} \quad ,$$

where $\langle p_n^2 \rangle_{s,t}$ is the space averaged mean square pressure attributable to the nth acoustic mode.

Equating W_{in} to W_{abs} on a mode-by-mode basis gives (upon setting $\langle p_1^2 \rangle_t = P_1^2/2 =$ mean square pressure of incoming wave)

$$\begin{aligned} \langle p_n^2 \rangle_{s,t} &= \frac{64 \langle p_1^2 \rangle_t L^2}{V^2} \left(\frac{mA}{4} \right)^2 \tau_{ML}^0 \frac{\omega_0^6}{\omega_n^4} c_0^2 \epsilon_n \\ &\times \left[\left(1 - \frac{\omega_0^2}{\omega_n^2} \right)^2 + \eta_n^2 \right]^{-1} \\ &\times \sum_{r=M,N} \frac{f'^2(n,r)}{M_r^2 \omega_r^4} \frac{j_M^2(\omega_0, a_z = \infty)}{|H_N^{(1)'}(k_x^0 a)|^2} \left[\left(1 - \frac{\omega_0^2}{\omega_r^2} \right)^2 + \eta_r^2 \right]^{-1}. \end{aligned} \quad (36)$$

In the above, as before

$$\begin{aligned} \epsilon_n &= \epsilon_{qNs} = V / \iiint_V \phi_{qNs}^2 dv \\ \iiint_V \phi_{qNs}^2 (\bar{\xi}) dv &= \left[\frac{m_{Ns}^2 a^2 - N^2}{2m_{Ns}^2} J_N^2(m_{Ns} a) \right] \frac{\pi L}{2} \epsilon_q \epsilon_N \\ \epsilon_q, \epsilon_N &= \begin{cases} 2; q, N = 0 \\ 1; q, N > 0 \end{cases} \end{aligned}$$

and

$$f'(n,r) = f'(qNs, MN) \quad .$$

Also

$$H_N^{(1)'}(k_x^0 a) = k_x^0 H_{N-1}^{(1)}(k_x^0 a) - \frac{N}{a} H_N^{(1)}(k_x^0 a) \quad .$$

The range on N is 0, 1, 2, ...
 M is 1, 2, 3, ...
 q is 0, 1, 2, ...
 s is 1, 2, 3, ...

Note, for instance

$$\begin{aligned} H_O^{(1)'}(k_X^O a) &= k_X^O H_{-1}^{(1)}(k_X^O a) \\ &= k_X^O e^{i\pi} H_1^{(1)}(k_X^O a) \quad , \end{aligned}$$

so

$$|H_O^{(1)'}(k_X^O a)|^2 = k_X^{O^2} |J_1(k_X^O a) + i Y_1(k_X^O a)|^2 \quad .$$

Also

$$H_1^{(1)'}(k_X^O a) = k_X^O H_O^{(1)}(k_X^O a) - \frac{1}{a} H_1^{(1)}(k_X^O a) \quad ,$$

etc.

Finally, the space average interior level at frequency ω_O is found using

$$\langle p_i^2 \rangle_{s,t} = \sum_n \langle p_n^2 \rangle_{s,t} \quad . \quad (37)$$

The joint acceptance function required for progressive wave excitation is obtained from Wilby [27],

$$j_M^2(\omega_o, a_z = \infty) = \frac{2}{(M\pi)^2 \Delta_M^2} \left[p_M \left\{ 1 - (-1)^M e^{-\frac{k_z^o L}{a_z}} \cos k_z^o L \right\} \right. \\ \left. + 4(-1)^M q_M e^{-\frac{k_z^o L}{a_z}} \sin k_z^o L + \frac{M\pi}{2} r_M \Delta_M \right]_{a_z = \infty},$$

with

$$\Delta_M = \left[1 + \left(\frac{k_z^o L}{M\pi} \right)^2 + \left(\frac{k_z^o L}{a_z M\pi} \right)^2 \right]^2 - 4 \left[\frac{k_z^o L}{M\pi} \right]^2 \\ p_M = \left[1 - \left(\frac{k_z^o L}{M\pi} \right)^2 + \left(\frac{k_z^o L}{a_z M\pi} \right)^2 \right]^2 - 4 \left[\frac{k_z^o L}{M\pi} \right]^2 \left[\frac{k_z^o L}{a_z M\pi} \right]^2 \\ q_M = \left[\frac{k_z^o L}{M\pi} \right] \left[\frac{k_z^o L}{a_z M\pi} \right] \left[1 - \left(\frac{k_z^o L}{M\pi} \right)^2 + \left(\frac{k_z^o L}{a_z M\pi} \right)^2 \right] \\ r_M = \left[\frac{k_z^o L}{a_z M\pi} \right] \left[1 + \left(\frac{k_z^o L}{M\pi} \right)^2 + \left(\frac{k_z^o L}{a_z M\pi} \right)^2 \right] \quad . \quad (38)$$

3.6 Response to Point Input Harmonic Mechanical Excitation

The displacement response of the cylinder is

$$W(\bar{x}) = \sum_r \bar{\xi}_r \psi^r(\bar{x}) \quad .$$

$\bar{\xi}_r = \bar{\xi}_r(\omega)$ is the modal displacement which is a solution of the equation

$$\left[-Y_r M_r + \rho \omega^2 (I^{rr} + J^{rr}) \right] \bar{\xi}_r + \rho \omega^2 \sum_{s \neq r} (I^{rs} + J^{rs}) \bar{\xi}_s = -\Gamma_{pbl}^r \quad . \quad (39)$$

Eq.(39) is the same as Eq.(4), Section I of [19]. The above can be written in the form

$$a_{rr} \bar{\xi}_r + \sum_{r \neq s} a_{rs} \bar{\xi}_s = -\Gamma_{pbl}^r \quad ,$$

or alternately as

$$[a_{rs}] \{ \bar{\xi}_s \} = \{ -\Gamma_{pbl}^r \} \quad ,$$

with solution

$$\{ \bar{\xi}_r \} = [\bar{\alpha}_{rt}] \{ -\Gamma_{pbl}^t \} \quad .$$

Equivalently

$$\bar{\xi}_r = - \sum_t \bar{\alpha}_{rt} \Gamma_{pbl}^t(\omega) \quad ,$$

so

$$W(\bar{x}, \omega) = - \sum_{r,t} \psi^r(\bar{x}) \bar{\alpha}_{rt} \Gamma_{pbl}^t(\omega) \quad . \quad (40)$$

In the above $\Gamma_{p_{bl}}^t(\omega)$ is the generalized blocked force

$$\Gamma_{p_{bl}}^t(\omega) = \int_{\bar{x}} p_{bl}(\bar{x};\omega) \psi^t(\bar{x}) d\bar{x} \quad .$$

For the present purpose, structural intermodal coupling will be neglected. This reduces the solutions for the modal displacements to

$$\begin{aligned} \bar{\xi}_r &= -\Gamma_{p_{bl}}^r(\omega)/a_{rr} \\ &= -\bar{\alpha}_{rr} \Gamma_{p_{bl}}^r(\omega) \quad , \end{aligned}$$

giving

$$W(\bar{x},\omega) = - \sum_r \psi^r(\bar{x}) \bar{\alpha}_{rr}(\omega) \Gamma_{p_{bl}}^r(\omega) \quad , \quad (41)$$

where

$$\bar{\alpha}_{rr} = \left\{ -Y_r M_r + \rho \omega^2 (I^{rr} + J^{rr}) \right\}^{-1} \quad .$$

Now consider the generalized blocked force. For the case of point harmonic mechanical excitation at $\bar{x} = \bar{x}_0 \equiv (a, \theta_0, z_0)$,

$$p_{bl}(\bar{x},\omega) = F(\omega) \delta(\bar{x}-\bar{x}_0) \quad .$$

Note that $p_{bl}(\bar{x},t) = F\delta(\bar{x}-\bar{x}_0)e^{-i\omega t}$, i.e., $F(\omega)$ is the amplitude of the force when the frequency is ω .

In this case, for the cylinder

$$\delta(\bar{x}-\bar{x}_o) = \frac{1}{a} \delta(\theta-\theta_o) \delta(z-z_o) \quad .$$

Therefore (for the ideal cylinder)

$$\begin{aligned} \Gamma_{pbl}^r(\omega) &= \int_o^{2\pi} \int_o^L \frac{F(\omega)}{a} \delta(\theta-\theta_o) \delta(z-z_o) \\ &\times \sin \frac{M\pi z}{L} \cos N(\theta - \theta_1) a d\theta dz \\ &= F(\omega) \sin \frac{M\pi z_o}{L} \cos N(\theta_o - \theta_1) \quad . \quad (42) \end{aligned}$$

θ_1 is a reference angle which is set equal to θ_o for the case of the ideal homogeneous cylinder. This gives

$$\Gamma_{pbl}^r(\omega) = F(\omega) \sin \frac{M\pi z_o}{L} = \Gamma_{pbl}^{MN}(\omega) \quad .$$

Substituting, the response is found to be

$$\begin{aligned} W(\bar{x}, \omega) &= - \sum_{M, N} \sin \frac{M\pi z}{L} \cos N(\theta - \theta_o) \\ &\times \left\{ -Y_{MN} M_{MN} + \rho \omega^2 \left(I^{MNMN} + J^{MNMN} \right) \right\}^{-1} \\ &\times F(\omega) \sin \frac{M\pi z_o}{L} \quad . \end{aligned}$$

The acoustic effects are negligible in the sense that the acoustic reactance is much smaller than the shell reactance. The internal radiation resistance is small compared to the external which may or may not be comparable to the mechanical resistance. Thus we can write

$$Y_{MN} M_{MN} + \rho \omega^2 \left(I^{MNMN} + J^{MNMN} \right) ,$$

as

$$\approx Y_{MN} M_{MN} ,$$

where

$$Y_{MN} = \omega_{MN}^2 \left[\left(1 - \frac{\omega^2}{\omega_{MN}^2} \right) - i \eta_{MN} \right] ,$$

in which η_{MN} is the sum of the mechanical (structural) and external radiation loss factors. Therefore,

$$W(z, \theta, \omega) = F(\omega) \sum_{\substack{M=1 \\ N=0}}^{\infty} \frac{\sin \frac{M\pi z_0}{L}}{Y_{MN} M_{MN}} \sin \frac{M\pi z}{L} \cos N(\theta - \theta_0) . \quad (43)$$

The time mean square displacement is

$$\langle w^2(z, \theta) \rangle_t = \frac{|W(z, \theta, \omega)|^2}{2} = \frac{1}{2} \text{Re} [W \cdot W^*] .$$

Therefore,

$$\begin{aligned}
\langle w^2(z, \theta) \rangle_t &= \frac{1}{2} \operatorname{Re} \left[F^2 \sum_{MN} \sum_{mn} \frac{\sin \frac{M\pi z_o}{L} \sin \frac{m\pi z_o}{L}}{Y_{MN} Y_{mn}^* M_{MN} M_{mn}} \right. \\
&\quad \left. \times \sin \frac{M\pi z}{L} \cos N(\theta - \theta_o) \sin \frac{m\pi z}{L} \cos n(\theta - \theta_o) \right] \\
&= \frac{F^2}{2} \sum_{MN} \frac{\sin^2 \frac{M\pi z_o}{L}}{|Y_{MN}|^2 M_{MN}^2} \sin^2 \frac{M\pi z}{L} \cos^2 N(\theta - \theta_o) \\
&\quad + \frac{F^2}{2} \operatorname{Re} \sum_{\substack{MN \\ MN \neq mn}} \sum_{mn} \frac{\sin \frac{M\pi z_o}{L} \sin \frac{m\pi z_o}{L}}{Y_{MN} Y_{mn}^* M_{MN} M_{mn}} \sin \frac{M\pi z}{L} \cos N(\theta - \theta_o) \\
&\quad \times \sin \frac{m\pi z}{L} \cos n(\theta - \theta_o) .
\end{aligned}$$

Consider the summation in which $MN \neq mn$. For every pair of modes $r = MN$, $s = mn$, there is a corresponding pair $r = mn$, $s = MN$. The sum of the two is

$$\frac{\sin \frac{M\pi z_o}{L} \sin \frac{m\pi z_o}{L} \sin \frac{M\pi z}{L} \sin \frac{m\pi z}{L} \cos N(\theta - \theta_o) \cos n(\theta - \theta_o)}{M_{MN} M_{mn}} \left\{ \frac{1}{Y_{MN} Y_{mn}^*} + \frac{1}{Y_{mn} Y_{MN}^*} \right\}$$

This can be written as

$$\begin{aligned}
&\frac{Q_{MNmn}(\theta, z; \theta_o, z_o)}{M_{MN} M_{mn}} \left\{ \frac{1}{Y_{MN} Y_{mn}^*} + \frac{1}{Y_{mn} Y_{MN}^*} \right\} \\
&= \frac{2Q_{MNmn}(\theta, z; \theta_o, z_o)}{M_{MN} M_{mn}} \left\{ \frac{\operatorname{Re}[Y_{MN}] \operatorname{Re}[Y_{mn}] + \operatorname{Im}[Y_{MN}] \operatorname{Im}[Y_{mn}]}{|Y_{MN}|^2 |Y_{mn}|^2} \right\},
\end{aligned}$$

which is a real quantity. Thus it is possible to write the time mean square displacement at a given point on the cylinder in the form

$$\begin{aligned} \langle w^2(z, \theta) \rangle_t = \frac{F^2}{2} \left\{ \sum_{MN} \frac{Q_{MNMN}(\theta, z; \theta_o, z_o)}{|Y_{MN}|^2 M_{MN}^2} \right. \\ \left. + \sum_{\substack{MN \\ MN \neq mn}} \sum_{mn} \frac{Q_{MNmn}(\theta, z; \theta_o, z_o)}{Y_{MN} Y_{mn}^* M_{MN} M_{mn}} \right\}, \quad (44) \end{aligned}$$

where

$$\begin{aligned} Q_{MNMn}(\theta, z; \theta_o, z_o) = \sin \frac{M\pi z_o}{L} \sin \frac{m\pi z_o}{L} \sin \frac{M\pi z}{L} \sin \frac{m\pi z}{L} \\ \cdot \cos N(\theta - \theta_o) \cos n(\theta - \theta_o). \end{aligned}$$

This is a fundamental result.

The acceleration is

$$\langle a^2(z, \theta) \rangle_t = \omega^4 \langle W^2(z, \theta) \rangle_t.$$

The space-average mean-square displacement is

$$\langle w^2(z, \theta) \rangle_{t, \bar{x}} = \frac{1}{2\pi a L} \int_0^L \int_0^{2\pi} \langle w^2(z, \theta) \rangle_t \, a d\theta dz.$$

Since all the cross terms integrate to zero,

$$\begin{aligned}
\langle w^2(z, \theta) \rangle_{t, \bar{x}} &= \frac{1}{2\pi aL} \int_0^L \int_0^{2\pi} \frac{F^2}{2} \sum_{MN} \frac{Q_{MNMN}(\theta, z; \theta_0, z_0)}{|Y_{MN}|^2 M_{MN}^2} a d\theta dz \\
&= \frac{F^2}{4\pi L} \sum_{MN} \frac{\sin^2 \frac{M\pi z_0}{L}}{|Y_{MN}|^2 M_{MN}^2} \int_0^L \sin^2 \frac{M\pi z}{L} dz \\
&\quad \times \int_0^{2\pi} \cos^2 N(\theta - \theta_0) d\theta .
\end{aligned}$$

Now

$$\begin{aligned}
\int_0^L \sin^2 \frac{M\pi z}{L} dz &= \frac{L}{2} \\
\int_0^{2\pi} \cos^2 N(\theta - \theta_0) d\theta &= \pi \epsilon_N
\end{aligned}$$

where

$$\epsilon_N = \begin{cases} 2 & N = 0 \\ 1 & N > 0 \end{cases} .$$

Therefore,

$$\langle w^2(z, \theta) \rangle_{t, \bar{x}} = \frac{F^2}{8} \sum_{MN} \frac{\epsilon_N \sin^2 \frac{M\pi z_0}{L}}{|Y_{MN}|^2 M_{MN}^2} .$$

For the cylinder

$$M_{MN} = \frac{\epsilon_N^{mA}}{4} = \frac{\epsilon_N^{M_T}}{4} ,$$

where M_T is the total mass of the cylinder wall, so

$$\langle w^2(z, \theta) \rangle_{t, \bar{x}} = \frac{2F^2}{M_T^2} \sum_{MN} \frac{\sin^2 \frac{M\pi z_0}{L}}{\epsilon_N |Y_{MN}|^2} . \quad (45)$$

This is a fundamental result.

Interior Sound Level - Point Harmonic Mechanical Excitation

At any point $\bar{\xi}$ in the cavity, the pressure is

$$p^i(\bar{\xi}) = -\rho\omega^2 \int_{\bar{x}} G_p(\bar{x}|\bar{\xi}; \omega) w(\bar{x}) d\bar{x} , \quad (46)$$

where the interior space Green's function is

$$G_p(\bar{x}|\bar{\xi}; \omega) = \sum_n \frac{\phi_n(\bar{x})\phi_n(\bar{\xi})}{\iiint \phi_n^2(\bar{\xi}) d\bar{v} (\bar{\lambda}_n^2 - k^2)} .$$

Substituting the results for the cylinder gives

$$\begin{aligned} G_p(\bar{x}|\bar{\xi}; \omega) &= G_p(a, \theta, z | r', \theta', z'; \omega) \\ &= \sum_{q, n, s} \frac{\epsilon_{qns} \cos n(\theta - \theta') J_n(m_{ns}a) J_n(m_{ns}r') \cos \frac{q\pi z}{L} \cos \frac{q\pi z'}{L}}{V(\bar{\lambda}_{qns}^2 - k^2)} . \end{aligned} \quad (47)$$

According to Eq. (43), for harmonic force F applied at z_o, θ_o

$$W(\bar{x}) = W(z, \theta) = F \sum_{MN} \frac{\sin \frac{M\pi z_o}{L}}{Y_{MN}^M M_{MN}} \sin \frac{M\pi z}{L} \cos N(\theta - \theta_o). \quad (48)$$

Substituting Eqs.(47) and (48) into Eq. (46) gives the interior pressure as

$$\begin{aligned} p_i(\bar{\xi}) = p_i(r', \theta', z') = & -\rho\omega^2 \sum_{qns} \sum_{MN} \frac{\epsilon_{qns} F \sin \frac{M\pi z_o}{L}}{V(\bar{\lambda}_{qns}^2 - k^2) Y_{MN}^M M_{MN}} \\ & \times J_n(m_{ns}a) J_n(m_{ns}r') \cos \frac{q\pi z'}{L} \\ & \times \int_0^{2\pi} \cos n(\theta - \theta') \cos N(\theta - \theta_o) d\theta \\ & \times \int_0^L \sin \frac{M\pi z}{L} \cos \frac{q\pi z}{L} dz \quad . \end{aligned}$$

Now consider the trigonometric identity

$$\cos n(\theta - \theta') = \cos n\theta \cos n\theta' + \sin n\theta \sin n\theta'$$

The product required under the integral $\int_0^{2\pi}$ above is

$$\begin{aligned} \cos n(\theta - \theta') \cos N(\theta - \theta_o) = & \\ & \cos n\theta \cos N\theta \cos n\theta' \cos N\theta_o + \cos N\theta \cos N\theta_o \\ & \times \sin n\theta \sin n\theta' + \cos n\theta \cos n\theta' \sin N\theta \sin N\theta_o \\ & + \sin n\theta \sin n\theta' \sin N\theta \sin N\theta_o \quad . \end{aligned}$$

In the integral, all cases in which $n \neq N$ vanish.

Also,

$$\int_0^{2\pi} \cos^2 N\theta d\theta = \pi \epsilon_N$$

$$\int_0^{2\pi} \sin^2 N\theta d\theta = \begin{cases} \pi & N > 0 \\ 0 & N = 0 \end{cases}$$

$$\int_0^{2\pi} \cos N\theta \sin N\theta d\theta = 0.$$

Therefore the integral

$$\begin{aligned} & \int_0^{2\pi} \cos N(\theta - \theta') \cos N(\theta - \theta_0) a d\theta \\ &= \epsilon_N \pi a \cos N(\theta' - \theta_0) \end{aligned}$$

Now let

$$D_{Mq} = \int_0^L \sin \frac{M\pi z}{L} \cos \frac{q\pi z}{L} dz = \begin{cases} L f_{qM} & M \neq q \\ 0 & M = q \end{cases}$$

Then the interior pressure becomes

$$\begin{aligned} p_i(r', \theta', z') &= -\rho \omega^2 \frac{F}{V} \sum_{MNqs} \frac{\epsilon_{qNs}}{(\bar{\lambda}_{qNs}^2 - k^2)} \frac{\sin \frac{M\pi z_0}{L}}{M_{MN}^Y MN} J_N(m_{Ns} a) D_{Mq} \\ &\times \epsilon_N \pi a \cos N(\theta' - \theta_0) J_N(m_{Ns} r') \cos \frac{q\pi z'}{L} \end{aligned} \quad (49)$$

This is a fundamental result.

The space-averaged mean square pressure is

$$\langle p_i^2(r', \theta', z') \rangle_{s,t} = \frac{1}{2V} \iiint_V [p_i(r', \theta', z') p_i^*(r', \theta', z')] r' dr' d\theta' dz' .$$

Consider the term

$$\iiint_V \left[\cos N(\theta' - \theta_0) J_N(m_{Ns} r') \cos \frac{q\pi z'}{L} \right] \times \left[\cos N'(\theta' - \theta_0) J_{N'}(m_{N's} r') \cos \frac{q'\pi z'}{L} \right] r' dr' d\theta' dz' .$$

This is non-zero only when $N=N'$, $s=s'$, $q=q'$ and becomes simply

$$\iiint_V \phi_{qNs}(\bar{\xi}) d\bar{v} = V/\epsilon_{qNs} .$$

The space-averaged mean square pressure in the interior therefore reduces to

$$\langle p_i^2 \rangle_{s,t} = \frac{\rho^2 c_o^4 \omega^4 A^2}{2V^2} F^2 \times \sum_{\substack{r=M,N \\ n=q,N,s}} \sin \frac{M\pi z_0}{L} \epsilon_{qNs} f'^2(n, r) \frac{1}{M_r^2} \times \frac{1}{\omega_n^4 \left[\left(1 - \frac{\omega^2}{\omega_n^2}\right) + \eta_n^2 \right]} \frac{1}{\omega_r^4 \left[\left(1 - \frac{\omega^2}{\omega_r^2}\right) + \eta_r^2 \right]} . \quad (50)$$

3.7 Interior Response for Progressive Wave Field Excitation

The solution for the band-limited case can be obtained by equating W_{in} of Eq.(7) to W_{diss} of Eq. (8). Here, as opposed to the case for the noise reduction where the ratio of the interior pressure to the exterior diffuse level was sought, the ratio of the space-average interior to the average blocked pressure is to be determined. Eqs.(1),(3),(7), and (8) give the solution to be used at low frequencies.

$$\begin{aligned} \frac{\langle p_i^2 \rangle_{s,t}}{\langle p_{bl}^2 \rangle_{s,t}} &= \frac{4}{c_\omega^\omega} \frac{A^2}{V^2} \left(\frac{mA}{4} \right)^2 \tau_{ML} c_o^2 \omega^3 \\ &\times \sum_n \epsilon_n \sum_r \frac{j_r^2(\omega) f'^2(n,r)}{M_r^2 D_{nr}} \\ &\times \left\{ \left(\frac{c_r - c_n}{4} \right) \ln_n + \left[\frac{2c_n(b_r - b_n) - b_n(c_r - c_n)}{4\eta_n \omega_n^2} \right] \arctan_n \right. \\ &\left. + \left(\frac{c_n - c_r}{4} \right) \ln_r + \left[\frac{2c_r(b_n - b_r) - b_r(c_n - c_r)}{4\eta_r \omega_r^2} \right] \arctan_r \right\}. \quad (51) \end{aligned}$$

The result is similar to Eq. (10), except that now $j_r^2(\omega) (= j_{MN}^2(\omega))$ is taken as the joint acceptance for the progressive wave field.

The joint acceptance is considered to be separable in the axial and circumferential directions, i.e.,

$$j_{MN}^2(\omega) = j_M^2(\omega) j_N^2(\omega) \quad .$$

The axial component, $j_M^2(\omega)$, is given by Eq. (26), where a_z is allowed to take on finite values to account for the decay in correlation. The joint acceptance for the circumferential bending modes is [23]

$$j_N^2(\omega) = \frac{2\left(\frac{k_y L_y}{a_y}\right)}{(2\pi N)^2 + \left(\frac{k_y L_y}{a_y}\right)^2} + 2 \frac{2\pi N - \frac{k_y L_y}{a_y}}{\left[(2\pi N)^2 + \left(\frac{k_y L_y}{a_y}\right)^2\right]^2} \times \left[1 - \exp\left(-\frac{k_y L_y}{a_y}\right)\right], \quad (52)$$

where k_y is the circumferential trace wavenumber, $L_y = 2\pi a$ is the circumference of the cylinder, and a_y is the decay coefficient. The decay constants a_y and a_z , and the trace wavenumbers k_y and k_z usually must be measured for any excitation field configuration.

The high frequency result is obtained by equating the net inflowing power given by Eq. (29) of Reference [19], i.e., Eq. (53) below,

$$W_{in} = \left[\frac{2\pi n_r}{\omega m^2} \frac{\langle j_r^2 \rangle_r}{\bar{n}_r} \langle p_{bl}^2 \rangle_{s,t} - \frac{2\pi^2 n_r c_o \langle p_i^2 \rangle_{s,t}}{\rho \omega^2 m A} \right] R_{rad}^{int} + \frac{4}{\pi} \frac{A^2}{m^2} \frac{\rho}{c_o} \left[\langle p_{bl}^2 \rangle_{s,t} \sum_{r < \Delta\omega} j_r^2(\omega) j_r^{2rev}(\omega) - 2 \langle p_i^2 \rangle_{s,t} \sum_{r < \Delta\omega} [j_r^{2rev}(\omega)]^2 \right], \quad (53)$$

to the power dissipated given by Eq. (14). The internal radiation resistance required is found with the relation

$$R_{\text{rad}}^{\text{int}}(\omega) = \frac{2\rho c_0 k^2 A^2}{\pi} \langle j_r^2(\omega) \rangle_r^{\text{rev}}, \quad (54)$$

where $\langle \rangle_r$ indicates an average over all structural modes resonant in the band.

3.8 Modifications for the Non-ideal Cylinder

Figure 4 shows the unpressurized, unstiffened cylinder that was used as the Phase I test article. The cylinder differs from an ideal cylinder in that there is a lap joint running longitudinally 0.00457 meters (0.18 inches) wide. At the joint, the cylinder thickness is doubled, as shown in Figure 5. This gives the cylinder a non-uniform surface density. Because of the narrow width of the joint in comparison to the cylinder circumference, the joint can be modeled as a mass discontinuity located at arbitrary angle $\theta = \theta_0$. Previously it has been noted that in the case of an ideal cylinder, acoustic modes with circumferential orders n can be excited only by structure modes with circumferential order $N = n$. The lap joint complicates this simple coupling, causing all of the acoustic modes to be excited by all of the structure modes, as will be shown.

In addition to the above, the test article has end caps which are not rigid. While the noise reduction capability is high, the caps do flank at extremely low frequencies, i.e., below the first acoustic mode of the cavity.



- 67 -

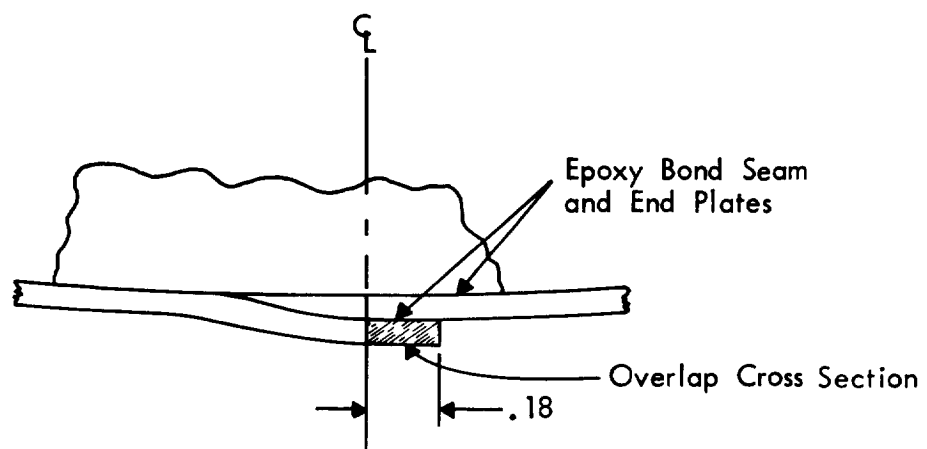


FIGURE 5. CYLINDER LAP JOINT DETAIL

3.8.1 Cylinder Lap Joint Effect

In general, the cylinder wall response for an arbitrary harmonically applied load is given by

$$w(\bar{x}) = \int G(\bar{x}|\bar{x}';\omega) q(\bar{x}') d\bar{x}' \quad , \quad (55)$$

where $q(\bar{x}')$ is the pressure load, $G(\bar{x}|\bar{x}';\omega)$ is the cylinder Green's function,

$$G(\bar{x}|\bar{x}';\omega) = \sum_r \frac{\psi^r(\bar{x}) \psi^r(\bar{x}')}{M_r \bar{Y}_r} \quad ,$$

and

$$\bar{Y}_r = \omega_r^2 \left[1 - \left(\frac{\omega}{\omega_r} \right)^2 - i\eta_r \right] \quad .$$

Consider the case where $q(\bar{x}')$ is a line load along the cylinder at $\theta = \theta_0$, i.e.,

$$q(\bar{x}') = \frac{F'}{a} \delta(\theta' - \theta_0) = q(z', \theta') \quad (56)$$

F' is the force per unit of length in the z direction (axially).

Let the damping be zero, i.e., take $\eta_r = 0$. Then $\bar{Y}_r(\omega) = Y_r(\omega)$. The question to be answered is how do the mode shapes and resonance frequencies change if F' is due to the vibration of a mass distributed along (z, θ_0) .

In terms of the cylindrical coordinates, Eq.(55) becomes

$$w(z, \theta) = \int_0^{2\pi} \int_0^L G(z, \theta | z', \theta'; \omega) q(z', \theta') a d\theta' dz'$$

with

$$G(z, \theta | z', \theta'; \omega) = \sum_r \frac{\psi^r(z, \theta) \psi^r(z', \theta')}{M_{rY_r}(\omega)},$$

and

$$\psi^r(z, \theta) = \psi^{MN}(z, \theta) = \psi_M(z) \psi_N(\theta) = \sin \frac{M\pi z}{L} \begin{Bmatrix} \cos N\theta \\ \sin N\theta \end{Bmatrix}.$$

This gives

$$w(z, \theta) = \sum_r \frac{\psi^r(z, \theta)}{M_{rY_r}(\omega)} \int_0^{2\pi} \int_0^L F' \psi^r(z', \theta') \delta(\theta' - \theta_0) d\theta' dz'.$$

Now let

$$F' = -\omega^2 m' \psi_M(z') w$$

where m' is the mass per unit of length of the line load, and w is an arbitrary amplitude of motion (meters). The hypothesis is that as the frequency of motion ω approaches $\omega_r(1-\delta_r)$, $w(z, \theta)$ takes on the value $\Psi_r(z, \theta) \approx \psi^r(z, \theta)$ which is the new mode shape accounting for the mass discontinuity, provided that m' is not too large. Also, $\omega_r(1-\delta_r)$ is the new resonance frequency. The negative sign is chosen because of the mass being added. δ_r is a constant, presumably small for the case of the lap joint, which must yet be determined. Substituting for F' gives

$$\begin{aligned} w(z, \theta) &= \sum_r \frac{\psi^r(z, \theta)}{M_{rY_r}(\omega)} \int_0^{2\pi} \int_0^L [-\omega^2 m' \psi_M(z') w] \psi^r(z', \theta') \delta(\theta' - \theta_0) d\theta' dz' \\ &= -m' w \sum_r \frac{\omega^2 \psi^r(z, \theta)}{M_{rY_r}(\omega)} \int_0^L \psi^r(z', \theta_0) \psi_M(z') dz' \\ &= -m' w \sum_{MN} \frac{\omega^2 \psi_M(z) \psi_N(\theta) \psi_N(\theta_0)}{M_{MN Y_{MN}}(\omega)} \int_0^L \psi_M^2(z') dz'. \end{aligned}$$

But

$$\begin{aligned} M_{MN} &= \int_0^{2\pi} \int_0^L m \psi_M^2(z) \psi_N^2(\theta) d\theta dz \\ &= m \int_0^L \psi_M^2(z) dz \int_0^{2\pi} \psi_N^2(\theta) d\theta \quad . \end{aligned}$$

Therefore

$$w(z, \theta) = \frac{-m'w}{m} \sum_M \omega^2 \psi_M(z) \sum_N \frac{\psi_N(\theta) \psi_N(\theta_0)}{Y_{MN}(\omega) \int_0^{2\pi} \psi_N^2(\theta) d\theta} \quad .$$

Now let

$$\omega \rightarrow \omega_{mn}(1-\delta_{mn}).$$

Then

$$\omega^2 \rightarrow \omega_{mn}^2(1-2\delta_{mn} + \delta_{mn}^2) \simeq \omega_{mn}^2(1-2\delta_{mn})$$

and

$$Y_{MN}(\omega) \rightarrow \omega_{MN}^2 \left[1 - \frac{\omega_{mn}^2(1-2\delta_{mn})}{\omega_{MN}^2} \right] \quad .$$

In the above, lower case m and n are used to distinguish the mode mn from the mode MN. An approximation for the mode shape for the mnth mode considering the lap joint is

$$\begin{aligned} w(z, \theta) \rightarrow \phi_{mn}(z, \theta) &= \frac{-m'w}{m} \sum_M \omega_{mn}^2(1-2\delta_{mn}) \psi_M(z) \\ &\times \sum_N \frac{\psi_N(\theta) \psi_N(\theta_0)}{\omega_{MN}^2 \left[1 - \frac{\omega_{mn}^2(1-2\delta_{mn})}{\omega_{MN}^2} \right] \int_0^{2\pi} \psi_N^2(\theta) d\theta} \end{aligned}$$

$$\approx - \frac{m'w}{m} \omega_{mn}^2 (1-2\delta_{mn}) \psi_m(z) \\ \times \sum_N \frac{\psi_N(\theta) \psi_N(\theta_o)}{\omega_{mN}^2 \left[1 - \frac{\omega_{mn}^2 (1-2\delta_{mn})}{\omega_{mN}^2} \right] \int_0^{2\pi} \psi_N^2(\theta) d\theta}$$

Now separate out the component "n"

$$\phi_{mn}(z, \theta) = -\frac{m'w}{m} \omega_{mn}^2 \psi_m(z) \left\{ \frac{\psi_n(\theta) \psi_n(\theta_o)}{2\delta_{mn} \omega_{mn}^2 \int_0^{2\pi} \psi_n^2(\theta) d\theta} \right. \\ \left. + \sum_{N \neq n} \frac{\psi_N(\theta) \psi_N(\theta_o)}{\omega_{mN}^2 \left[1 - \frac{\omega_{mn}^2 (1-2\delta_{mn})}{\omega_{mN}^2} \right] \int_0^{2\pi} \psi_N^2(\theta) d\theta} \right\}$$

From this form, it is seen that one can take

$$\phi_m(z) = \psi_m(z)$$

and write

$$\phi_n(\theta) = \left[- \frac{m'w \psi_n(\theta_o)}{2m\delta_{mn} \int_0^{2\pi} \psi_n^2(\theta) d\theta} \right] \psi_n(\theta) \\ - \frac{m'w}{m} \sum_{N \neq n} \frac{\omega_{mn}^2 \psi_N(\theta_o) \psi_N(\theta)}{\omega_{mN}^2 \left[1 - \frac{\omega_{mn}^2}{\omega_{mN}^2} \right] \int_0^{2\pi} \psi_N^2(\theta) d\theta}$$

Now multiply through by

$$\left[- \frac{m'w \psi_n(\theta_o)}{2m\delta_{mn} \int_0^{2\pi} \psi_n^2(\theta) d\theta} \right]^{-1},$$

and let

$$\int_0^{2\pi} \psi_n^2(\theta) d\theta = \gamma_n \quad .$$

Renormalize and call the new mode shape $\Psi_n(\theta)$ (note the capital letter) by setting

$$\left[-\frac{2m\delta_{mn}\gamma_n}{m'w\psi_n(\theta_o)} \right] \phi_n(\theta) = \Psi_n(\theta).$$

Then, it follows that

$$\Psi_n(\theta) \approx \psi_n(\theta) - 2\delta_{mn} \sum_{N \neq n} \frac{\gamma_n}{\gamma_N} \frac{\psi_N(\theta_o)}{\psi_n(\theta_o)} \left[1 - \frac{\omega_{mN}^2}{\omega_{mn}^2} \right]^{-1} \psi_N(\theta) \quad . \quad (57)$$

This result states that the lap joint causes the circumferential mode shape $\psi_n(\theta)$ of the ideal cylinder to take the new value $\Psi_n(\theta)$; this mode shape is approximately equal to $\psi_n(\theta)$, but differs in that components of all other n order are present. Eq. (57) may be thought of as a Fourier representation of $\Psi_n(\theta)$ over the range $0 \leq \theta \leq 2\pi$, i.e.,

$$\Psi_n(\theta) = \psi_n(\theta) + \sum_{N \neq n} A_N \psi_N(\theta) \quad , \quad (58)$$

where

$$A_N = -2\delta_{mn} \frac{\gamma_n}{\gamma_N} \frac{\psi_N(\theta_o)}{\psi_n(\theta_o)} \left[1 - \frac{\omega_{mN}^2}{\omega_{mn}^2} \right]^{-1} \quad .$$

As can be seen, the values of the coefficients A_N depend on the shift in resonance frequency caused by the addition of the line load. Thus, to solve for the coefficients A_N , an estimate for δ_{mn} is needed as a function of m' (i.e., the added mass per unit of length). It can be shown that

$$\delta_{mn} = \frac{B\psi_n^2(\theta_o)a}{2\pi h\gamma_n},$$

where B is the overlap cross-sectional area, A, divided by the radius of the cylinder, i.e.,

$$B = A/a.$$

This gives

$$\delta_{mn} = \frac{A\psi_n^2(\theta_o)}{2\pi h\gamma_n}.$$

3.8.2 Effects of End Caps and Longitudinal Flexibility

The test cylinder has a wall thickness of 0.0016 meters (0.063 inches). The end caps are 0.0127 meters (0.050 inches) thick. Nevertheless the noise reduction of the test article can be limited at low frequencies, i.e., below the lowest acoustic mode of the cavity, by the end caps. The problem is illustrated in Figure 6. At low frequencies, the noise reduction afforded by the cylinder wall can be high, higher perhaps than the noise reduction afforded by the end caps. Whenever this occurs, the effects of the end caps must be taken into account.

The cylinder also has longitudinal flexibility. Whenever a uniform pressure acts on the cylinder, the cylinder shortens. This occurs in addition to the bowing-in of the end caps and shrinking of the circumference of the cylinder. The shrinking of the circumference is accounted for in the dynamics of the present cylinder model. However, the other two effects are not included.

Low Frequency = Long Wavelengths = Uniform Exterior Pressure

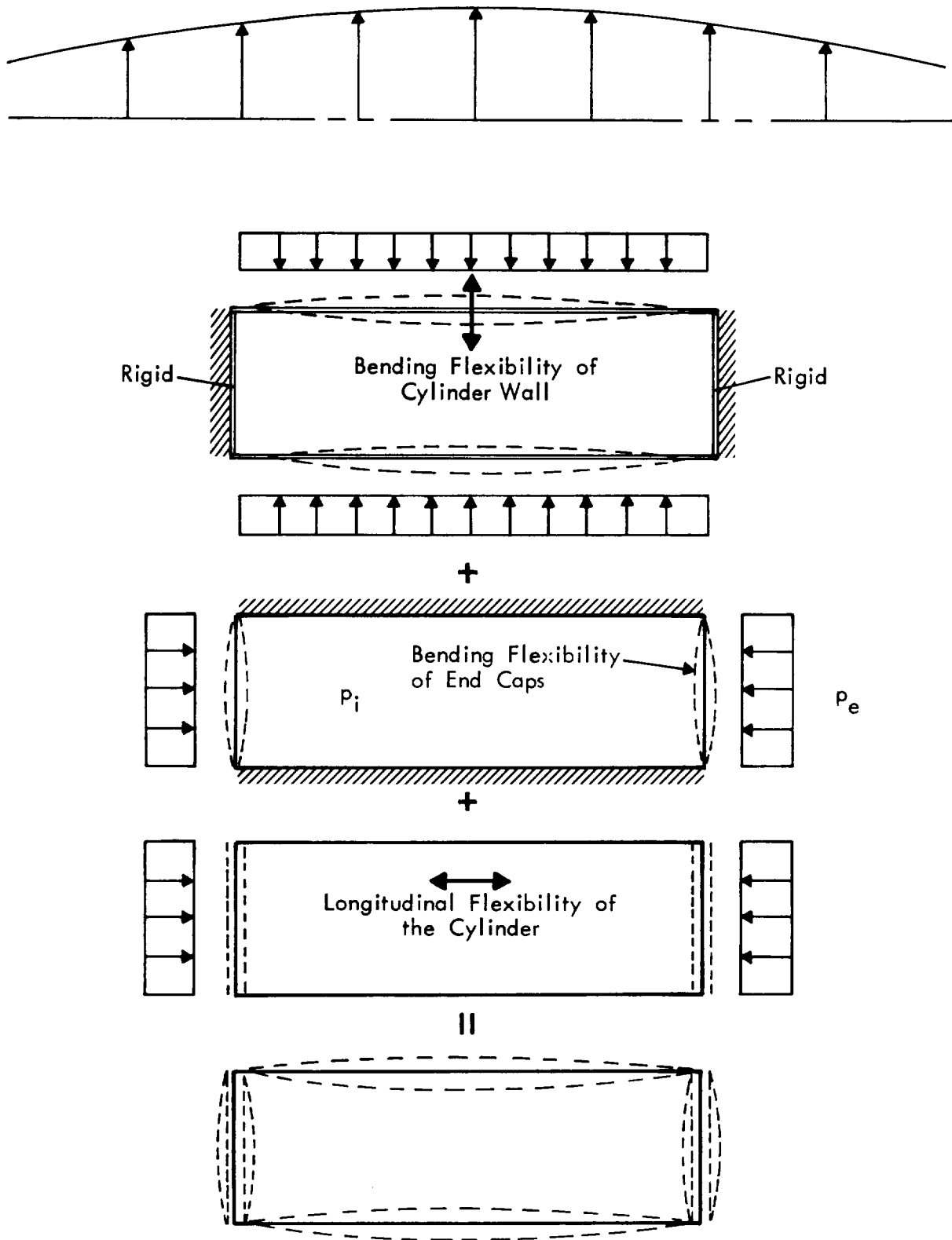


FIGURE 6. LOW FREQUENCY MODEL

Following Lyon [14], the exterior pressure p_e produces an interior pressure p_i through a volume deformation of the end-cap denoted by ΔV . The interior pressure is $p_i = k_c \Delta V$ where k_c is the stiffness of the acoustic volume, i.e., $k_c = 1/C_c$, C_c being the acoustic compliance $C_c = V/\rho c^2$. The volume displacement ΔV is determined from the pressure difference acting on the end cap, $q = p_e - p_i$, and the end cap compliance, C_p , i.e., $\Delta V = (p_e - p_i)C_p$. But ΔV is the same by both calculations, hence

$$(p_e - p_i)C_p = p_i C_c \quad .$$

This gives

$$\frac{p_e}{p_i} = 1 + \frac{C_c}{C_p} \quad ,$$

and the noise reduction as

$$NR = 20 \log \left(1 + \frac{C_c}{C_p} \right) \quad .$$

Hence an expression for the compliance of the end-cap is required

$$C_p = \left(\frac{\Delta V}{p_e - p_i} \right) \quad .$$

Roark [28], gives the displacement of a circular plate, of radius a , with simply supported edges, loaded under uniform pressure q , as

$$y(r) = y_c + \frac{M_c r^2}{2D(1+\mu)} + L T_y,$$

where

$$\begin{aligned} y_c &= \frac{-qa^4(5+\mu)}{64D(1+\mu)} \\ M_c &= \frac{qa^2(3+\mu)}{16} \\ LT_y &= \frac{-qr^4 G_{11}}{D} \end{aligned}$$

and

$$G_{11} = 1/64 \quad .$$

q is the load per unit of area in psi, and D is the bending rigidity, $D = Et^3/12(1-\mu^2)$.

The volume displaced per unit pressure is

$$\begin{aligned} \frac{\Delta V}{q} &= \int_0^{2\pi} \int_0^a y(r) r d\theta dr \\ &= 2\pi \int_0^a (k_1 r + k_2 r^3 + k_3 r^5) dr \end{aligned}$$

where

$$\begin{aligned} k_1 &= \frac{-a^4(5+\mu)}{64D(1+\mu)} \\ k_2 &= \frac{a^2(3+\mu)}{32D(1+\mu)} \\ k_3 &= \frac{-1}{64D} \quad . \end{aligned}$$

This gives for one end cap

$$C_p = \frac{\Delta V}{q} = \frac{\pi a^6}{16D} \left[\frac{2}{4(1+\mu)} + \frac{1}{12} \right] \quad ,$$

and for two end caps

$$C_p = \frac{\pi a^6}{8D} \left[\frac{2}{4(1+\mu)} + \frac{1}{12} \right] \quad . \quad (59)$$

Longitudinal Flexibility

If the cylinder stiffness as a column is taken into account, it is found that the compliance, $C'_p = \Delta V/q$ is

$$C'_p = \frac{\pi a^3 L}{2hE} \quad . \quad (60)$$

Test Article Noise Reduction

The noise reduction owing to the end caps and longitudinal flexibility is denoted here by a bar, i.e.,

$$\overline{NR} = 20 \log \left(1 + \frac{C_c}{C_p + C'_p} \right) \quad (61)$$

where C_p is given by Eq. (59) and C'_p by Eq.(60).

If NR is the cylinder wall noise reduction, then the test article noise reduction, NR_t , is

$$NR_t = -10 \log \left[\frac{1}{2} \left(10^{-NR/10} + 10^{-\overline{NR}/10} \right) \right] \quad . \quad (62)$$

4.0 EXPERIMENTAL INVESTIGATIONS

The Phase I study has a two-fold objective: *development* and *validation* of preliminary analytical models. The development of the analytical models was presented in Section 3. Section 5 will consider the validation. In order to validate the models, an experimental program had to be undertaken to obtain a reasonably comprehensive data base. Experiments were done in joint effort at NASA Langley Research Center, under the supervision of Mr. William H. Mayes and Mr. Conrad Willis, and at BBN in Los Angeles. In some cases, identical tests were performed at both locations. The series of tests was the following:

- 1) Measurements of the structural and acoustic loss factors of the cylinder and of the cavity.
- 2) Measurement of the noise reduction of the cylinder, i.e., the difference between the exterior and the interior sound pressure levels given a random, diffuse (reverberant) exterior acoustic field.
- 3) Measurement of the interior sound level given excitation by a harmonic plane acoustic wave incident at various angles relative to the cylinder axis.
- 4) Measurements of the interior sound level and the acceleration response of the cylinder given a point harmonic (tonal) mechanical excitation of the cylinder wall. [The difference between the interior pressure level (or the cylinder acceleration level) and the applied force level was measured using a broad band noise force input as opposed to a tone. The resulting "transfer functions" are directly comparable to the tonal predictions.]

- 5) Measurement of the interior sound level for the case of excitation by a random, progressive wave field with decaying correlation.

The tests related to the measurements of the acoustic and structural loss factors and the cylinder noise reduction were performed both at LaRC and at BBN. The tone transmission, mechanical excitation, and progressive wave field experiments were done at BBN. In addition to the primary tests above, measurements were made of the cylinder modal characteristics for comparison against the analytical model.

4.1 Phase I Test Article

The cylinder of concern has been briefly described in Section 3 (refer to Figure 4). The cylinder is 1.2192 meters (48 inches) long and has a wall thickness of 0.0016 meters (0.063 inches). Inserted into each end of the cylinder is a 0.0127 meter (0.50 inch) thick ring, which has an inner diameter of 0.4064 meters (16 inches). The rings shorten the cylinder somewhat relative to the length of the enclosed volume. They also disturb the otherwise perfect nature of the cylindrical cavity. However, the effect on the cavity shape is not considered important. Basically, the end rings affect only the cylinder structural dynamics, i.e., they make the cylinder shorter by stiffening the ends. At the same time, the rings provide the important function of maintaining the ends circular. The cylinder is considered to be 1.1938 meters (47 inches) long because of the rings.

4.1.1 Resonance Frequencies

A small acoustic source was mounted inside the bare cylinder and driven with broad-band noise. A Bruel and Kjaer (B&K) Type 4131 25mm microphone was used to measure the resulting sound level and the corresponding spectrum was displayed on a Spectral Dynamics SD 360 analyzer in order to identify the resonance frequencies of acoustic modes. Figure 7 shows a typical response spectrum, in which the lower-frequency resonances have been identified. Acoustic resonances up to about 850 Hz have been identified by comparing measured and calculated results. These are shown in Table 1.

Figure 8 shows the spectrum of the acceleration response of the cylinder surface given acoustic excitation from inside the cylinder. Many peaks in the spectrum correspond to the acoustic modes of the contained volume. The others are the vibration modes of the cylinder structure itself. Some of these are identified in Figure 8 and a more comprehensive comparison is shown in Table 2. Fair agreement exists between measurements and the prediction models, as expected for this ideal configuration. It is clear that as frequency increases, both structure and acoustic modes accumulate quickly and are so closely spaced that their resolution becomes impractical -- hence the recourse to statistical analytical models whenever appropriate. Note that the resonance peaks for both structure and cavity are very sharp, characteristic of a very lightly damped system. More heavily damped systems have wider modal bandwidths and resolution becomes more difficult still.

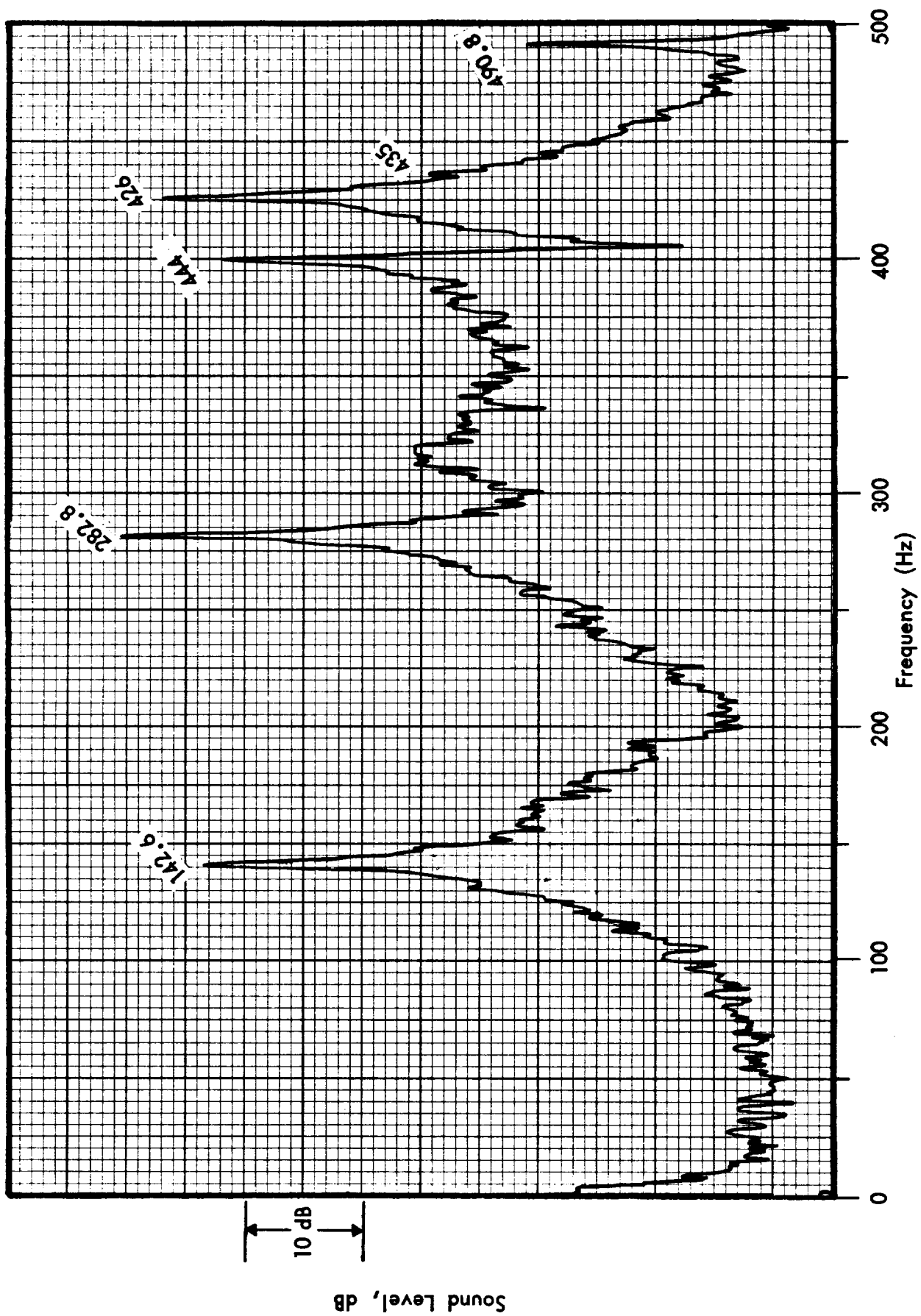


FIGURE 7. INTERIOR ACOUSTIC RESPONSE TO ACOUSTIC SOURCE INSIDE

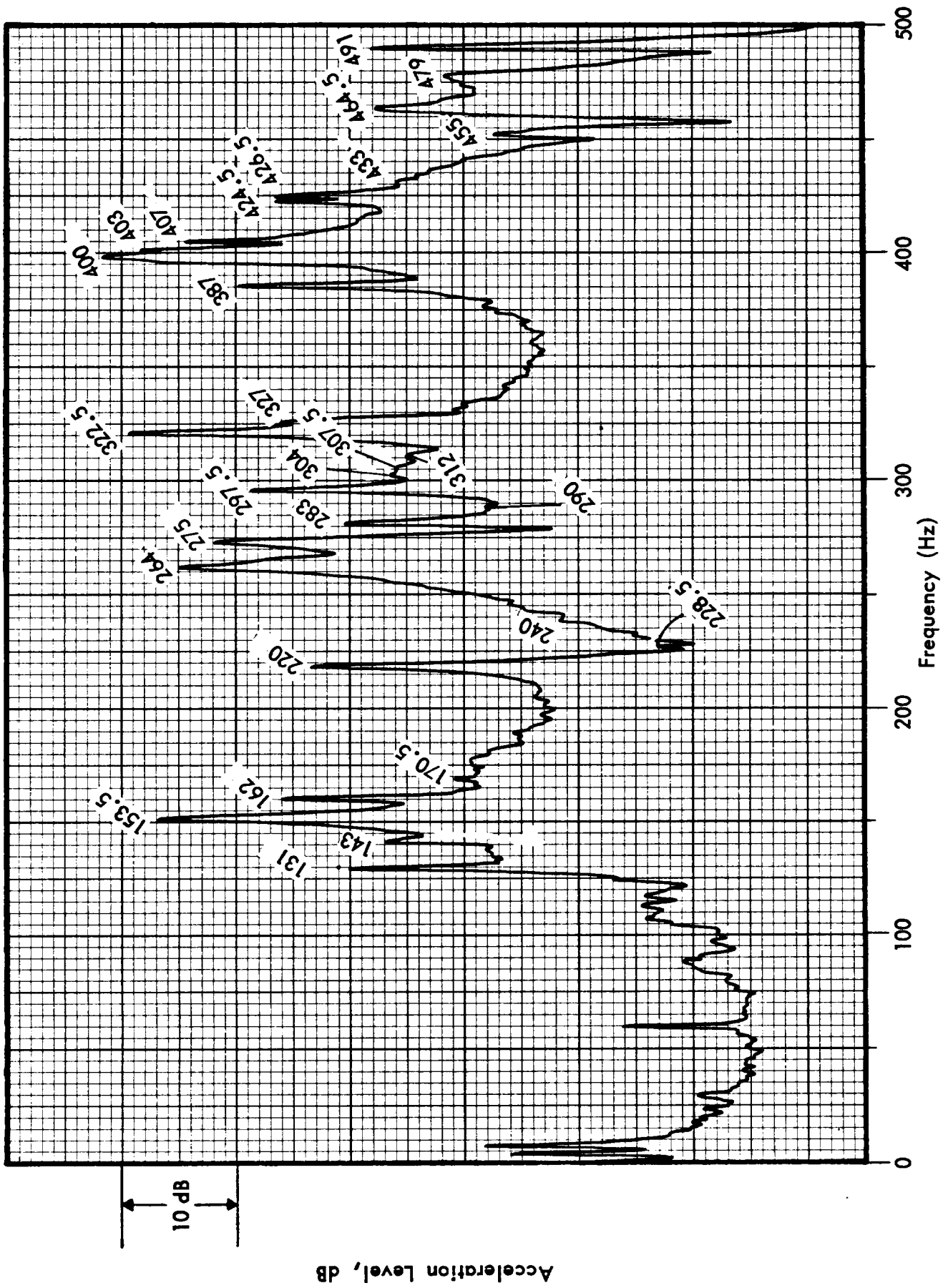


FIGURE 8. CYLINDER ACCELERATION RESPONSE TO INTERIOR ACOUSTIC EXCITATION

Table 1. Acoustic Resonance Frequencies of LaRC Cylinder

Mode q	Order N	s	Calculated Frequency (Hz)	Measured Frequency (Hz)
1	0	1	140.7	142.6
2	0	1	281.4	282.8
0	1	1	395.7	400.0
1	1	1	420.0	--
3	0	1	422.1	426.0
2	1	1	485.6	490.8
4	0	1	562.8	568.0
3	1	1	578.6	585.0
0	2	1	656.4	641.0
1	2	1	671.3	670.0
4	1	1	688.0	685.0
5	0	1	703.4	709.0

Cavity Dimensions $L_c = 1.2192 \text{ m}$
 $a = 0.254 \text{ m}$
 $c_o = 343 \text{ m/s}$

Table 2. Structural Resonance Frequencies of LaRC Cylinder

Mode M	Order N	Calculated Frequency (Hz)	Measured Frequency (Hz)
1	4	126.6	131.0
1	3	153.4	153.5
1	5	159.7	163.0
1	6	221.9	220.0
2	5	264.0	264.0
2	6	272.2	275.0
1	2	289.0	283.0
1	7	301.1	297.5
2	4	331.0	318.0
2	7	327.8	322.5
3	6	400.7	387.0
3	7	403.0	403.0
1	8	394.1	407.0
2	8	410.9	424.0
3	5	456.9	453.0
3	8	456.6	464.0
1	9	500.0	479.0
2	3	510.0	506.0
2	9	512.6	529.0
4	7	531.6	539.0
Cylinder Dimensions		L = 1.1938m (47 in) a = 0.254m (10 in) h = 0.00160m (.063 in)	

Figures 9 and 10 show the computed resonance frequencies for the cylinder and cavity over the range of N orders required for the present study. The cylinder data are for the 1.1938 meter (47 inch) cylinder and differ only slightly from the data for a 1.2192 meter (48 inch) cylinder.

4.1.2 Damping

Estimates of structural and acoustic loss factors are required for use as input data for the various analytical formulations. In general the loss factors vary from mode-to-mode. When band-averaged measurements are made, the resulting loss factor is determined by the most lightly-damped, most strongly excited modes. In general, since the modal forcing function for the driven modes can vary significantly over the band, different excitations can produce different values of band-averaged loss factor, which means that the actual excitation under investigation should be used in the measurement of the average loss factors.

Measurement of the decay of steady-state vibration energy levels after removal of the excitation gives correct estimates of the average loss factors for mechanical or acoustic excitation, but when the coupling, for example, controlling the power flow from the vibrating cylinder to the interior acoustic field depends on, say, only one out of a group of modes resonant in the frequency band of interest, large errors can be produced. In such cases detailed modal measurements are required, and this can be done using single-frequency excitation tuned to the particular modal resonance frequency of interest, measuring the decay rate of the modal energy level or by using a broad band noise and measuring

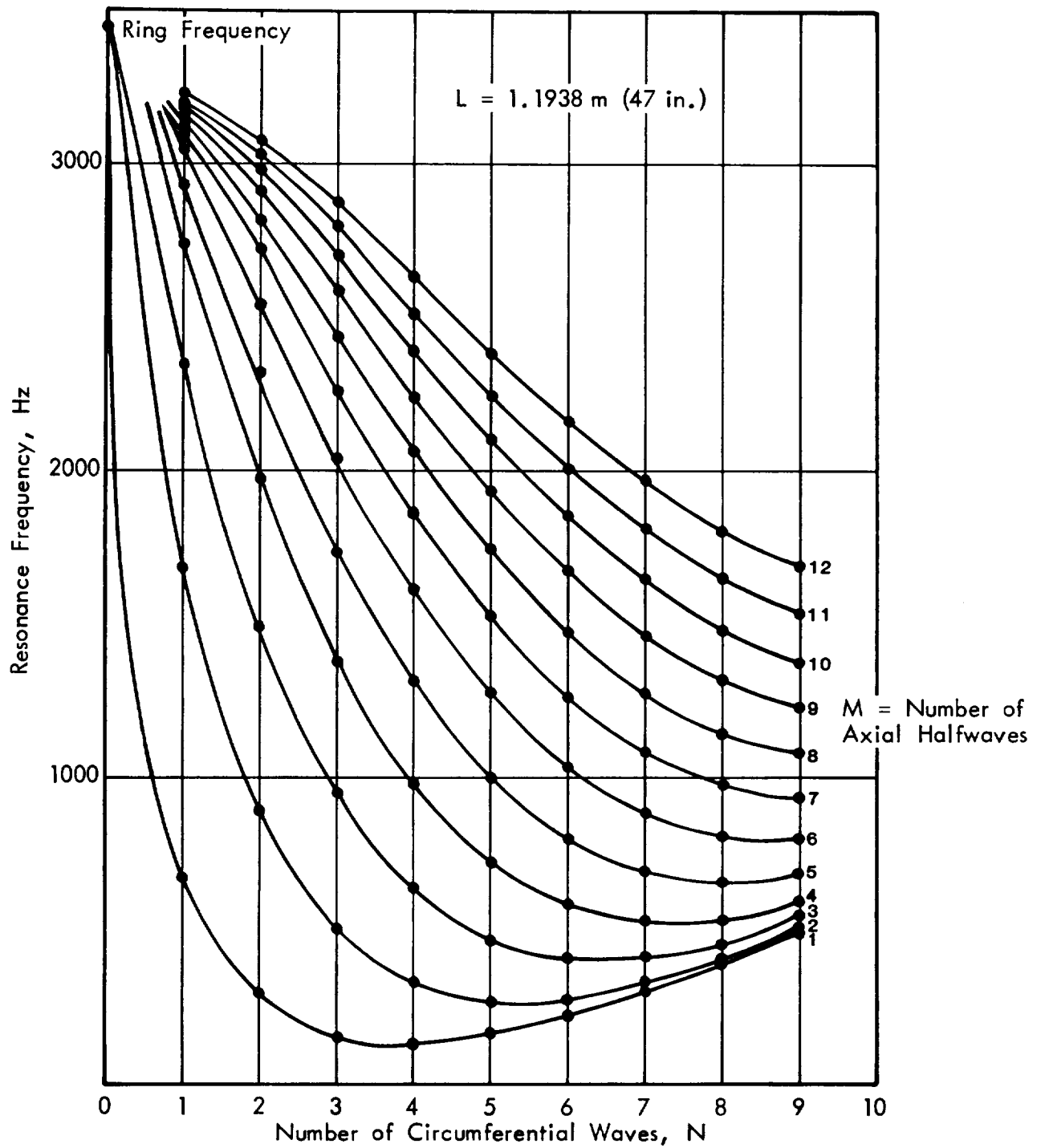


FIGURE 9. CYLINDER STRUCTURE RESONANCE FREQUENCIES

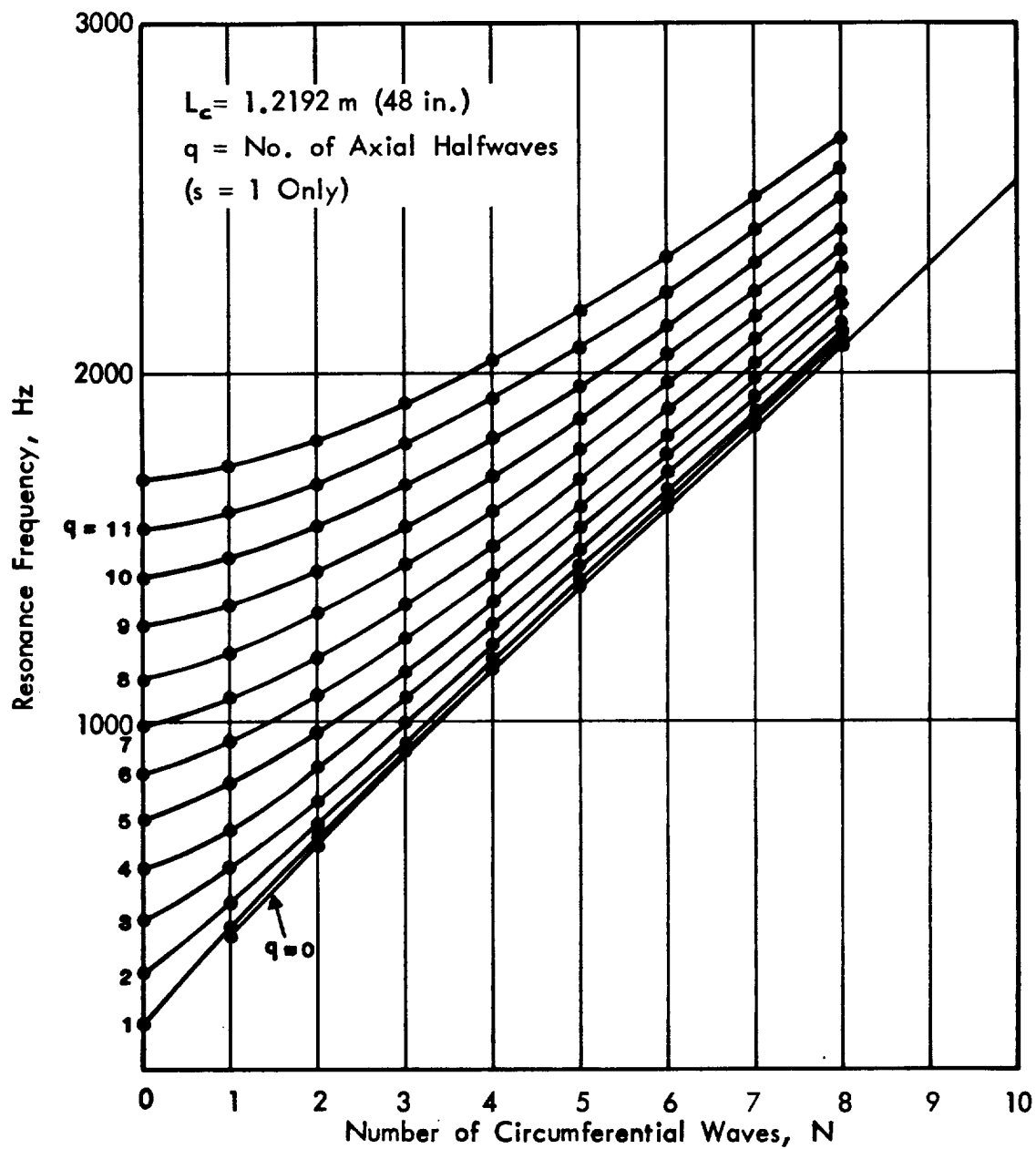


FIGURE 10. CYLINDER ACOUSTIC RESONANCE FREQUENCIES

the bandwidth of the resonance. Both approaches were employed, particularly at low frequencies where modes were widely separated in frequency.

The "response-decay" method involves measurement of the rate of decay of vibration or pressure level from its initial steady-state level after the excitation has been removed. Figure 11 shows the instrumentation used. The amplified response signal is passed to a linear-log converter and then to a variable time-base storage oscilloscope, where the decay rate (ideally, a straight line) is measured with a calibrated protractor. For "response-amplitude" measurements, the analog signal for broad-band excitation is passed to a Spectral Dynamics SD360 Narrow Band Analyzer, fitted with translators, and the bandwidths of particular modes measured by fitting a smooth curve through the digital output response data close to the resonance frequency.

Acoustic loss factors were measured using both methods outlined above, and close agreement was found for the resonant modes. Data were also taken using the response decay method at frequencies well removed from the resonance peaks, thereby reflecting the absence of resonant response. The loss factors were generally an order of magnitude higher than those measured on or close to the resonance frequencies themselves. The measured data are shown in Figure 12. It is clear that the loss factors of the resonant acoustic modes of the bare cylinder are very low.

The LaRC data are also shown in Figure 12. The loss factors of concern correspond to the LaRC case measured without the lead cover. The LaRC data appear to give the damping characteristics of the nonresonant acoustic response at low frequencies.

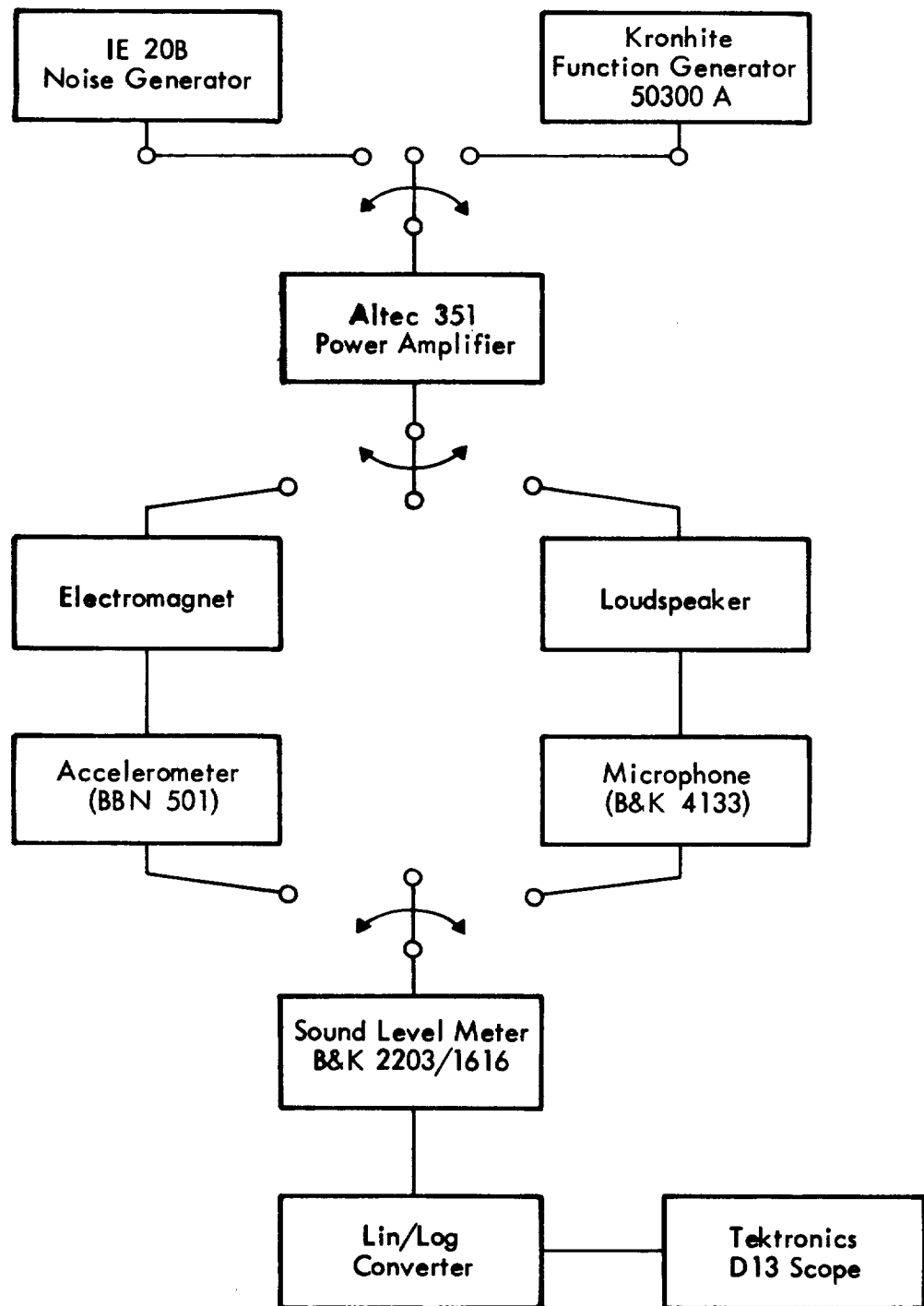


FIGURE 11. TYPICAL INSTRUMENTATION FOR LOSS FACTOR MEASUREMENT

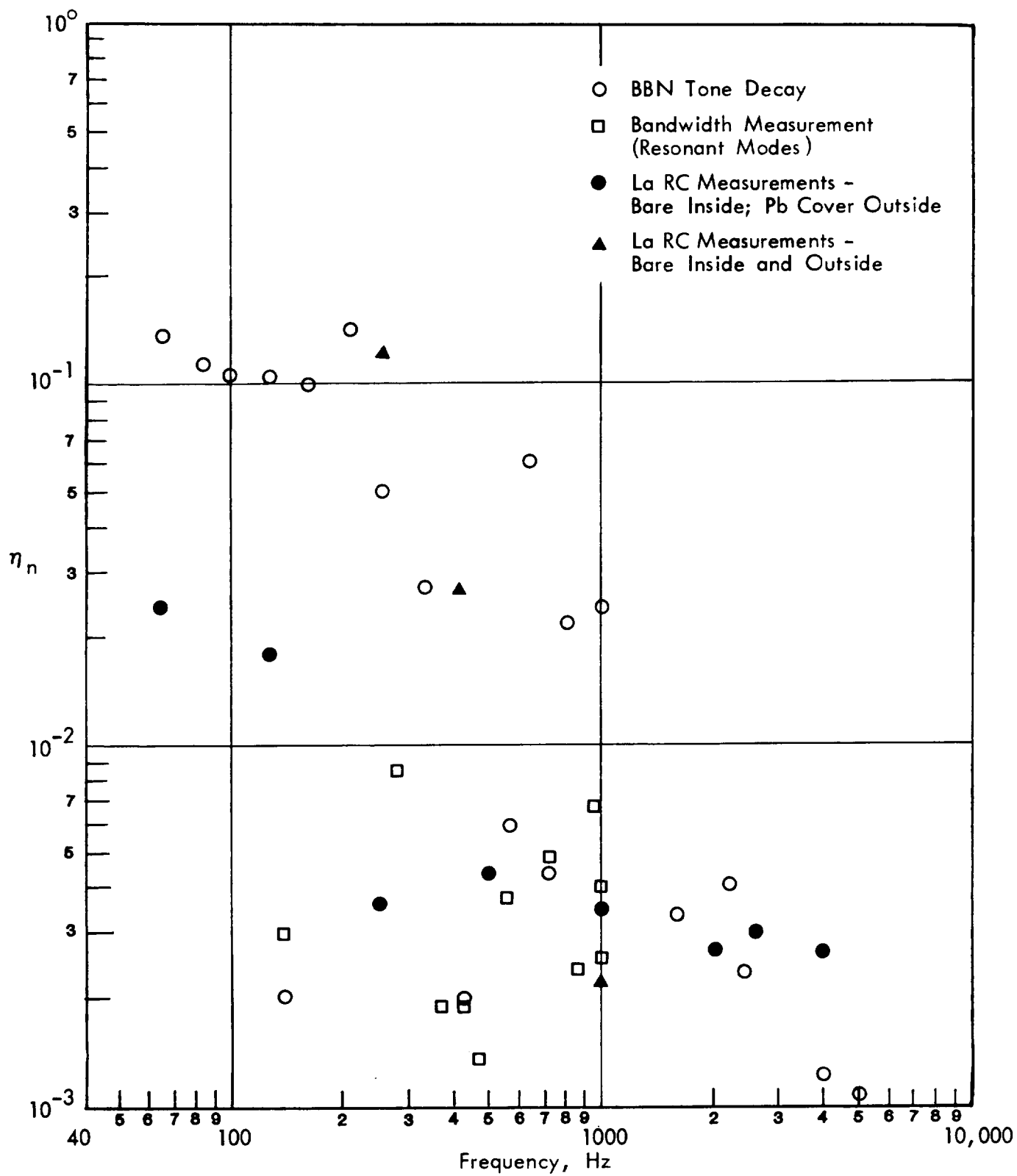


FIGURE 12. ACOUSTIC LOSS FACTORS OF BARE CYLINDER

A precise explanation for the measured behavior, i.e., low modal loss factors for resonant response of the modes, and high loss factors for nonresonant response of the modes cannot be given. It is believed to be caused by different loss mechanisms (absorption and radiation). The nonresonant acoustic response is composed of many acoustic modes that may be driven above or below their resonance frequencies. As a group, these modes have more ways to shed their energies; whereas a single acoustic mode excited at or near resonance has not so many options. However, because of the fact that the response is nonresonant, the dissipation should play little role in determining the response (the response will be of a forced nature, either stiffness or inertially controlled). Thus, the average loss factors for the one-third octave bands where no modes are resonant should not influence the interior predictions. Knowledge of the loss factors for those bands where acoustic modes will respond in a resonant fashion is, however, very necessary. Table 3 summarizes the data which were used as input to the computer program. Where available, the bandwidth measurements were averaged to obtain a value for each band. All modes resonant in that band use the average value during computations. Where no acoustic modes are resonant in a band, the acoustic loss factor corresponds to that measured with the response decay method for tonal excitation.

Structural loss factors were measured using the response decay method with magnetic, acoustic, and point impact excitations. Modal data were also obtained using the bandwidth method described previously. The measured data are presented in Figure 13. Also shown are LaRC measurements. In general, the structural loss factors lie in the range below 5×10^{-3} , which of course is indicative of a fairly lightly damped system.

Table 3. Band Average Loss Factors--Undamped LaRC Cylinder

Frequency (Hz)	Acoustic Loss Factors, η_n	Structural Loss Factors, η_r
50	0.143	--
63	0.143	--
80	0.120	--
100	0.107	--
125	0.0031	0.0030
160	0.100	0.0035
200	0.155	0.0027
250	0.050	0.0045
315	0.0087	0.0023
400	0.0019	0.0015
500	0.0014	0.0017
630	0.0044	0.0025
800	0.0025	0.0036
1000	0.0097	0.0018
1250	0.0065	0.0013
1600	0.0032	0.0020
2000	0.0042	0.0025
2500	0.0025	0.0023
3150	0.0019	0.0025
4000	0.0013	0.0019
5000	0.0011	0.0020

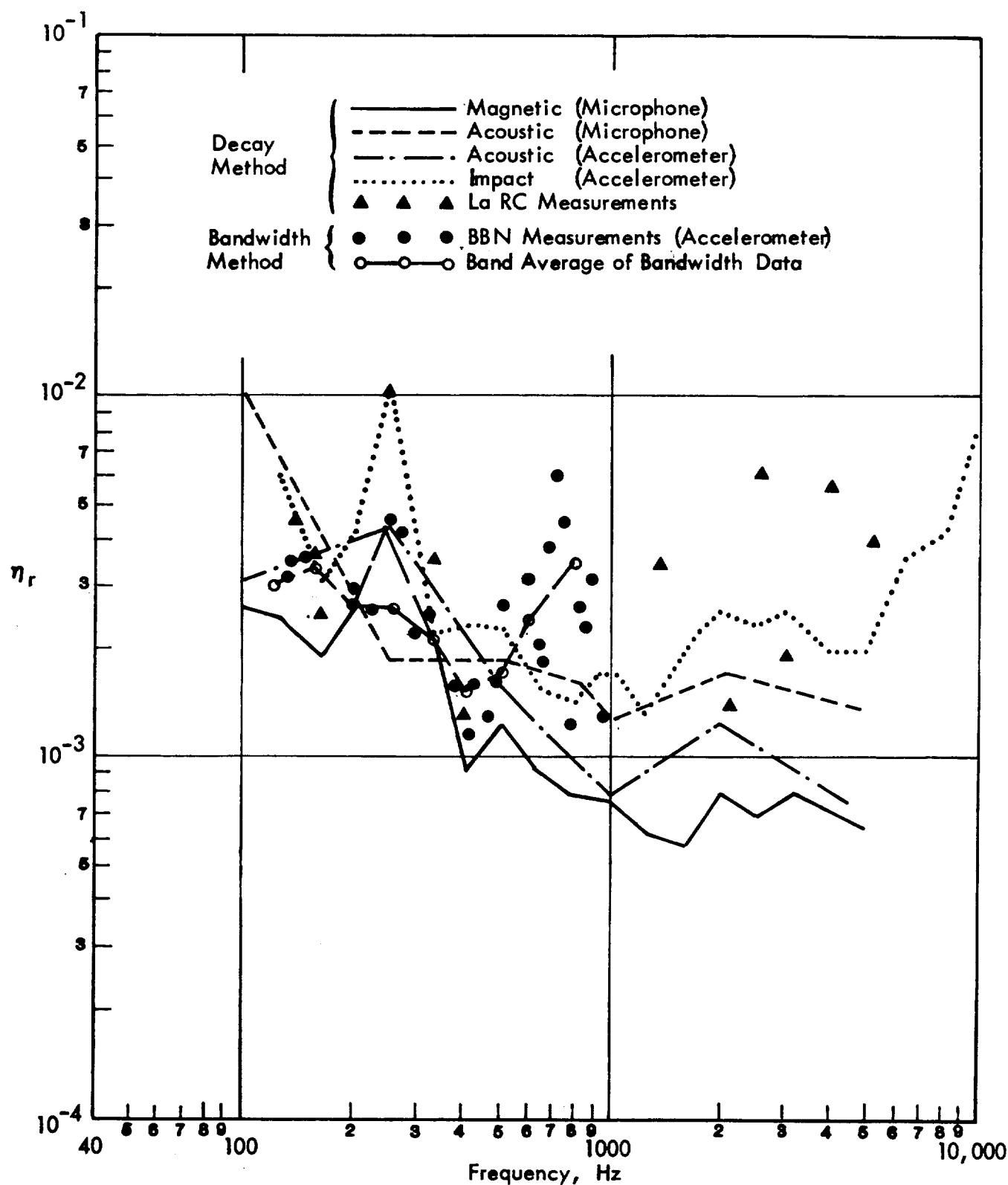


FIGURE 13. MEASURED STRUCTURAL LOSS FACTORS FOR BARE CYLINDER

Table 3 gives the structural loss factors used for computations. If a structure mode is resonant in a given band, it is assigned a loss factor equal to the value listed in Table 3 for that band, in the same manner as is done for the acoustic modes. The structure data in Table 3 are a composite of the BBN bandwidth and impact measurements. There are no structure modes resonant below 125 Hz.

4.2 Noise Reduction Measurements

Noise reduction measurements were conducted at NASA LaRC and at BBN on the bare cylinder. The excitation was a random, diffuse (reverberant) acoustic field. The layout and instrumentation for the BBN test is shown in Figure 14. The interior microphone arrangements are shown in Figure 4. The BBN locations are not correct for measuring a true space average. The LaRC locations are correct in that sampling of equal volumes is achieved. Unfortunately the BBN microphone axial locations were not discovered to be in error until after the tests were concluded. Comparison of BBN data to the LaRC data indicates that the erroneous axial locations did not introduce too much bias in the results (as will be seen shortly).

For both LaRC and BBN tests, the cylinder was supported at its two ends via two soft suspension spring/cords. At BBN the experiment was conducted in a room with a volume of 420 m³ (14,820 ft³) with dimensions 6 x 10 x 7 meters. The cylinder was approximately in the floor center about 1.5 meters above the floor. Scattering panels were positioned at the edges of the room and four JBL 4311 loud speakers, directed away from the cylinder, were used to develop a reasonably diffuse excitation field. The space-average excitation levels in the room were measured with a B&K 4134 condenser microphone, connected through

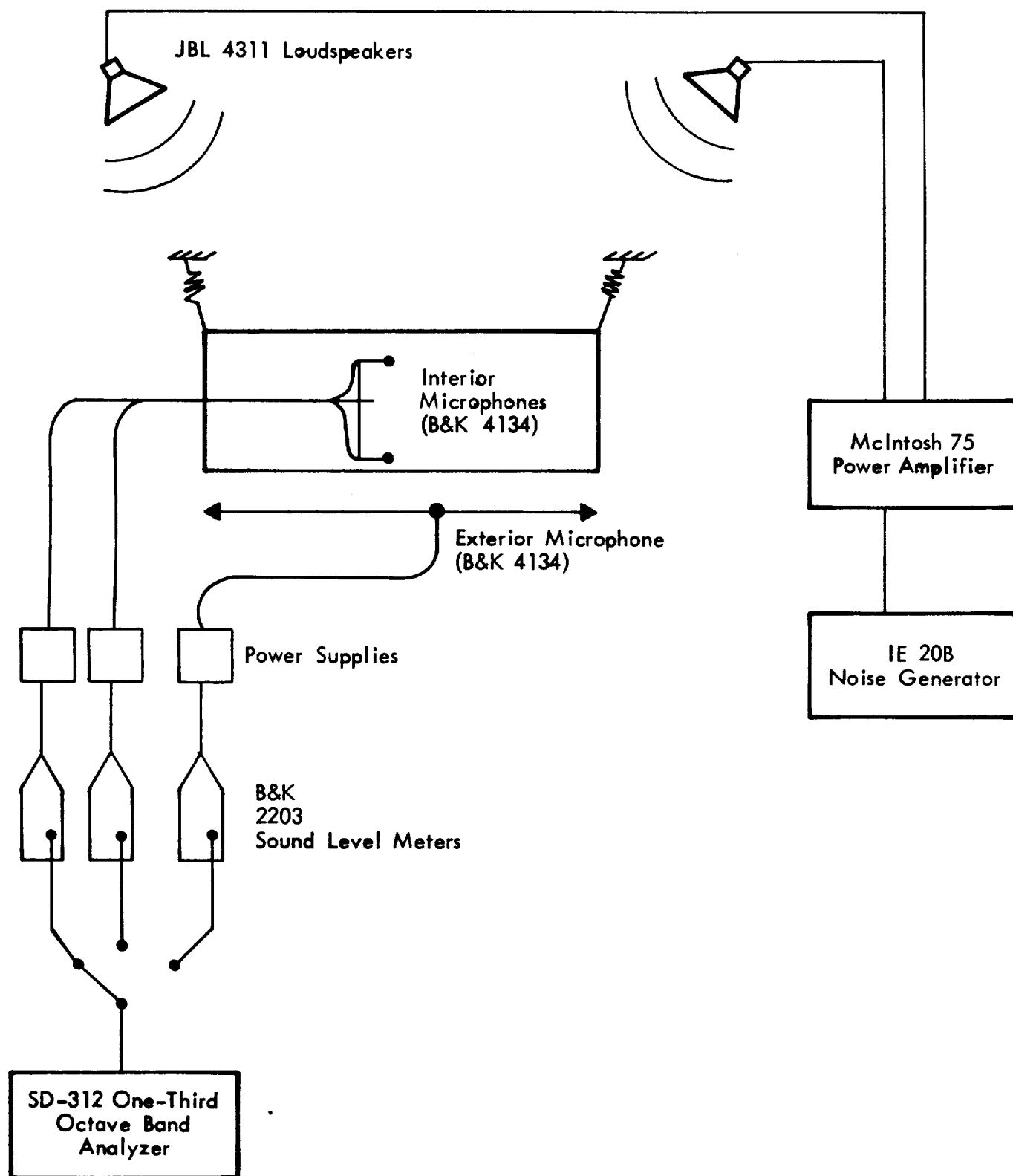


FIGURE 14. INSTRUMENTATION DIAGRAM FOR CYLINDER NOISE REDUCTION MEASUREMENTS WITH REVERBERANT FIELD EXCITATION

a B&K 2203 Sound Level Meter to a Spectral Dynamics SD-312 One-Third Octave Band Analyzer. The space-average levels were measured by traversing the microphone, mounted on a 2 meter boom, slowly over a path through the room volume. The interior sound levels were measured with similar instrumentation at radial and axial positions as indicated in Figure 4. Circumferential averages over four positions 90° apart were performed at each axial station using the "pause" facility available on the SD 312. Measurements were concentrated over one half of the cylinder since by symmetry one expects the interior level to be reflected about the center.

Noise reductions, NR_i , defined as the difference between the mean exterior sound pressure level and the interior level, at measurement position, i , were calculated and averaged in accordance with the relation

$$NR = -10 \log_{10} \left[\frac{1}{N} \sum_{i=1}^N 10^{(-NR_i/10)} \right],$$

where N is the number of sampled interior points. The result is the cylinder noise reduction, NR . The associated standard deviation for the noise reduction measurements was also calculated with

$$s = \left[\frac{1}{N-1} \sum_{i=1}^N (10^{-NR_i/10} - 10^{-NR/10})^2 \right]^{1/2}$$

The BBN results are shown in Figure 15, together with $\pm 1\sigma$ limits. The lower bound lies closer to the mean curve than does the upper reflecting the energy averaging procedure used to calculate the mean, i.e., the higher interior levels (lower noise reductions) have greater contribution to the mean than do the lower levels (higher noise reductions).

Figure 16 shows the LaRC measured noise reduction. Comparison of Figures 15 and 16 indicates rather consistent results. It is felt that the LaRC 4000 and 5000 Hz results are in error. At these frequencies, the LaRC noise reduction increases significantly. The two frequencies were the last two bands analyzed at LaRC. The BBN test specifically looked at the high end to determine whether this effect was real and although at 4000 and 5000 Hz, the noise reduction increased, it remained below 10 dB as can be seen in Figure 15. Also at the extreme low frequency, (i.e., 40 Hz) a noise reduction of 50 dB was achieved through careful sealing of the cylinder in the BBN test. The noise reduction was measured to be 6 dB lower at LaRC. Nevertheless, the noise reduction curves are in good agreement. Both exhibit a trough at 125 and 160 Hz, a peak at 200 Hz, and then a general decrease to below 10 dB by 630 Hz.

A more complete statistical analysis of the measured noise reductions is considered in Section 5, which deals with verification of the analytical model.

4.3 Plane-Wave Tonal Excitation

Sound levels were measured within the bare cylinder when excited by harmonic plane acoustic waves incident at angles of $\phi = 15^\circ$ and 45° relative to the cylinder axis. The experimental set-up

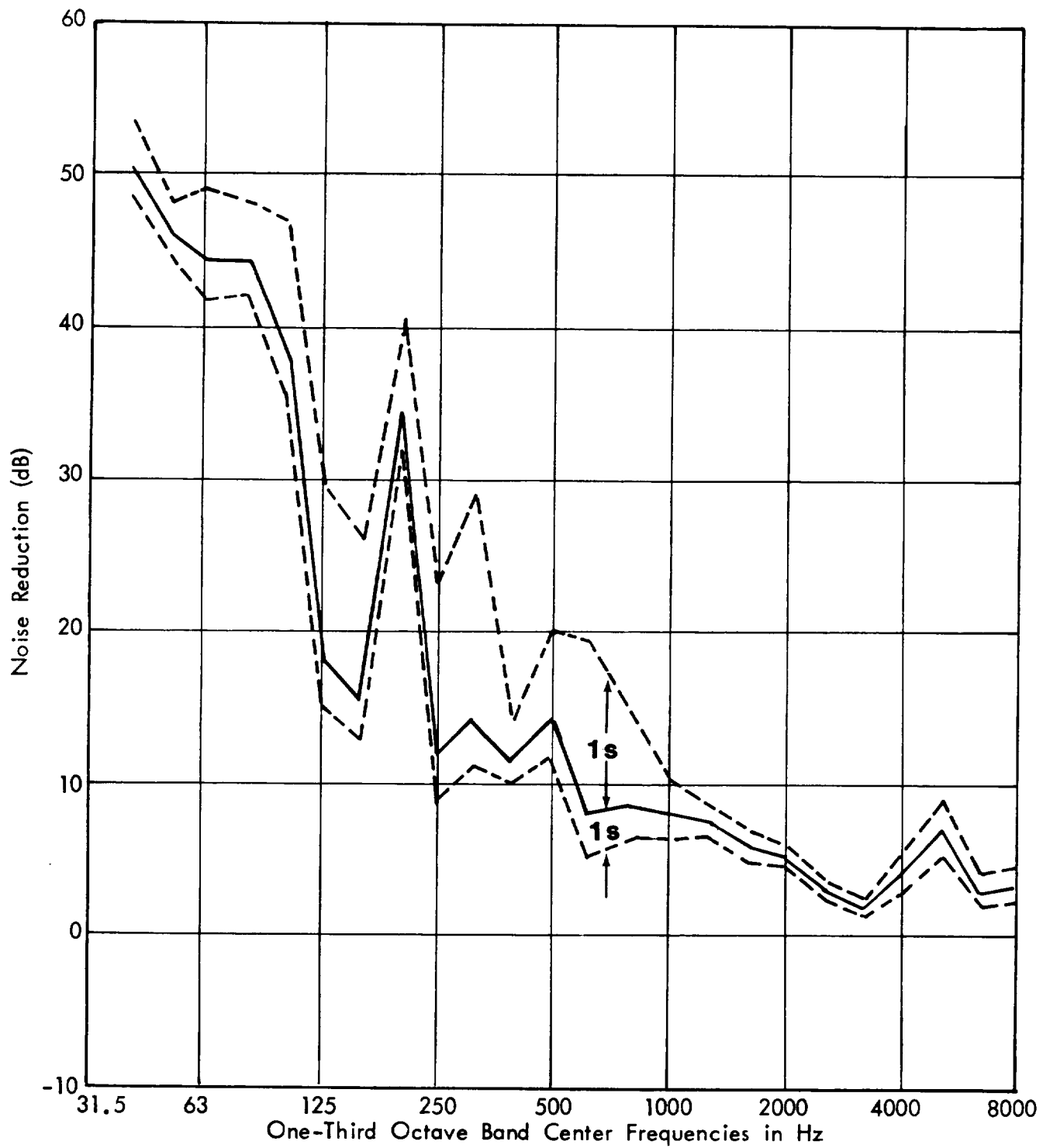


FIGURE 15. BBN MEASURED NOISE REDUCTION (BARE CYLINDER)

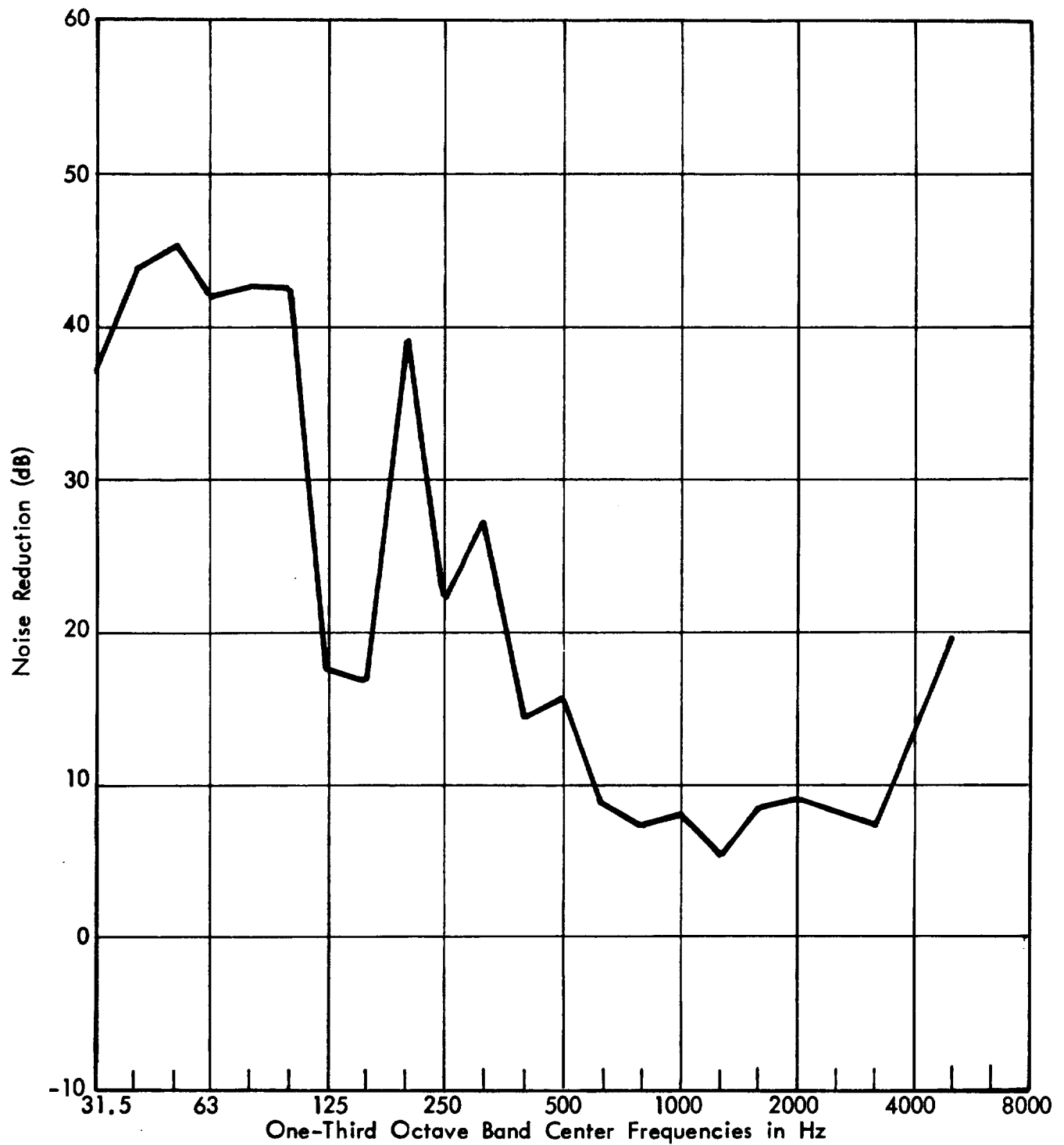


FIGURE 16. L_a RC MEASURED NOISE REDUCTION (BARE CYLINDER)

was similar to that for the noise reduction tests except that the room was lined with absorptive foam, the cylinder was shrouded in foam wedges to prevent the development of a reverberant field in the room, and only one loudspeaker source, located about 4 meters from the cylinder center, was used as the excitation. Figure 17 shows the test layout. A progressive wave field was produced along the cylinder axis. The equipment used for the tone transmission measurements is shown in Figure 18. An exterior microphone was located at the surface of the cylinder to monitor the excitation level, which was maintained constant to within ± 1 dB and equal to 90 dB (re 20 μ Pa) using the compressor circuit available on the B&K 1024 Sine Random Generator. The interior sound level was measured at 12 positions as shown in Figure 19, the microphone output being plotted on a B&K 2305 Graphic Level Recorder. Representative measured data for 15° and 45° angles of incidence are shown in Figures 20(a) and (b). All other measured data are presented in Appendix A. Table 4 summarizes the measurements which were made.

It should be emphasized that the curves in Figures 20 and in Appendix A, are ratios of incident to interior pressure at specific locations. It was simply impractical to measure the ratio of incident to space-average interior, since many microphones would have had to have been used simultaneously. However, the interior levels from point to point have similar characteristics. By selecting two extreme incidence angles $\phi = 15^\circ$ and 45° , it is obvious that the transmission characteristics of the cylinder can change dramatically. For instance, the 15° and 45° cases look pretty similar out to about 400 to 500 Hz. However it is clear that the maximum interior levels (minimum ratio of $\langle p_{inc}^2 \rangle / \langle p_i^2 \rangle$) occurs first at about 3000 Hz for 15° but much sooner, between about 1000 and 1600 Hz for 45° . At 2000 Hz the

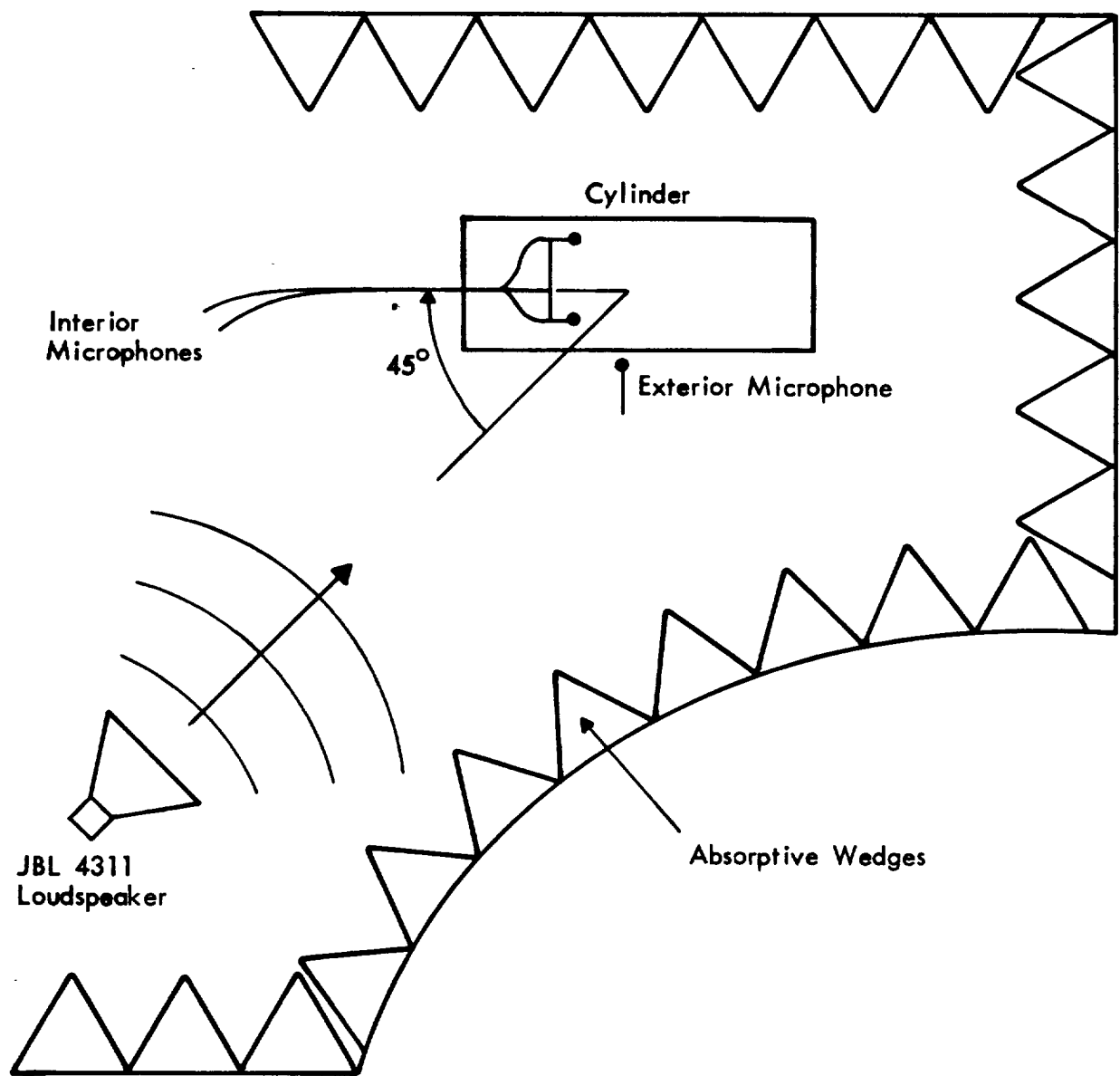


FIGURE 17. TEST LAYOUT FOR PLANE WAVE EXCITATION OF CYLINDER

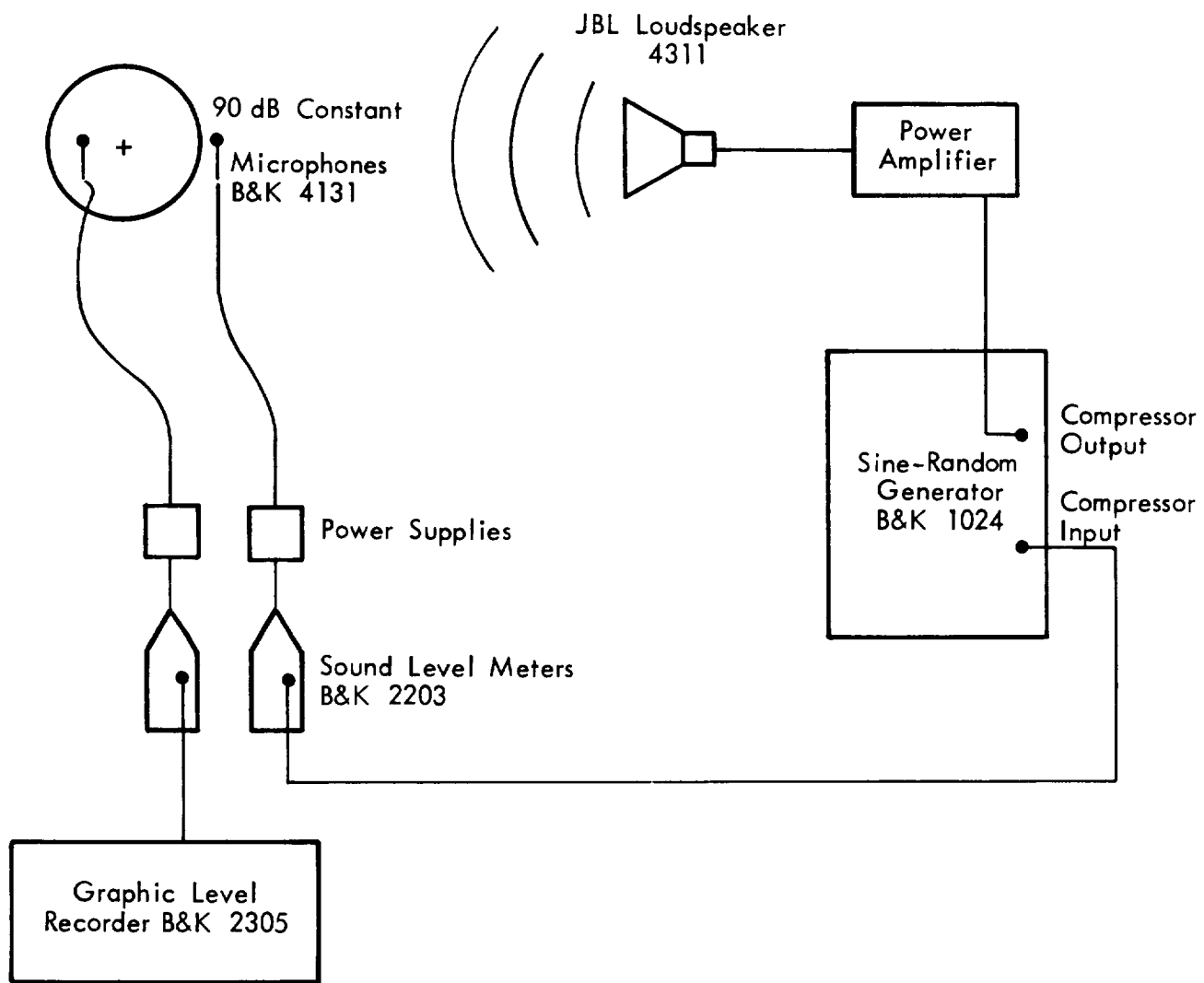
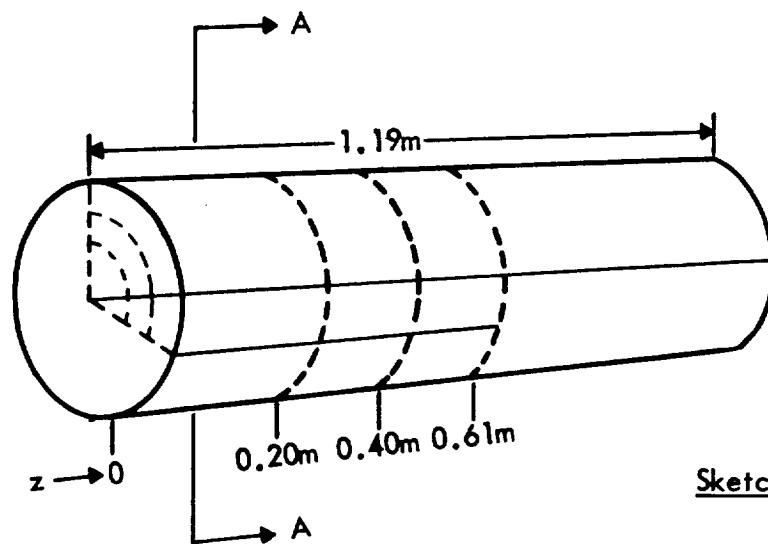
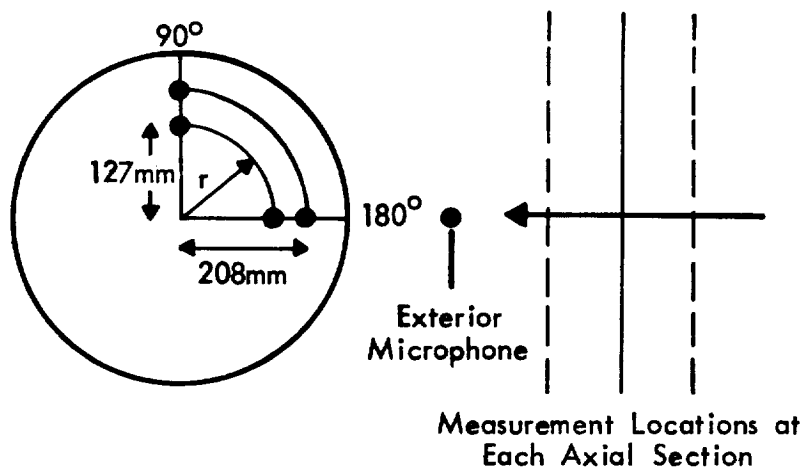


FIGURE 18. EQUIPMENT SCHEMATIC FOR TONAL PLANE
WAVE EXCITATION

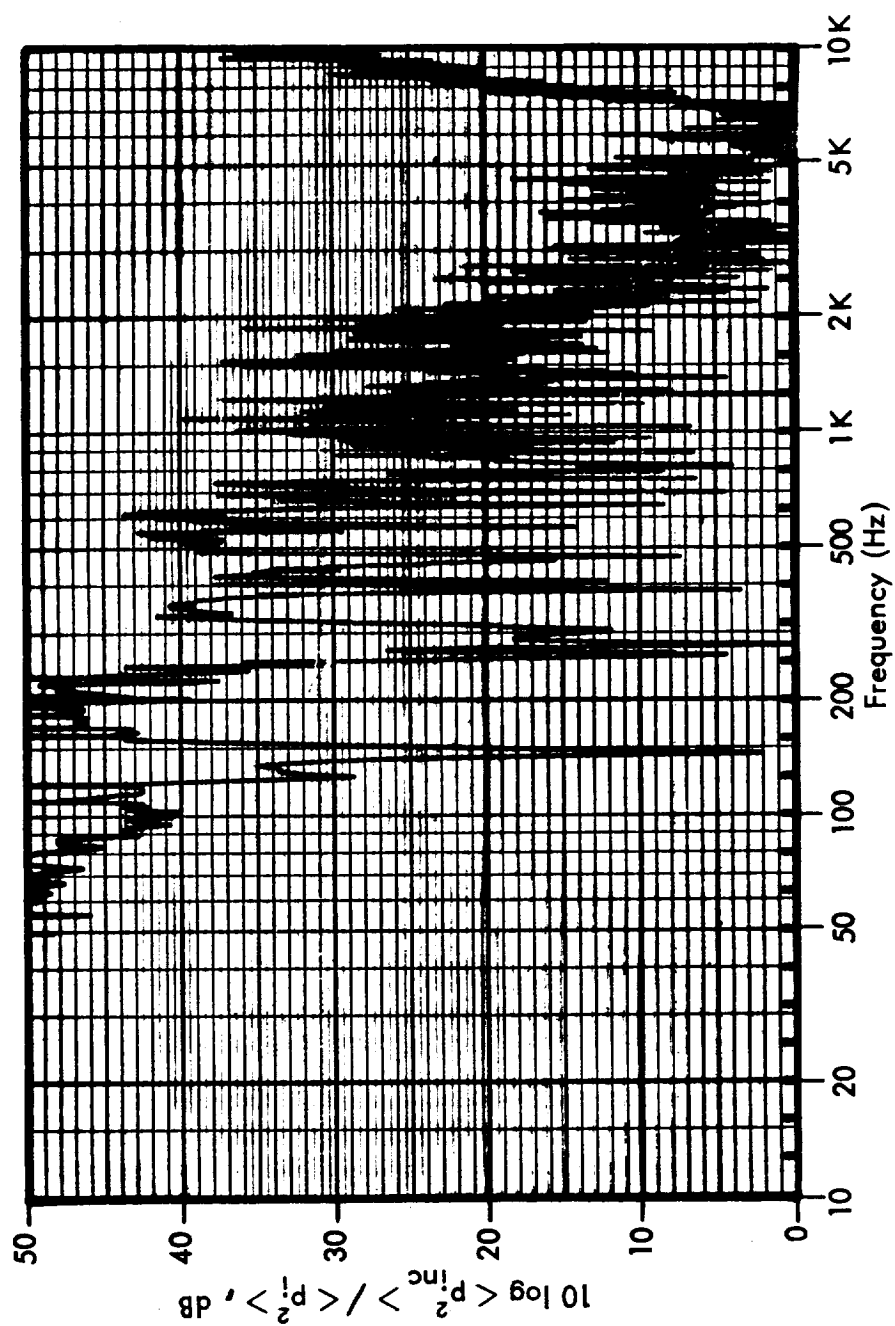


Sketch of Cylinder Measurement
Planes



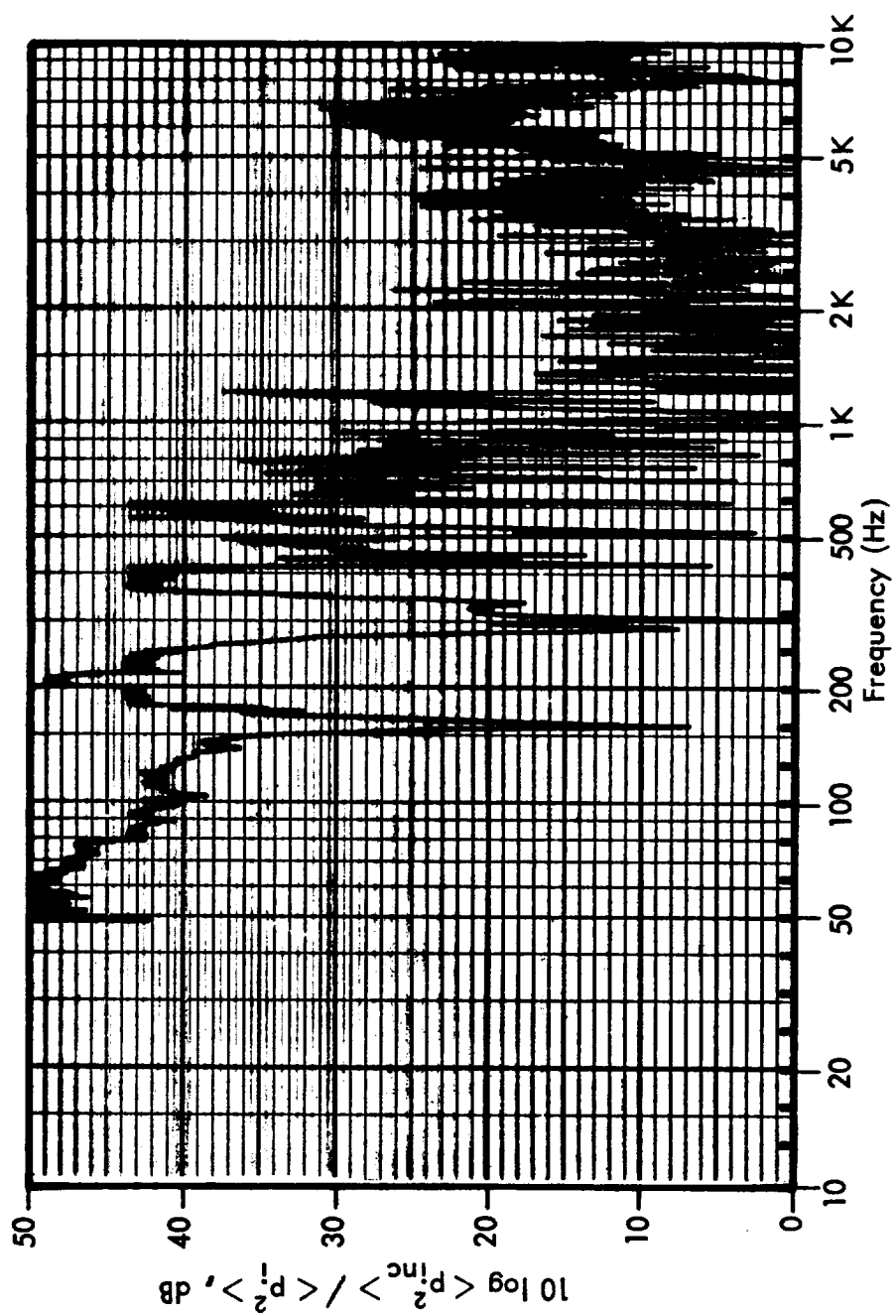
Section A - A

FIGURE 19. MEASUREMENT LOCATIONS FOR TONAL
PLANE-WAVE EXCITATION



Record No. 06

FIGURE 20(a) RATIO OF INCIDENT PRESSURE TO INTERIOR PRESSURE,
TONAL PLANE WAVE EXCITATION, $\phi = 15^\circ$.



Record No. 19

FIGURE 20(b) RATIO OF INCIDENT PRESSURE TO INTERIOR PRESSURE,
TONAL PLANE WAVE EXCITATION, $\phi \approx 45^\circ$.

ratio of incident to interior pressure for the cases shown in Figure 20 is about 20 dB for 15° angle of incidence, and on its way down, while at 45° incidence angle, the ratio of incident to interior has reached its minimum and is on its way up. Thus the two selected incidence angles are sufficiently different to challenge the analytical model to duplicate the observed behavior.

Table 4. Details of Interior Microphone Locations
for Tone Transmission Measurements

Rec. No.	Axial Position (mm)	Angle (degrees)	Radial Position (mm)	
02	203	180	208	} Angle of Incidence, $\phi = 15^\circ$
03	203	180	127	
04	203	0	127	
05	203	0	208	
06	406	0	208	
07	406	0	127	
08	406	180	127	
09	406	180	208	
10	610	180	208	
11	610	180	127	
12	610	0	127	
13	610	0	208	
16	610	0	208	} Angle of Incidence, $\phi = 45^\circ$
17	610	0	127	
18	406	0	127	
19	406	0	208	
20	203	0	208	
21	203	0	127	

4.4 Point Mechanical Excitation

Transfer functions between cylinder acceleration response and force input and between cylinder interior sound level and force input were measured on the test cylinder. Measurement procedures, instrumentation, and results are described below.

The cylinder "inertance" will be defined as the difference between acceleration output and force input, viz.,

$$H(\omega) = \frac{a(\omega)}{F(\omega)} = \frac{|a|e^{-i\alpha}}{|F|e^{-i\beta}} = \frac{|a|}{|F|} e^{-i(\alpha-\beta)}$$

so that

$$|H(\omega)| = \frac{|a|}{|F|} ,$$

is the inertance magnitude, with units of (mass⁻¹), and

$$\phi(\omega) = (\alpha-\beta) ,$$

is the inertance phase angle. Acceleration measurement and force input locations may be different; $H(\omega)$ is then considered a "transfer inertance". The sound level-to-force input transfer function is defined by

$$H_s(\omega) = \frac{p(\omega)}{F(\omega)} = \frac{|p|}{|F|} \frac{e^{-i\gamma}}{e^{-i\delta}} = \frac{|p|}{|F|} e^{-i(\gamma-\delta)}$$

so that

$$|H_s(\omega)| = \frac{|p|}{|F|} ,$$

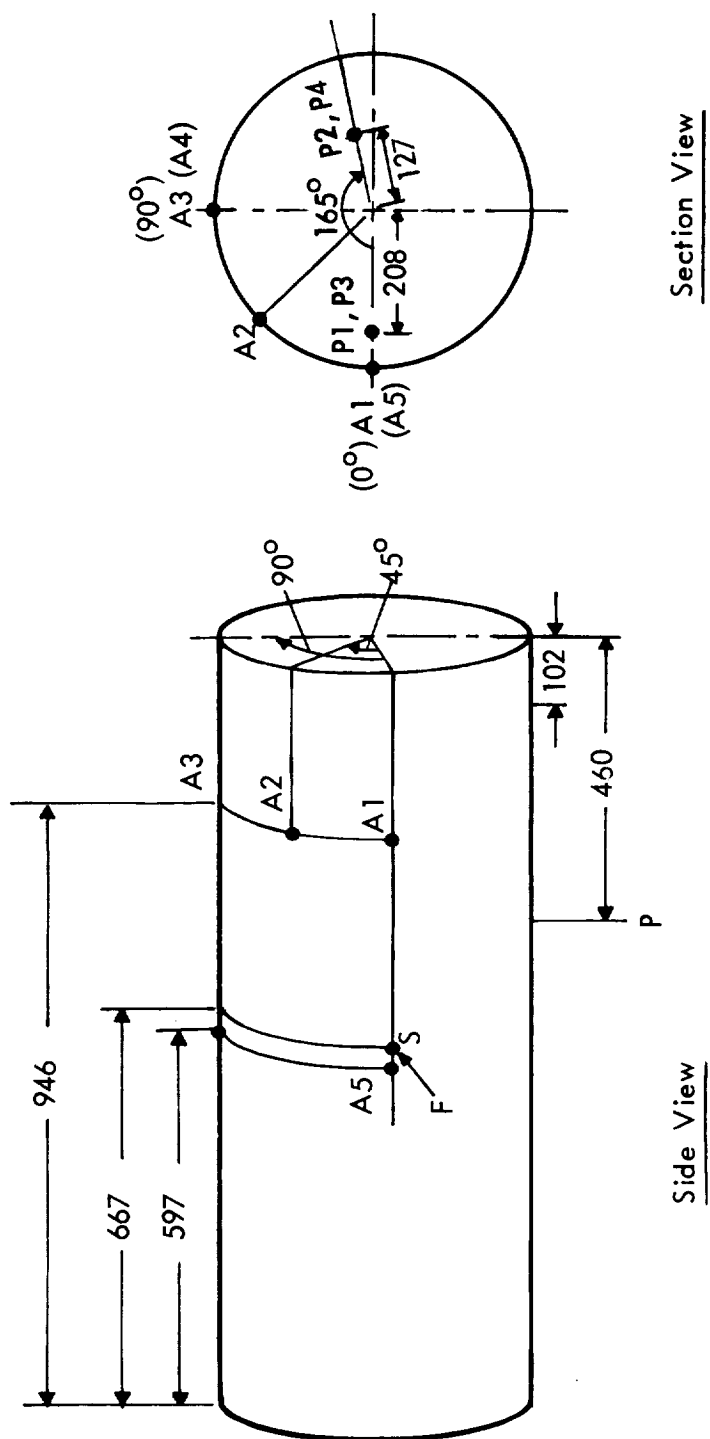
is the magnitude of sound-to-force transfer function, with units of (area⁻¹), and

$$\phi_s(\omega) = (\gamma-\delta) ,$$

is the corresponding phase angle.

The experimental configuration for these measurements is shown in Figure 21, and an instrumentation schematic is presented in Figure 22. Broad-band noise from the IE-20 Noise Generator was amplified and fed to the input of a Goodman's V50 Shaker. The shaker drove the test cylinder through a Wilcoxon Z602 Impedance Head which was glued with dental cement through a point stud attachment to the cylinder. The axis of the shaker was perpendicular to the cylinder skin. Figure 21 shows the locations of the single shaker force input (S), and of the five response measurement accelerometers (A1 to A5) and of the interior microphones (P1 to P4).

The impedance head contains its own (small) internal mass which loads the force gauge to produce a voltage even when the impedance head is unloaded (i.e., not attached to a test structure) and which is comparable to the force required to drive the test cylinder at, for example, cylinder resonance frequencies. Cancellation of this force due to the internal mass is required to give accurate transfer function measurements. A mass cancellation circuit was inserted into the impedance head circuit to subtract from the force gauge output, a voltage proportional to the acceleration of the force gauge in such a manner as to minimize the force gauge signal when the impedance head was driven unattached to the cylinder. In this circuit, the accelerometer signal from the impedance head was inverted, proportioned, and subtracted from the force gauge output to minimize output signal. Figure 23 shows the signal spectra from the output of the mass cancellation circuit with and without the cancellation circuit in operation (driving only the impedance head); a 30 dB reduction in force output has been produced at most frequencies.



S = SHAKER LOCATION
A = ACCELEROMETER LOCATION
P = MICROPHONE LOCATION

FIGURE 21. EXPERIMENTAL CONFIGURATION FOR POINT MECHANICAL EXCITATION OF TEST CYLINDER, SHOWING SHAKER AND MEASUREMENT LOCATIONS

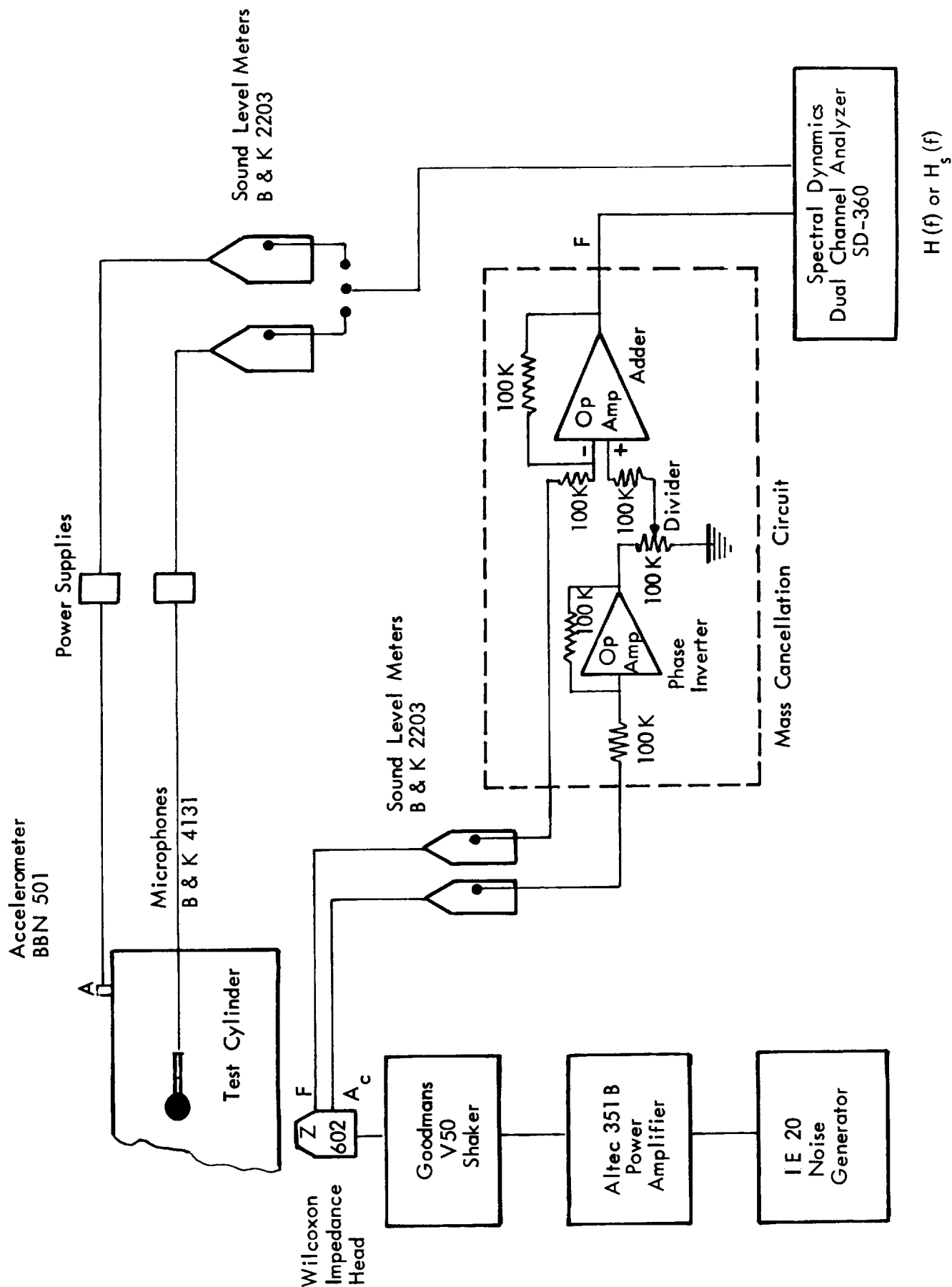


FIGURE 22. INSTRUMENTATION FOR CYLINDER INERTANCE AND TRANSFER FUNCTION MEASUREMENTS

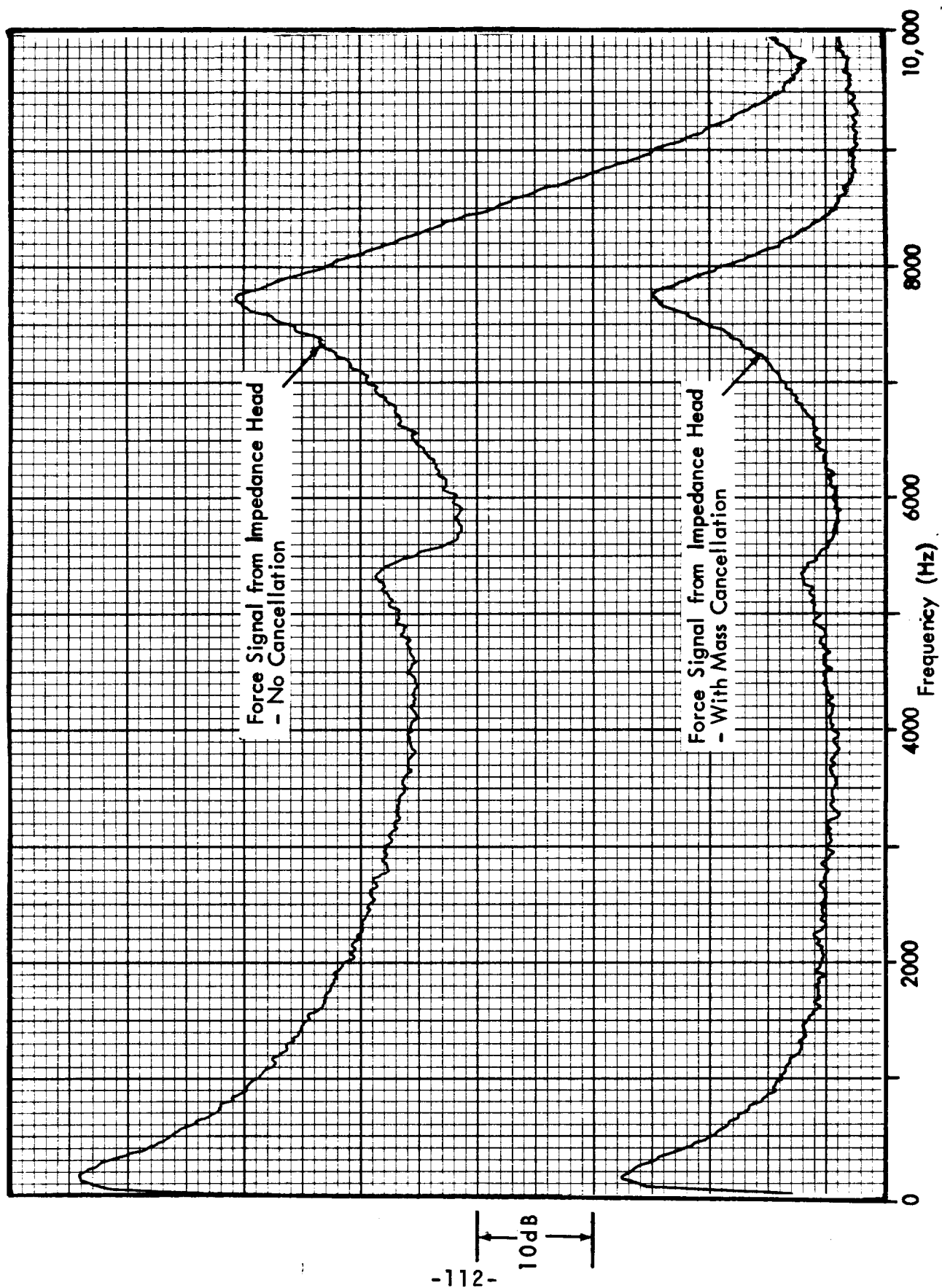


FIGURE 23. FORCE OUTPUT SIGNAL FOR FIXED DRIVING VOLTAGE TO UNLOADED SHAKER, SHOWING EFFECT OF MASS CANCELLATION CIRCUIT.

Calibration of the force gauge was achieved by adding a small dummy mass (37.5g) to the impedance head, driving at a known acceleration (1g) and noting the force signal level. The force and acceleration signals were fed to the Spectral Dynamics SD-360 Dual Channel Analyzer, operating in transfer function mode and the magnitude, phase, and coherence of $H(\omega)$ were determined and set for calibration. The sound level-to-force transfer function calibration was achieved by feeding the same voltage simultaneously to microphone and force sound level meters and adjusting the output levels.

Representative transfer functions are presented in Figures 24 and 25 respectively. All other measured data are presented in Appendix B. Table 5 summarizes the measurement data by record number, measurement, frequency range, and sensor location; reference should be made to Figure 21.

Figure 24 shows the inertance magnitude $|H(f)|^2$ and the phase angle ϕ between the acceleration and force. Also shown is the coherence function γ^2 which provides an estimate of the errors associated with the transfer function measurement. When $\gamma^2 \approx 1.0$, the errors in $|H|^2$ and ϕ are small but the errors increase as γ^2 tends to zero. In general in the present measurements, $\gamma^2 > 0.2$ and the estimates for $|H|^2$ are accurate to within about ± 1 dB.

Minima in the coherence are associated with maxima and minima in the acceleration response and to a lesser degree to spectral variations in the force input. At low frequencies the inertance magnitude $|H|^2$ increases with the cube of the frequency as expected for a stiffness-controlled response until the frequency of the lowest structural resonance. At this frequency the $|H|^2$

ϕ , Phase Angle Between Acceleration and Force

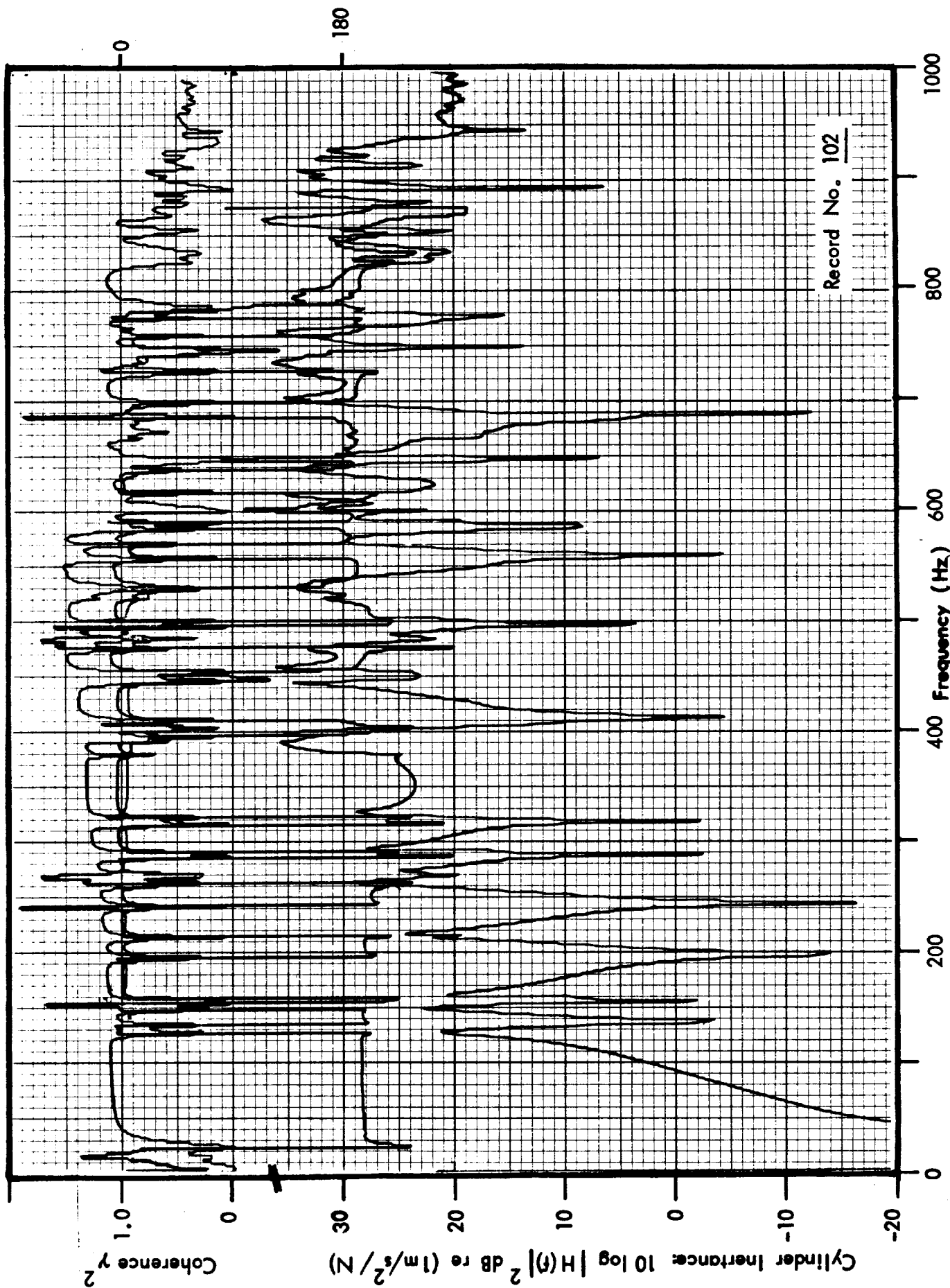


FIGURE 24. INERTANCE FUNCTION, $H(f)$, FOR POINT MECHANICAL EXCITATION

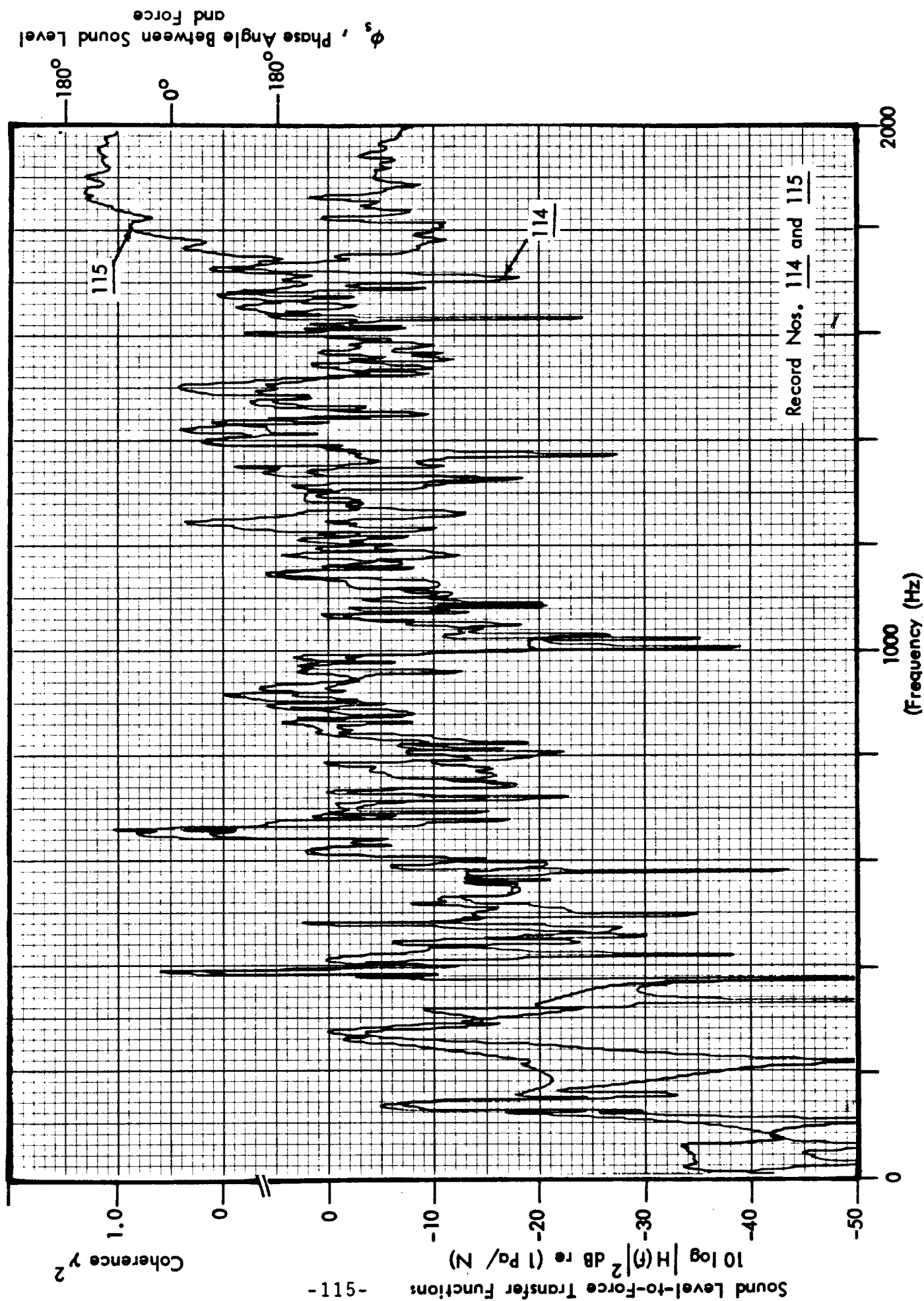






FIGURE 25. SOUND LEVEL-TO-FORCE INPUT TRANSFER FUNCTION, $H_s(f)$, FOR POINT MECHANICAL EXCITATION.

Table 5. Summary of Measurement Information for Point Mechanical Excitation.

Record No.	Transfer Function	Sensor Location	Frequency Range
102	 Inertance	A1	0 to 1 kHz
103		A1	0 to 500 Hz
104		A2	0 to 500 Hz
105		A3	0 to 500 Hz
105A		A4	0 to 500 Hz
106		A5	0 to 500 Hz
106R	ϕ and γ^2	A5	0 to 500 Hz
107		A5	0 to 2 kHz
108		A4	0 to 2 kHz
109		A2	0 to 2 kHz
110		A3	0 to 2 kHz
111		A1	0 to 2 kHz
112	 Sound level- to-force	P2	0 to 500 Hz
113		P1	0 to 500 Hz
114		P1	0 to 2 kHz
115		P2	0 to 2 kHz
116		P4	0 to 2 kHz
117		P3	0 to 2 kHz
118		P3	0 to 500 Hz
119		P4	0 to 500 Hz

spectrum peaks and the phase angle changes from 180° to 0° , both phenomena being quite consistent with the behavior of a single degree-of-freedom system at resonance. Above the fundamental structure mode $|H|^2$ decreases in accordance with mass-controlled behavior, to a minimum value which coincidentally is the frequency of the lowest acoustic mode of the cavity. Successive peaks in $|H|^2$ and phase changes of $\pm 180^\circ$ are associated with the presence of other structure modes. Comparison of the phase angle at different positions over the cylinder surface at particular frequencies reflects the modal structure of the acceleration response although such discrimination is only possible for lower frequency modes. Further it appears that all structure modes at most frequencies are driven by the point excitation and that circumferentially the antinodes of the modes lie along the axial surface line containing the excitation point.

Figure 25 shows the magnitude and phase of the sound level-to-force transfer function, $|H_s(f)|^2$ and ϕ_s , respectively, as well as the coherence function γ^2 for the measurement. As indicated, spectral peaks in $|H_s|^2$ correspond to the presence of acoustic and structural resonant modes. Phase changes of 180° occur at each of these peaks and also at minima in $|H_s|^2$, corresponding to changes from mass to stiffness controlled cylinder response. The highest peaks in $|H_s|^2$ in a frequency band encompassing both structural and acoustic modes occur at the resonance frequencies of the acoustic modes, as, for example, at 142 Hz and 284 Hz, the (1,0,1) and (2,0,1) acoustic modes respectively. It is clear that the resonant structure modes do not couple as effectively to the interior acoustic field when poor circumferential matching in wavelength exists.

4.5 Progressive Wave Excitation

Measurement of the sound transmission for the case of a random progressive wave traveling along the length of the test cylinder was the final test. The experimental configuration is shown in Figure 26. Four JBL 4311 Loudspeakers were placed in a plane perpendicular to the cylinder axis and approximately 3.5 meters from the center of the cylinder. These speakers were placed about 1 meter from the cylinder axis and at 90° positions. The speakers' axes were directed to point at the cylinder mid-length position; the effective angle-of-incidence was about 15°. The cylinder was supported in a position similar to that used in the previous plane wave tests and surrounded by sheets of absorptive foam on all sides to simulate an anechoic environment. Noise levels were measured with B&K 4133 12.5 mm condenser microphones close to the cylinder surface at four equi-spaced circumferential locations (E1 to E4) at each of the three axial stations ($z/L = 0.25, 0.50$ and 0.75), as shown in Figure 26. Noise levels were measured inside the cylinder at four axial stations ($z/L = 0.125, 0.25, 0.375, 0.50$) with two interior microphones (B&K 4131 25.4 mm Condenser Microphones), at 127 mm (PI) and 208mm (PO) radial distances. Circumferential averages over the 0°, 90°, 180°, and 270° positions were carried out by use of the 'pause' facility on the SD312 1/3 Octave Band Analyzer. Figure 27 provides an instrumentation schematic.

Initially the gains of the power amplifiers for each speaker were adjusted so that the sound level spectra at the circumferential exterior locations (E1 to E4) at $z/L = 0.50$ were as similar as practical. Table 6 and Figure 28 contain sound level spectra measured in one-third octave bands which illustrate the variation in excitation levels, both circumferentially at each

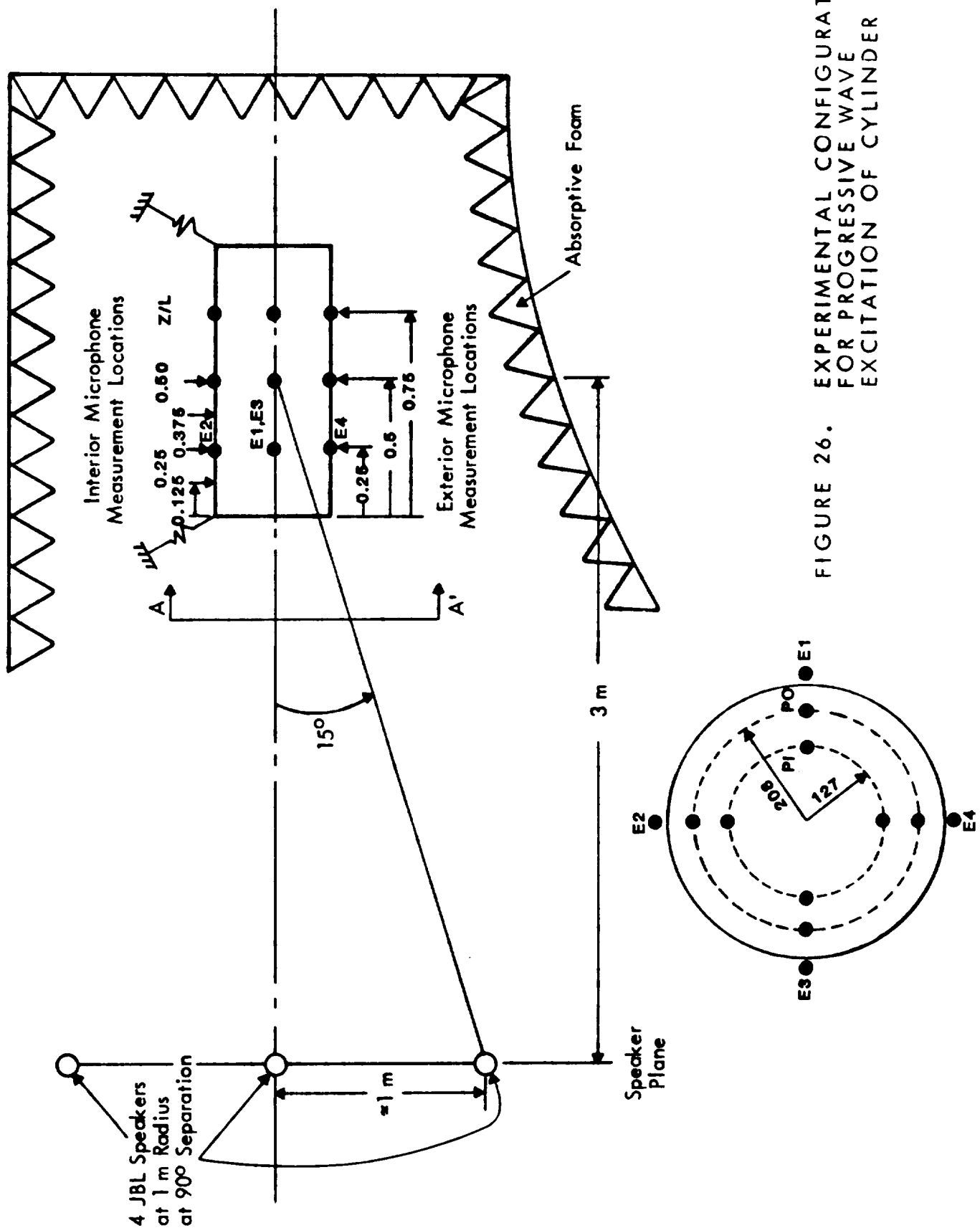


FIGURE 26. EXPERIMENTAL CONFIGURATION FOR PROGRESSIVE WAVE EXCITATION OF CYLINDER

Section A - A': Microphone Locations Inside and Outside Cylinder.

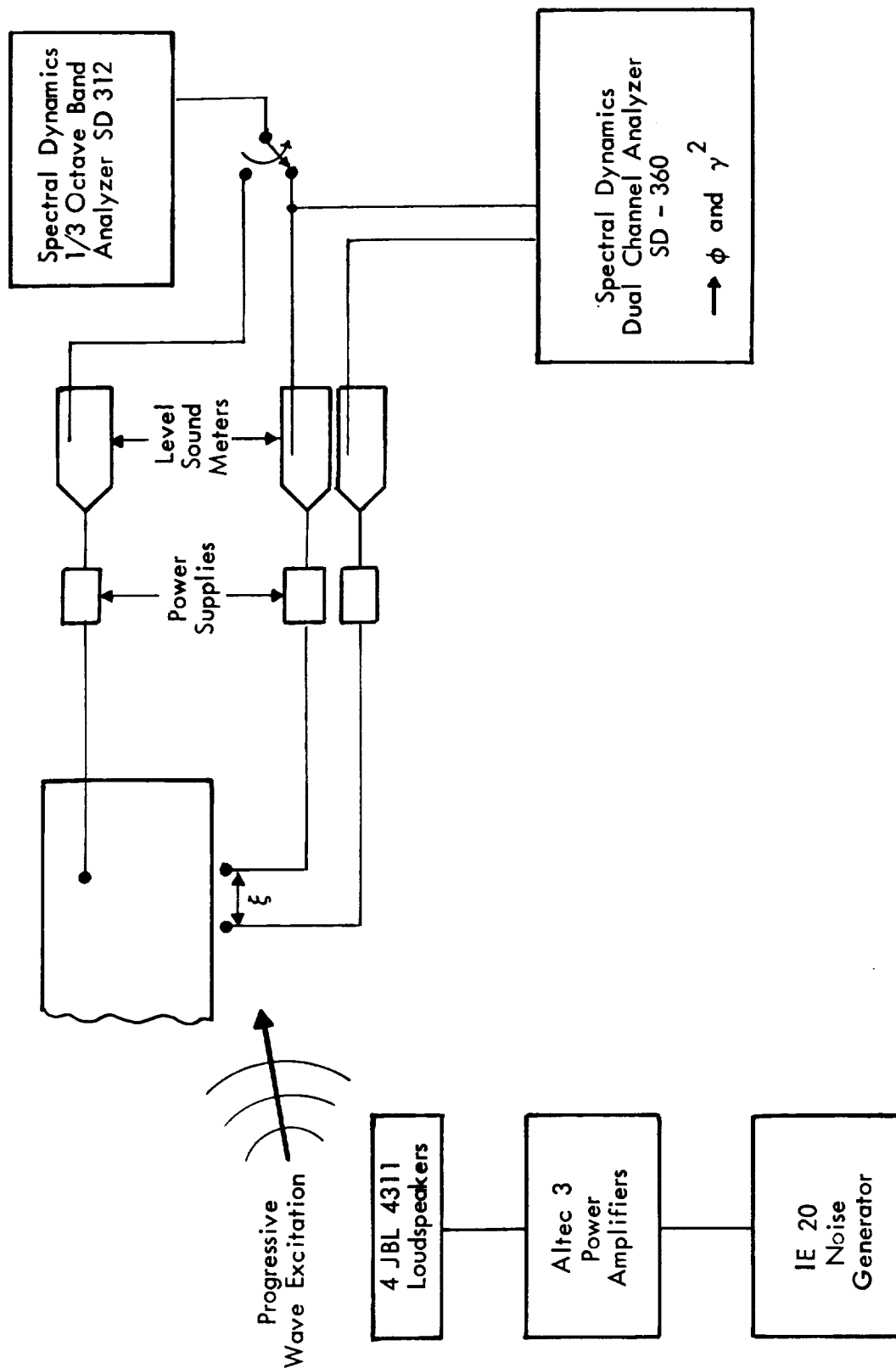


FIGURE 27. INSTRUMENTATION SCHEMATIC FOR PROGRESSIVE WAVE EXCITATION

Table 6. Exterior Sound Levels for Progressive Wave Excitation

Axial Station ($z/L = 0.25$):

Frequency	Microphone SPL	E1 SPL	E2 SPL	E3 SPL	E4 SPL	Mean SPL
63		89.50	78.75	87.20	90.00	89.00
80		90.75	91.50	87.50	92.75	91.00
100		92.75	92.75	89.75	92.75	92.20
125		89.00	90.75	89.50	90.50	90.00
160		84.50	88.00	83.00	85.75	85.70
200		87.25	74.50	86.00	89.00	87.00
250		90.25	78.50	91.00	80.50	89.90
315		93.75	79.50	90.00	79.50	91.10
400		92.75	80.50	90.00	81.50	91.30
500		90.00	83.25	87.75	83.00	91.50
630		90.25	80.50	88.50	81.50	90.30
800		89.50	80.50	84.75	81.50	84.70
1000		88.75	77.25	89.75	83.00	90.20
1250		88.00	76.50	90.75	81.50	81.60
1600		88.50	79.75	92.00	81.50	90.70
2000		89.25	76.75	91.00	81.00	89.80
2500		83.75	74.50	89.25	86.25	86.50
3150		83.00	81.50	85.25	86.50	84.50
4000		82.25	86.00	86.75	86.25	85.60
5000		82.25	85.50	90.50	90.00	85.20
6300		84.75	84.50	88.25	90.25	87.60
8000		86.25	82.50	81.00	89.25	85.90
10000		83.00	81.00	86.50	87.00	85.00

Table 6. Cont'd.

Exterior Sound Levels for Progressive Wave Excitation

Axial Station ($z/L = 0.50$):					
Microphone	E1	E2	E3	E4	Mean
Frequency	SPL	SPL	SPL	SPL	SPL
63	88.75	88.00	88.00	87.75	88.10
80	89.00	89.00	85.50	91.00	89.00
100	92.25	93.00	88.00	91.50	91.60
125	89.00	90.00	88.75	90.00	89.50
160	86.00	88.75	83.50	87.25	86.80
200	86.00	86.25	82.25	87.00	85.70
250	88.25	83.50	88.25	89.25	87.80
315	90.50	86.75	87.75	89.50	88.90
400	92.25	83.25	87.50	89.00	91.10
500	91.50	88.50	86.75	92.75	90.50
630	86.25	87.25	85.75	92.75	89.00
800	88.00	87.50	85.00	88.75	87.50
1000	89.50	88.75	88.50	91.75	89.80
1250	87.25	85.25	89.25	90.25	83.50
1600	86.50	89.50	90.50	91.50	89.90
2000	88.25	87.00	90.50	90.75	89.40
2500	83.50	84.50	89.25	86.75	86.60
3150	81.75	82.75	86.50	85.00	84.40
4000	80.00	85.00	87.00	87.75	85.80
5000	80.75	83.75	89.50	88.50	86.90
6300	82.75	84.00	84.25	90.00	86.30
8000	84.00	73.75	84.75	88.25	85.60
10000	81.00	72.75	86.25	88.25	85.50

Table 6. Cont'd.

Exterior Sound Levels for Progressive Wave Excitation					
Axial Station ($z/L = 0.75$):					
Microphone	E1	E2	E3	E4	Mean
Frequency	SPL	SPL	SPL	SPL	SPL
63	89.75	89.75	90.00	90.50	90.00
80	87.75	87.50	85.50	90.00	88.00
100	92.25	92.75	88.50	89.50	91.10
125	88.00	89.50	87.25	85.75	87.80
160	86.25	86.50	83.50	87.00	86.00
200	83.00	88.50	82.00	86.50	85.80
250	85.00	85.50	84.50	87.75	85.90
315	90.25	78.75	86.75	87.25	87.30
400	91.75	88.25	86.75	89.75	89.50
500	89.75	89.50	83.25	88.00	88.30
630	85.75	88.25	83.75	92.00	88.60
800	88.00	85.75	83.75	91.50	88.20
1000	88.75	85.50	87.50	90.75	88.50
1250	87.00	85.25	87.25	90.50	87.90
1600	87.00	87.75	89.25	90.50	88.80
2000	87.25	87.25	88.50	91.00	88.80
2500	82.75	86.00	87.75	88.00	86.60
3150	82.75	82.00	85.75	85.50	84.30
4000	83.50	83.50	88.50	84.50	85.60
5000	81.00	86.25	88.50	87.75	86.70
6300	80.75	84.50	86.50	88.50	85.80
8000	78.00	84.00	85.00	87.50	84.70
10000	75.25	82.75	80.50	87.00	83.30

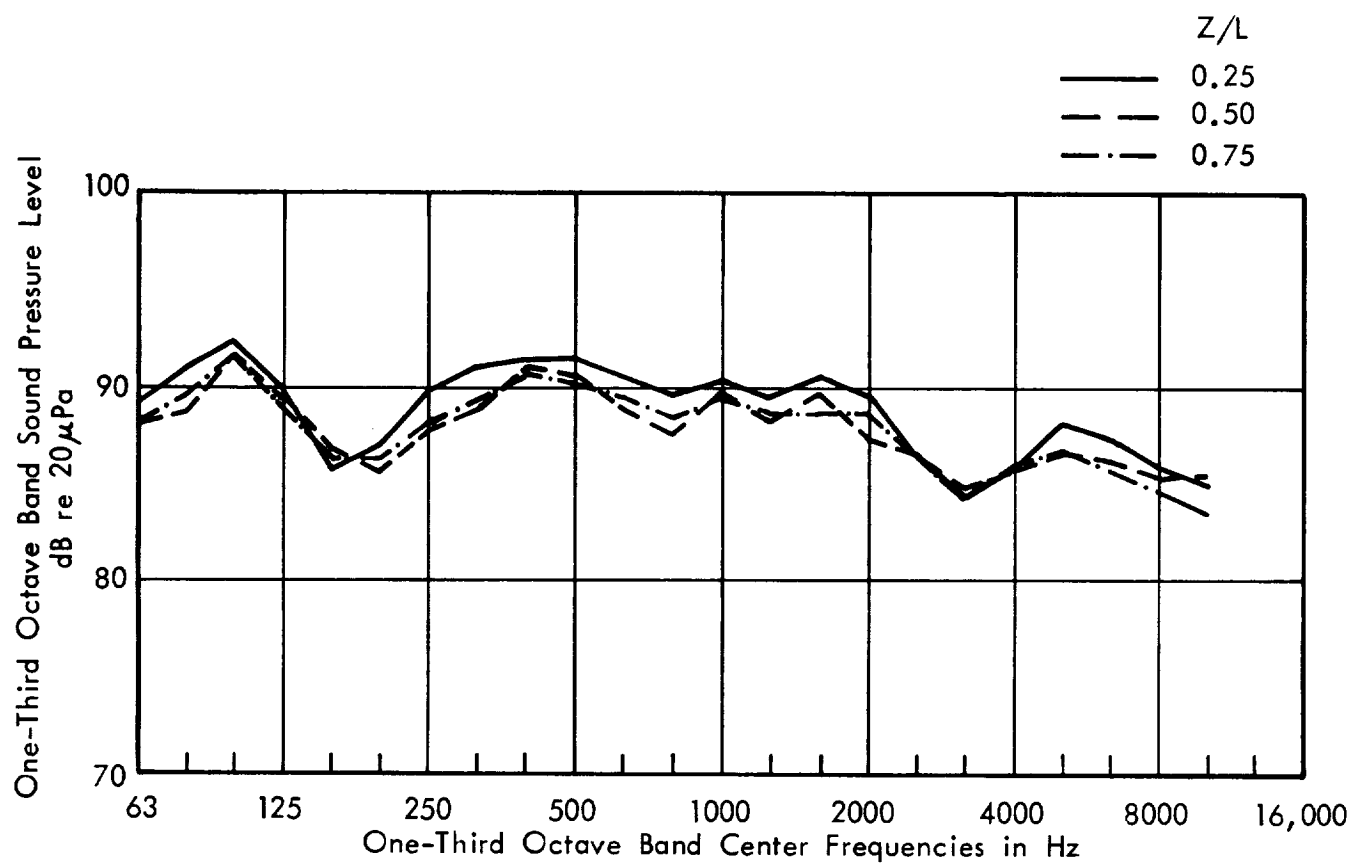


FIGURE 28. VARIATION OF MEAN CIRCUMFERENTIAL LEVEL ALONG CYLINDER LENGTH

axial station, and also between axial stations. The standard deviation between axial stations is generally less than 1 dB over the whole frequency range, while the standard deviation circumferentially is only marginally greater. The decay in axial level over the cylinder length is generally less than 1 dB based on the mean circumferential sound level spectra. Considered from the viewpoint of excitation levels, the plane of speakers provides a circumferentially homogeneous excitation, with minimal axial decay in level.

Coherence and phase measurements of the exterior pressure field were made over the cylinder surface, both circumferentially at $z/L = 0.5$ and along four equi-spaced axial lines.

Figure 29 shows the locations of these measurement planes, while details are summarized in Table 7. The axial microphone separations were 150mm, 300mm, and 450mm, with the microphone closest to the speaker plane located at $z/L = 0.25$. The circumferential separations varied from $22\frac{1}{2}^\circ$ (100mm) to 90° (400mm), and measurements concentrated on the top surface of the cylinder. Representative coherence and phase measurements are shown for axial and circumferential separations in Figures 30 and 31 respectively. For the axial coherence measurement (Figure 30), the phase variation with frequency is essentially continuous with constant slope, characteristic of a non-dispersive traveling wave. The coherence is fairly high in a broad-band sense but varies strongly from frequency to frequency, reflecting contamination of the cross-spectrum measurement by multi-path transmission between transducers, due, for example, to weak reflections from the absorptive surfaces.

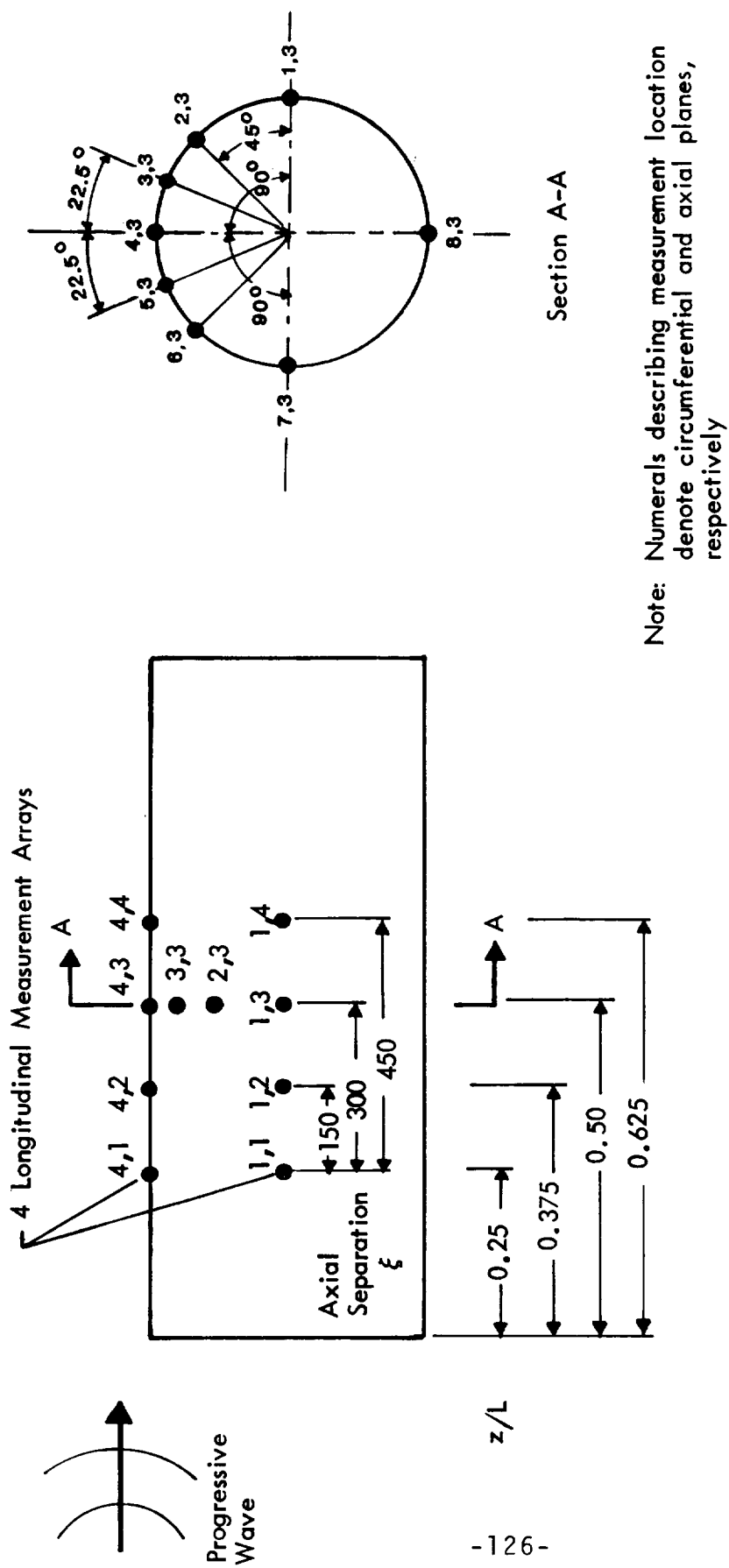


FIGURE 29. MICROPHONE LOCATIONS FOR MEASUREMENT OF COHERENCE AND PHASE OF PROGRESSIVE WAVE FIELD

Table 7. Summary of Coherence and Phase Measurements

Run No.	Figure No.	Measurement Direction	Microphone Locations	Separation (mm)
201	30	(1,1) and (1,2)	Longitudinal (axial)	150
202		(1,1) and (1,3)		300
203		(1,1) and (1,4)		450
204		(7,1) and (7,2)		150
205		(7,1) and (7,3)	Measurement	300
206		(7,1) and (7,4)		450
207		(8,1) and (8,2)		150
208		(8,1) and (8,4)		450
209		(4,1) and (4,2)		150
210		(4,1) and (4,4)		450
211	31	(1,3) and (4,3)	Circumferential	400 (90°)
212		(2,3) and (4,3)		200 (45°)
213		(3,3) and (4,3)	Measurement	100 (22.5°)
214		(3,3) and (4,3)		100 (22.5°)
215		(6,3) and (4,3)		200 (45°)
216		(5,3) and (4,3)		100 (22.5°)

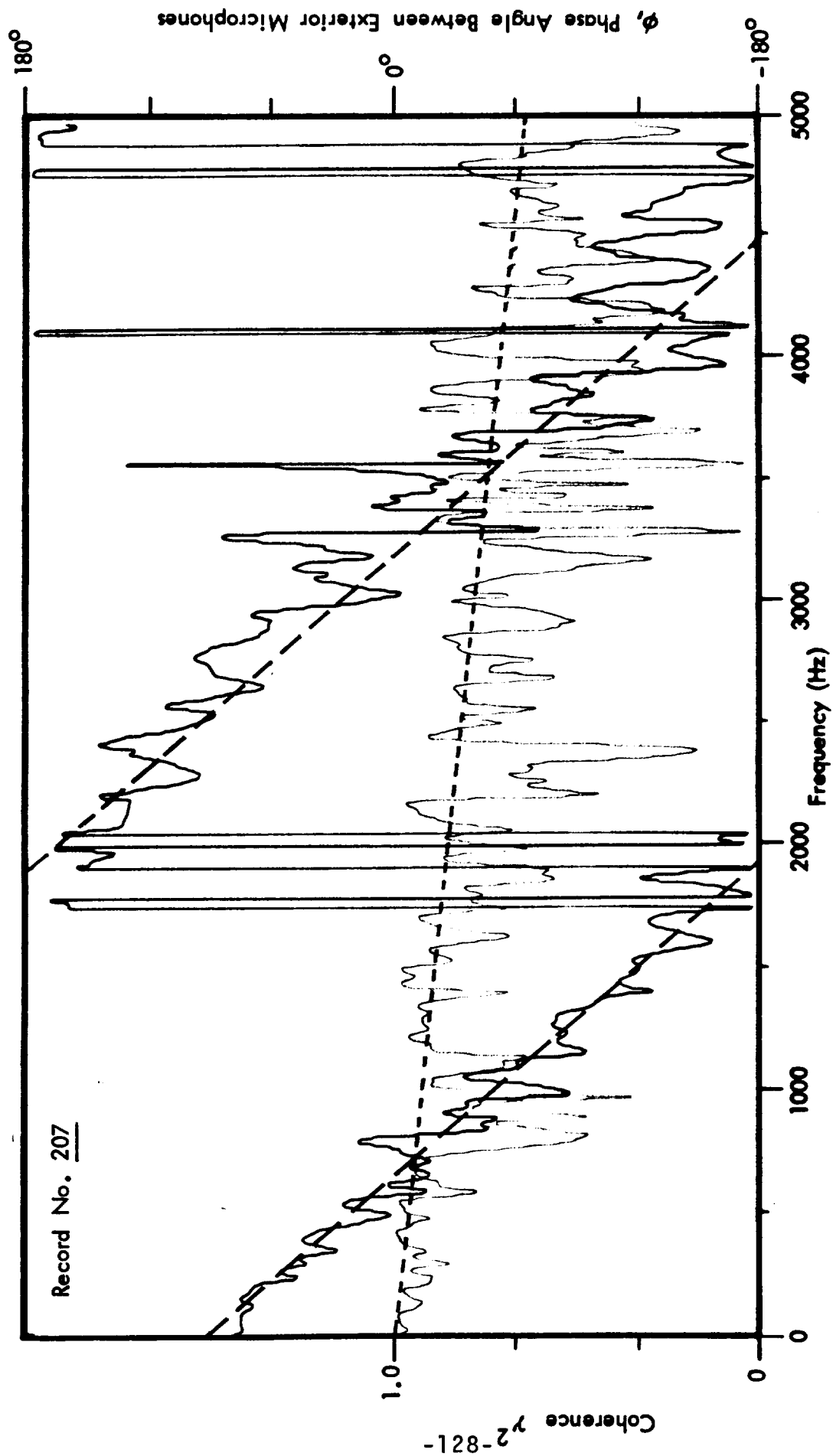


FIGURE 30. TYPICAL AXIAL COHERENCE AND PHASE DATA FOR PROGRESSIVE WAVE TEST.

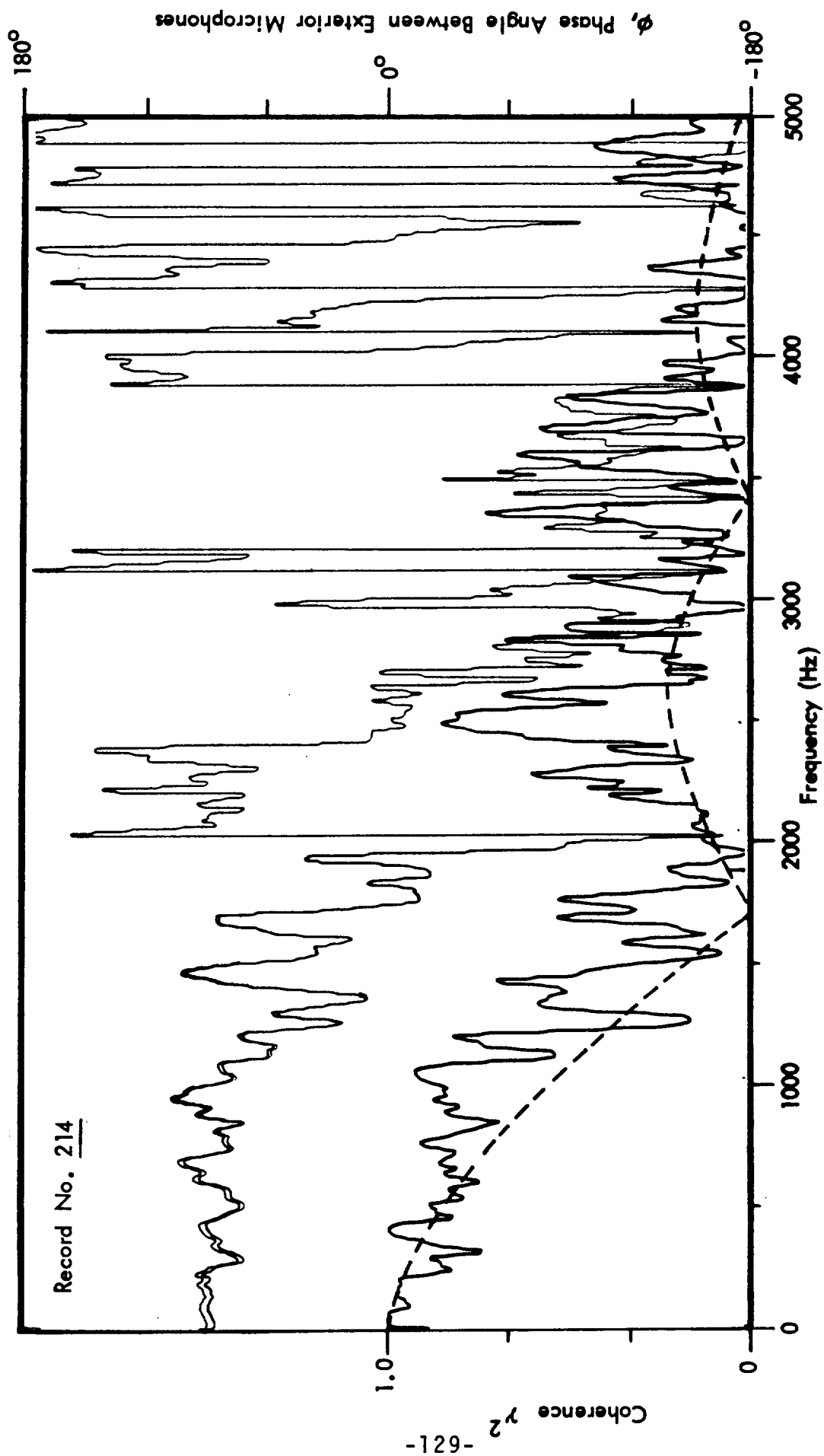


FIGURE 31. TYPICAL CIRCUMFERENTIAL COHERENCE AND PHASE DATA FOR PROGRESSIVE WAVE TEST.

For progressive wave excitation, the cross power spectral density of the external pressure field in the axial direction is assumed to be of the form

$$\phi_p(\omega) = \exp\left(-\frac{\omega\xi}{a_z U_z}\right) \exp\left(\frac{i\omega\xi}{U_z}\right) ,$$

where ξ is the separation distance (meters), U_z is the trace velocity in the axial direction (meters/sec), and a_z is the decay parameter. The trace velocity U_z may be estimated from the average slope of the phase curve (Figure 30), using

$$U_z = \frac{360\xi}{\text{Slope}} ,$$

where the "Slope" is the frequency in Hz divided by the phase in degrees. Similarly the decay parameters may be estimated from the coherence γ^2 (Figure 30). Since axially it is assumed that $\gamma^2 = \exp[-\omega\xi/(a_z U_z)]$, for large values of a_z (≈ 50), a straight line approximation can be fitted to the coherence function giving

$$a_z = \frac{2\pi\xi}{U_z} \left[\frac{2500}{\log_e \gamma_f^2} \right] .$$

Appendix C contains all of the measured data. From these, a mean value of the axial decay parameter $a_z = 56.3$ was determined and a trace velocity $U_z = 360\text{m/sec}$ was found.

In the circumferential direction, the phase plots do not show evidence of a progressive wave field. The circumferential field was assumed to have the characteristics of diffuse excitation which gives a coherence function of the form $(\sin k\eta)/k\eta$, where k is the acoustic wavenumber and η is the separation distance

between observer points. Figure 31 shows the measured coherence in the circumferential direction together with the diffuse field approximation. These show some agreement. However, it is clear that the analytical representation is weak.

Following the measurements of the coherence and phase, the space average interior levels were obtained. Measured exterior and interior sound levels are presented in Table 8 along with calculated mean levels and standard deviations. The mean exterior excitation levels are also shown, together with the resulting mean differences between blocked and interior levels. One standard deviation limits are also given. Where no upper limit to the difference is shown, the variation in the measured data is too great to allow a prediction of the upper limiting value. The spectra are plotted in Figure 32.

Table 8. Data for Progressive Wave Field Excitation

Frequency (Hz)	Mean Exterior Level, dB	Interior Levels, dB										Difference		
		z/L =		0.125		0.25		0.375		0.50				
		PI	PO	PI	PO	PI	PO	PI	PO	PI	PO	Mean	Mean x̄+s	x̄-s
63	86.80	52.00	40.00	40.20	36.00	48.25	38.75	41.00	38.00	45.9	40.9	37.5	---	
80	88.90	54.00	51.00	50.50	47.50	47.50	42.00	41.50	44.50	49.2	39.7	37.8	54.7	
100	92.50	68.25	67.00	52.50	52.25	49.00	46.50	44.25	47.00	61.8	30.7	26.3	---	
125	88.80	62.25	71.00	65.50	64.25	60.25	53.25	42.50	45.50	64.4	24.4	20.4	---	
160	86.70	71.00	64.00	69.00	68.00	63.25	58.50	44.75	50.00	66.1	20.6	17.4	---	
200	85.30	69.00	72.00	46.50	47.25	46.75	59.25	51.00	69.00	66.1	19.2	15.3	---	
250	84.90	73.00	75.00	62.00	64.50	68.50	64.75	75.75	76.25	72.6	12.3	9.4	23.7	
315	87.80	75.00	74.50	64.00	60.25	71.50	71.50	79.25	77.50	74.6	13.2	10.2	31.5	
400	90.50	72.00	75.25	71.25	73.00	71.50	73.50	69.75	74.00	72.8	17.7	16.2	19.9	
500	89.00	72.00	79.00	64.00	67.75	70.00	74.00	74.75	76.76	74.3	14.7	11.8	27.9	
630	87.20	72.25	76.00	72.00	78.25	69.25	76.50	71.00	73.50	74.5	12.7	10.4	18.1	
800	86.30	70.25	77.50	71.00	75.00	72.75	75.50	69.50	74.25	74.0	12.3	10.4	18.1	
1000	88.50	72.00	78.00	69.50	76.50	70.25	76.00	72.00	77.75	74.7	13.8	11.6	18.3	
1250	87.10	69.00	75.50	69.00	75.25	69.75	76.00	71.50	76.75	73.8	13.3	11.1	18.0	
1600	85.70	75.75	75.00	72.75	75.25	72.00	75.75	73.75	76.75	74.9	10.8	9.5	12.6	
2000	85.25	80.00	75.25	75.00	76.25	74.25	75.50	75.00	77.00	76.4	8.9	7.0	12.3	
2500	81.90	79.00	76.50	77.00	76.75	77.25	77.25	77.75	78.75	77.6	4.3	3.4	10.8	
3150	81.20	79.75	75.75	81.00	77.50	81.00	77.25	80.75	79.75	79.4	1.8	0.3	4.0	
4000	82.30	79.25	74.75	79.25	76.50	79.50	72.50	79.50	78.00	78.0	4.3	2.7	6.9	
5000	82.30	78.75	76.50	76.50	74.00	76.00	79.25	69.75	76.00	76.6	5.7	3.8	9.0	
6300	80.00	76.50	77.00	79.25	78.00	79.25	74.50	79.00	79.00	78.1	1.9	0.7	3.6	
8000	79.3	77.75	70.50	79.75	79.00	79.75	71.50	79.25	77.75	77.9	1.4	-0.5	4.7	
10000	76.5	61.00	56.75	64.50	62.50	64.50	77.00	65.00	61.25	69.0	7.5	2.5	---	

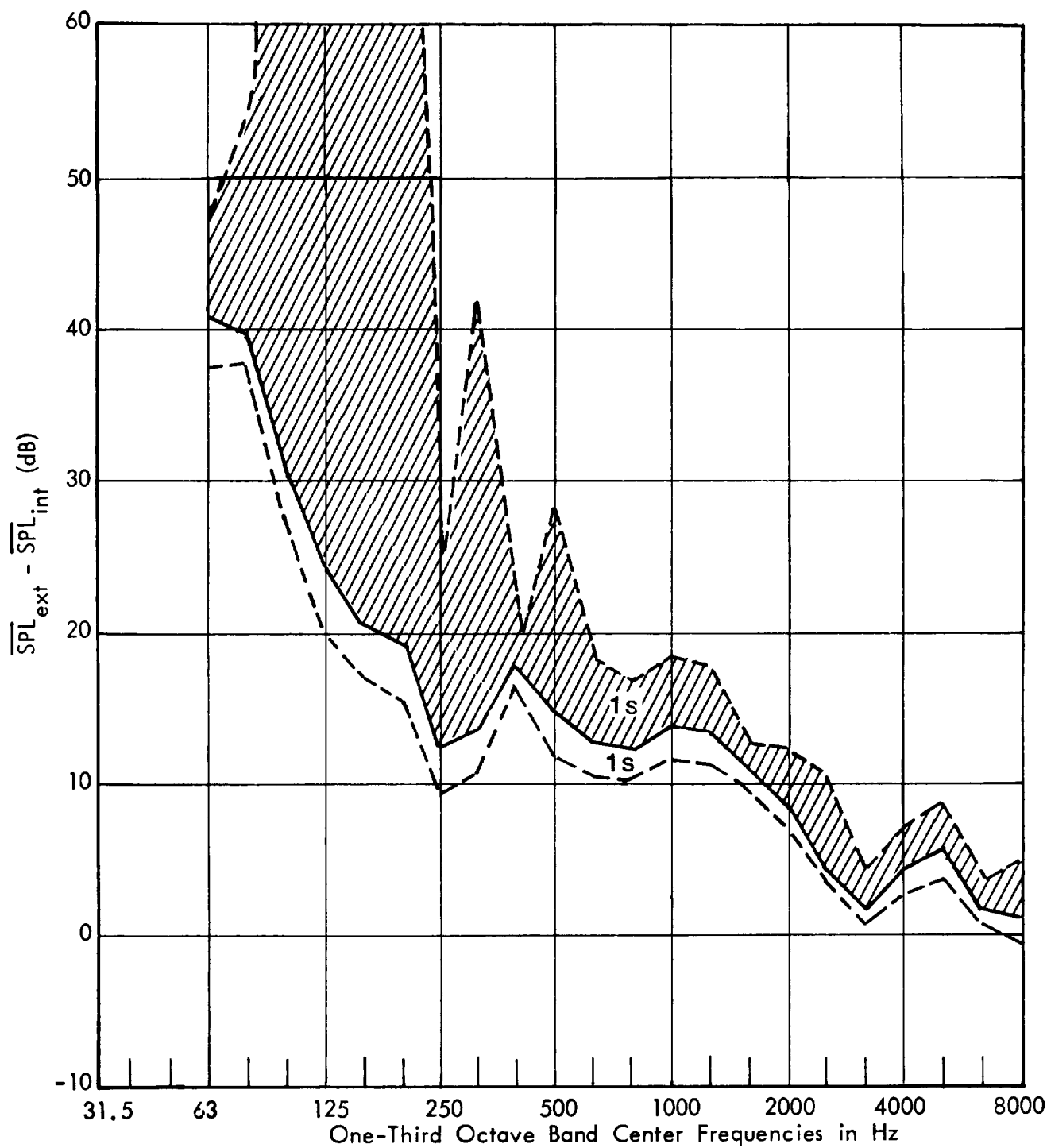


FIGURE 32. RATIO OF EXTERIOR PRESSURE TO AVERAGE INTERIOR PRESSURE, PROGRESSIVE WAVE EXCITATION

5.0 COMPARISONS AND VALIDATION OF ANALYTICAL MODELS

Basically, validation is obtained through comparison of computed and measured results. An analytical model can be said to be validated if predictions made with the model are in agreement with experimental results, i.e., to some required degree of accuracy.

One type of validation involves a comparison of a point prediction against a measurement having an uncertainty associated with it. The "true" value of the quantity being measured is known only within certain limits for any given level of confidence. The noise reduction measurement for the cylinder is an example of this type. Suppose that the average exterior level is known precisely. The measured space average interior level has associated with it an uncertainty due to the finite number of sampling points. The noise reduction computed from the measurements is an *estimate* of the *true* (real) noise reduction (which can be obtained only by sampling an infinite number of interior points).

The variance of the interior measurements for each band can be calculated using the unbiased variance estimator

$$s^2 = \frac{1}{N-1} \sum_{i=1}^N (x_i - \bar{x})^2$$

where N is the sample size, x_i is the sound level at i th location, and \bar{x} is the average of sound levels at N locations. Given the variance estimate for the measured space average levels in the cylinder, the critical value of the anticipated discrepancy between the predicted, \bar{x}_p , and measured averages, say in each one-third octave band due to statistical variability is [29]

$$|\bar{x} - \bar{x}_p| \leq \frac{s}{\sqrt{N}} t_{m;\alpha/2} \quad , \quad (63)$$

where s is the variance of the interior measurements, N is the sample size of the interior measurements, and $t_{m;\alpha/2}$ is the $\alpha/2$ percentage point of the Student "t" distribution with m degrees of freedom. The number of degrees of freedom is $m = N-1$. Eq.(63) simply defines the $(1-\alpha)$ percent confidence intervals. The critical values of the differences between the measured and predicted space-average interior levels, or, equivalently, the noise reductions, are then predicted with Eq.(63) by selecting, say, $\alpha = 0.01$ for a 1% level of significance.

The interpretation of the result is as follows. If the true space-average levels inside the cylinder were exactly equal to the analytical predictions then there would be a probability of only 1% that an indicated discrepancy between the measured and predicted levels based upon the experimental data would exceed the associated critical value. Hence, when an indicated discrepancy does exceed its associated critical value, i.e., lies outside the confidence intervals, it is very unlikely that the true space-average level and prediction are in fact equal, and one would accept the conclusion that a discrepancy actually exists. The indicated discrepancy is considered statistically significant at the 1% level. On the other hand, if an indicated discrepancy does not exceed its associated critical value, the evidence is considered insufficient to assert that an actual discrepancy exists.

Unfortunately, this type of analysis really only gives an indication of the accuracy of a given prediction, one which is developed not just with an analytical model, but with an analytical model that utilizes input data that may or may not be correct. Thus in the overall scheme of things, what is being validated is not just the analytical model, but the ability to parameterize the model (with a reasonable effort) as well. For this reason, in considering the noise reduction, a best and final prediction is made for comparison against the measurements, i.e., through manipulation of the input data, a best estimate within the bounds of the available theory and input data is made and the quality of this prediction is compared, from a statistical standpoint, against the measurements.

5.1 Basics of Computer Program

The analytical models of Section 3 were computerized to automate the calculations of the cylinder noise reduction and the various transfer functions as required for comparison with experimental results. An outline of the overall computational procedure, with details of how the various components of the analytical model are assembled together within the computer program, is presented below.

The initial step in all computations is to calculate, using the given dimensions, the resonance frequencies of all structure modes of the cylinder and to classify them into frequency bands. For the high-frequency regime, band-averaged response quantities including joint acceptances, modal densities, radiation efficiencies, etc., are then calculated over the frequencies of concern using appropriate excitation models as required. These results are calculated in a separate preparatory program and

stored on disc. The initial function of the main program is to calculate and order the resonance frequencies of the cylindrical volume in frequency bands, and to combine this acoustic modal data, including acoustic loss factors, with previously calculated and stored structural data (including structural loss factors). The detailed calculation of the cylinder noise reduction or transfer function is carried out with a series of subroutines which are structured in a similar manner to allow separation of resonance, stiffness, and mass-controlled structure and acoustic response. In particular, for the noise reduction, in each one-third octave band, the five modal pairs (structure and acoustic) which contribute most to the overall interior response are identified and rank-ordered. In addition, the contribution of resonant and non-resonant acoustic modes and of resonant and non-resonant structure modes to the interior sound level is determined in each frequency band.

5.2 Noise Reduction of the Test Article

Prediction of the test cylinder noise reduction is now considered, i.e., the development of the prediction which is used in the statistical comparison. This is followed by the statistical analysis itself.

5.2.1 Calculated Results

The initial calculation was for the case of an ideal 1.2192 meter (48 inch) cylinder enclosing a 1.2192 meter (48 inch) cylindrical cavity. The input data consisted of the measured acoustic and structural loss factors as detailed in Table 3. The noise reductions for the one-third octave bands with center frequencies from 40 Hz to 1250 Hz inclusive were computed with Eq.(10).

Beginning with the one-third octave band centered at 1600 Hz, the noise reductions were computed with the high frequency relation, Eq. (17). The selected division between low and high frequency regimes means that for predictions using the low frequency model, there were 30 or fewer acoustic modes resonant in each one-third octave band (for the cylinder of concern, the 1250 Hz band has 28 resonant acoustic modes). It should be kept in mind that in addition to comparing the predictions against measurements, one can also examine the transition from low to high frequency models.

Figure 33 shows the initial prediction (Curve No. 1) plotted against the BBN measurement from Figure 15. As can be seen the prediction has a shape similar to the measurement. The predicted noise reduction exceeds the measured out to 315 Hz, but is less than the measured beyond that frequency until about 1600 Hz. Note that a negative noise reduction is predicted at 1000 Hz and at 1250 Hz. Also there appears to be a step change in predictions as one moves from the low frequency to the high frequency models (from 1250 Hz to 1600 Hz).

In order to determine if the step change was an artifact of the analysis, the cylinder length was taken to be 1.1938 meters (47 inches), which is more in keeping with the actual construction of the test article. The cavity length remained 1.2192 meters (48 inches). The resulting prediction is Curve No. 2. With this new length, the prediction for the 1250 Hz band changed from -10.2 dB to +3.0 dB. The 1000 Hz band, which for the 48 inch case was -5.3 dB, dropped to -11.8 dB. Predictions for other bands are, in comparison to measurements, in some instances better, in others, worse. The transition from the 1250 Hz band to the 1600 Hz band is now reasonably good.

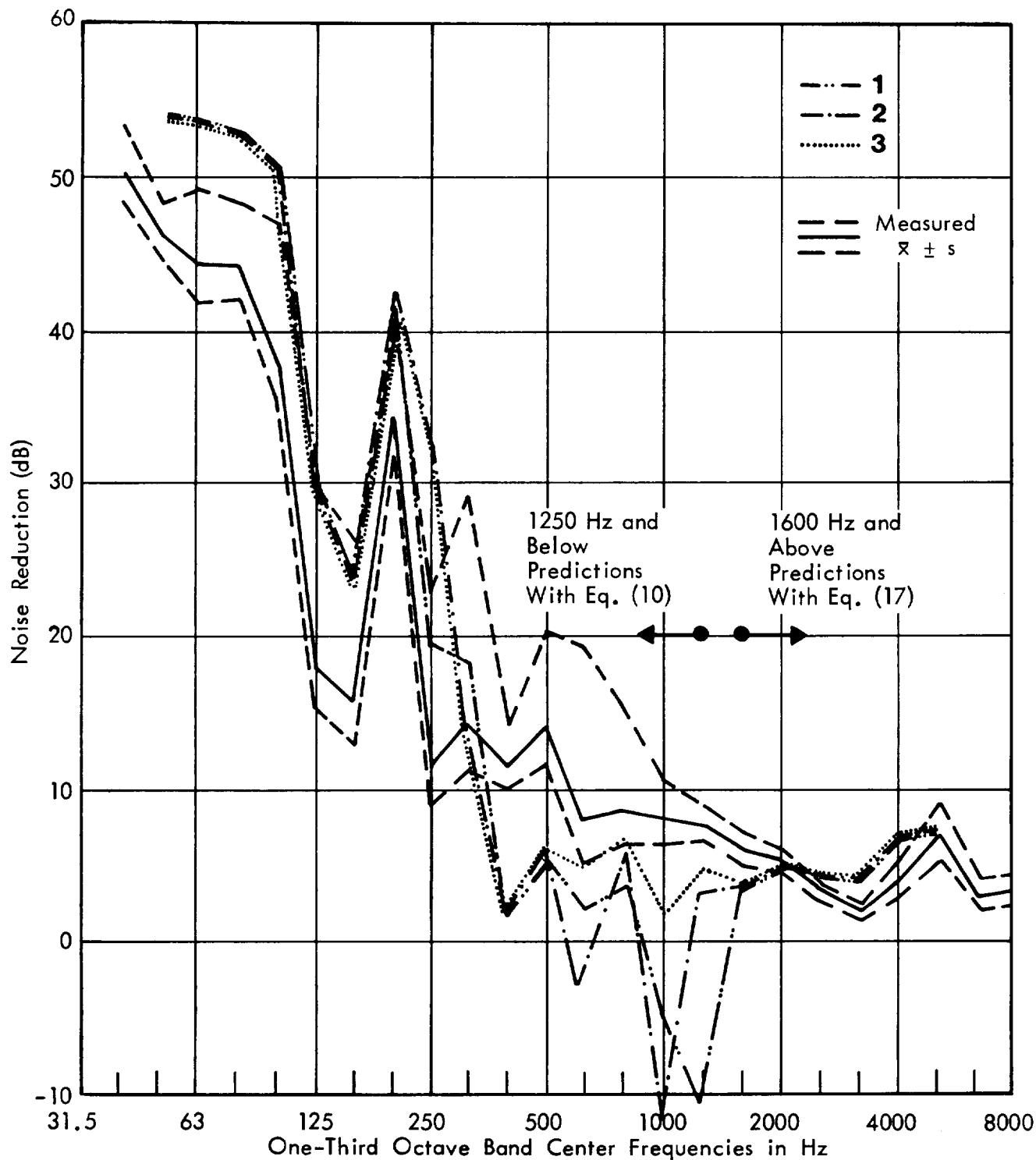


FIGURE 33. INITIAL NOISE REDUCTION PREDICTIONS WITH ANALYTICAL MODEL

As has been stated, the computer program can output the five highest contributing modal pairs. A sample of this output for the 1000 Hz band for Curve 2 of Figure 33 is given below.

Noise Reduction for Frequency 1000 Hz

Acoustic Mode				Structure Mode			P(INT)**2/
Q	N	S	Freq.	M	N	Freq.	P(EXT)**2
1	2	1	671.3	2	2	892.0	.1780E-01
3	2	1	780.4	2	2	892.0	.2555E-01
4	3	1	1063.9	3	3	951.4	.6043E-01
0	3	1	902.9	3	3	951.4	.9543E-01
2	3	1	945.8	3	3	951.4	.1501E+02
TOTAL				P(INT)**2/ NOISE P(EXT)**2 REDUCTION .1525E+02 -11.83			
Contributions from Acoustic Modes							
Below Band		In Band		Above Band			
.4346E-01		.1519E+02		.1960E-01			

It is obvious from this data that the large negative noise reduction predicted is due to a single modal pair. Both of the problem modes are resonant in the 1000 Hz band and they are closely spaced. The (2,3,1) acoustic mode is resonant at 945.8 Hz; the (3,3) structure mode is resonant at 951.4 Hz. The analytical model thus predicts a 5.6 Hz difference in resonance frequencies.

The modal bandwidths of the two modes can be calculated with the data of Table 3. For the acoustic mode (2,3,1) the half power

bandwidth is

$$B_n = \eta_n f_n = .0097(945.8) = 9.17 \text{ Hz} \quad .$$

The structure mode (3,3) half power bandwidth is

$$B_r = \eta_r f_r = .0018(951.4) = 1.71 \text{ Hz} \quad .$$

These are therefore two closely coupled modes. If these two modes were in fact truly closely coupled in the test article, the noise reduction might be less than that presently measured (perhaps negative). The interpretation of the measurements is that this close coupling does not occur in the test article. The coupling can be excluded in the computer model by forcing the difference between resonance frequencies to be greater than the modal bandwidths.

In addition to the problem above, the loss factor η_r for the structure modes used in the analytical model is the sum of the measured dissipative loss factor and the computed band average radiation loss factor. Examination of the principal structure mode contributors, such as the (3,3) mode in the 1000 Hz band, shows that from 630 Hz to 1250 Hz, all are acoustically fast modes and should have a radiation efficiency of unity. The average radiation loss factors which are used are five to six dB below the radiation loss factors of the principal contributing modes; thus the value of η_r is being underestimated.

Curve 3 of Figure 33 is, again, the case of the 47 inch cylinder with a 48 inch cavity, except the spacing between the closely coupled modes (such as (2,3,1) and (3,3)) has been increased so

that there is no modal overlap. From 630 Hz to 1250 Hz, account has been taken of the higher radiation damping due to the principal contributing structure modes being acoustically fast. This new prediction shows how important the input data are. If two closely coupled modes actually occur at low frequencies (in the real situation) the noise reduction will depend almost solely on the damping present.

Proceeding with the analysis of the noise reduction curve, it is seen in Curve 3 of Figure 33, that between 400 Hz and 630 Hz, more transmission is predicted than measured. Shown below is the computer output for the bands from 315 Hz to 800 Hz.

Noise Reduction for Frequency 315 Hz							
Acoustic Q	Mode N	Mode S	Freq.	Structure M	Mode N	Freq.	$P(INT)**2 / P(EXT)**2$
3	4	1	1218.3	2	2	331.0	.7875E-04
1	4	1	1151.5	2	4	331.0	.2353E-03
0	1	1	395.7	1	1	692.9	.7253E-03
2	2	1	714.2	1	2	289.0	.4580E-02
0	2	1	656.4	1	2	289.0	.2791E-01
Total				$P(INT)**2 / P(EXT)**2$		NOISE REDUCTION	
				.3367E-01		14.73	

Contributions from Acoustic Modes		
Below Band	In Band	Above Band
.7077E-07	.1874E-04	.3365E-01

Noise Reduction for Frequency 400 Hz

Acoustic Mode				Structure Mode			P(INT)**2/ P(EXT)**2
Q	N	S	Freq.	M	N	Freq.	
1	1	1	395.7	3	1	2349.7	.1178E-03
2	1	1	485.6	1	1	692.9	.3197E-03
0	2	1	656.4	1	2	289.0	.5150E-03
1	1	1	420.0	2	1	1661.6	.7326E-02
0	1	1	395.7	1	1	692.9	.5887E+00
Total				P(INT)**2/ P(EXT)**2			NOISE REDUCTION
							.5972E+00 2.24

Contributions From Acoustic Modes

Below Band	In Band	Above Band
.1626E-06	.5963E+00	.9437E-03

Noise Reduction for Frequency 500 Hz

Acoustic Mode				Structure Mode			P(INT)**2/ P(EXT)**2
Q	N	S	Freq.	M	N	Freq.	
2	1	1	485.6	3	1	2349.7	.1034E-02
3	3	1	996.7	2	3	510.0	.1609E-02
0	1	1	395.7	1	1	692.9	.1779E-02
1	3	1	913.8	2	3	510.0	.6124E-02
2	1	1	485.6	1	1	692.9	.2184E+00
Total				P(INT)**2/ P(EXT)**2			NOISE REDUCTION
							.2302E+00 6.38

Contributions from Acoustic Modes

Below Band	In Band	Above Band
.1811E-02	.2195E+00	.8953E-02

Noise Reduction for Frequency 630 Hz

Acoustic Mode				Structure Mode			P(INT)**2/ P(EXT)**2
Q	N	S	Freq.	M	N	Freq.	
2	1	1	485.6	1	1	692.9	.6262E-02
0	1	1	395.7	1	1	692.9	.1361E-01
4	1	1	688.0	1	1	692.9	.4765E-01
1	2	1	671.3	2	2	892.0	.9216E-01
0	2	1	656.4	1	2	289.0	.1075E+00

P(INT)**2/ NOISE
P(EXT)**2 REDUCTION
.2719E+00 5.66

Total

Contributions from Acoustic Modes

Below Band	In Band	Above Band
.1988E-01	.2488E+00	.3169E-02

Noise Reduction for Frequency 800 Hz

Acoustic Mode				Structure Mode			P(INT)**2/ P(EXT)**2
Q	N	S	Freq.	M	N	Freq.	
2	2	1	714.2	3	2	1491.4	.3191E-02
4	1	1	688.0	1	1	692.9	.3850E-02
1	2	1	671.3	2	2	892.0	.7937E-02
2	2	1	714.2	1	2	289.0	.1908E-01
3	2	1	780.4	2	2	892.0	.1642E+00

P(INT)**2/ NOISE
P(EXT)**2 REDUCTION
.2124E+00 6.73

Total

Contributions from Acoustic Modes

Below Band	In Band	Above Band
.1416E-01	.1911E+00	.7161E-02

The one thing that stands out in the data is that the (1,1) structure mode is the predicted dominant transmitter at 400 Hz and at 500 Hz. It also contributes significantly at 630 Hz.

The structure model used is that of a freely supported cylinder. The (1,1) mode is a beam mode, i.e., a translational ring mode. However, the test article is suspended on soft spring/cords. If there is any mode which would be difficult to excite, it would be the (1,1) mode. In fact, an argument can be made for excluding all N=1 structure modes since they represent translation rather than bending in the circumferential direction.

If one excludes the (1,1) mode, the predicted noise reduction is as shown in Figure 34. The measurements are more or less bounded from 400 Hz to 630 Hz by the predictions made with and without the participation of the (1,1) structure mode.

Consider now the frequency range 125 Hz to 250 Hz. The computer output is

Noise Reduction for Frequency 125 Hz							
Acoustic Mode				Structure Mode			P(INT)**2/ P(EXT)**2
Q	N	S	Freq.	M	N	Freq.	
1	0	1	140.7	2	0	3437.2	.3597E-05
4	4	1	1273.9	1	4	126.6	.4927E-05
0	3	1	902.9	1	3	153.4	.1205E-04
2	4	1	1177.0	1	4	126.6	.1758E-03
0	4	1	1142.9	1	4	126.6	.7998E-03
				P(INT)**2/			NOISE
Total				P(EXT)**2			REDUCTION
				.1006E-02			29.98
Contributions for Acoustic Modes							
Below Band			In Band			Above Band	
0.			.3755E-05			.9977E-03	

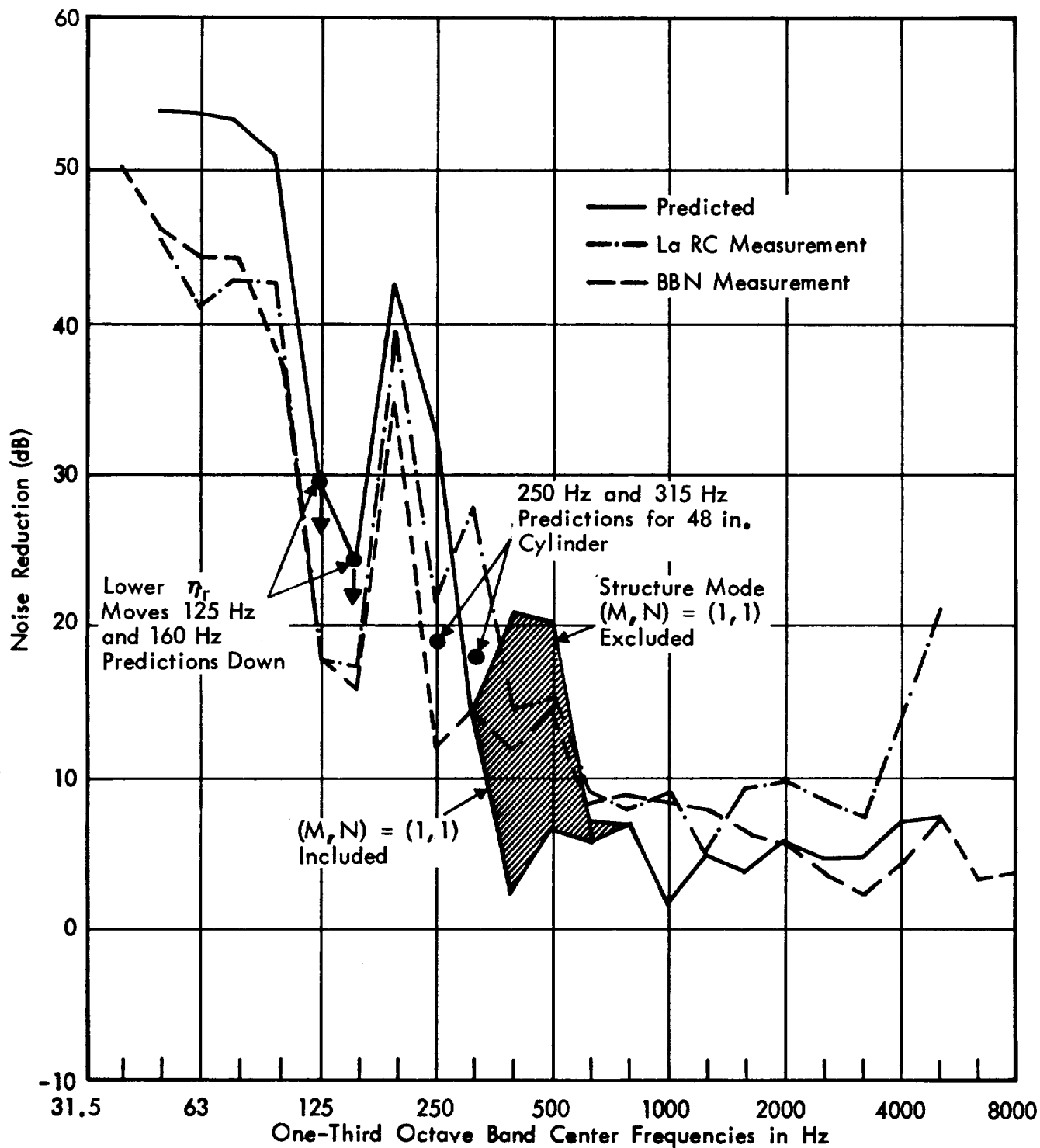


FIGURE 34. COMPARISON OF PREDICTED AND MEASURED NOISE REDUCTIONS

Noise Reduction for Frequency 160 Hz							
Acoustic Mode				Structure Mode			P(INT)**2/ P(EXT)**2
Q	N	S	Freq.	M	N	Freq.	
2	5	1	1407.3	1	5	159.7	.4868E-04
1	0	1	140.7	2	0	3437.2	.5613E-04
0	5	1	1378.9	1	5	159.7	.2136E-03
2	3	1	945.8	1	3	153.4	.5755E-03
0	3	1	902.9	1	3	153.4	.2813E-02

P(INT)**2/ NOISE
P(EXT)**2 REDUCTION
.3739E-02 24.27

Total

Contributions for Acoustic Modes

Below Band	In Band	Above Band
.6831E-04	0.	.3680E-02

Noise Reduction for Frequency 200 Hz							
Acoustic Mode				Structure Mode			P(INT)**2/ P(EXT)**2
Q	N	S	Freq.	M	N	Freq.	
2	2	1	714.2	1	2	289.0	.2624E-02
2	3	1	945.8	1	3	153.4	.2714E-02
0	3	1	902.9	1	3	153.4	.1331E-04
0	2	1	656.4	1	2	289.0	.1536E-04
0	1	1	395.7	1	1	692.9	.1614E-04

P(INT)**2/ NOISE
P(EXT)**2 REDUCTION
.5561E-04 42.55

Total

Contributions from Acoustic Modes

Below Band	In Band	Above Band
.2026E-06	0.	.5541E-04

Noise Reduction for Frequency 250 Hz							
Acoustic Mode				Structure Mode			P(INT)**2/ P(EXT)**2
Q	N	S	Freq.	M	N	Freq.	
2	1	1	485.6	1	1	692.9	.5411E-05
2	2	1	714.2	1	2	289.0	.5245E-04
1	5	1	1386.0	2	5	264.0	.6209E-04
0	1	1	395.7	1	1	692.9	.7710E-04
0	2	1	656.4	1	2	289.0	.3157E-03
				P(INT)**2/			NOISE
Total				P(EXT)**2			REDUCTION
				.5244E-03			32.80
Contributions from Acoustic Modes							
Below Band			In Band			Above Band	
.1052E-05			0.			.5243E-03	

From these data, it can be seen that the dip in the noise reduction at 125 Hz is due to the resonant response of the (1,4) structure mode at 126.6 Hz. Note that an acoustic mode of N order equal to 4, occurring at 1142.9 Hz, and responding in a non-resonant fashion in the 125 Hz band, is the principal contributor. This shows clearly that it is no simple matter to make general statements regarding transmission at low frequencies. The prediction at 125 Hz is pretty much dependent on the loss factor of the (1,4) structure mode.

At 160 Hz, the (1,3) structure mode is resonant and the noise reduction is predicted to be below 25 dB. At 200 Hz, the measured and predicted noise reductions are near 40 dB (LaRC measurement). In this band, there are no resonant acoustic or structure modes.

At frequencies below 125 Hz, the cylinder volume is stiffness controlled and the noise reduction is predicted to asymptote to about 53 dB, based on the volume displacement afforded by the end caps.

At frequencies in the range 1250 to 5000 Hz, the noise reduction is predicted and measured to be quite low. The BBN measurement shows values as low as 3 dB. This indicates that radiation damping is playing a significant role in the energy dissipation of the structure modes. In this case, the transmission is resonance controlled. The mass controlled transmission terms in Eq. (17) are negligible, i.e., $\tau_f \ll \tau_R$. and Eq. (17) goes to

$$\frac{\langle p_e^2 \rangle_{s,t}}{\langle p_i^2 \rangle_{s,t}} = \frac{\bar{\alpha}_s}{\tau_R A} + \frac{\bar{\eta}_r}{\eta_{rad}^{ext}} \quad .$$

Since the absorption inside is small compared to the radiation damping, the above becomes

$$\frac{\langle p_e^2 \rangle_{s,t}}{\langle p_i^2 \rangle_{s,t}} = \frac{\bar{\eta}_r}{\eta_{rad}^{ext}} \quad .$$

Further with $\eta_r \ll \eta_{rad}$, it is found that

$$\frac{\langle p_e^2 \rangle_{s,t}}{\langle p_i^2 \rangle_{s,t}} \approx 2$$

or

$$NR \approx 3 \text{ dB} \quad .$$

Apparently the correct explanation for the observed transmission at high frequencies (beyond 1250 Hz), is that the cylinder damping is radiation controlled.

In Figures 35 and 36 the various modal contributions are shown. The interior pressure is always due to either stiffness or resonance controlled acoustic response (Fig.35). At high frequencies, resonant structure modes are transmitting to resonant acoustic modes (Figures 35 and 36).

5.2.2 Statistical Analysis of Cylinder Noise Reduction Data

As discussed in Section 4, considerable data were collected for the experimental cylinder in the form of exterior and interior sound pressure level measurements from which noise reductions in one-third octave bands were calculated. The data were the following:

- 1). LaRC tests - 40 noise reduction measurements using fixed interior microphone locations at
 - (a) four angular locations ($\theta = 0, 90, 180, \text{ and } 270$ degrees)
 - (b) two radial locations ($r = 0.1397$ and 0.2077 meters)
 - (c) five longitudinal locations ($z/L = 0.56, 0.69, 0.75, 0.85, \text{ and } 0.95$).
- 2). BBN tests - 32 noise reduction measurements using fixed interior microphone locations at
 - (a) four angular locations ($\theta = 0, 90, 180, \text{ and } 270$ degrees)
 - (b) two radial locations ($r = 0.1397$ and 0.2077 meters)
 - (c) four longitudinal locations ($z/L = 0.56, 0.69, 0.75, \text{ and } 0.88$).

Some of the data from the BBN test were machine averaged over the four angular locations so individual noise reduction estimates at all angles are not available.

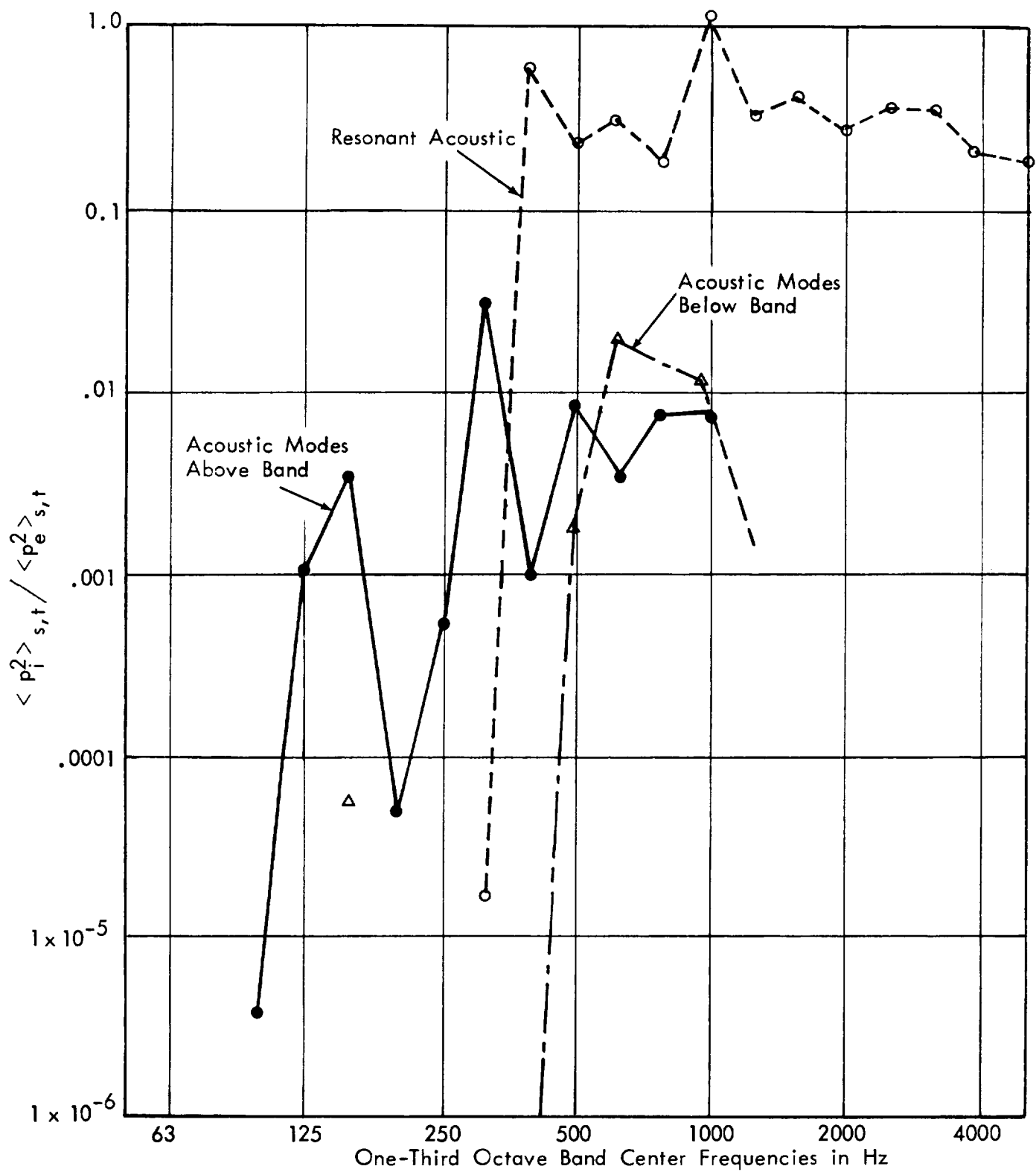


FIGURE 35. MODAL CONTRIBUTIONS TO INTERIOR SOUND LEVELS

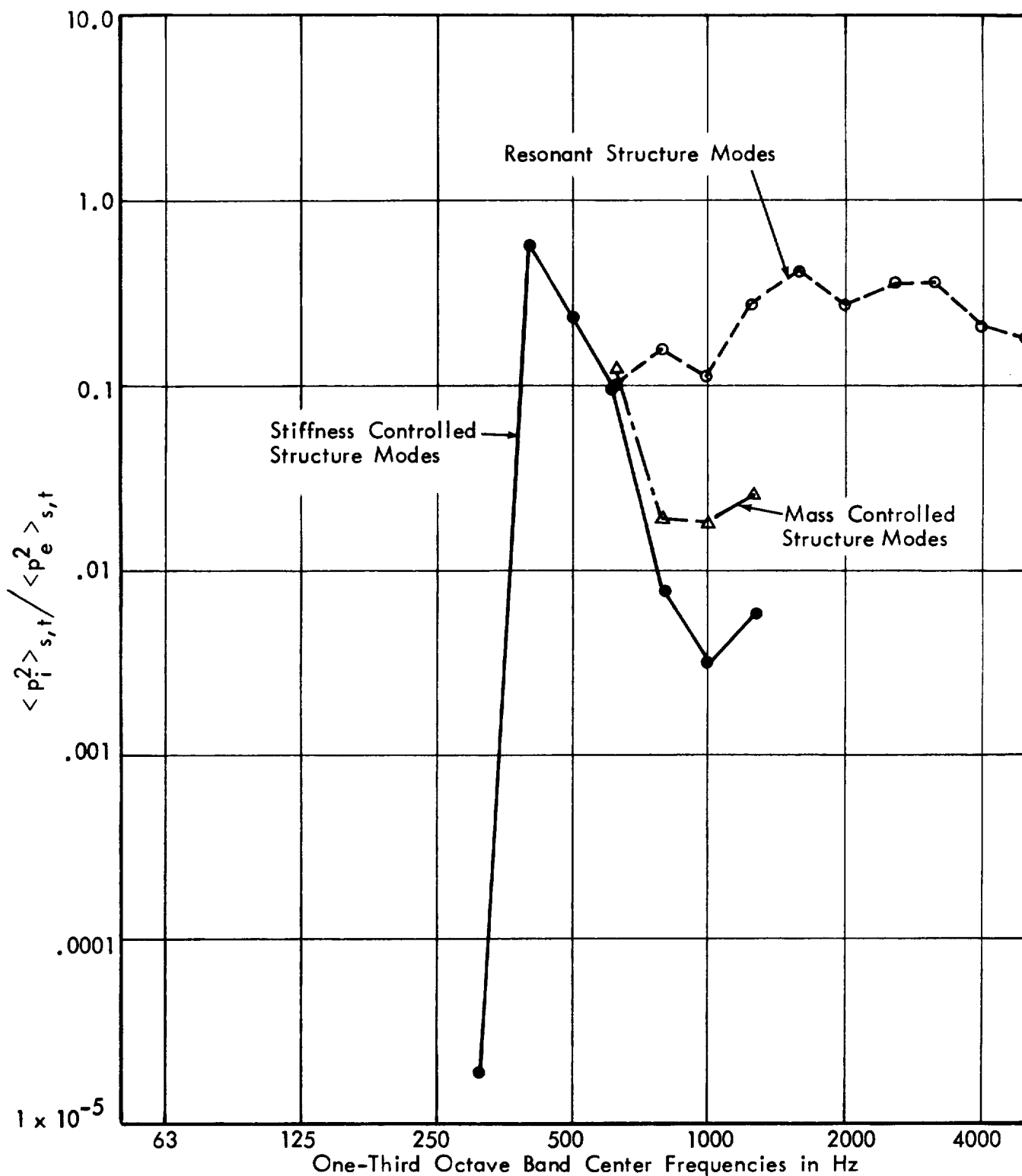


FIGURE 36. STRUCTURE RESPONSE CONTRIBUTIONS TO RESONANT ACOUSTIC RESPONSE ONLY

To obtain an estimate of the cylinder noise reduction, a collection of noise reduction measurements representing approximately equal acoustic subvolumes inside the cylinder is required. The angular and radial locations of the measurements for both the LaRC and BBN experiments fall reasonably close to the centers of equal subvolumes along these axes. The longitudinal measurement locations of the BBN tests do not represent equal subvolumes, but they are sufficiently spread along the longitudinal axis to provide an acceptable approximation over half the cylinder length. Symmetry permits these measurements to be used to represent the entire cylinder length. Since some of the angular measurements were machine average, the data at various angular positions for all the radial and longitudinal locations for both the LaRC and BBN tests were averaged to arrive at noise reduction estimates representing similar subvolumes for both tests. This provided a total of ten noise reduction estimates (two radial locations at five longitudinal locations) for the LaRC tests, and eight noise reduction estimates (two radial locations at four longitudinal locations) for the BBN tests. The resulting noise reduction estimates are presented in Tables 9 and 10.

The noise reduction of the cylinder was computed using the 18 estimates from the LaRC and BBN tests, assumed to represent equivalent subvolumes, as follows:

$$NR = -10 \log \left[\frac{1}{N} \sum_{i=1}^N 10^{-NR_i/10} \right] ,$$

where NR_i represents each of the $N = 18$ noise reduction estimates. To quantify the accuracy of the estimates, 99% confidence intervals for the noise reduction estimates were also calculated using the relationship

Table 9. Noise Reduction Estimates from LaRC Experiments

1/3 Octave Band Center Freq. (Hz)	Noise Reduction in dB at Various Locations				
	r = 0.1397 meters			r = 0.2077 meters	
	0.56	0.69	0.75	0.85	0.95
40	49.7	50.8	48.3	49.4	47.9
50	51.9	50.4	52.4	51.7	50.0
63	45.1	46.4	45.2	42.9	42.5
80	47.8	48.8	45.0	41.9	39.6
100	46.2	47.4	44.0	42.1	41.6
125	24.9	20.3	15.9	17.1	16.5
160	24.9	19.3	14.9	16.1	16.2
200	43.3	43.8	40.6	42.3	43.0
250	22.8	26.6	26.9	29.1	20.5
315	28.4	32.0	35.3	30.8	26.8
400	15.5	18.2	14.6	15.0	17.5
500	14.7	18.6	23.4	17.7	16.6
630	13.5	13.8	12.3	11.7	7.7
800	11.7	9.6	11.2	11.1	9.2
1000	11.7	14.2	13.8	12.6	11.2
1250	10.0	12.6	10.2	11.2	11.2
1600	9.9	12.1	11.5	11.7	11.5
2000	9.7	10.9	9.4	9.2	13.7
2500	8.2	8.6	7.8	8.2	8.7
3150	6.5	8.1	6.7	7.0	6.3
4000	12.2	13.8	13.0	12.3	13.4
5000	21.6	22.1	21.2	21.1	20.8
	37.8	46.6	42.8	43.7	41.7
	37.9	44.3	46.5	49.2	47.7
	41.3	39.0	39.3	42.9	40.0
	45.7	43.9	42.9	40.8	39.2
	44.7	42.4	42.0	40.4	39.6
	23.6	19.4	15.4	16.0	16.1
	21.7	18.3	14.2	15.2	15.6
	36.6	38.2	36.2	39.6	39.5
	17.6	19.3	18.9	23.0	24.9
	24.8	25.4	27.6	28.4	25.6
	12.6	14.0	12.4	11.8	15.1
	14.2	14.2	15.8	15.2	12.6
	7.7	8.8	7.3	5.8	4.0
	7.6	5.0	6.5	6.6	3.3
	5.5	7.3	7.1	6.9	3.9
	2.1	4.0	2.6	4.3	2.7
	6.3	7.5	7.6	6.8	9.1
	8.0	8.0	7.7	8.6	12.6
	8.0	8.1	7.9	8.0	9.4
	8.6	8.7	8.2	8.8	7.2
	13.6	13.2	13.2	13.7	13.7
	21.2	21.1	21.0	21.0	21.6

Table 10. Noise Reduction Estimates from BBN Experiments

1/3 Octave Band Center Freq. (Hz)	Noise Reduction in dB at Various Locations							
	r = 0.1397 meters				r = 0.2077 meters			
	0.50	0.63	0.75	0.87	0.50	0.63	0.75	0.87
40	54.0	52.4	50.6	49.7	52.0	50.6	64.1	47.1
50	47.0	48.6	45.4	44.2	49.1	47.2	45.6	45.0
63	47.7	49.8	41.9	40.6	46.2	46.7	44.5	43.5
80	49.8	47.5	42.8	42.0	48.8	46.1	42.4	41.7
100	46.8	46.9	37.2	36.9	43.6	40.9	34.7	34.5
125	43.2	24.2	15.3	17.5	37.7	21.0	14.5	15.2
160	38.6	21.5	13.2	14.7	33.7	18.8	12.3	13.1
200	34.5	32.7	41.5	37.8	30.4	34.3	38.3	35.6
250	10.7	8.9	25.1	16.3	7.7	11.9	21.6	14.2
315	13.6	11.9	30.9	18.3	9.7	14.4	28.9	15.8
400	15.8	12.1	11.3	15.1	11.0	9.4	10.3	12.2
500	12.2	14.2	20.4	19.9	10.7	11.9	18.3	17.0
630	12.1	13.5	10.0	11.3	10.7	9.3	5.2	3.5
800	11.8	9.4	11.5	15.4	10.1	4.6	7.0	9.7
1000	6.9	10.8	11.4	12.8	7.2	7.0	7.3	6.8
1250	8.2	9.4	8.2	9.3	7.4	8.2	6.4	6.8
1600	4.3	6.3	5.5	6.2	5.8	7.3	7.1	6.9
2000	4.4	5.6	4.3	5.5	6.2	5.8	5.6	6.2
2500	2.8	4.2	3.5	3.9	3.5	2.9	3.0	2.9
3150	1.6	1.6	1.5	1.7	2.4	2.1	3.1	2.8
4000	2.6	3.7	3.3	3.3	4.6	4.9	6.3	5.4
5000	5.3	5.9	5.4	6.7	8.4	8.4	9.5	9.5

$$NR_{99} = -10 \log \left[10^{-NR/10} \pm \frac{s}{\sqrt{N}} t_{m;0.005} \right] ,$$

where

$$s = \left[\frac{1}{N-1} \sum_{i=1}^N \left(10^{-NR_i/10} - 10^{-NR/10} \right)^2 \right]^{\frac{1}{2}} ,$$

and $t_{m;0.005}$ is the 0.005 percentage point of the Student "t" variable with $m = N - 1 = 17$ degrees-of-freedom. It is assumed that the individual noise reduction estimates are statistically independent, which is believed to be an acceptable assumption. The resulting space averaged noise reduction calculations and their 99% confidence intervals are detailed in Table 11 and plotted in Figure 37. Note that in two frequency bands (the 1/3 octave intervals centered at 250 and 315 Hz), it was necessary to define the lower confidence limit for a 95% interval because a 99% interval produced an infinite upper bound.

Also shown in Figure 37 is the analytical prediction for the noise reduction of the cylinder. In the 400 to 630 Hz region where the (1,1) mode of the cylinder dominates, the analytical result represents an arithmetic average of the case where (a) the (1,1) mode fully participates, and (b) the (1,1) mode does not participate. Note that the shape of the measured and predicted noise reduction curves are similar, but the measured noise reductions generally exceed the predictions by statistically significant amounts at frequencies below 160 Hz. The results at 125 and 160 Hz show that the loss factors of the (1,4) and (1,3) structure modes have likely been overestimated. In the volume stiffness controlled region, 100 Hz and below, the noise reduction clearly does not achieve as high a level as

Table 11. Estimated Mean Value of Noise Reduction
and 99% Confidence Intervals

1/3 Octave band center frequency (Hz)	Mean Value of Estimated Noise Reduction (dB)	99% Confidence Interval	
		Lower Bound (dB)	Upper Bound (dB)
40	45.7	42.7	62.2
50	45.7	42.9	56.0
63	42.7	41.1	45.3
80	43.2	41.5	45.9
100	39.9	37.6	45.2
125	17.8	16.1	20.6
160	16.3	14.4	19.4
200	36.6	34.3	41.6
250	14.9	11.8	25.7*
315	17.6	14.3	25.4*
400	12.9	11.6	14.9
500	14.9	13.2	17.6
630	8.1	6.2	11.6
800	8.0	6.2	11.0
1000	8.2	6.6	10.7
1250	6.3	4.5	9.6
1600	7.4	6.2	9.1
2000	7.2	5.8	9.1
2500	5.4	3.9	7.5
3150	4.3	2.7	6.7
4000	7.0	4.9	11.4
5000	10.4	7.8	17.6

* 95% Confidence Limits

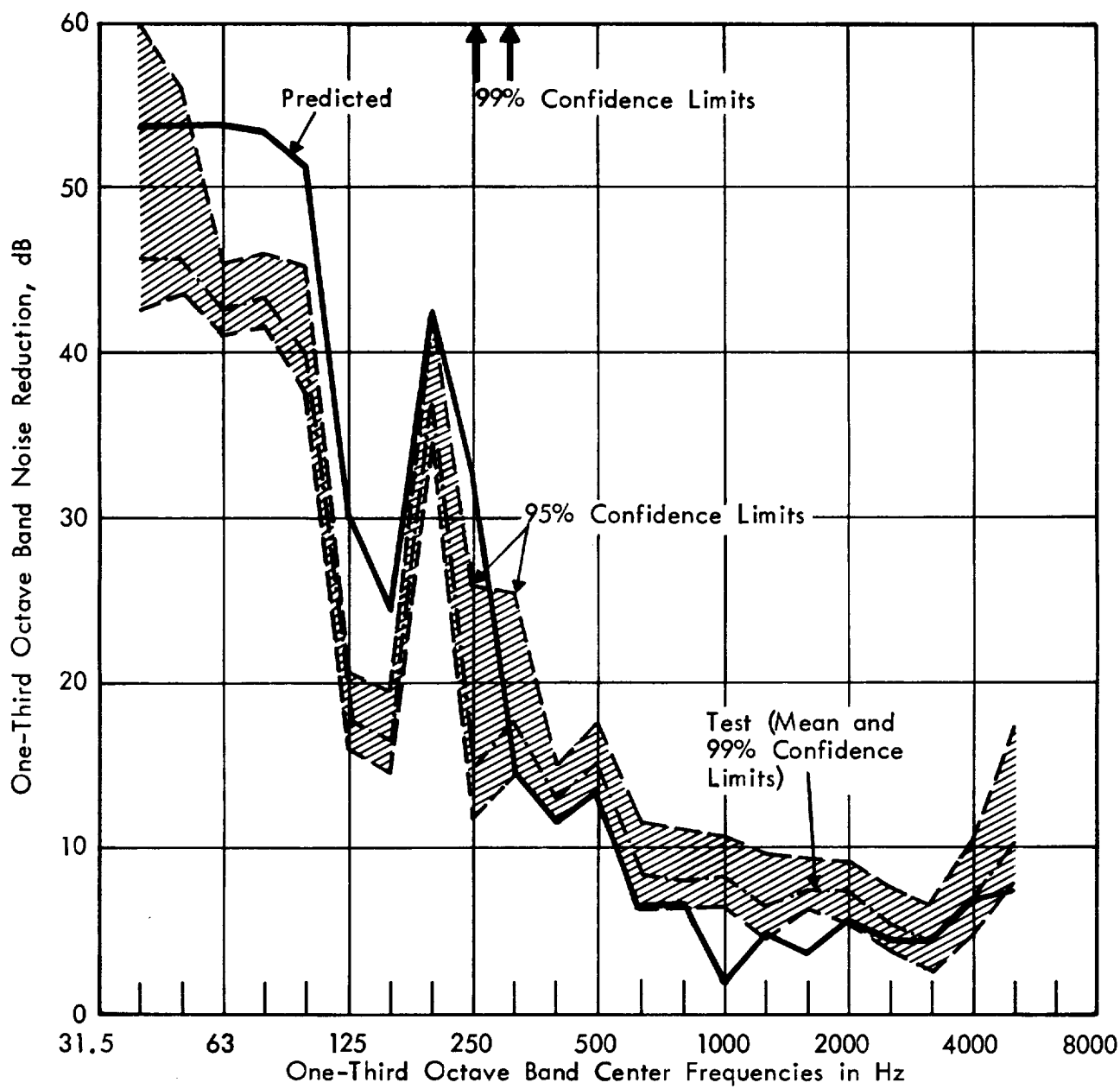


FIGURE 37. MEASURED AND PREDICTED NOISE REDUCTION FOR CYLINDER

predicted. There was suspicion that the lap joint was the cause of the measured low frequency noise reduction being lower than predicted. When the lap joint effect was added to the computer model, the difference in the computed results with and without lap joint was less than 0.1 dB.

5.3 Tone Transmission Comparison

The computer mechanization for the tone transmission study is Eqs.(36) and (37). These give the difference between the incident pressure level and the space average interior pressure level at frequency ω_0 . The predicted interior space averages are to be compared against the two composite sets for the 15° and 45° angles of incidence which are given in Appendix A, representing differences between incident pressure and interior pressure *at various points* (as opposed to the space average).

Since the results in Figure 20 are typical, they are repeated here as Figures 38(a) and 39(a). Figures 38(b) and 39(b) are the computed results. The computations were made every 20 Hz from 100 Hz out to 800 Hz, then in 50 Hz increments to 1400 Hz, and in 100 Hz increments to 2200 Hz. The predictions are in fairly good agreement with the measured results, basically exhibiting the measured behavior as discussed in Section 4.3.

Table 12 lists the most significant contributing acoustic and structure modes at the various frequencies for the 45° angle of incidence. The data may be compared against the most significant contributing modes found for the noise reduction (band-limited) calculation as given in Section 5.2.1. At high frequencies, say 1250 Hz and above, it is clear that coupled acoustic and structure modes lying close to the excitation contribute most to the interior level.

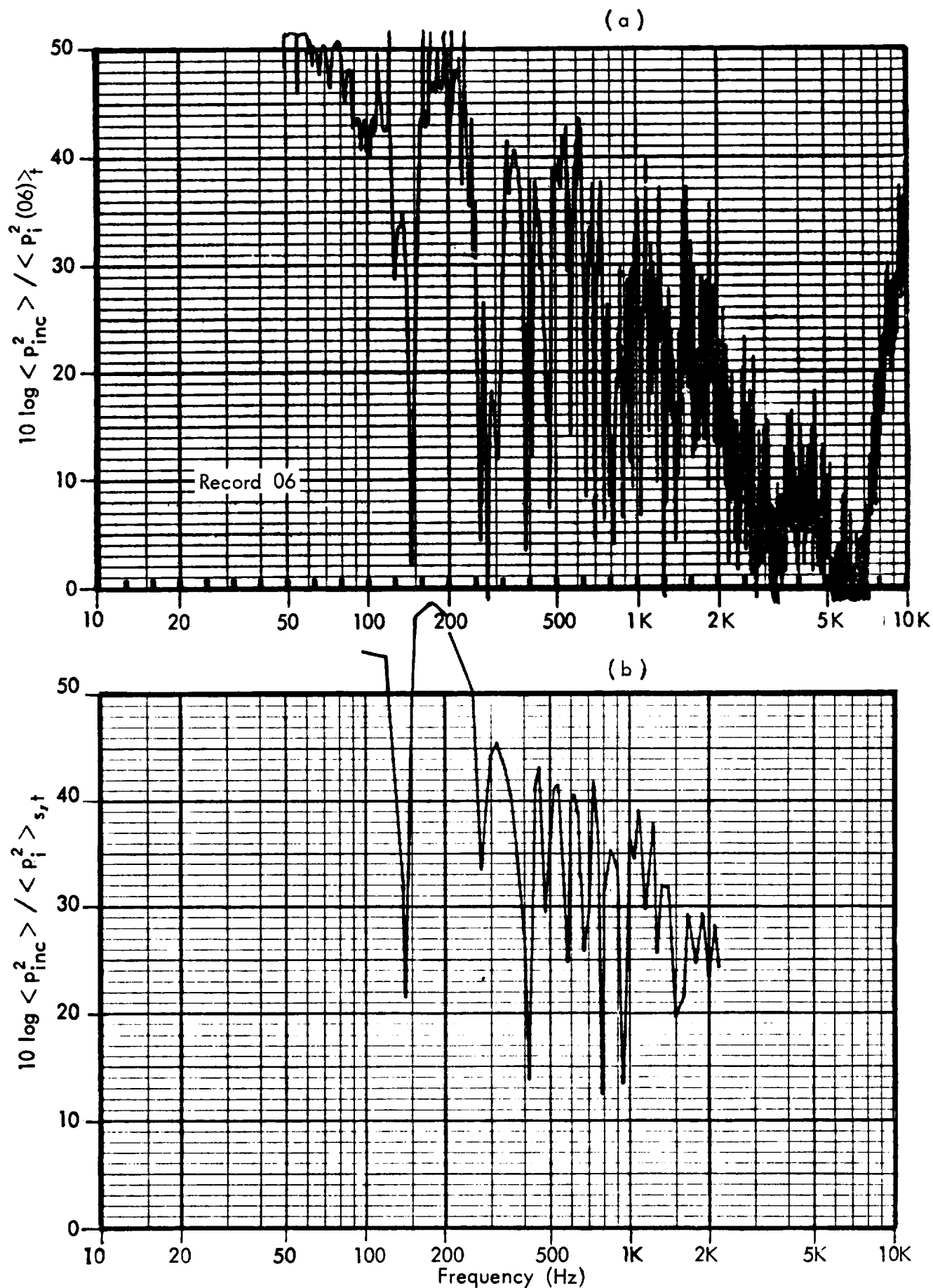


FIGURE 38. PREDICTED TONE TRANSMISSION, 15° ANGLE OF INCIDENCE

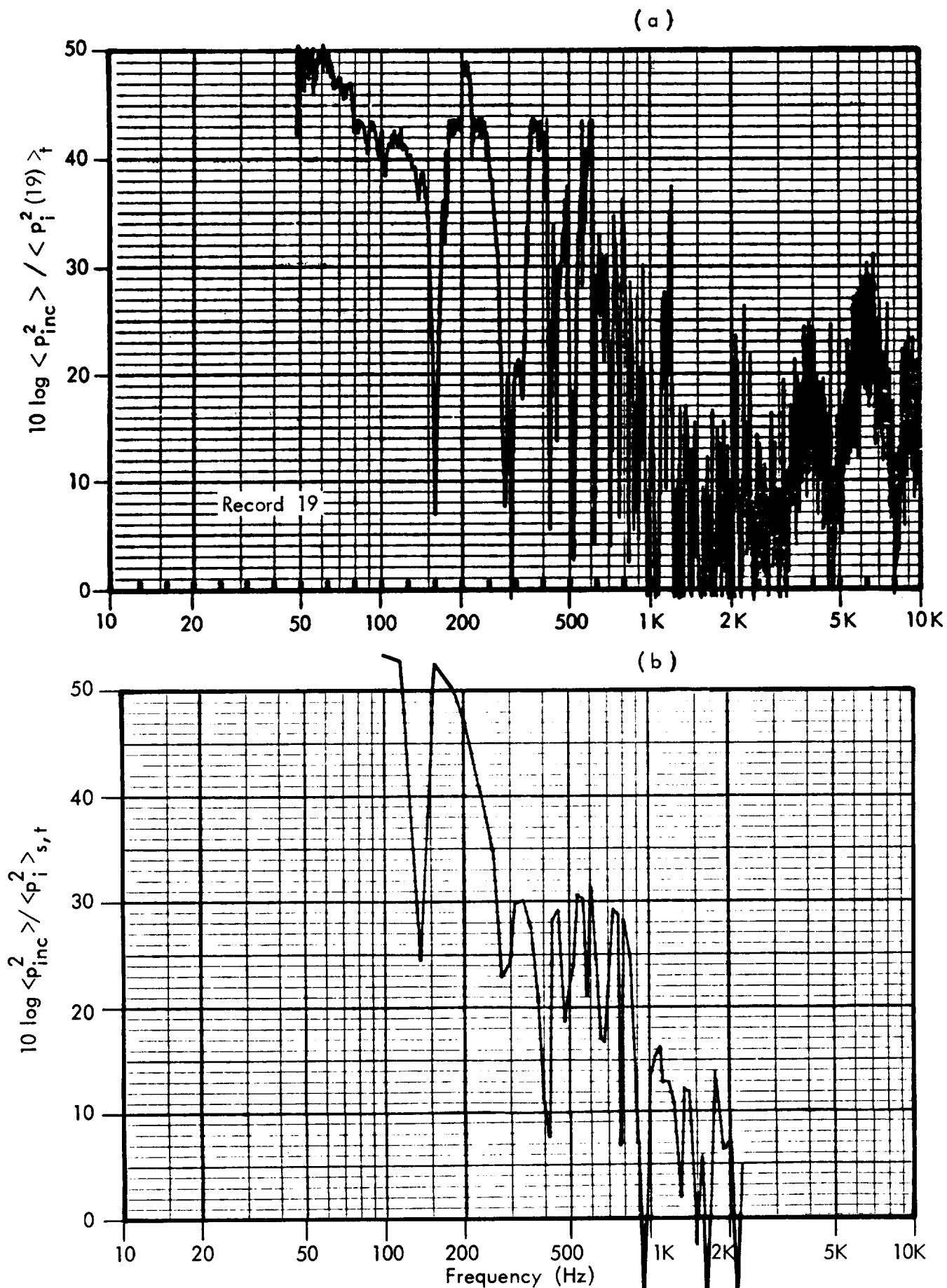


FIGURE 39. PREDICTED TONE TRANSMISSION, 45° ANGLE OF INCIDENCE

Table 12. Most Significant Contributions to $\langle p_i^2 \rangle / \langle p_{inc}^2 \rangle$
Plane Wave Excitation of ($\phi = 45^\circ$)

Freq.	Acoustic Mode		Structural Mode		Modal	
	q,N,S	Freq.	M,N	Freq.	Contrib.	Total
100	0,1,1	396	1,1	693	.17E-6	.44E-5
140	1,0,0	140	2,0	3437	.0033	.0034
200	0,1,1	396	1,1	693	.114E-4	.179E-4
240	0,2,1	656	1,2	289	.467E-4	.931E-4
280	0,2,1	656	1,2	289	.00410	.00504
300	0,2,1	656	1,2	289	.00315	.00385
340	0,1,1	396	1,1	693	.00058	.00098
360	0,1,1	396	1,1	693	.00149	.00181
380	0,1,1	396	1,1	693	.00829	.00861
400	0,1,1	396	1,1	692	.0742	.0748
420	1,1,1	420	2,1	1662	.162	.165
440	0,1,1	396	1,1	693	.00083	.00150
460	2,1,1	486	1,1	693	.00050	.00119
480	2,1,1	486	1,1	693	.0116	.0134
500	1,3,1	914	2,3	510	.00308	.00532
520	1,3,1	914	2,3	510	.00305	.00427
540	1,3,1	914	2,3	510	.00047	.00089
560	4,0,1	563	3,0	3437	.00027	.00095
580	3,1,1	579	2,1	1662	.00586	.00762
600	1,2,1	671	2,2	892	.00040	.00071
620	1,2,1	671	2,2	892	.00075	.00112
640	1,2,1	671	2,2	892	.00190	.00345
660	1,2,1	671	2,2	892	.0140	.0196
680	1,2,1	671	2,2	892	.0157	.0207
700	2,2,1	714	3,2	1491	.00194	.00703

Table 12. Cont'd.
Most Significant Contributions to $\langle p_i^2 \rangle / \langle p_{inc}^2 \rangle$
Plane Wave Excitation of ($\phi = 45^\circ$)

Acoustic Mode		Structural Mode		Modal		
Freq.	q,N,S	Freq.	M,N	Freq.	Contrib.	Total
720	2,2,1	714	3,2	1491	.00737	.00887
740	2,2,1	714	3,2	1491	.00043	.00118
760	3,2,1	780	2,2	892	.00043	.00128
780	3,2,1	780	4,2	1966	.1256	.2052
800	5,1,1	807	4,1	2725	.00048	.00152
850	2,3,1	946	3,3	951	.00117	.00329
900	0,3,1	903	3,3	951	.1750	.1968
950	2,3,1	946	3,3	951	5.000	5.035
1000	3,3,1	997	4,3	1376	.0297	.0431
1050	4,3,1	1064	5,3	1740	.0142	.0293
1100	4,3,1	1064	5,3	1740	.00473	.0236
1150	1,4,1	1151	6,4	1602	.0134	.0505
1200	2,4,1	1177	5,4	1308	.0224	.0514
1250	4,4,1	1274	5,4	1308	.0631	.0823
1300	4,4,1	1274	5,4	1308	.5863	.6414
1350	5,4,1	1342	6,4	1602	.0420	.0606
1400	2,5,1	1407	7,5	1518	.0397	.0606
1500	4,5,1	1489	7,5	1518	1.650	1.818
1600	8,4,1	1604	7,4	1855	.1200	.2578
1700	7,5,1	1694	8,5	1739	5.355	5.838
1800	9,5,1	1872	8,5	1739	.0126	.0410
1900	7,6,1	1889	10,6	1848	.1400	.2373
2000	8,6,1	1966	11,6	2011	.0862	.1984
2100	11,5,1	2073	10,5	2105	5.080	5.165
2200	12,5,1	2180	11,5	2255	.313	.358

5.4 Mechanical Excitation

Figures 40 and 41 show the predicted cylinder response for mechanical excitation plotted against the measured response. The measurements are for two different locations, Records 103 and 104 (see Table 5 and Figure 21 for interpretation).

Figures 42 and 43 give the predicted space average interior pressure for unit force input plotted on typical measured data for three interior points (Records 112, 118, and 119). Again Table 5 and Figure 21 should be consulted for the measurement locations. The predictions are in fairly good agreement with the measured data.

5.5 Excitation by a Random Progressive Wave Field

Before considering the results for excitation by a random progressive wave field, a few more words are required concerning the experimental data.

It was found in Section 4.5 that the standard deviation was very large for the one-third octave bands from 100 Hz to 200 Hz inclusive (refer to Figure 32). A comparison of predicted and measured results is not feasible over this range. Sampling of many more interior points would be required to define the true space average interior level. However, the progressive wave test was an experiment outside the scope of work which was undertaken mainly for the purpose of obtaining additional experience with the cylinder for future consideration. Therefore, a prediction was made in spite of the experimental shortcomings, and is shown in Figure 44. As stated in Section 4.5, the circumferential wave field was hard to model, i.e., the analytical

ϕ , Phase Angle Between Acceleration and Force

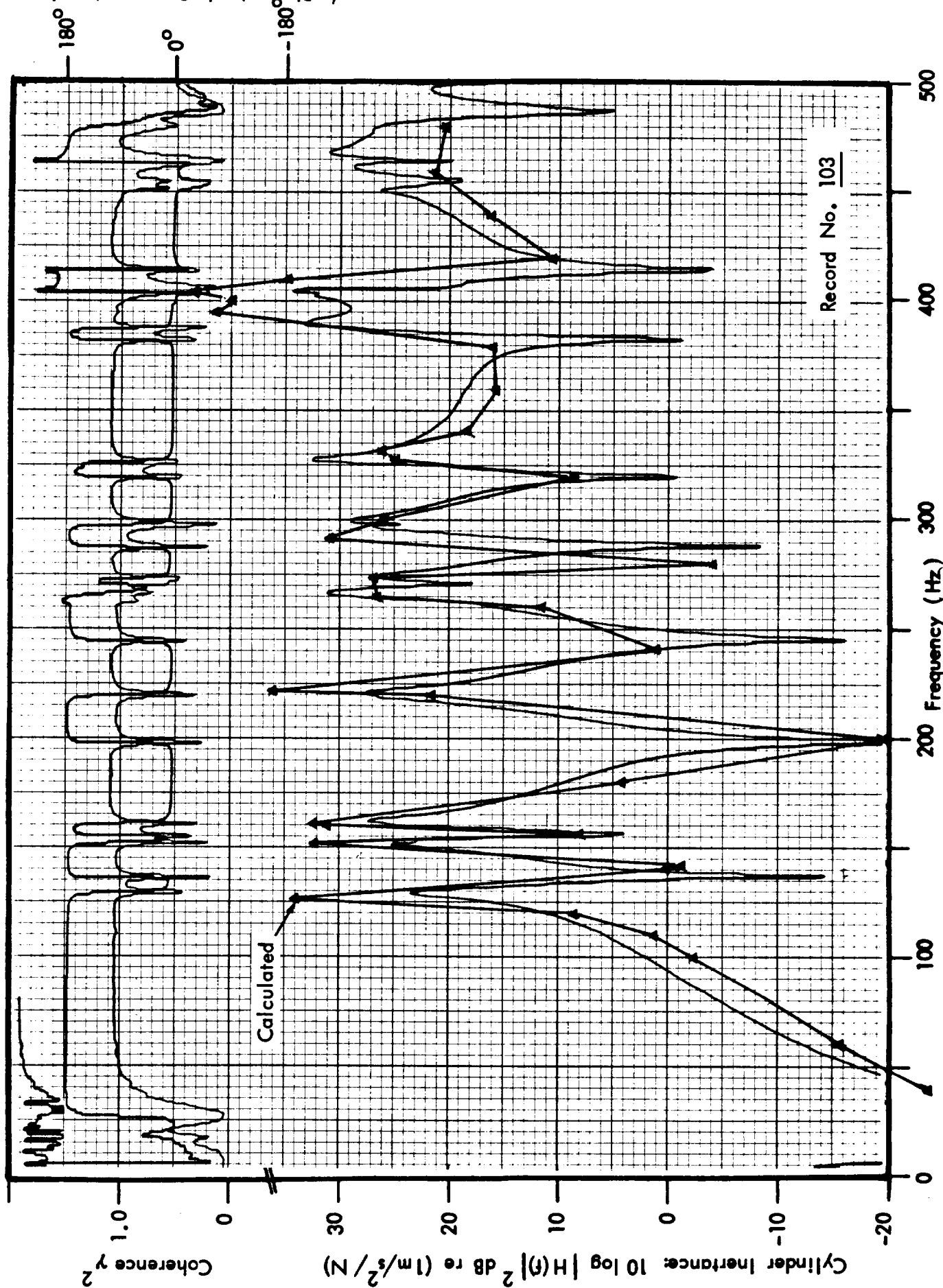


FIGURE 40. COMPARISON OF PREDICTED AND MEASURED ACCELERATION, POINT MECHANICAL EXCITATION.

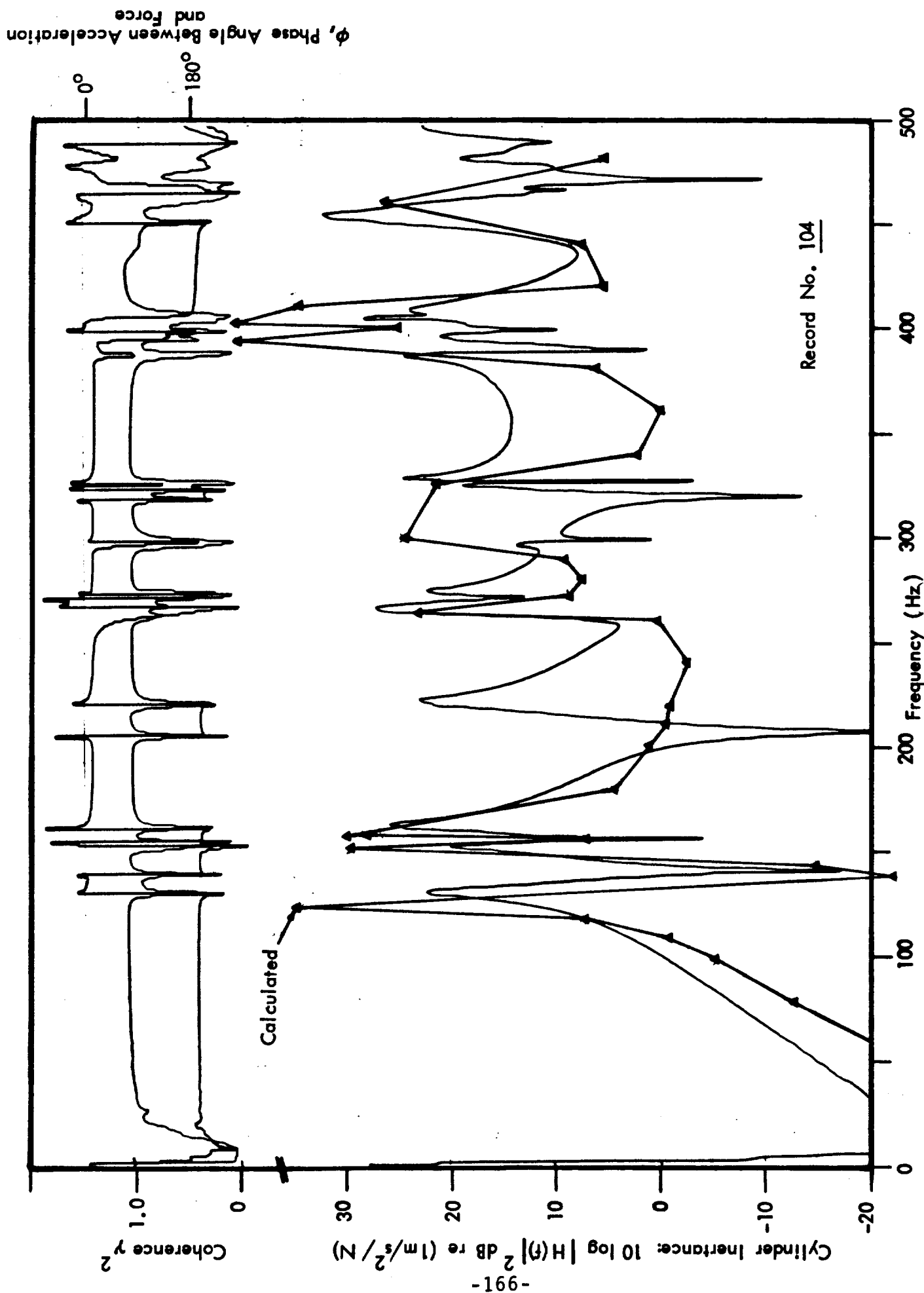


FIGURE 41. COMPARISON OF PREDICTED AND MEASURED ACCELERATION, POINT MECHANICAL EXCITATION.

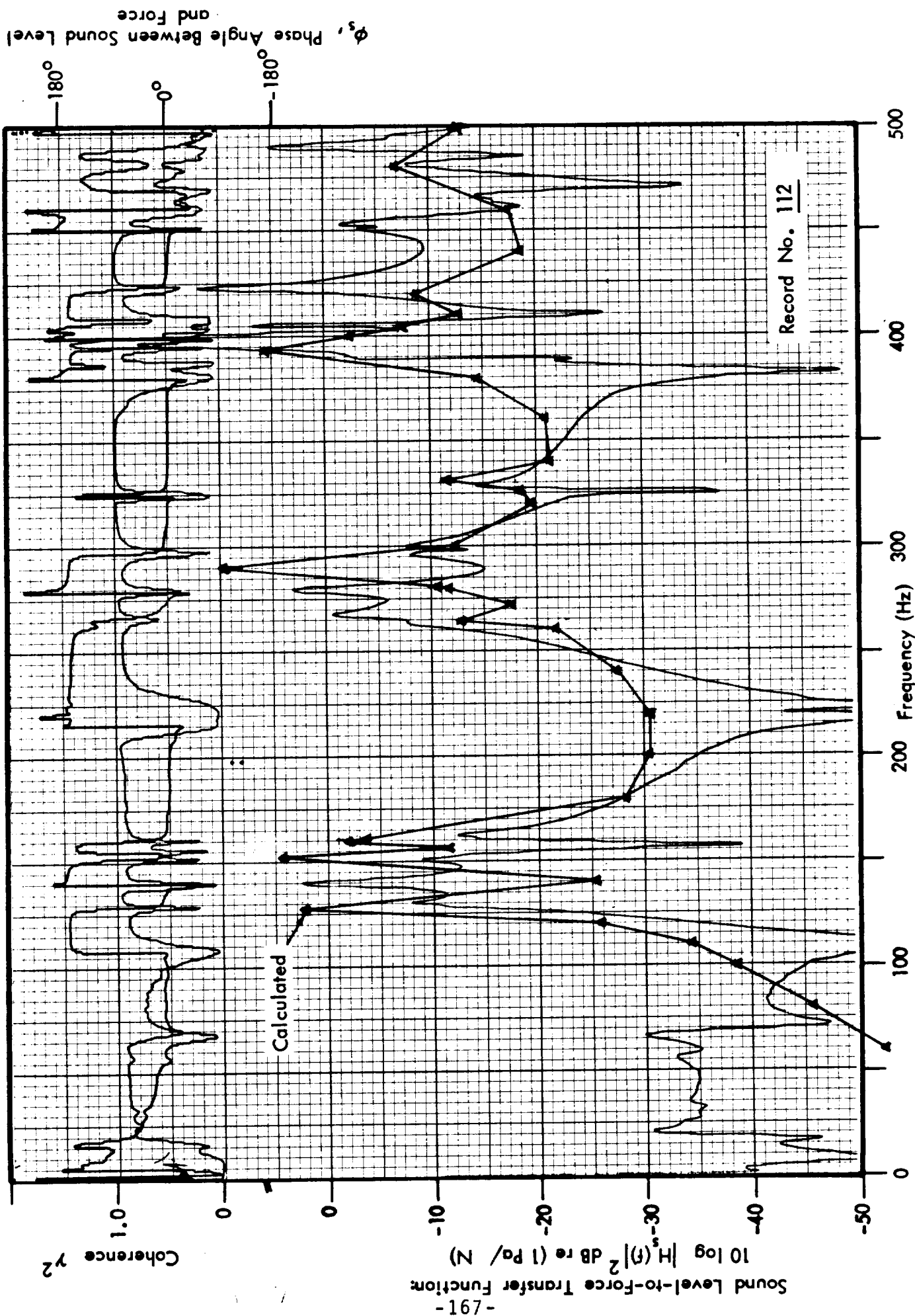


FIGURE 42. COMPARISON OF PREDICTED AND MEASURED INTERIOR PRESSURE, POINT MECHANICAL EXCITATION.

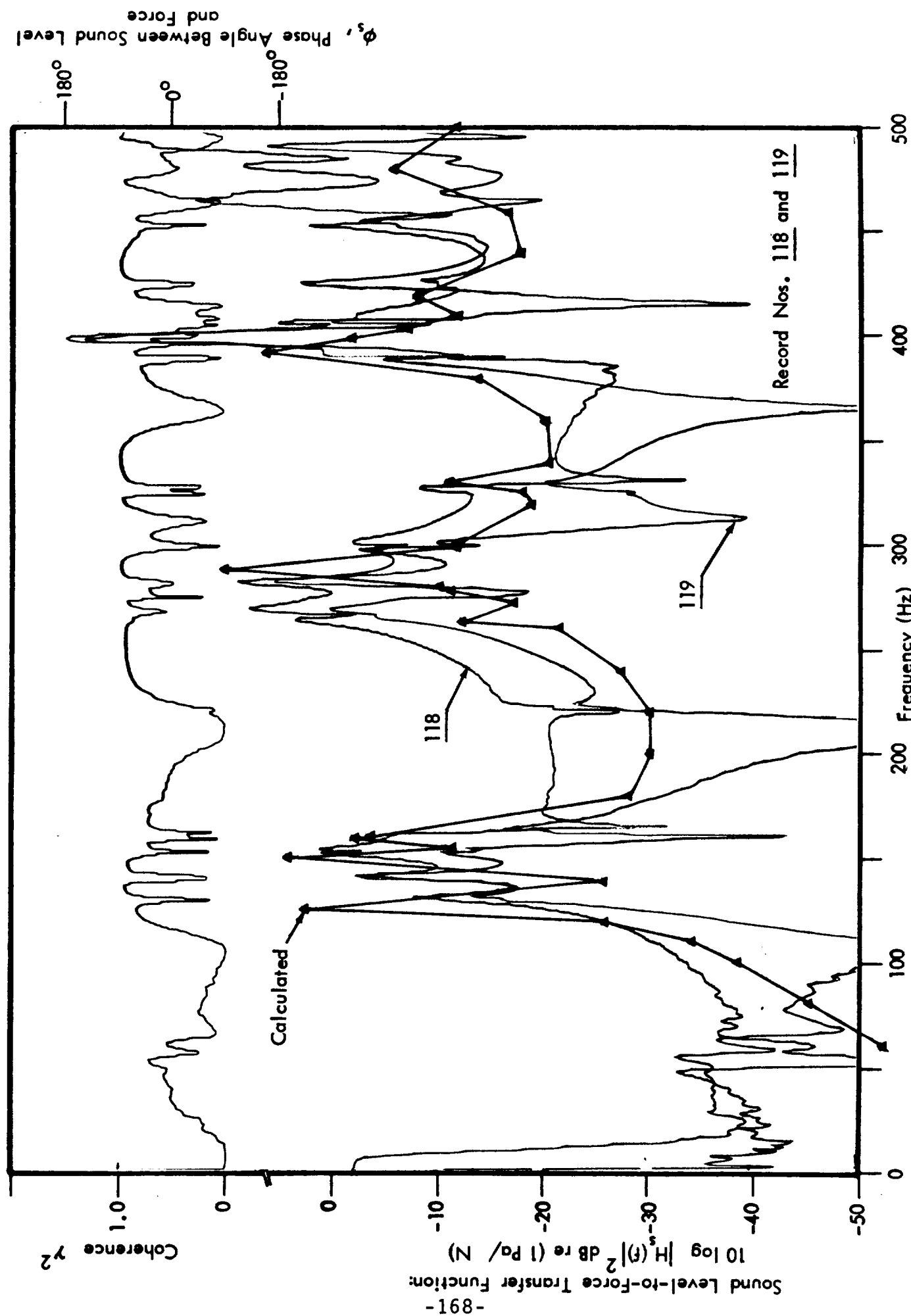


FIGURE 43. COMPARISON OF PREDICTED AND MEASURED INTERIOR PRESSURE, POINT MECHANICAL EXCITATION.

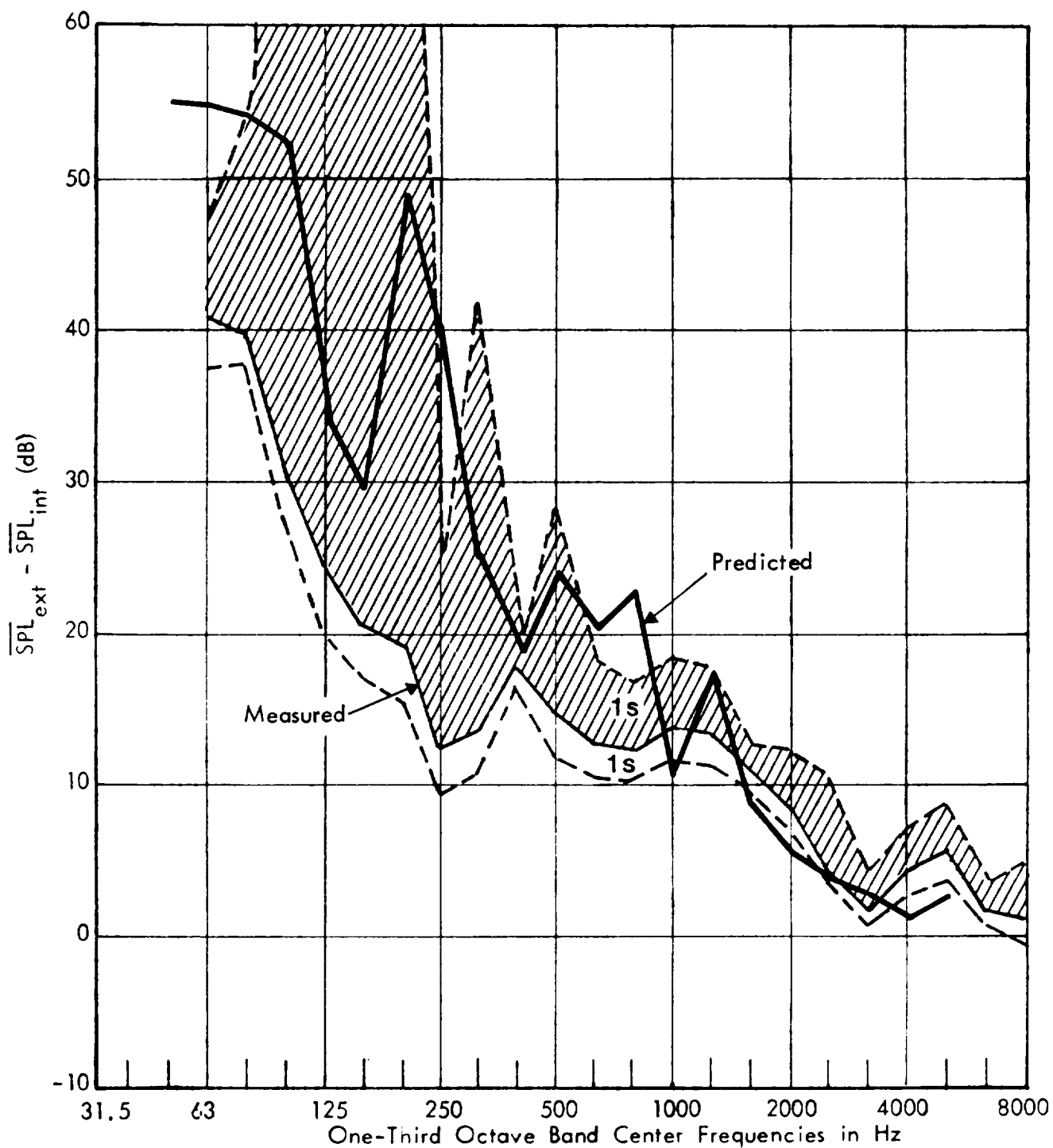


FIGURE 44. PREDICTIONS VERSUS MEASUREMENTS, BAND-LIMITED RATIO OF EXTERIOR PRESSURE TO AVERAGE INTERIOR PRESSURE, PROGRESSIVE WAVE EXCITATION

representation is weak and therefore the prediction was not expected to be as good as it might have been had this representation had a more solid basis.

5.6 Noise Reduction for Increased Interior Absorption

In addition to the noise reduction tests discussed in Section 4, another experiment performed at LaRC considered the effect of additional interior absorption. Figure 45 shows the measured data for various points in the cylinder when a 0.00635 meter (0.25 inch) thick layer of Soundcoat acoustical foam was laid against the inside wall of the cylinder. The data are insufficient to compute a space-average interior level and the actual noise reduction. However the noise reduction will lie close to the lower curves. Also plotted in Figure 45 is a BBN prediction of the noise reduction. Data from a Soundcoat Company brochure were used to estimate the acoustic loss factors (i.e., absorption coefficients) needed in the analysis. Since the damping of the cylinder structure modes was unknown, the prediction is based on a value $\bar{\eta}_r=0.01$ for all bands, i.e., it was assumed that the addition of the foam would increase the structure loss factors to at least that level. A comparison is not intended other than, perhaps, the statement that in general the same trends are shown.

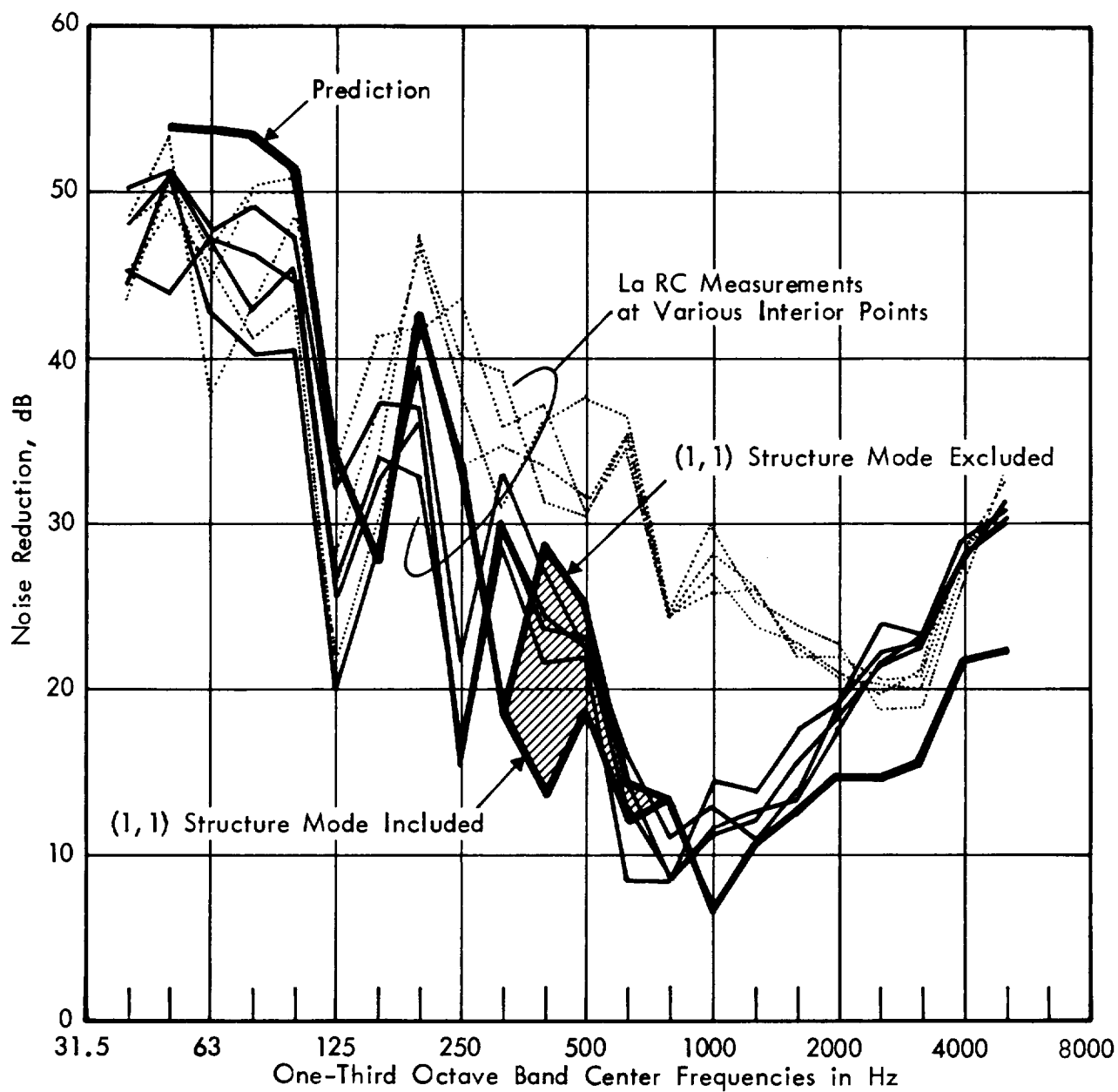


FIGURE 45. CYLINDER NOISE REDUCTION WITH A 0.00635 METER (0.25 INCH) LAYER OF ACOUSTICAL FOAM

REFERENCES

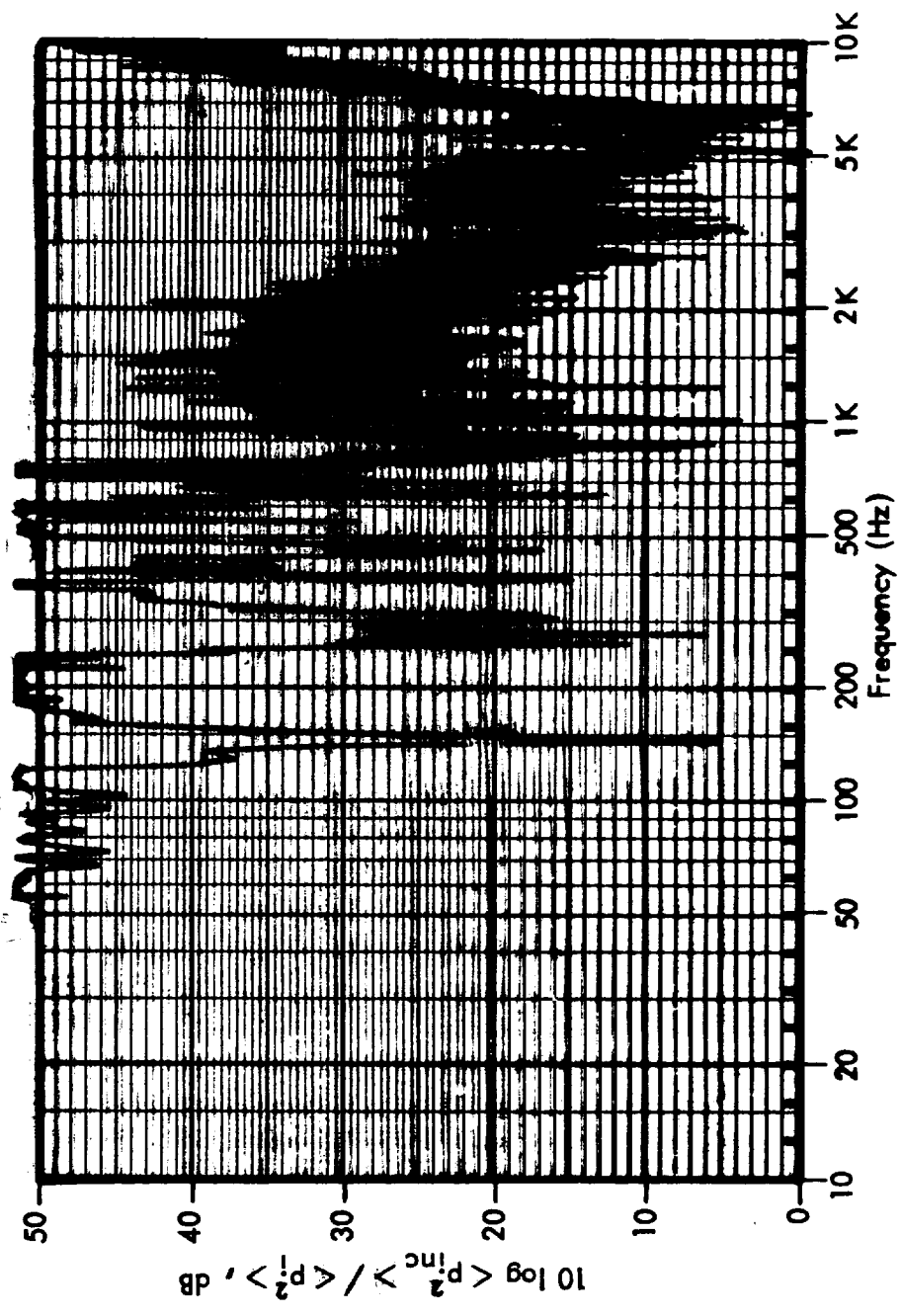
1. Catherines, J. J., and Mayes, W.H., "Interior Noise Levels of Two Propeller-Driven Light Aircraft", NASA TM X-72716 (1975).
2. Mixson, J. S., Barton, C. K., and Vaicaitis, R., "Investigation of Interior Noise in a Twin-Engine Light Aircraft", *J. Aircraft*, 15, 4, 227-233 (1978).
3. Barton, C. K., "Interior Noise Considerations for Powered-Lift Aircraft", NASA TM X-72675 (1975).
4. Howlett, J. T., Williams, L. H., and Catherines, J. J., "Measurement, Analysis and Prediction of Aircraft Interior Noise", AIAA Paper No. 76-551 (1976).
5. Cockburn, J. A., and Jolly, A. C., "Structural-Acoustic Response, Noise Transmission Losses and Interior Noise Levels of an Aircraft Fuselage Excited by Random Pressure Fields", AFFDL-TR-68-2. August 1968.
6. Koval, L. R., "Effect of Airflow, Panel Curvature and Internal Pressurization on Field-Incidence Transmission Loss", *J. Acoust. Soc. Am.* 59, 6, 1379-1385 (1978).
7. Koval, L.R., "On Sound Transmission into a Thin Cylindrical Shell Under Flight Conditions", *J. Sound Vib.*, 48, 2, 265-275 (1976).
8. Koval, L. R., "Effects of Cavity Resonances on Sound Transmission into a Thin Cylindrical Shell", *J. Sound Vib.*, 59, 1, 23-33 (1978).
9. Vaicaitis, R., "Noise Transmission by Viscoelastic Sandwich Panels", NASA TN D-8516 (1977).
10. Rennison, D. C., and Wilby, J. F., "A Review of Analytical Models for Sound Transmission through Fuselage Sidewalls with Application to General Aviation Aircraft", BBN Report 3851, (1978).

11. Rennison, D. C., et al., "Interior Noise Control Prediction Study for High-Speed Propeller-Driven Aircraft", NASA CR-159200 (1979).
12. Pope, L. D., "On the Transmission of Sound through Finite Closed Shells: Statistical Energy Analysis, Modal Coupling, and Nonresonant Transmission", *J. Acoust. Soc. Am.*, **50**, 3, 1004-1018 (1971).
13. Plotkin, K. J., et al., "Prediction of Low Frequency Sound Transmission through Aerospace Structures, with Application to Space Shuttle", Wyle Research Report WR78-5, February 1978.
14. Lyon, R. H., "Noise Reduction of Rectangular Enclosures with One Flexible Wall", *J. Acoust. Soc. Am.*, **35**, 11, 1791-1797 (1963).
15. White, P. H., "Sound Transmission through a Finite, Closed Cylindrical Shell", *J. Acoust. Soc. Am.*, **40**, 5, 1124-1130 (1966).
16. Scharton, T. D., "Response of a Ring-Stiffened Cylinder to Acoustical and Mechanical Excitation", BBN Report 1197 (1971).
17. Eichler, E., "Thermal Circuit Approach to Vibrations in Coupled Systems", *J. Acoust. Soc. Am.*, **38**, 6, 995-1007 (1965).
18. Pope, L. D., and Wilby, J. F., "Space Shuttle Payload Bay Acoustics Prediction Study, Volume II Analytical Model", BBN Report 3286 (1976). (Reissued as NASA CR 159956 (1980)).
19. Pope, L. D., and Wilby, J. F., "Band-limited Power Flow into Enclosures", *J. Acoust. Soc. Am.*, **62**, 4, 906-911 (1977).
20. Pope, L. D. and Wilby, J. F., "Band-limited Power Flow into Enclosures, II", *J. Acoust. Soc. Am.*, **67**, 3, 823-826 (1980).
21. Wilby, J. F., and Pope, L. D., "Prediction of the Acoustic Environment in the Space Shuttle Payload Bay", *J. Spacecraft and Rockets*, **17**, 3, 232-239 (1980).
22. Leissa, A. W., Vibrations of Shells, NASA SP-288, 44-45 (1973).

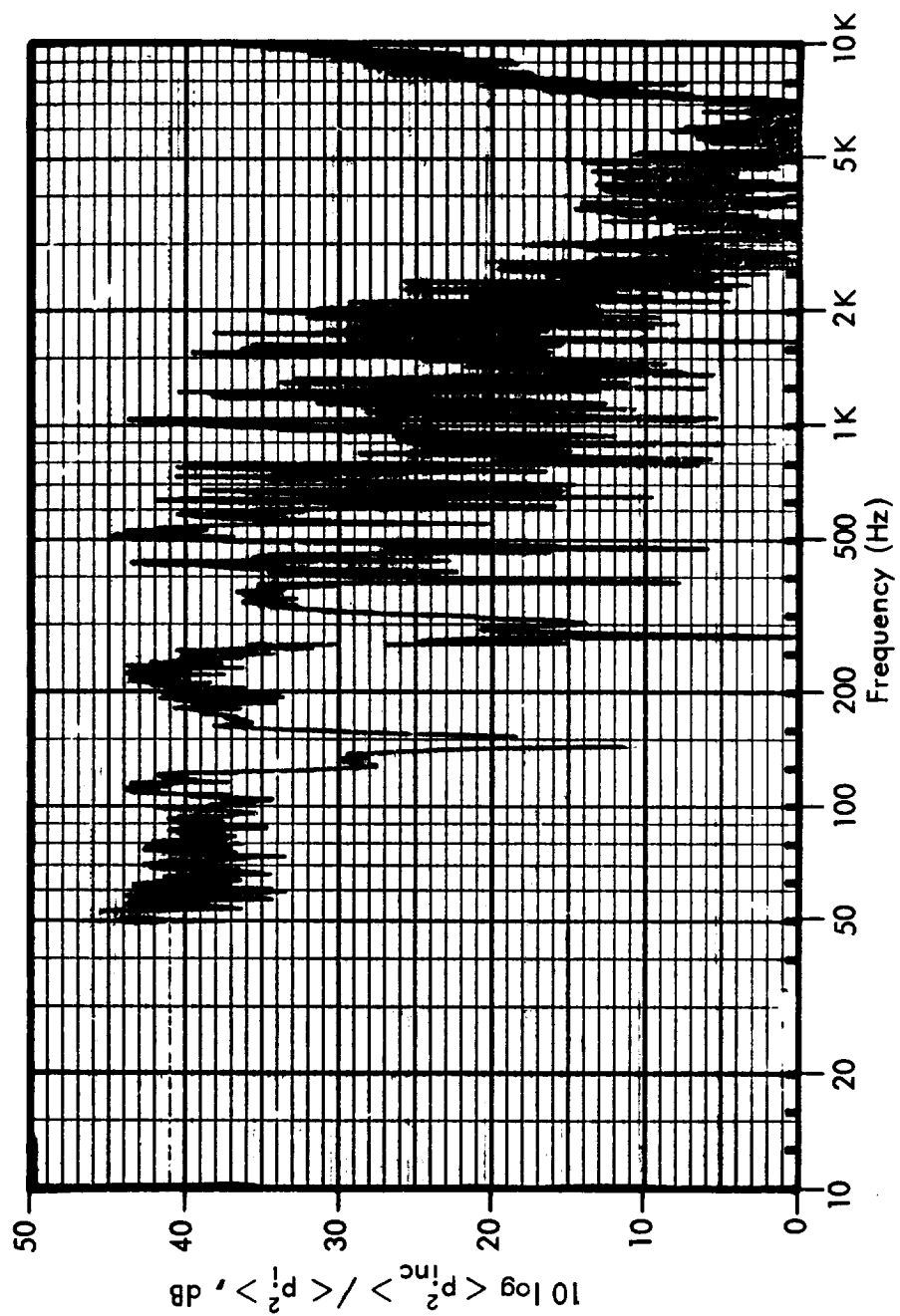
23. White, R. W., "Predicted Vibration Responses of Apollo Structure and Effects of Pressure Correlation Lengths on Response", Wyle Laboratories Report WR67-4 (Revised March 1968).
24. Abramowitz, M., and Stegun, I. A., Handbook of Mathematical Functions, United States Department of Commerce, National Bureau of Standards, Amer.Math Series 55, Washington: Government Printing Office, 1964.
25. McLachlan, N. W., Bessel Functions for Engineers, Oxford University Press, 2nd Edition, 1955, p. 196.
26. Morse, P. M., and Ingard, K. U., Theoretical Acoustics, McGraw-Hill, New York, 1968.
27. Wilby, J. F., "The Response of Simple Panels to Turbulent Boundary Layer Excitation", AFFDL-TR-67-70 (1967).
28. Roark, R. K., Formulas for Stress and Strain, McGraw-Hill, New York, 1975, p. 326.
29. Guttman, I., Wilks, S. S., and Hunter, J. S., Introductory Engineering Statistics, 2nd edition, Wiley, New York 1971.

APPENDIX A

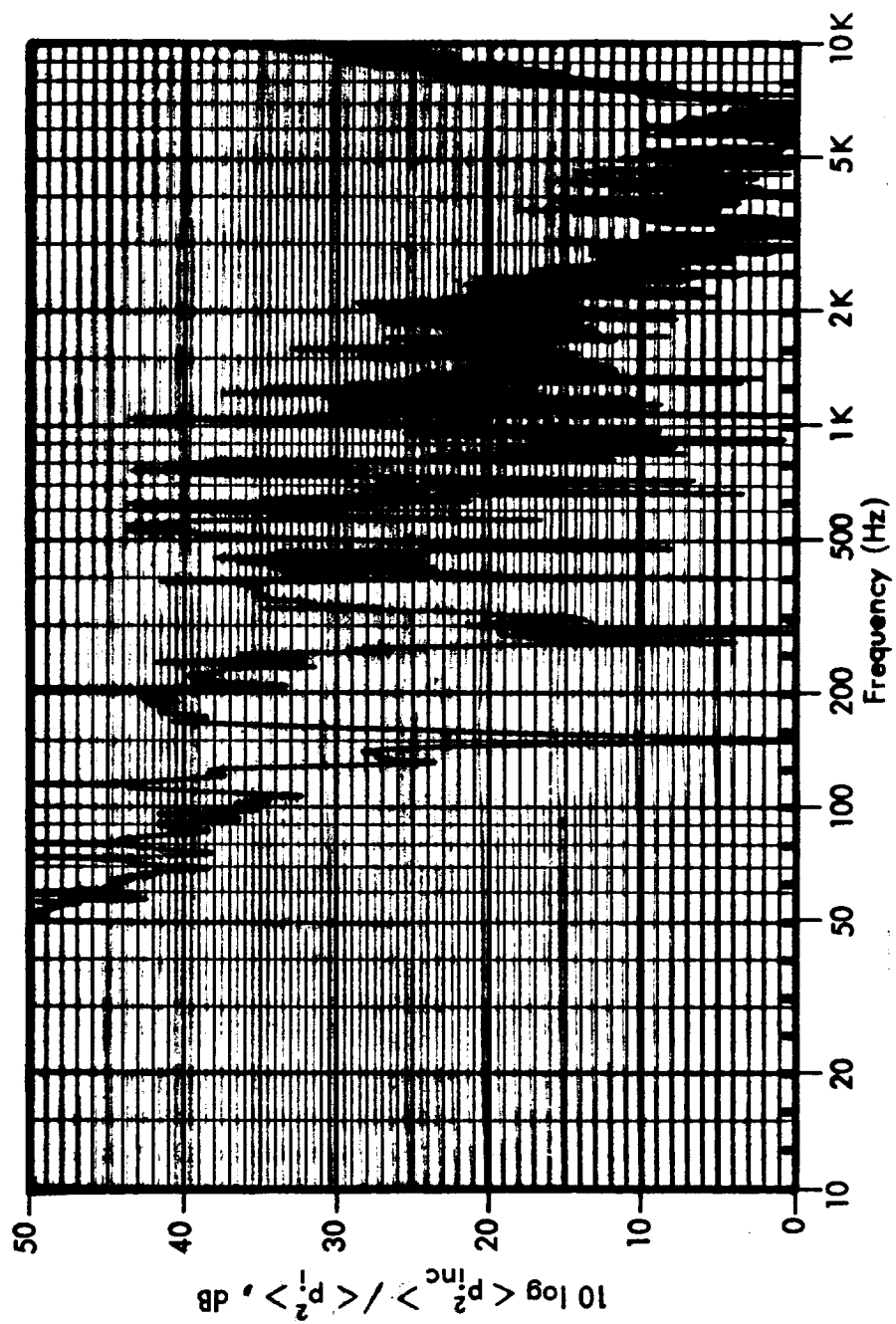
Plane Wave Tonal Transmission Data



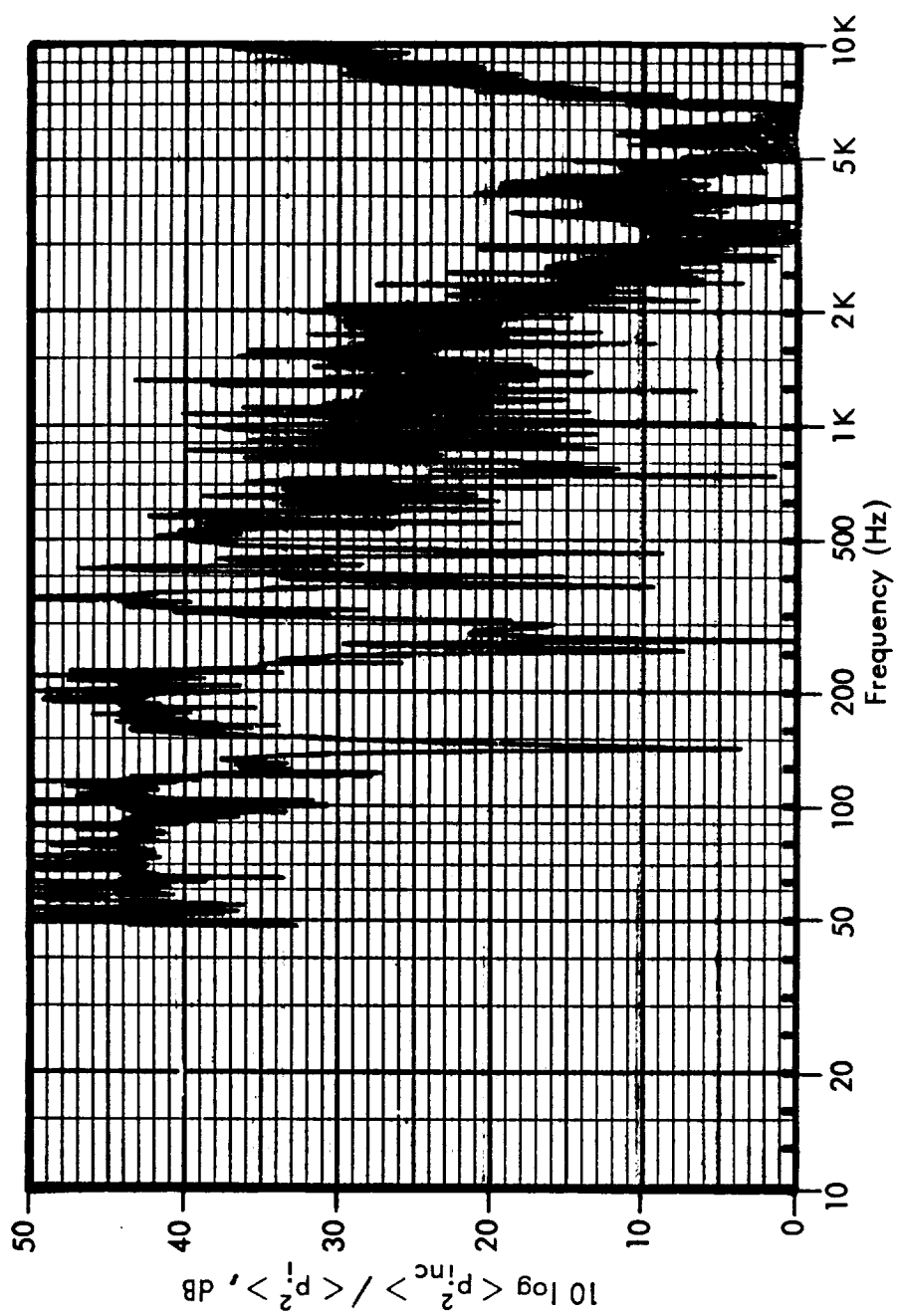
Record No. 02



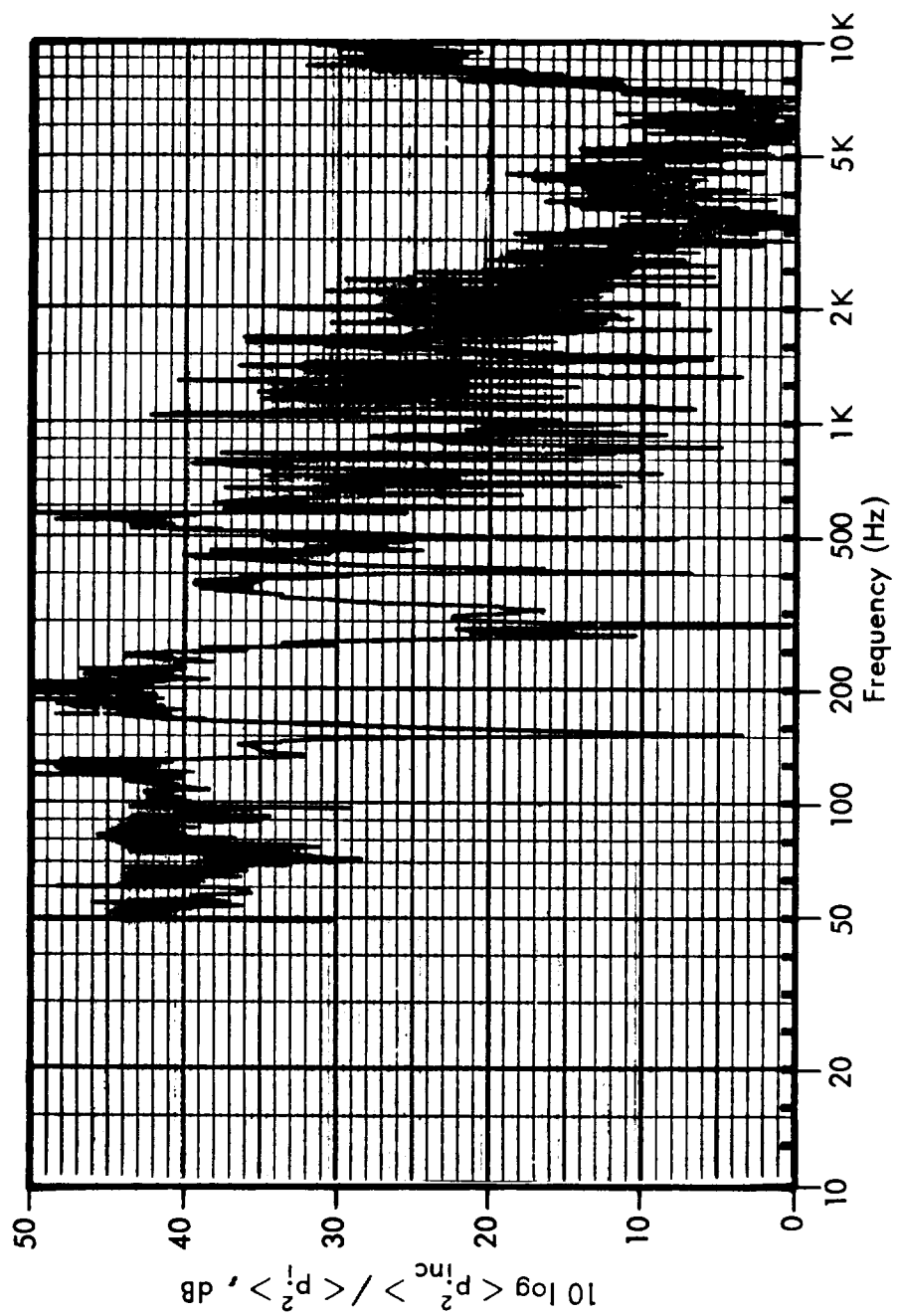
Record No. 04



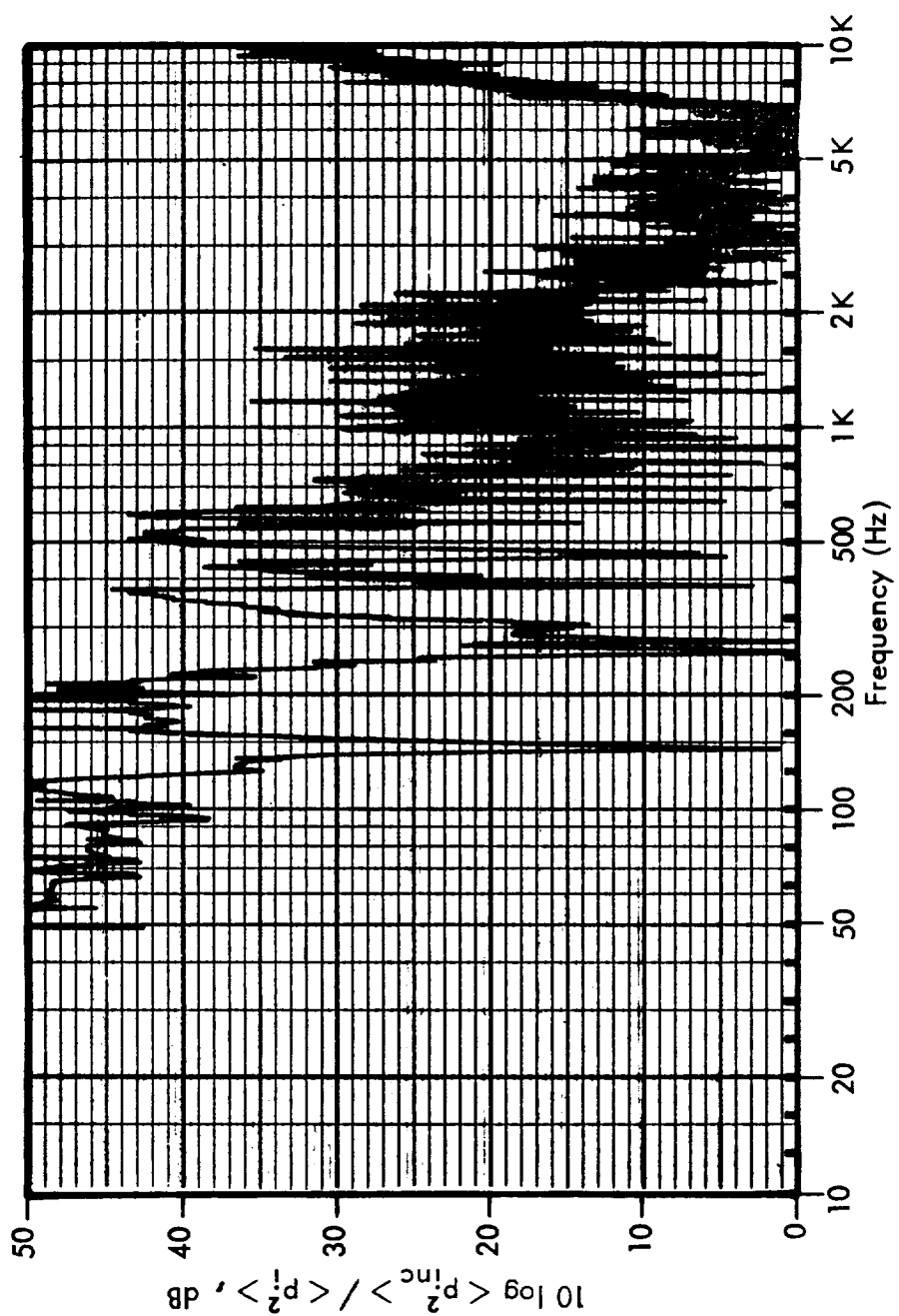
Record No. 05



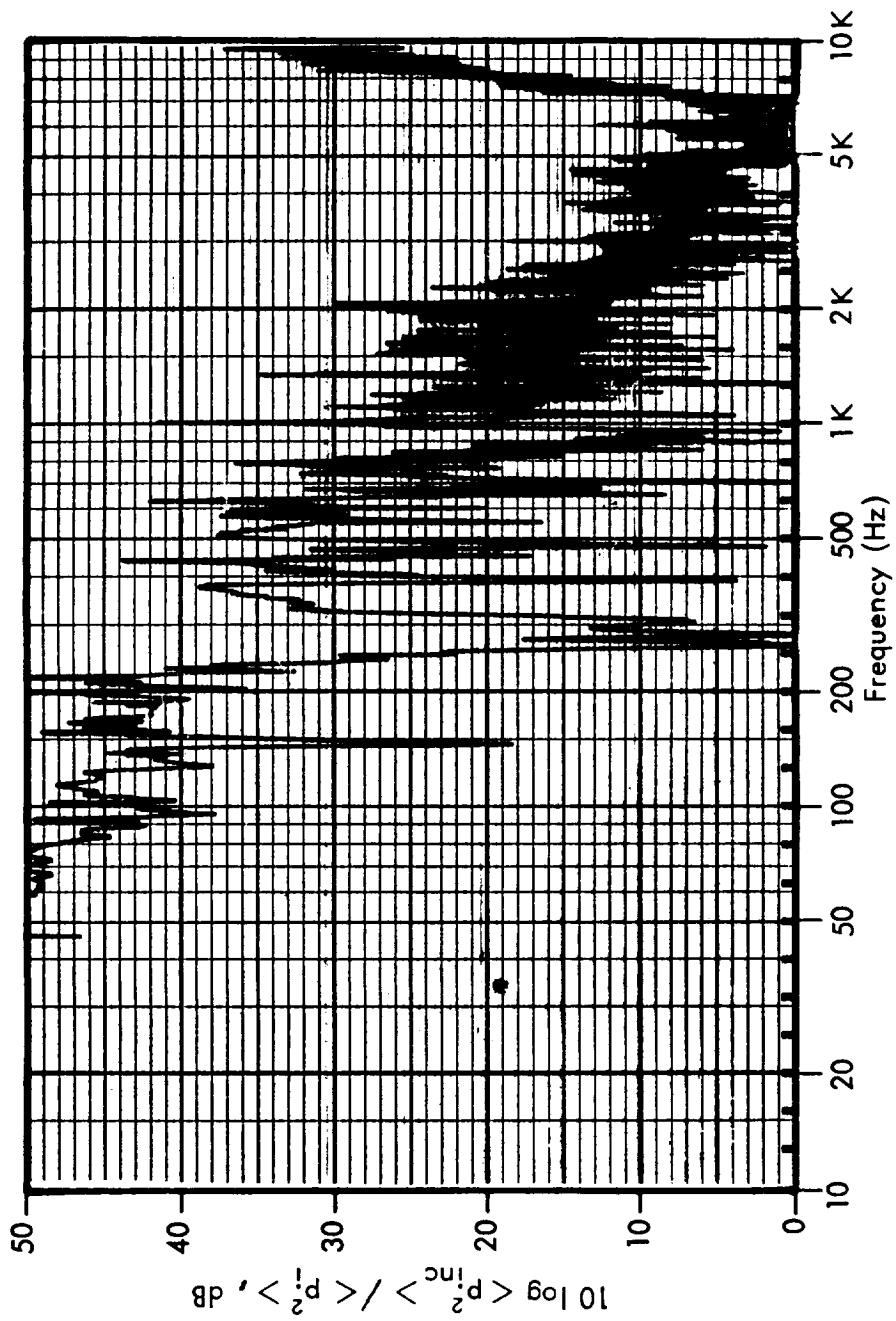
Record No. 07



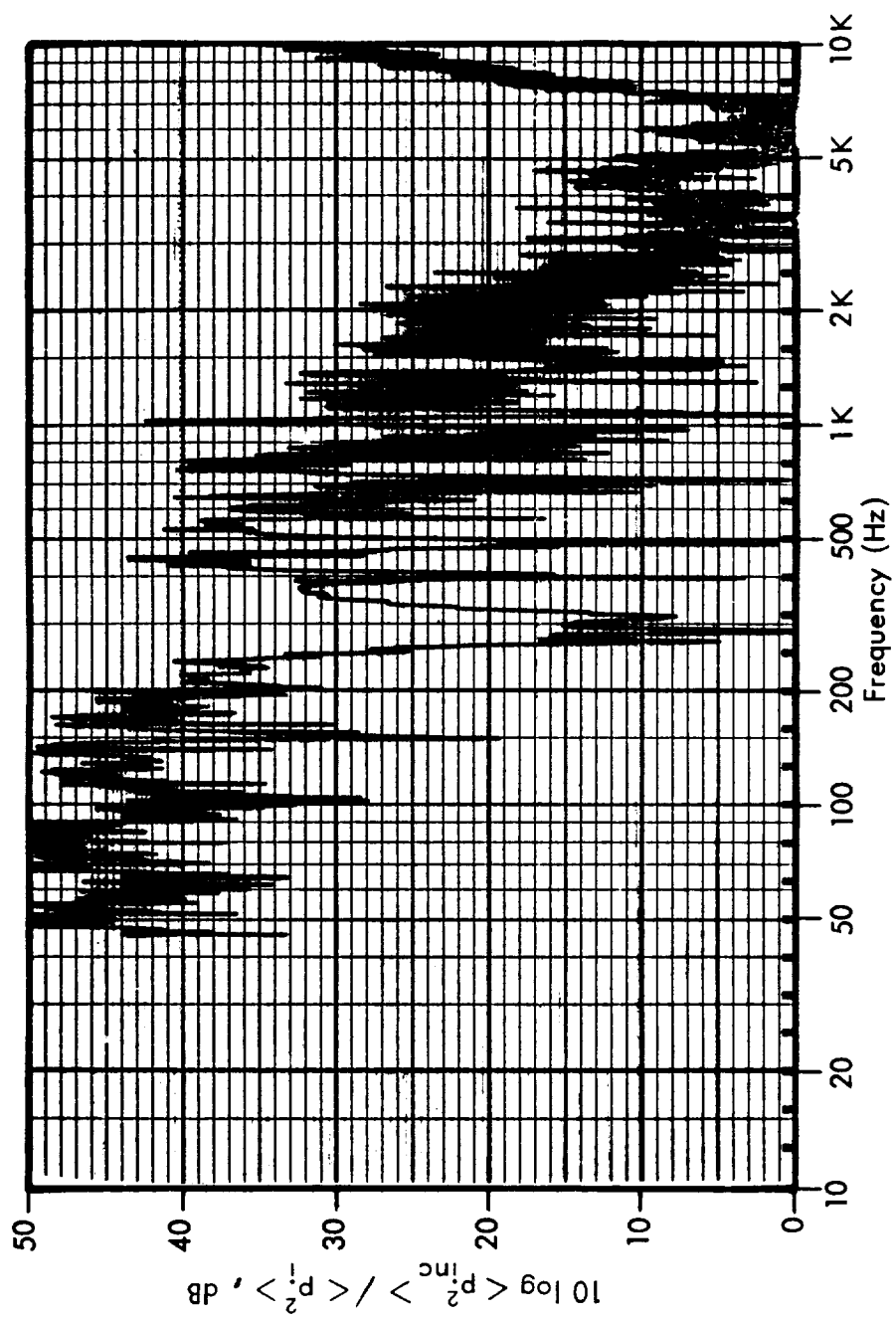
Record No. 08



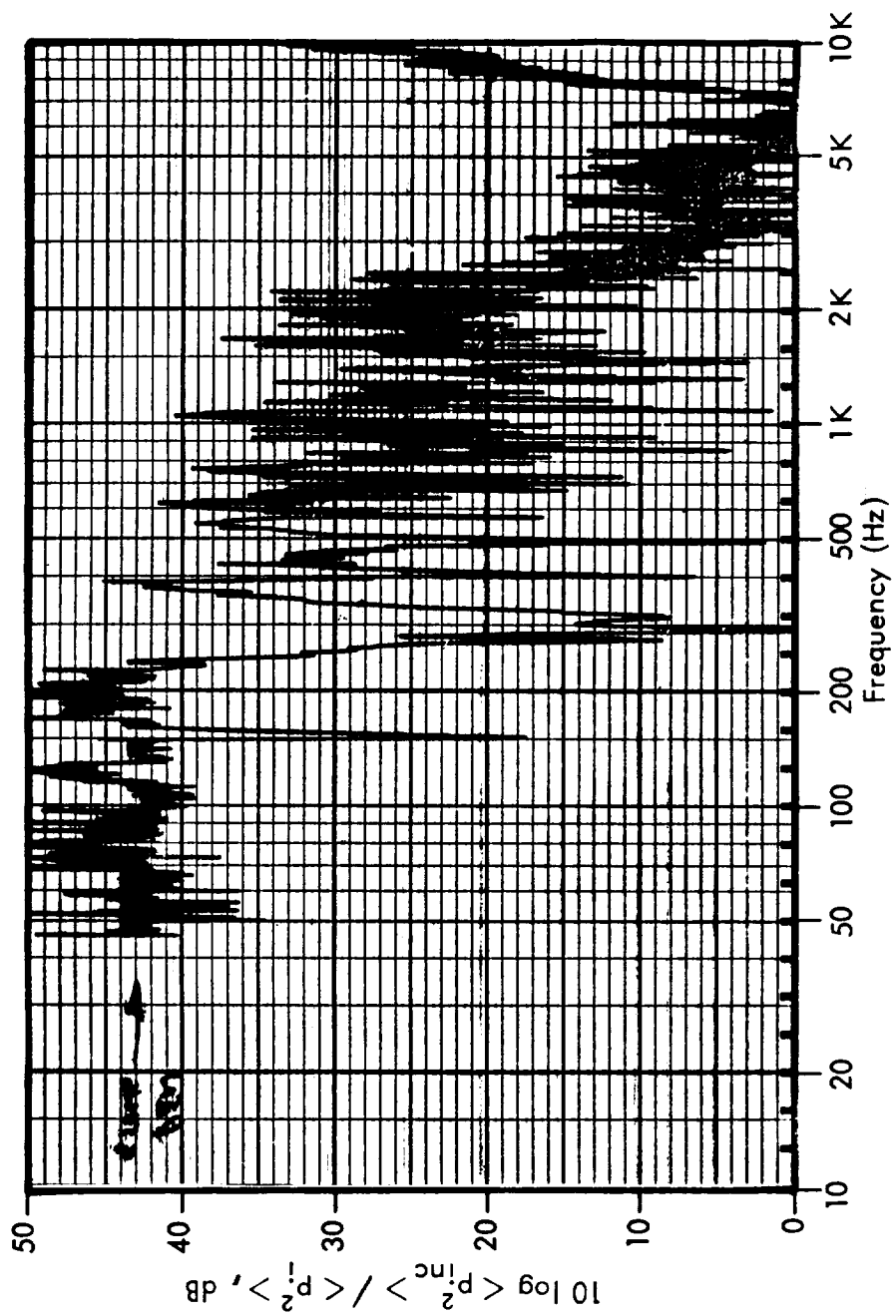
Record No. 09



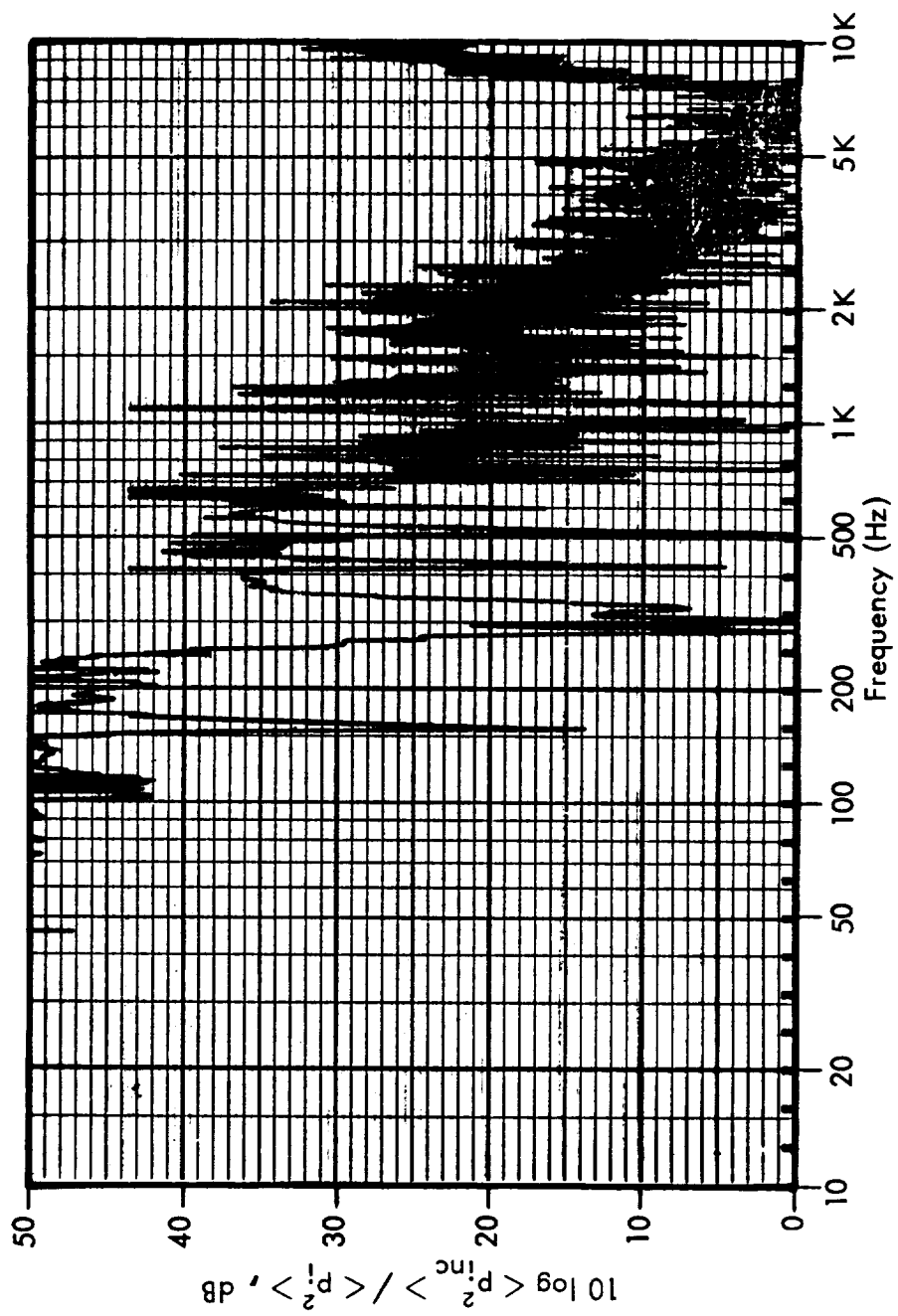
Record No. 10



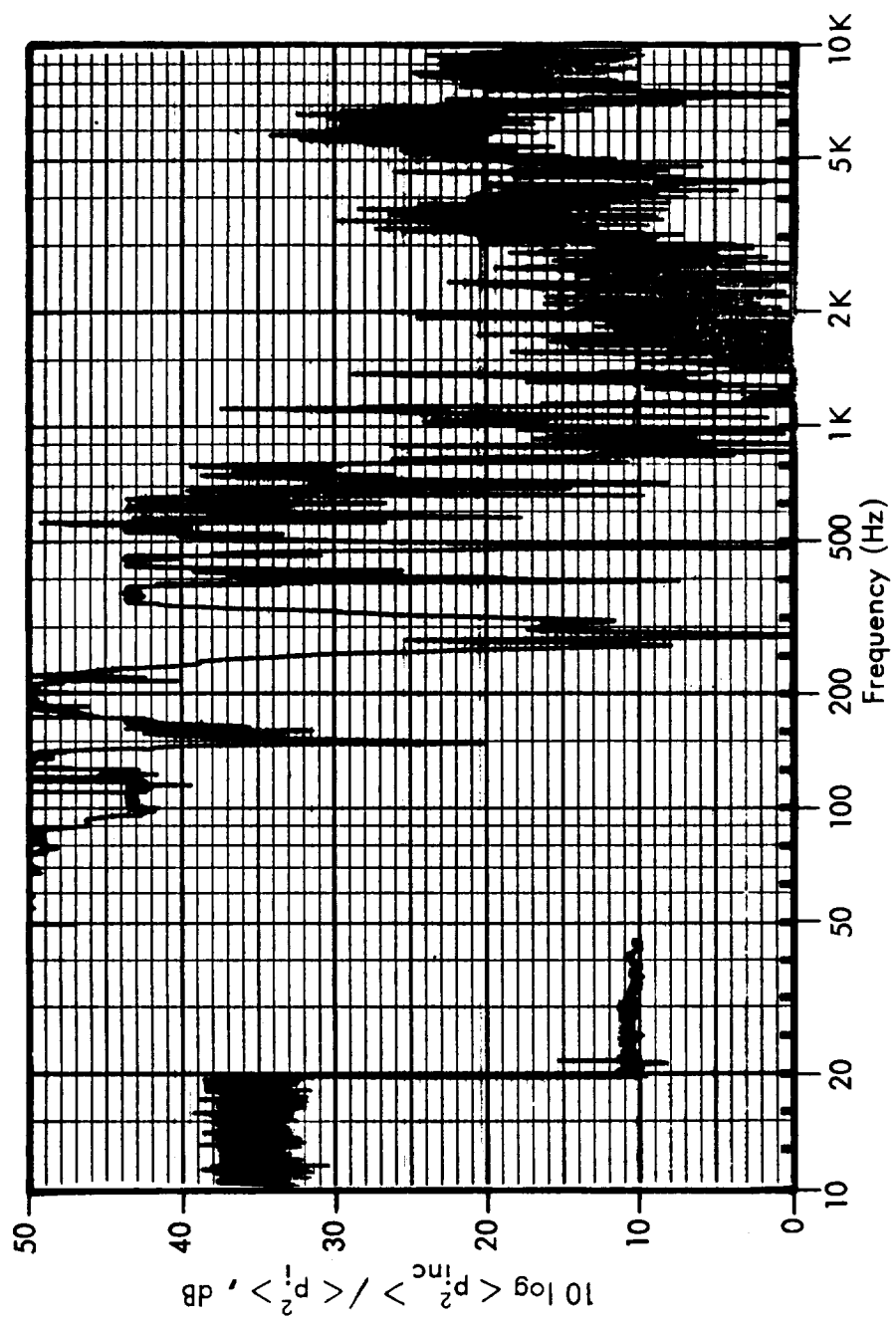
Record No. 11



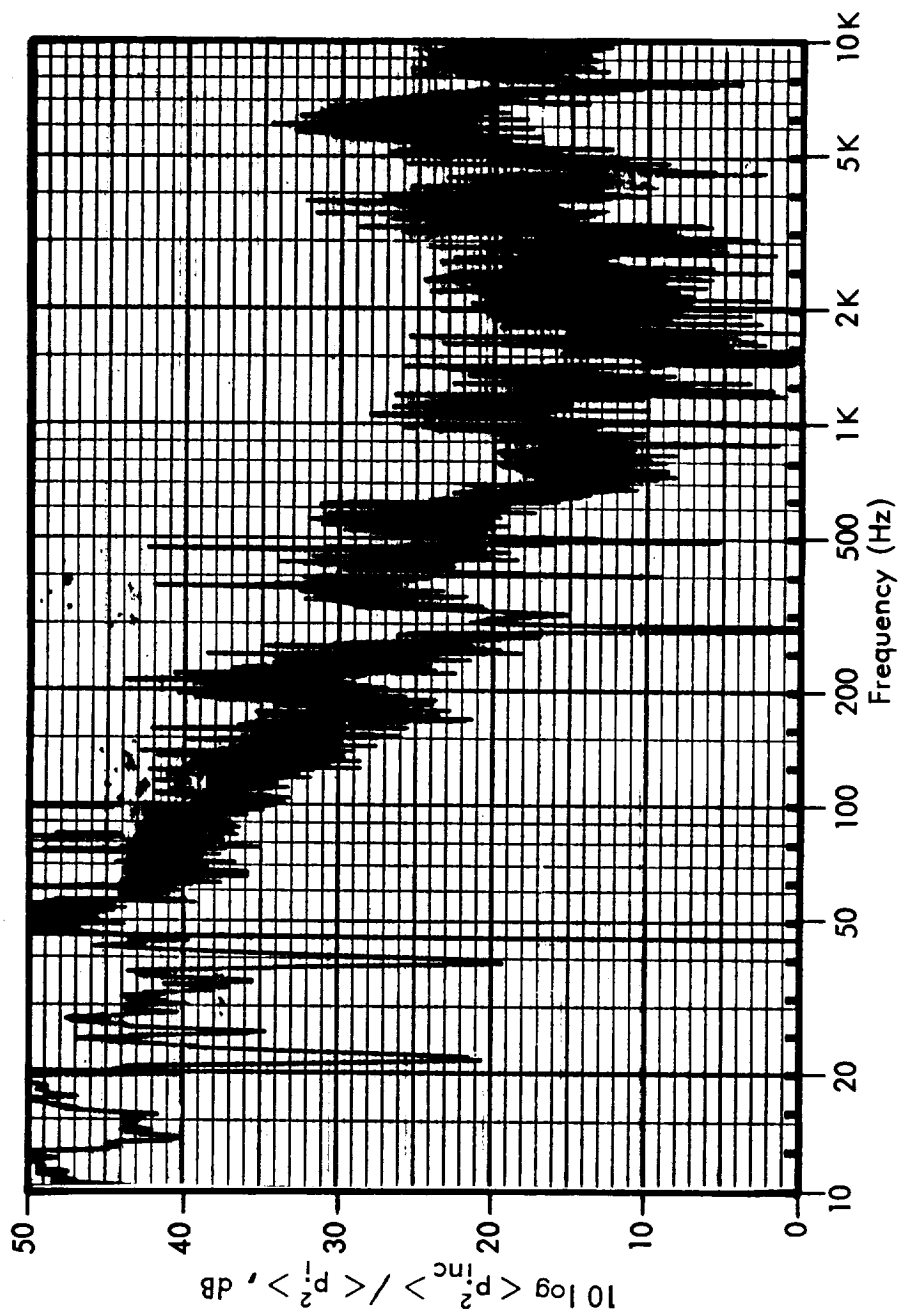
Record No. 12



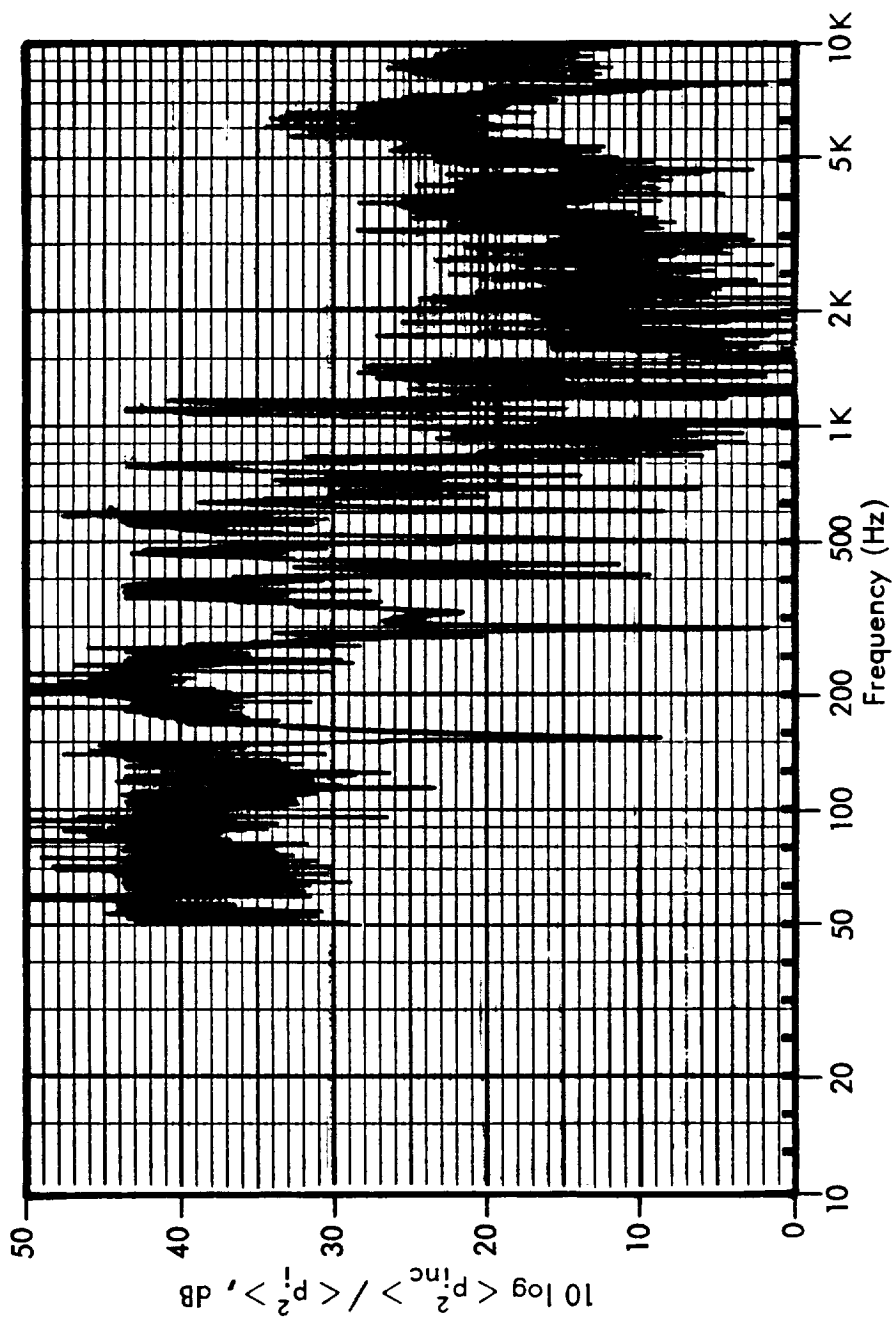
Record No. 13



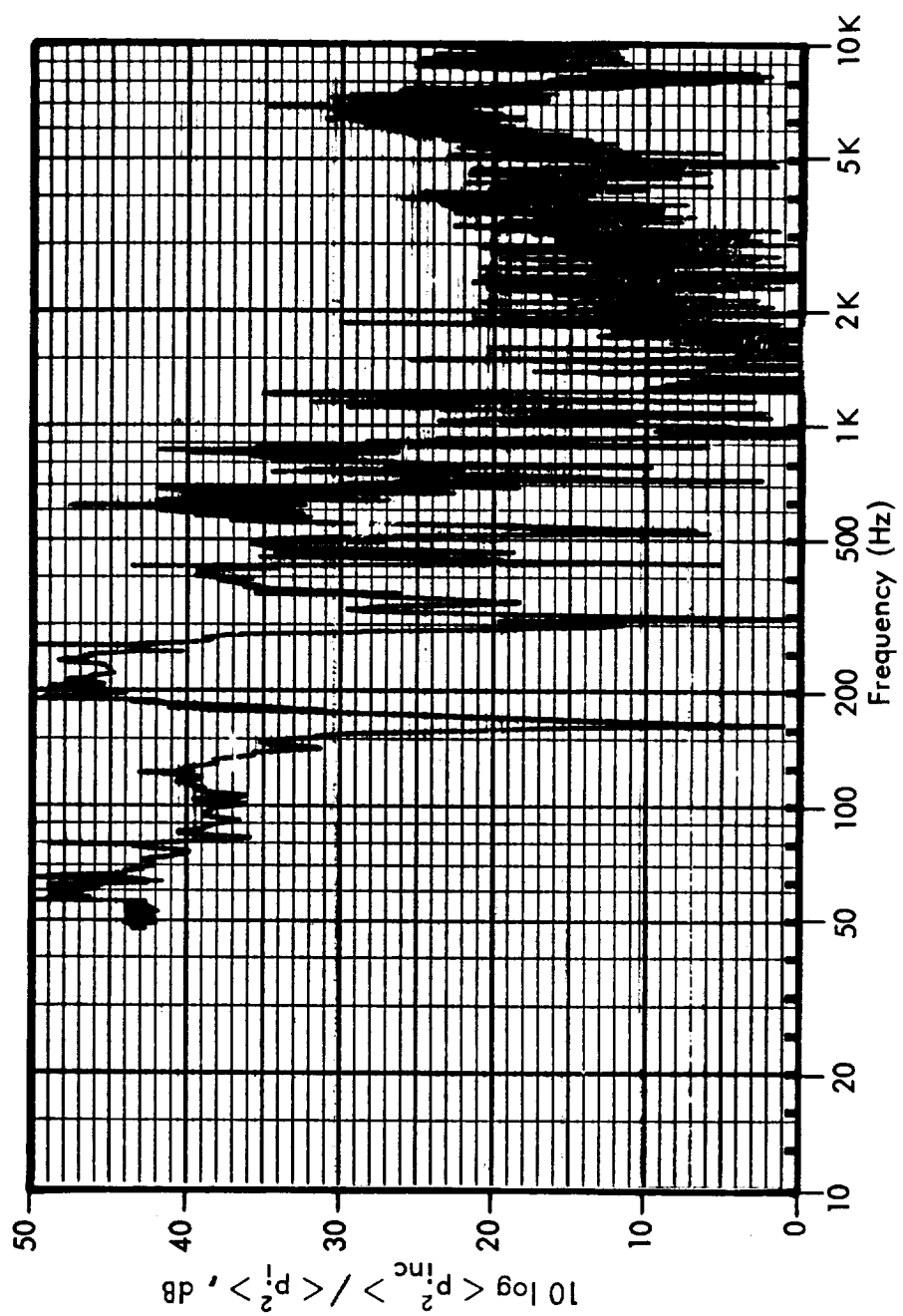
Record No. 16



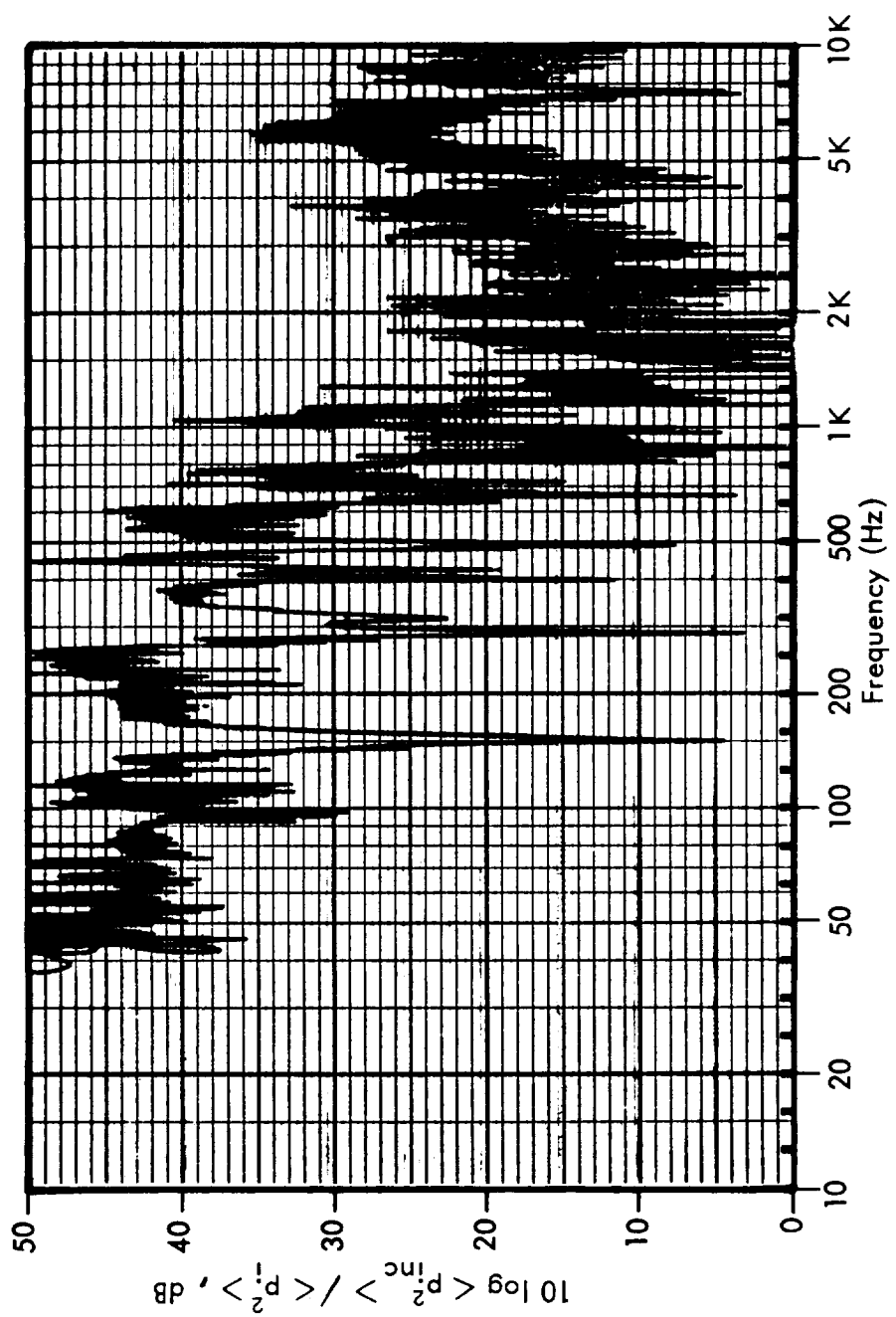
Record No. 17



Record No. 18



Record No. 20

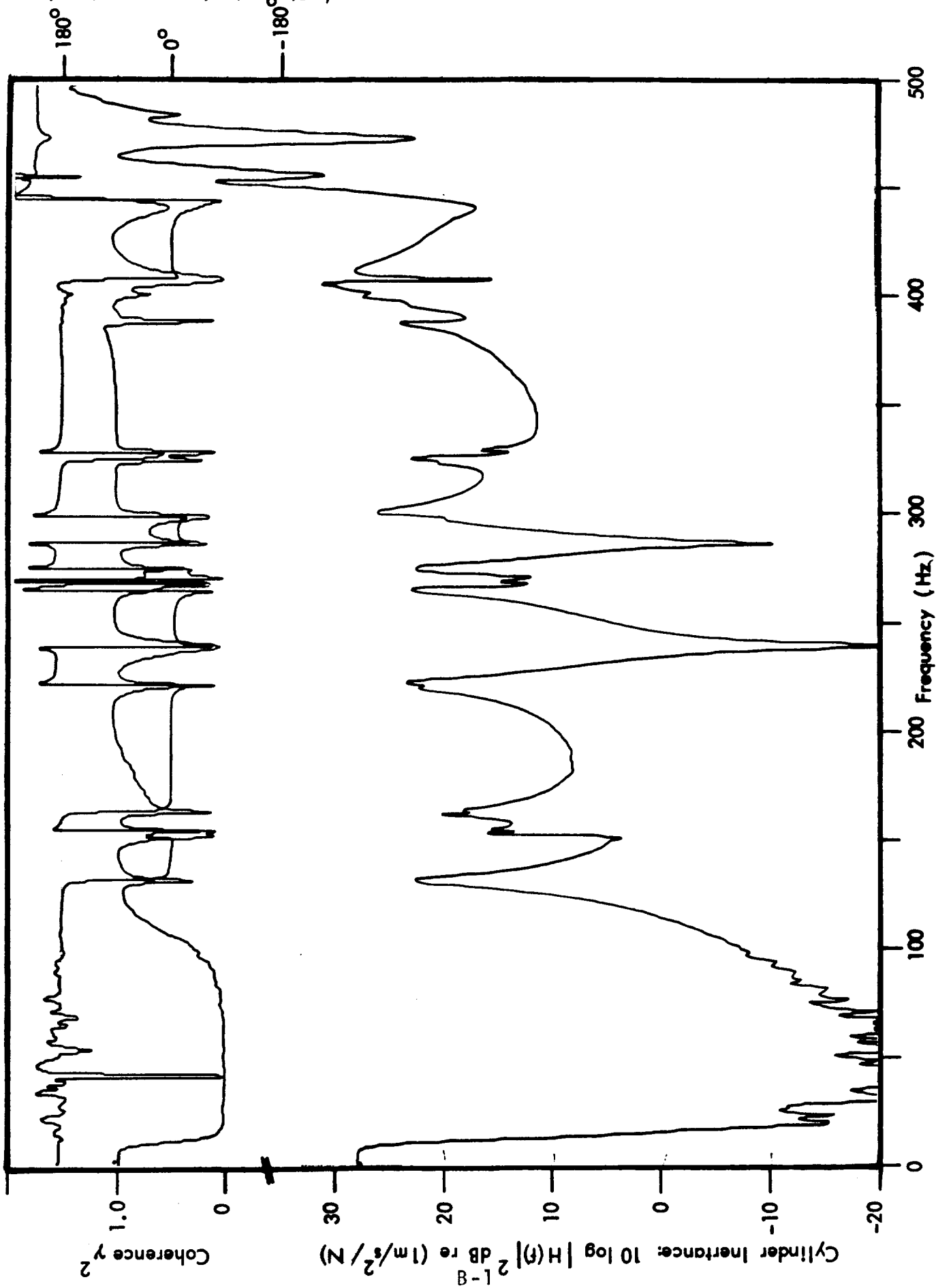


Record No. 21

APPENDIX B

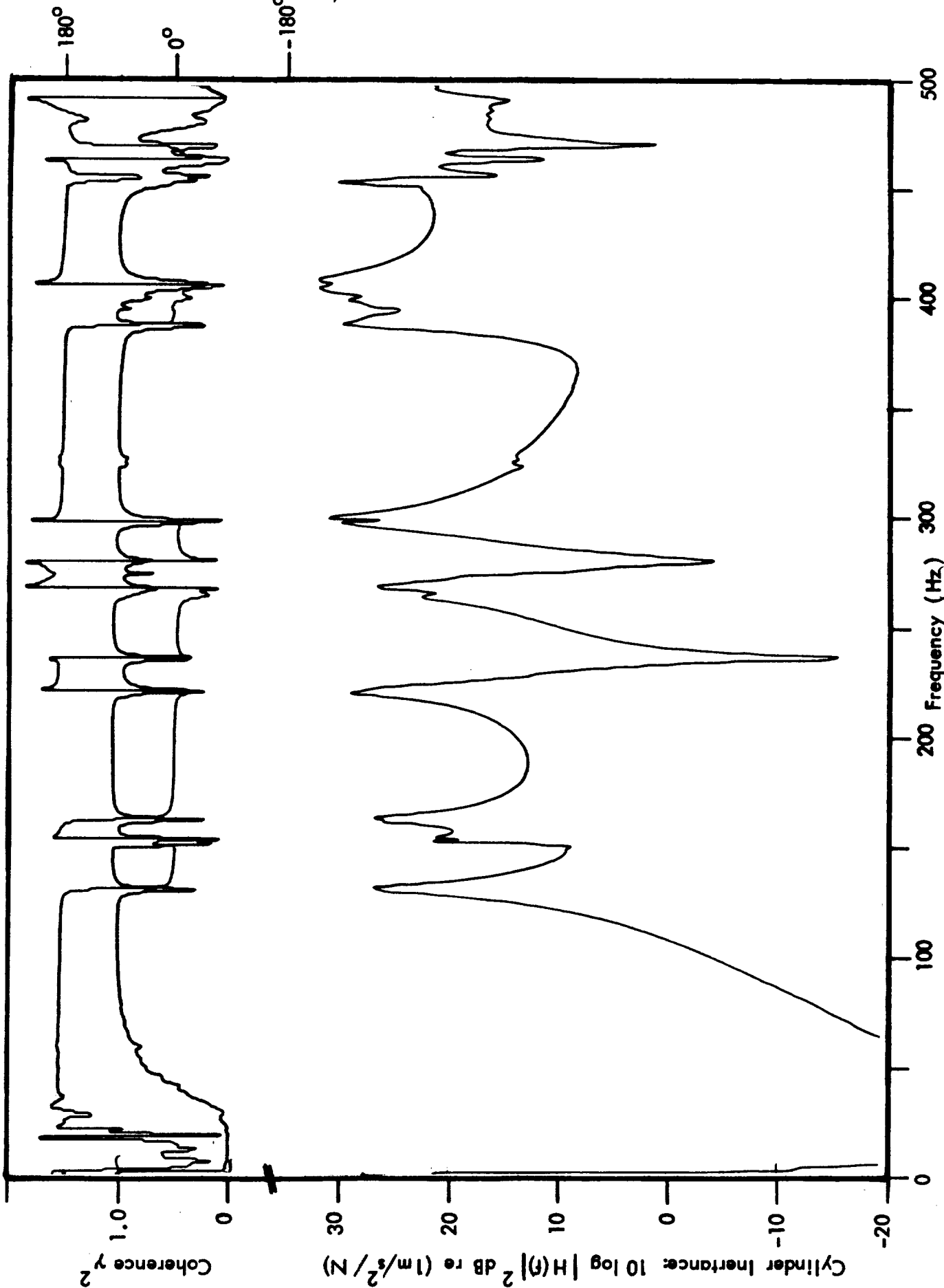
Mechanical Excitation Data

ϕ , Phase Angle Between Acceleration
and Force



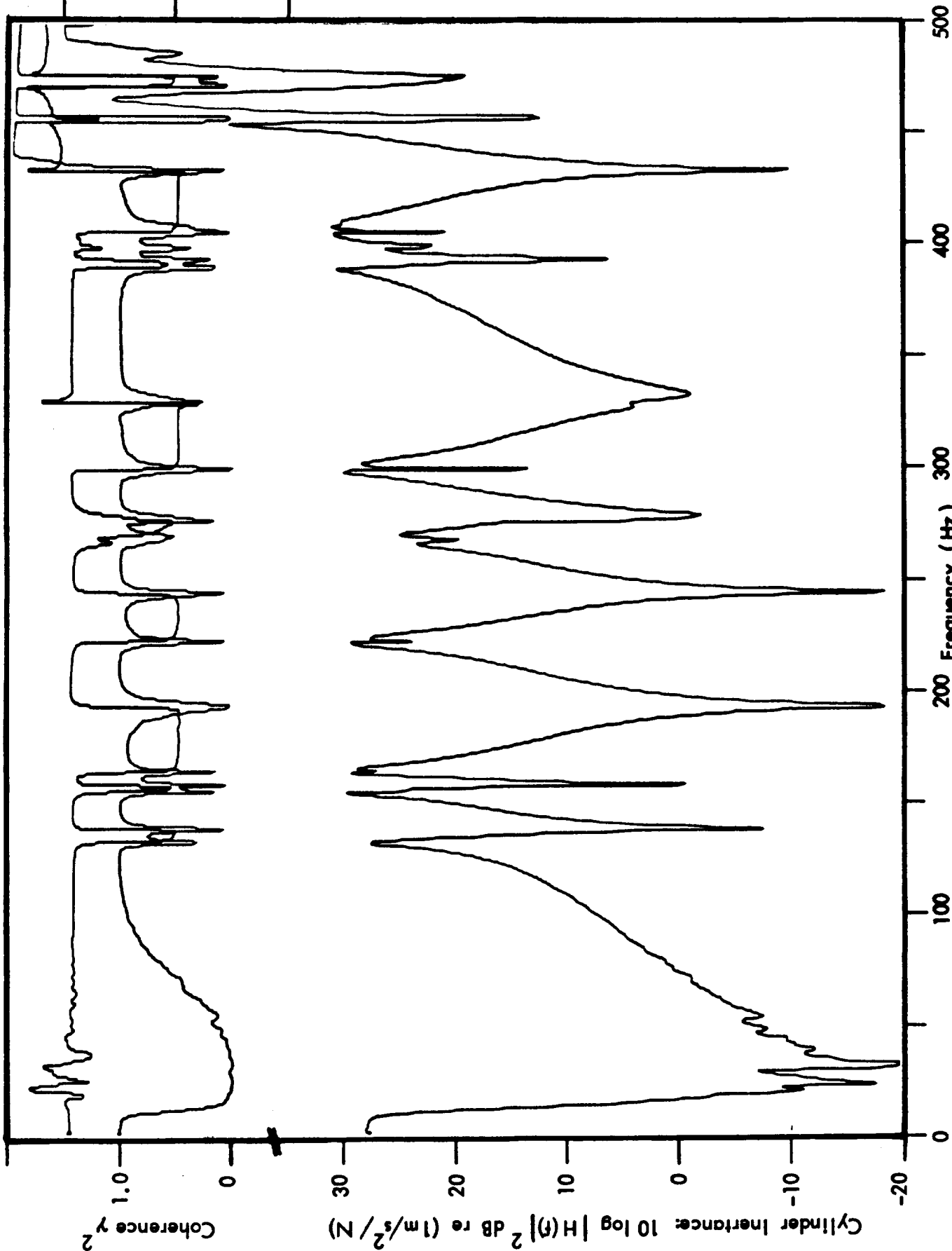
Record No. 105

ϕ , Phase Angle Between Acceleration
and Force

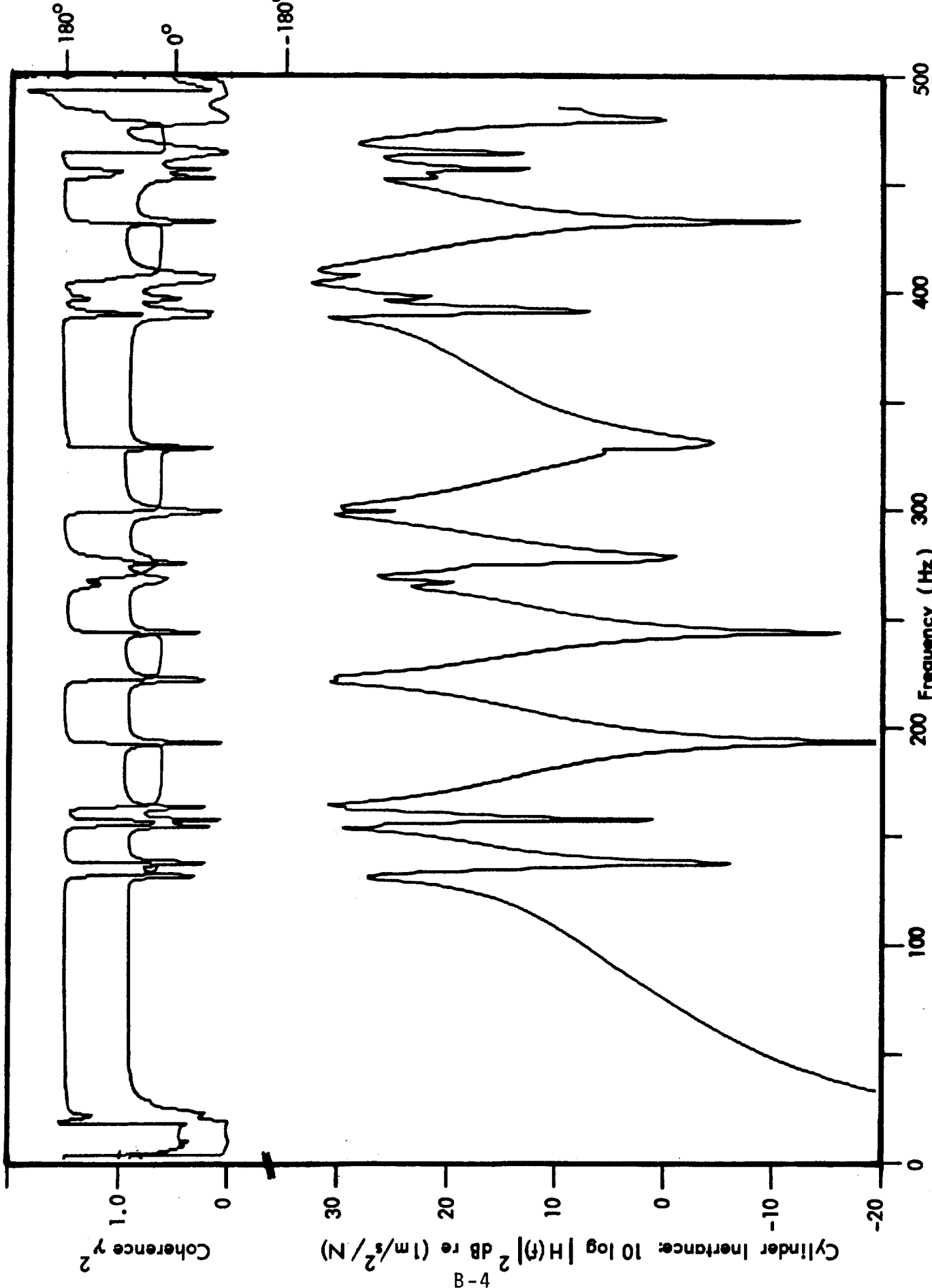


Record No. 105A

ϕ , Phase Angle Between Acceleration and Force

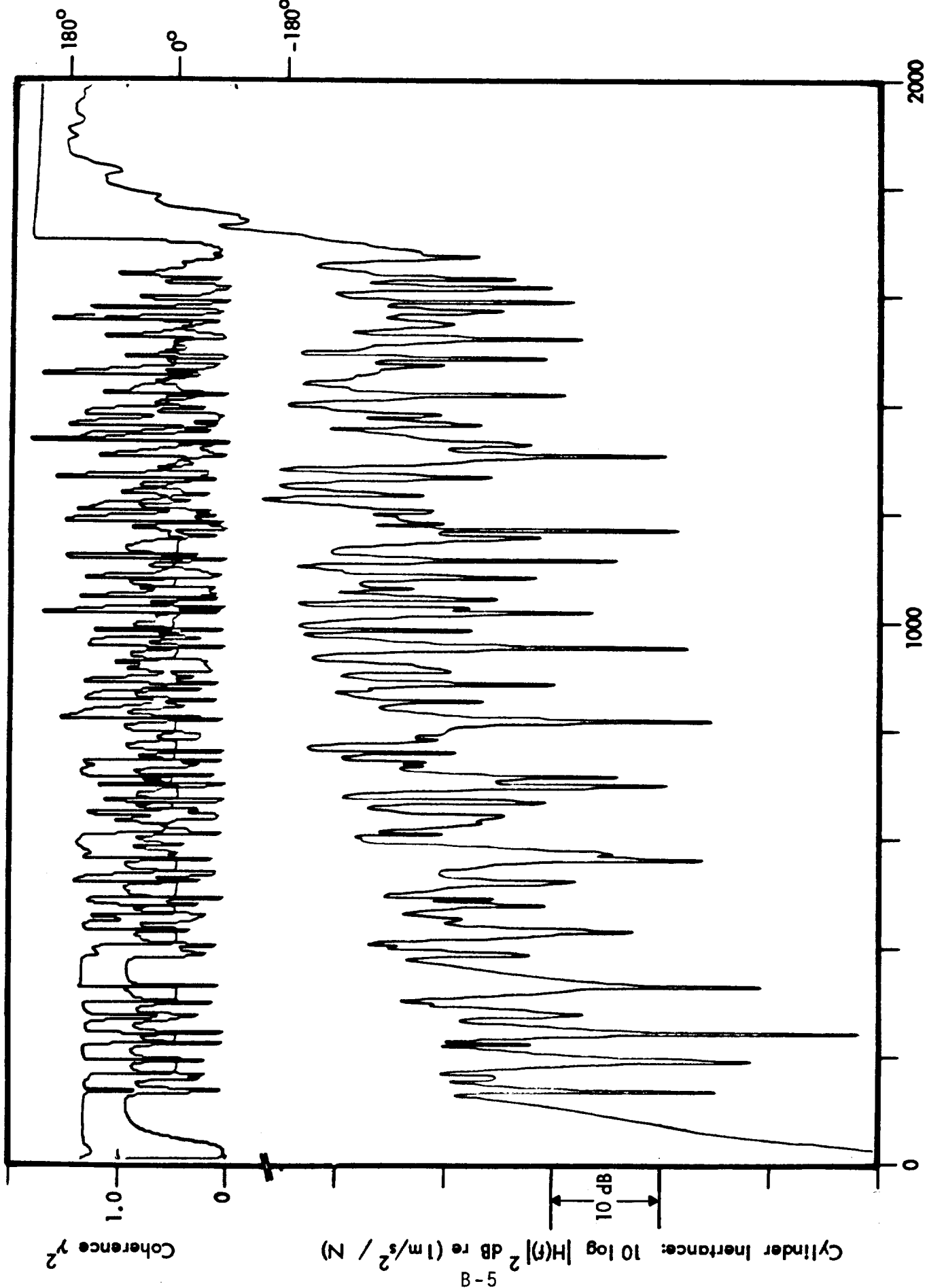


ϕ , Phase Angle Between Acceleration and Force

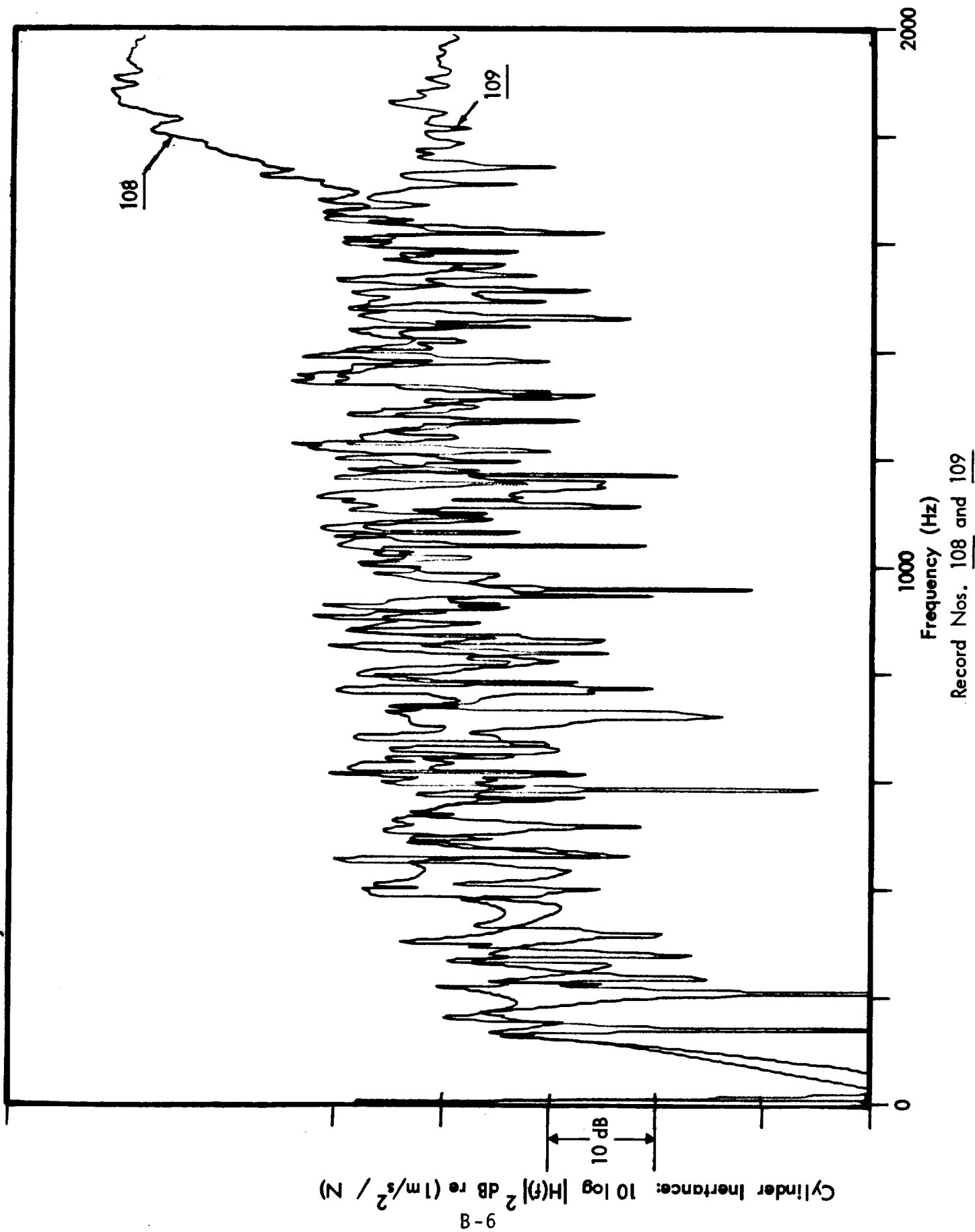


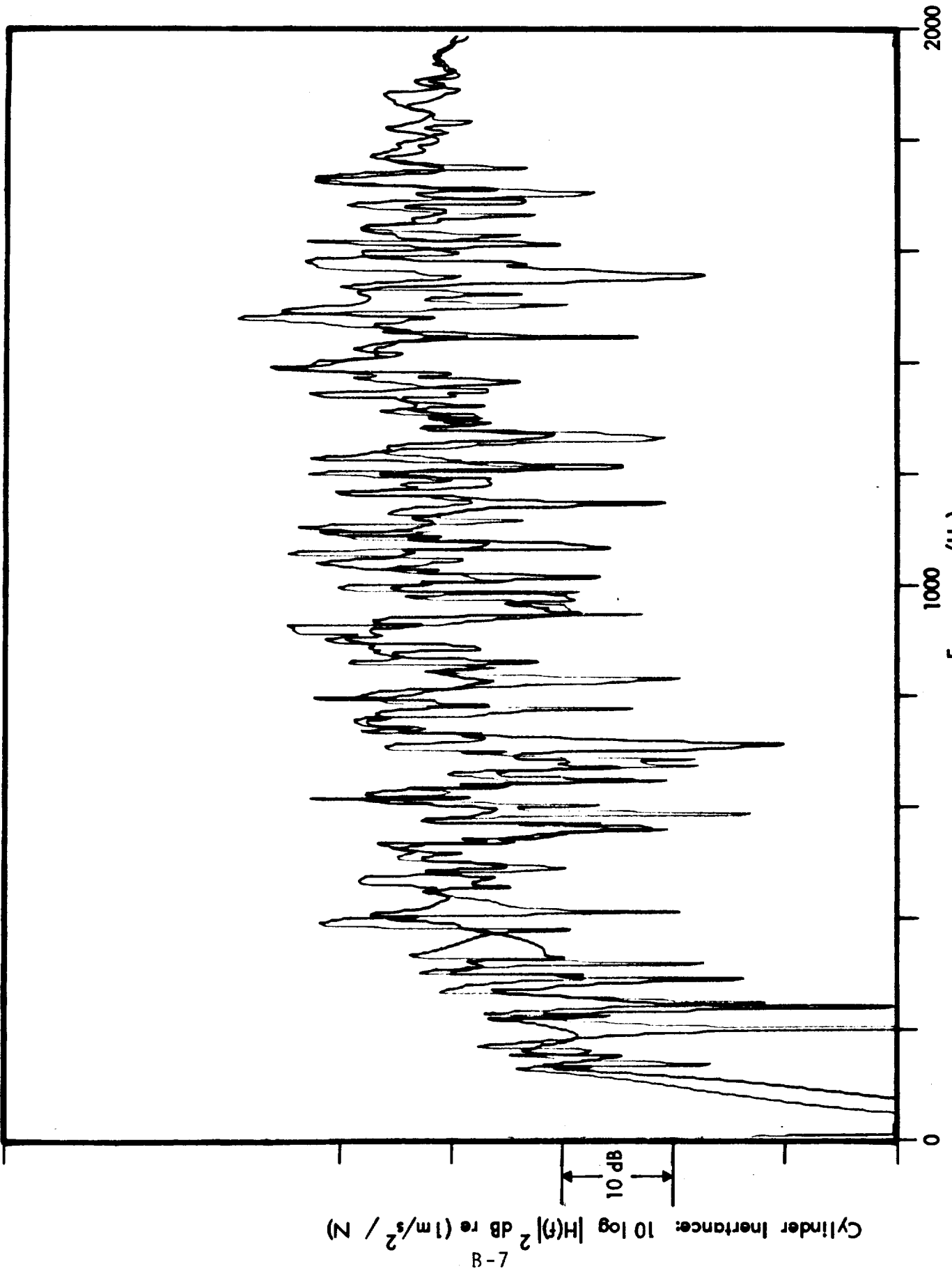
Record No. 106R

ϕ , Phase Angle Between Acceleration and Force



Record No. 107

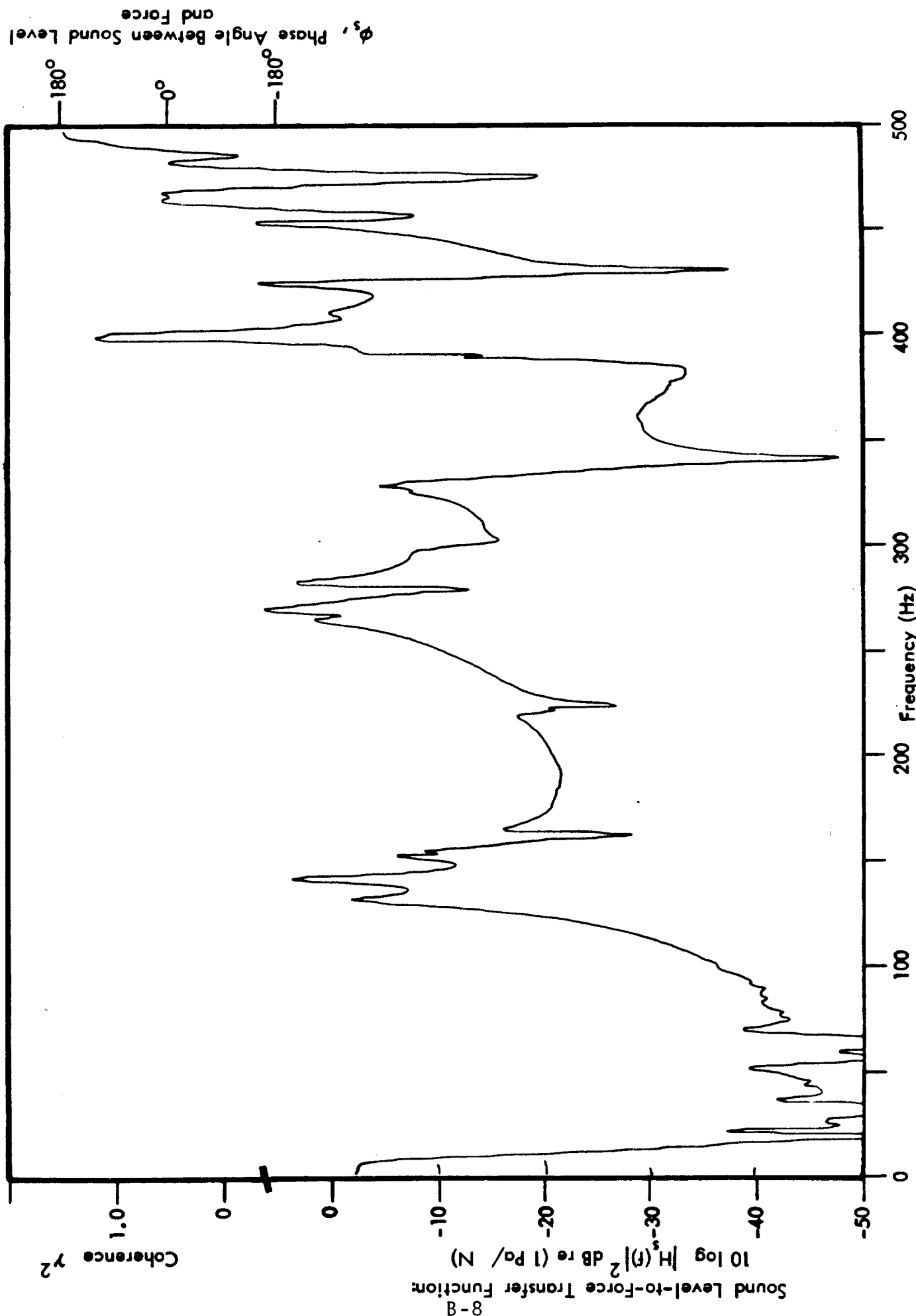




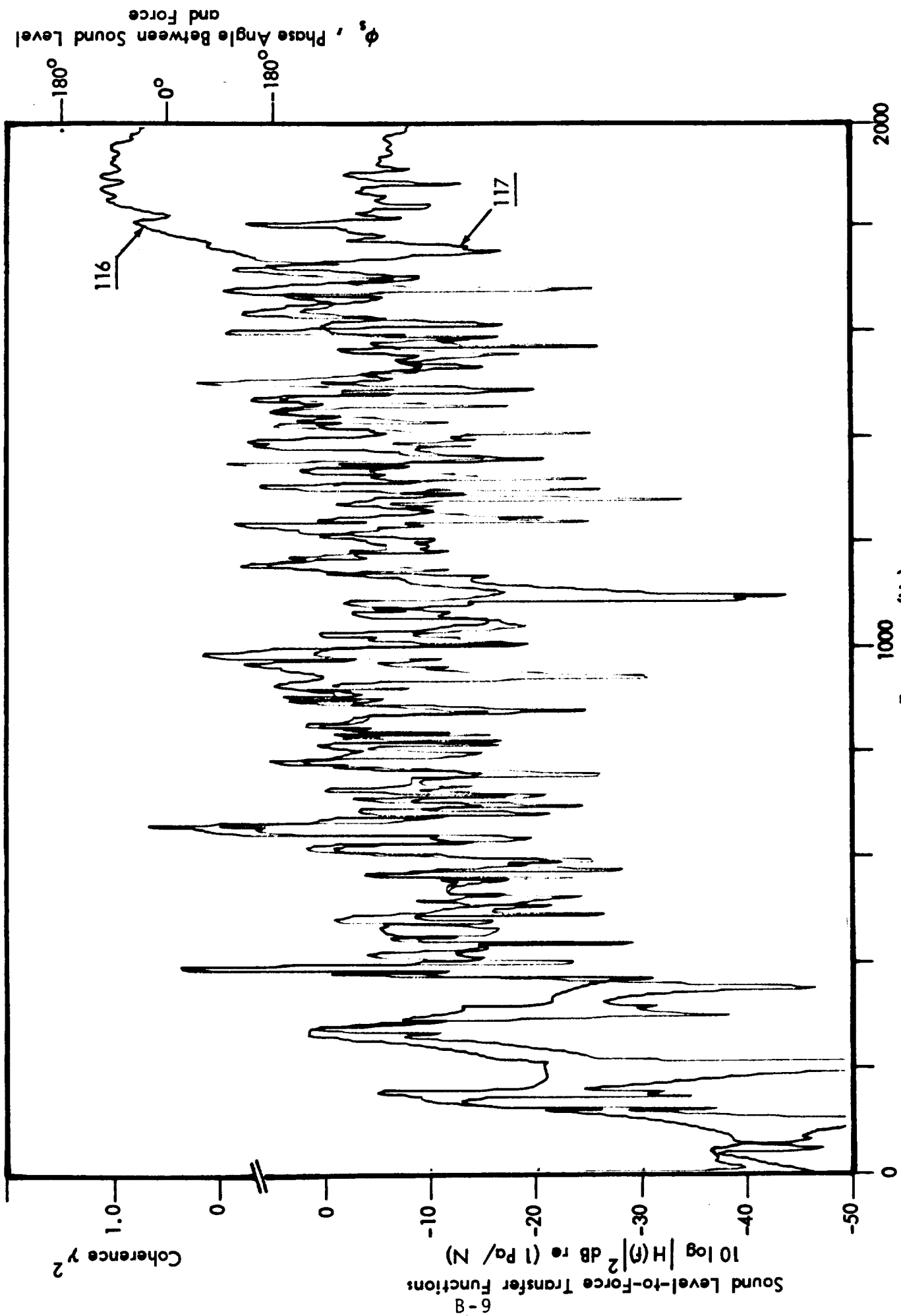
Cylinder Inertance: $10 \log |H(f)|^2 \text{ dB re } (1 \text{ m/s}^2 / \text{N})$

B-7

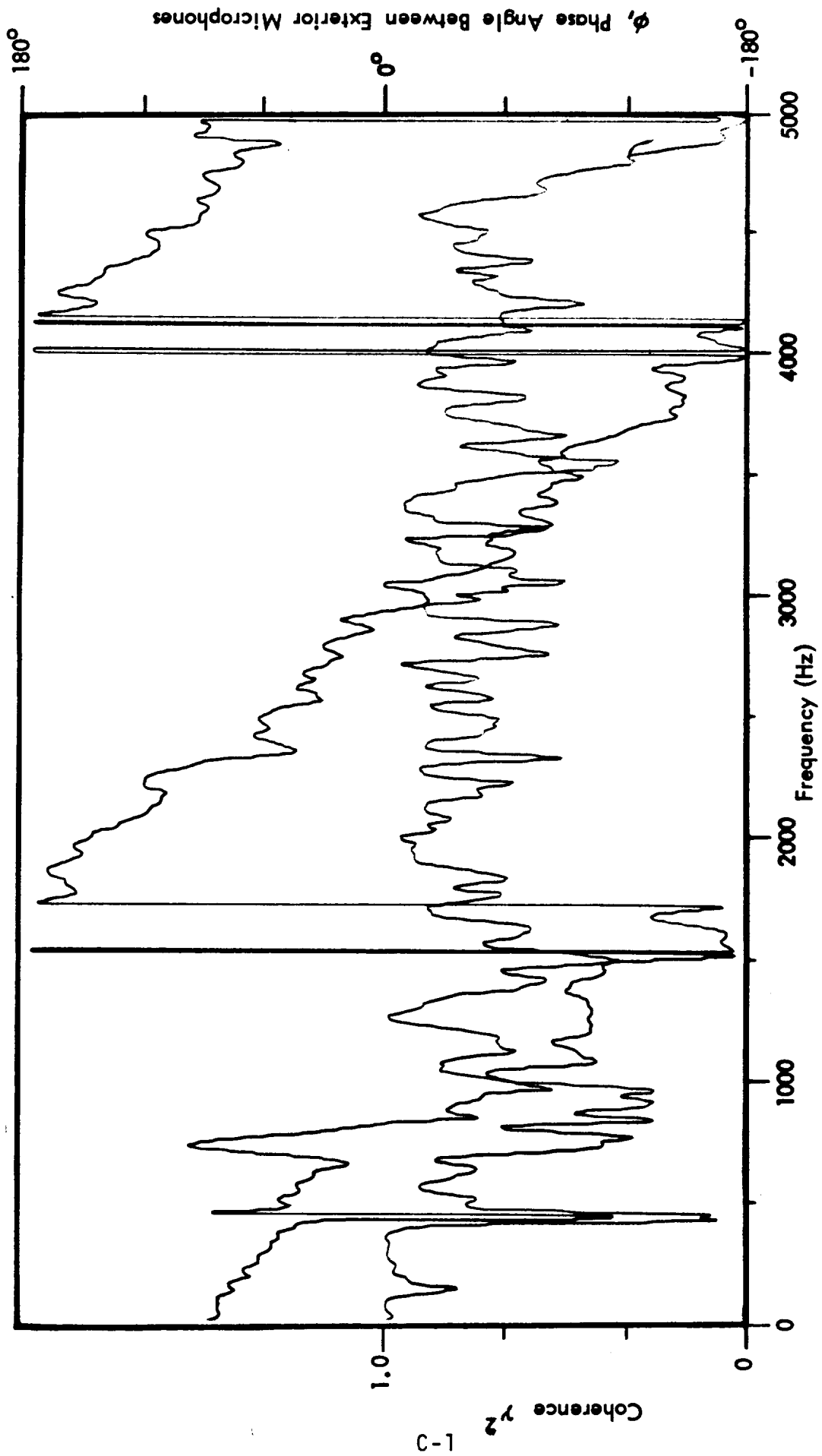
Frequency (Hz)
Record No. 110



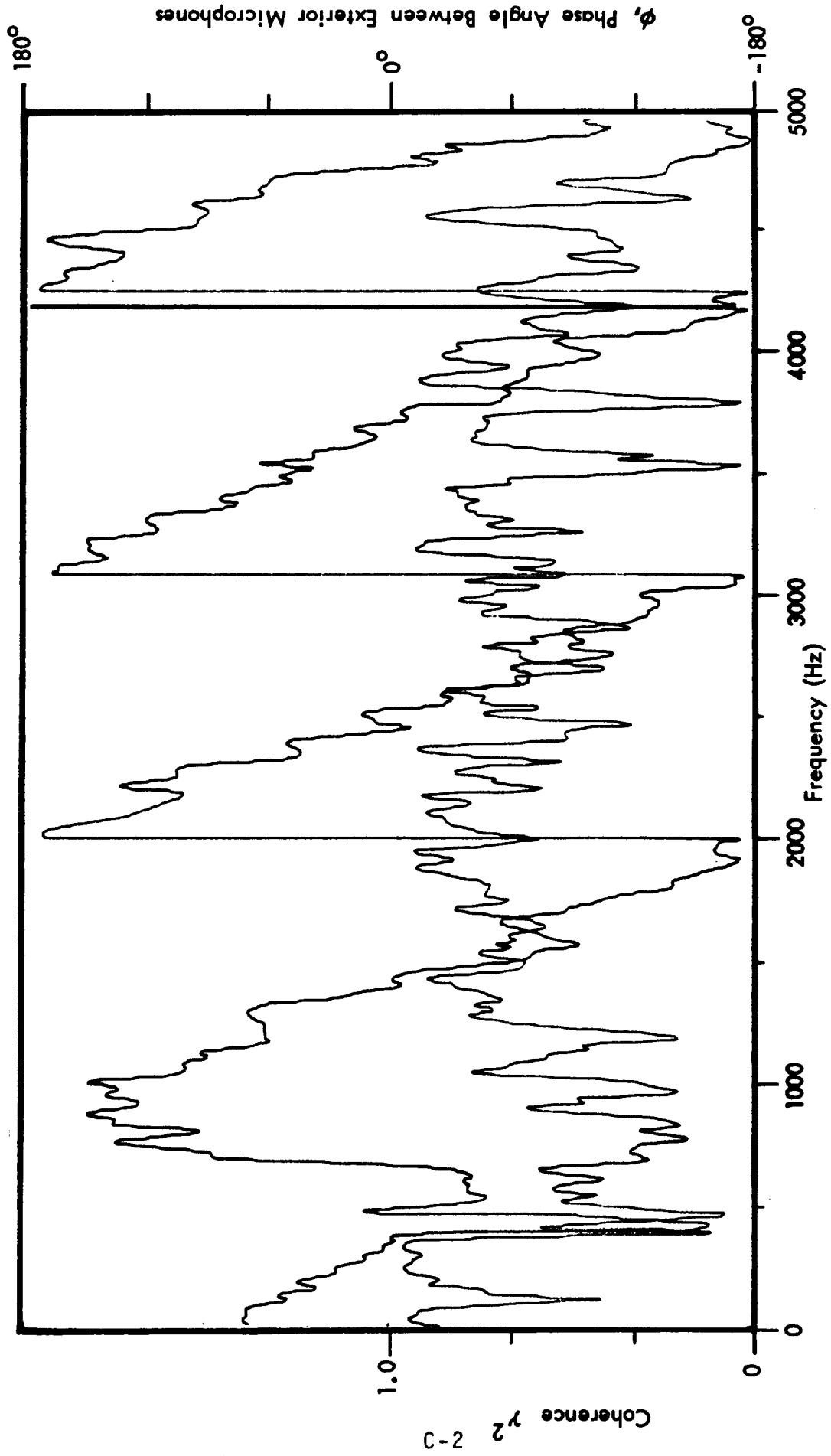
Record No. 113



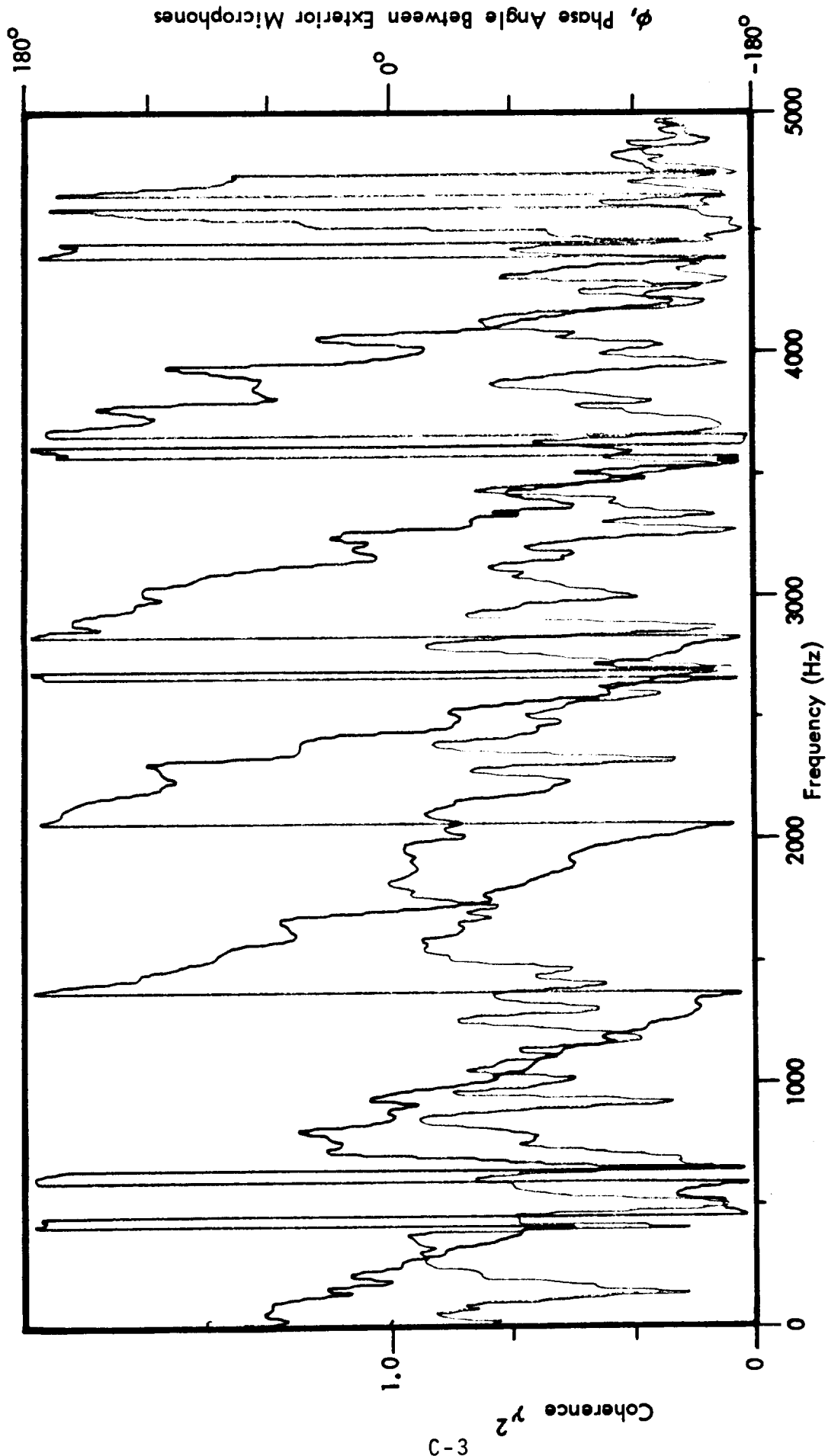
APPENDIX C
Progressive Wave Field Data



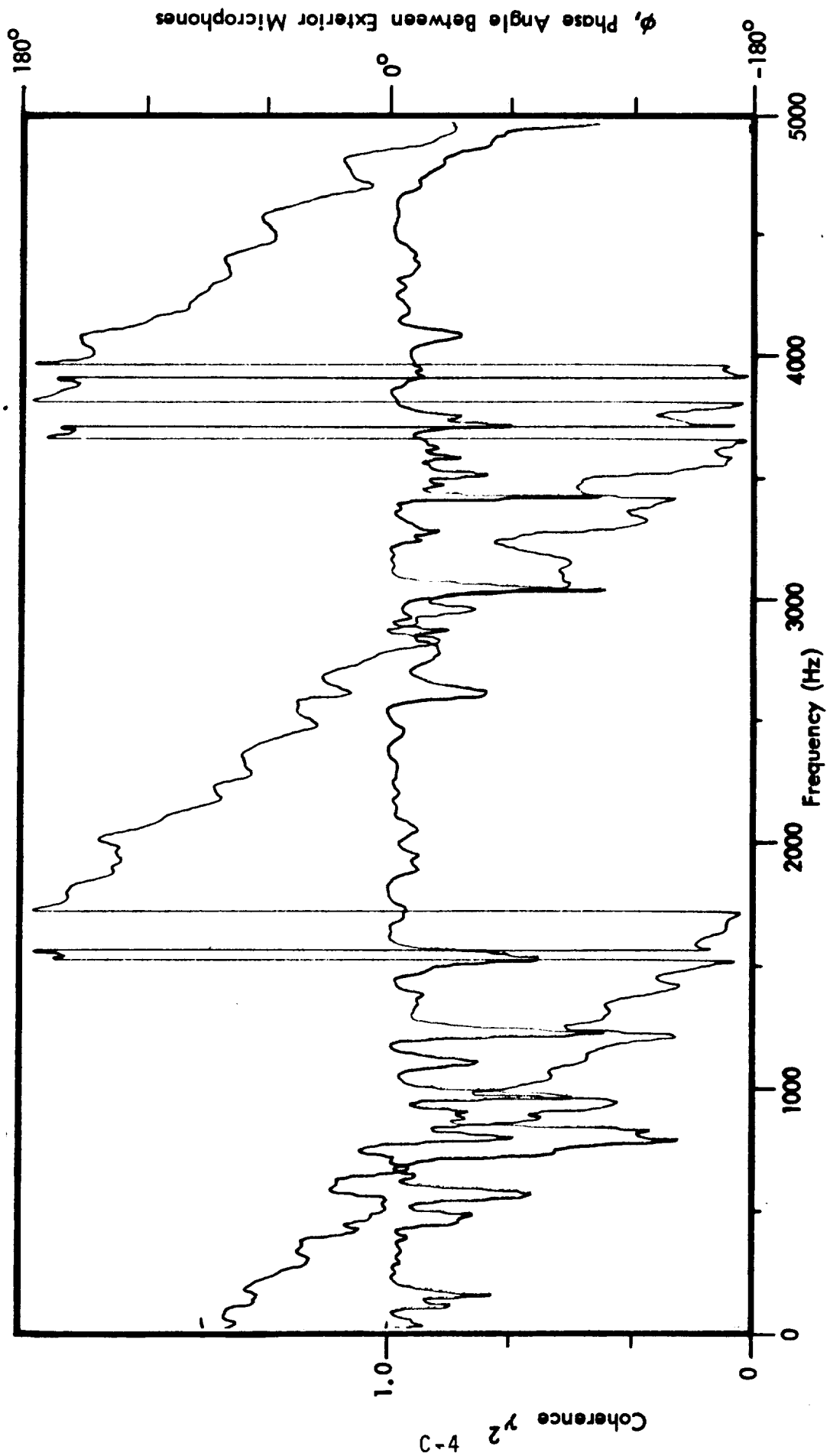
Record No. 201



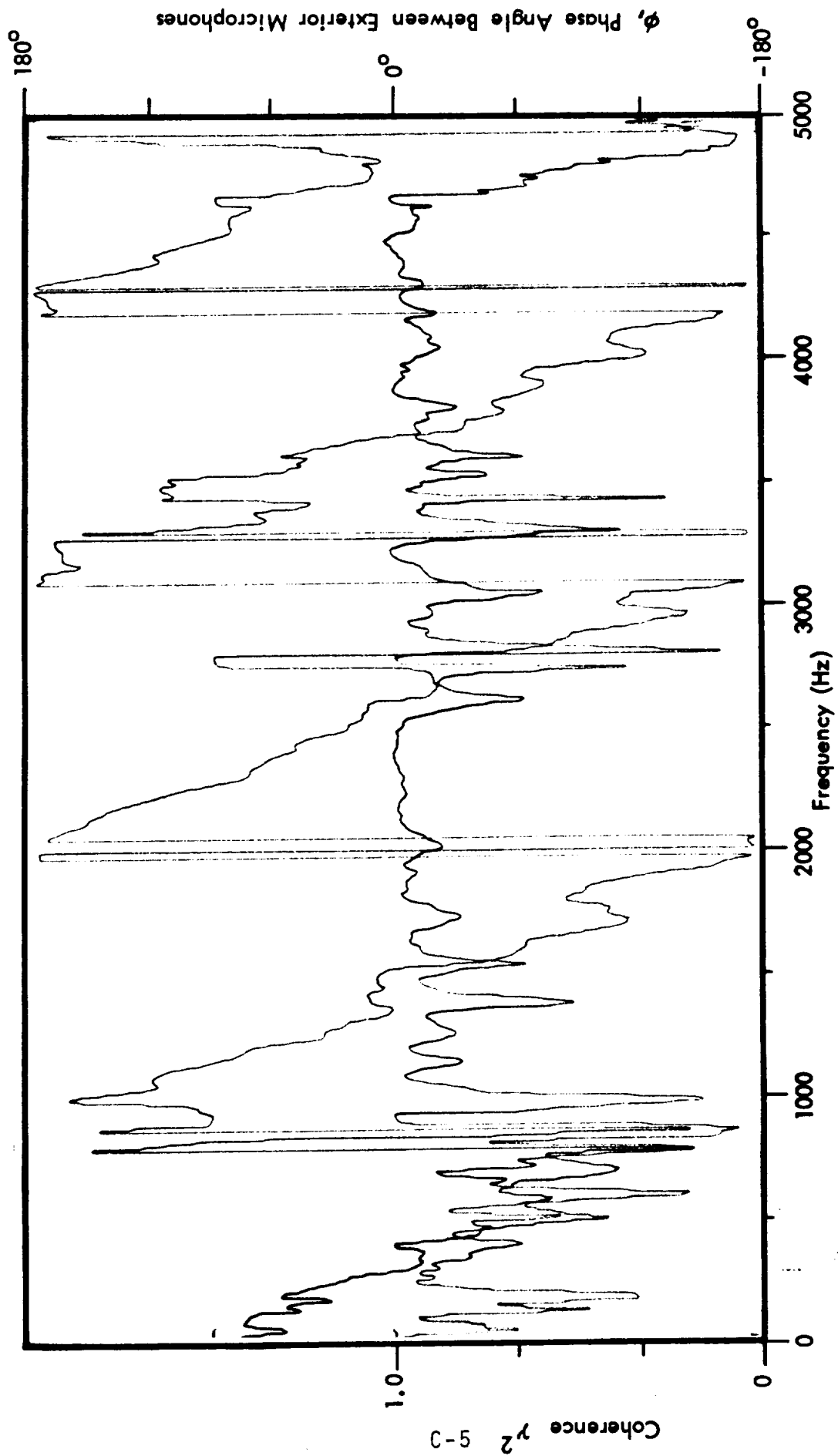
Record No. 202



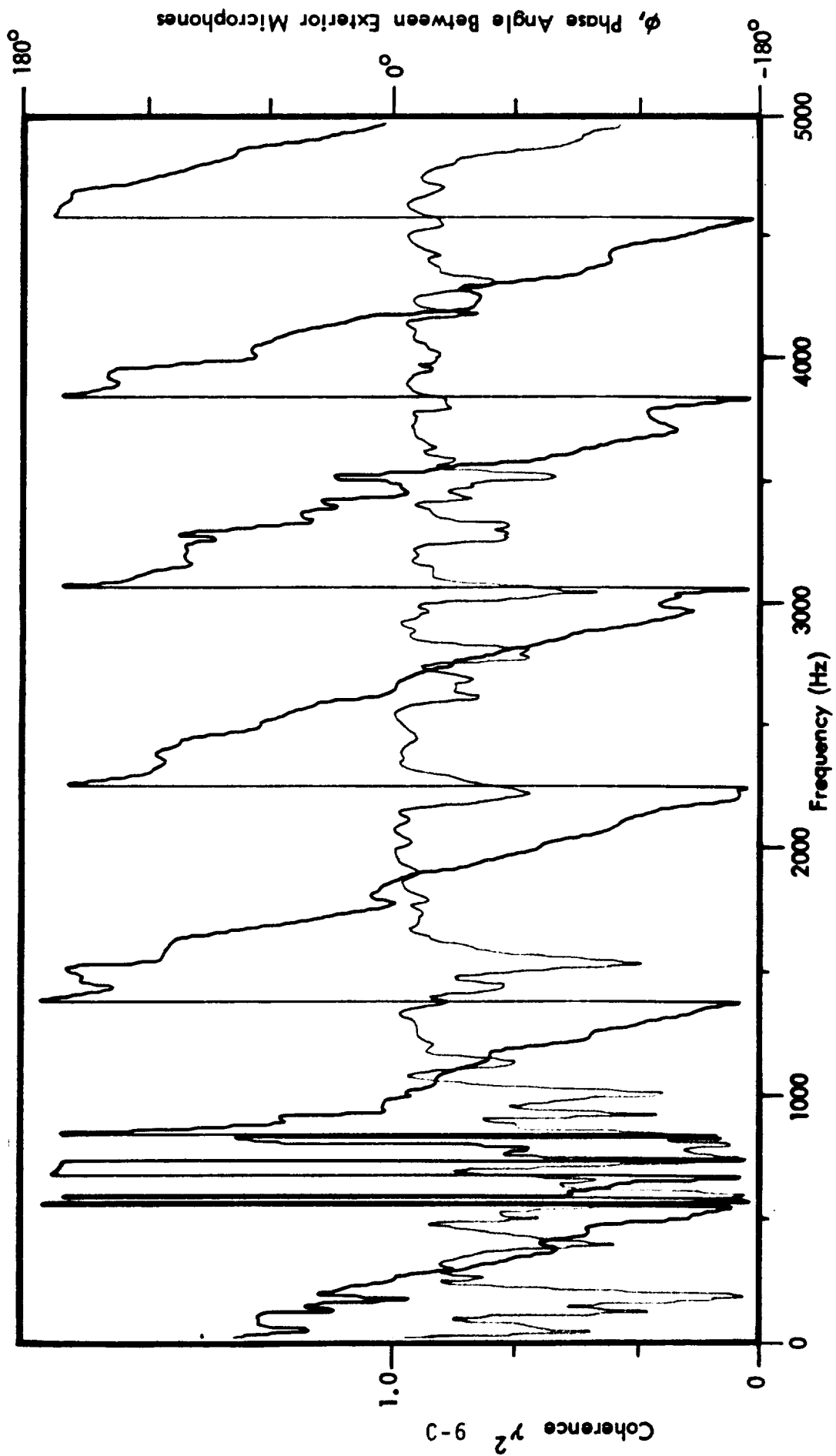
Record No. 203



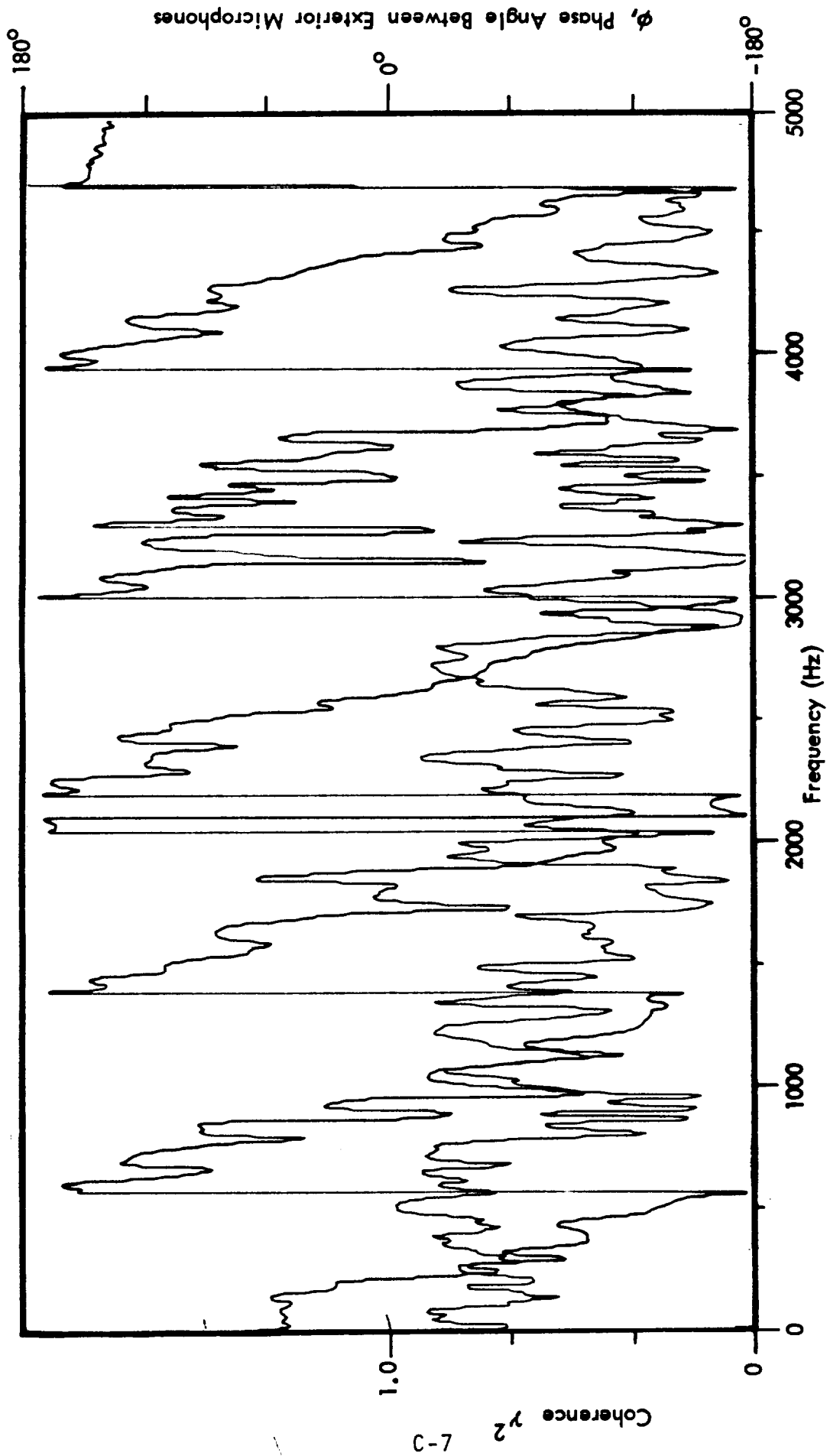
Record No. 204



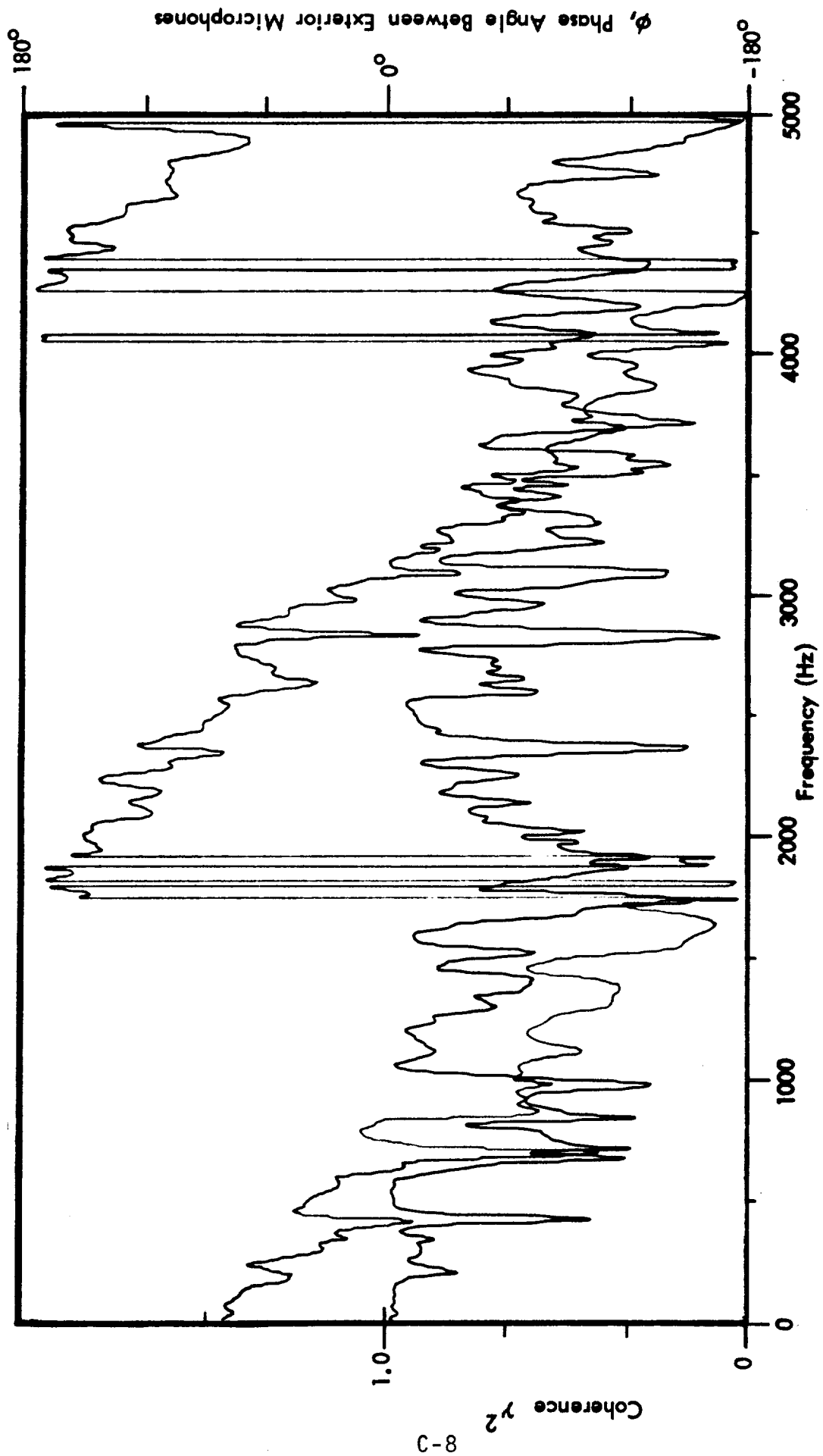
Record No. 205



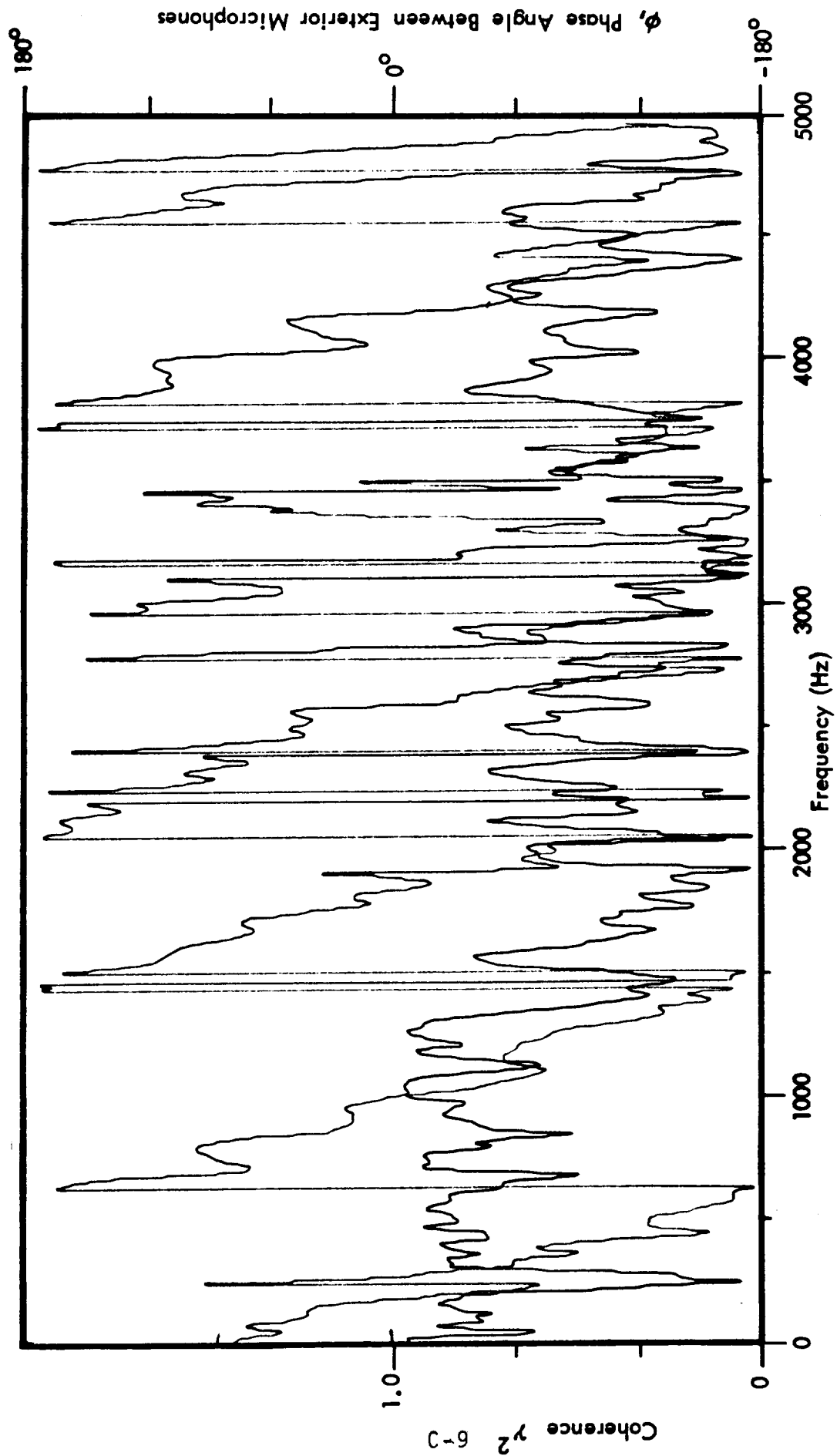
Record No. 206



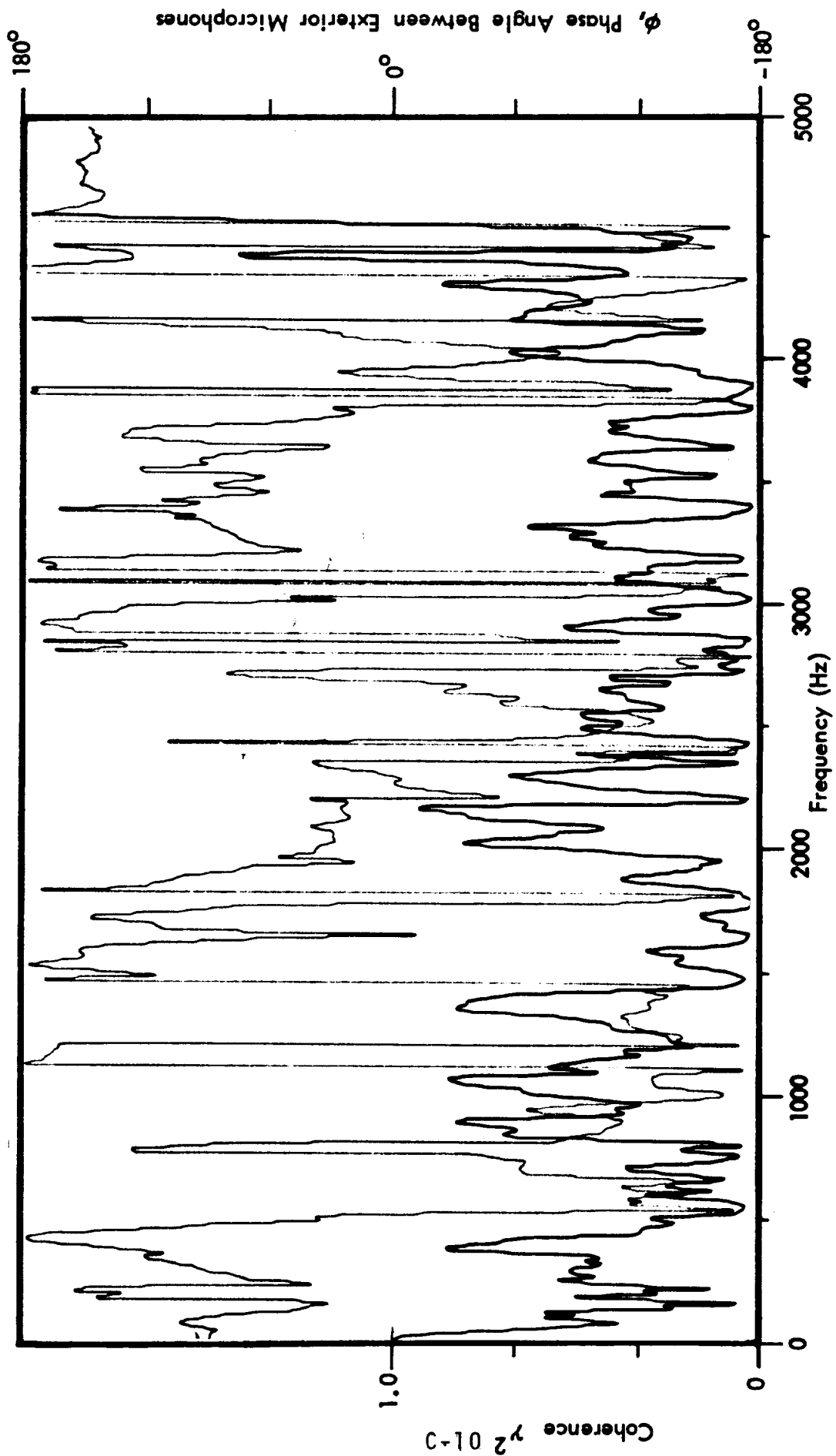
Record No. 208



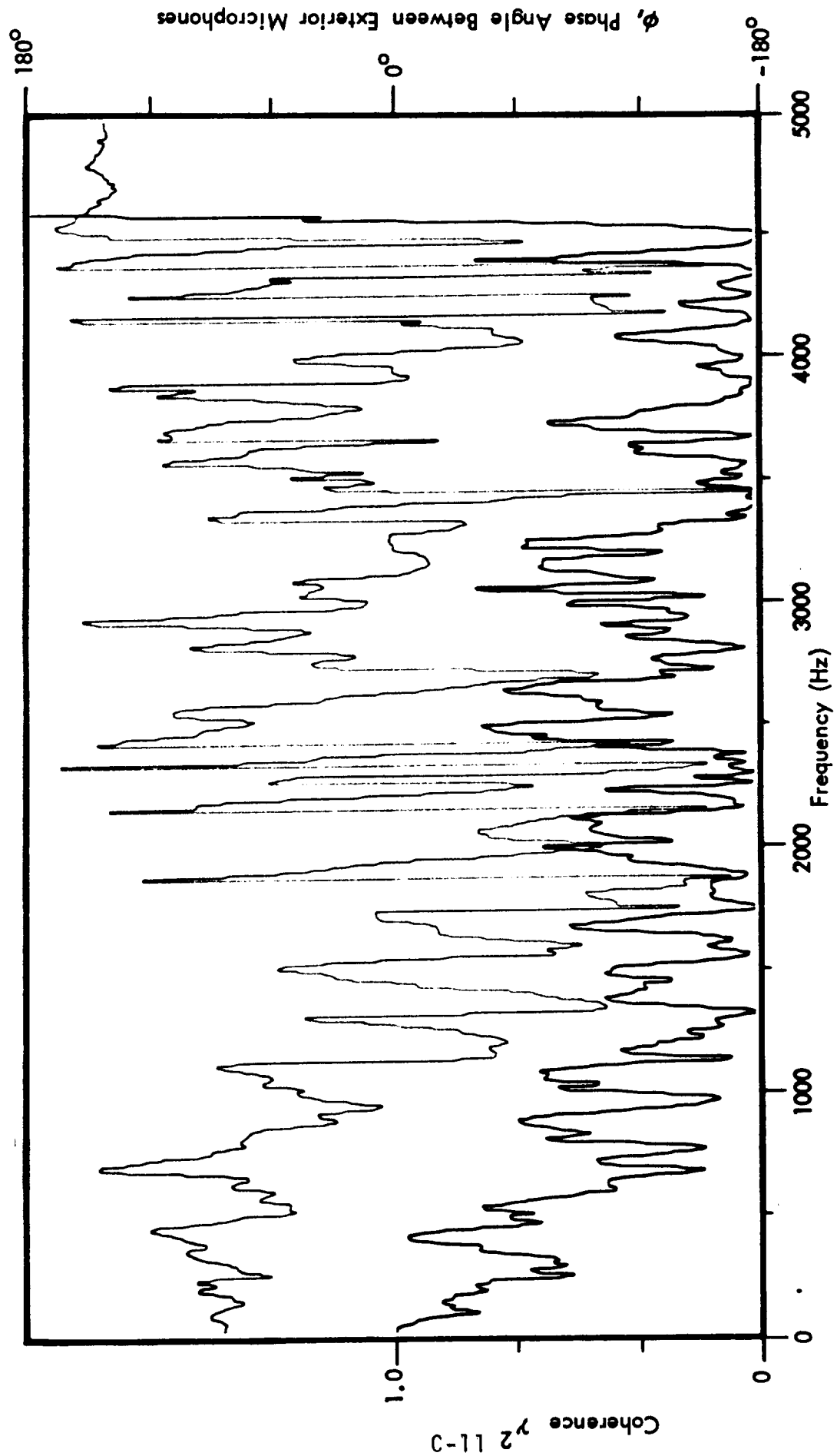
Record No. 209



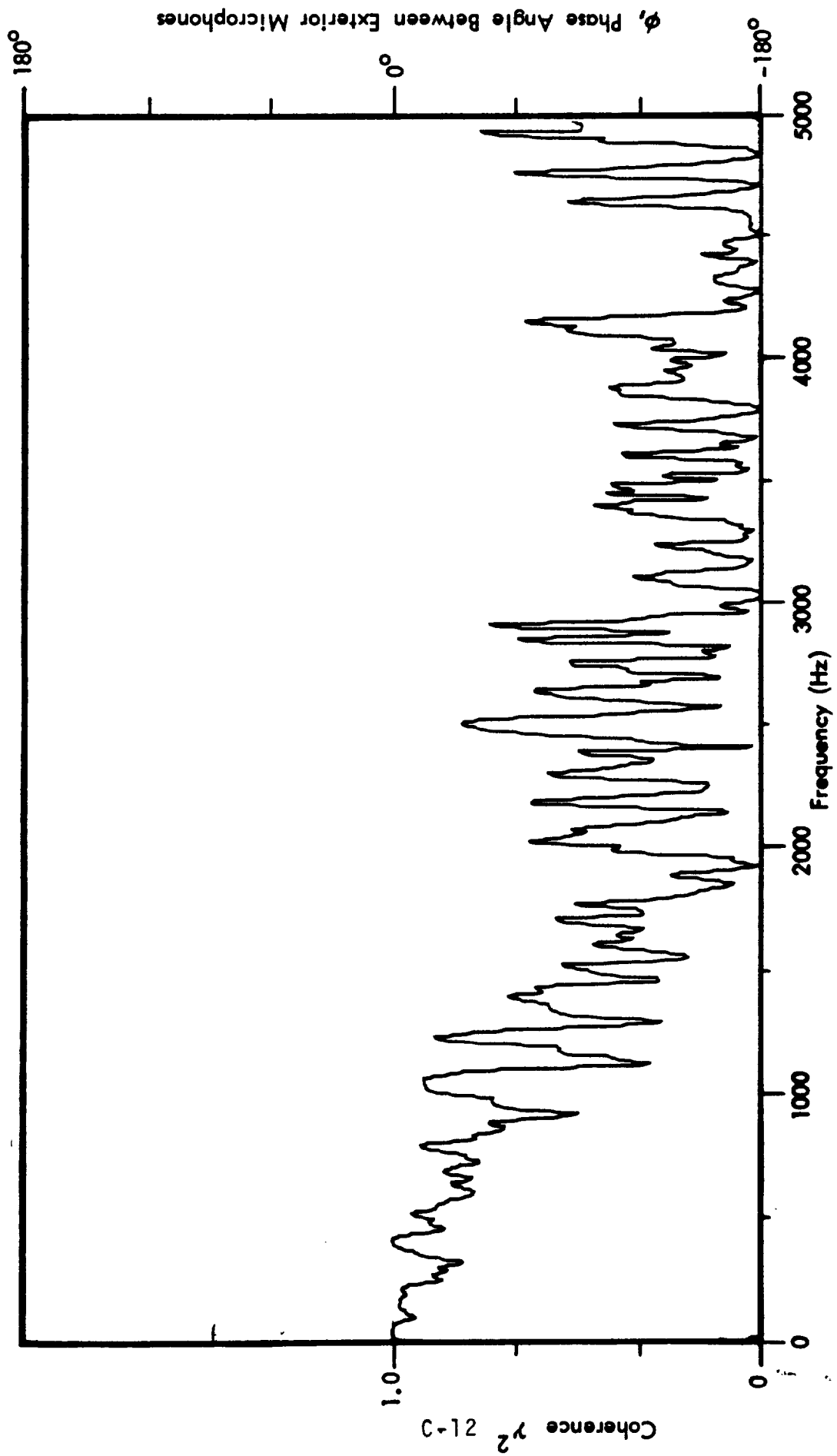
Record No. 210



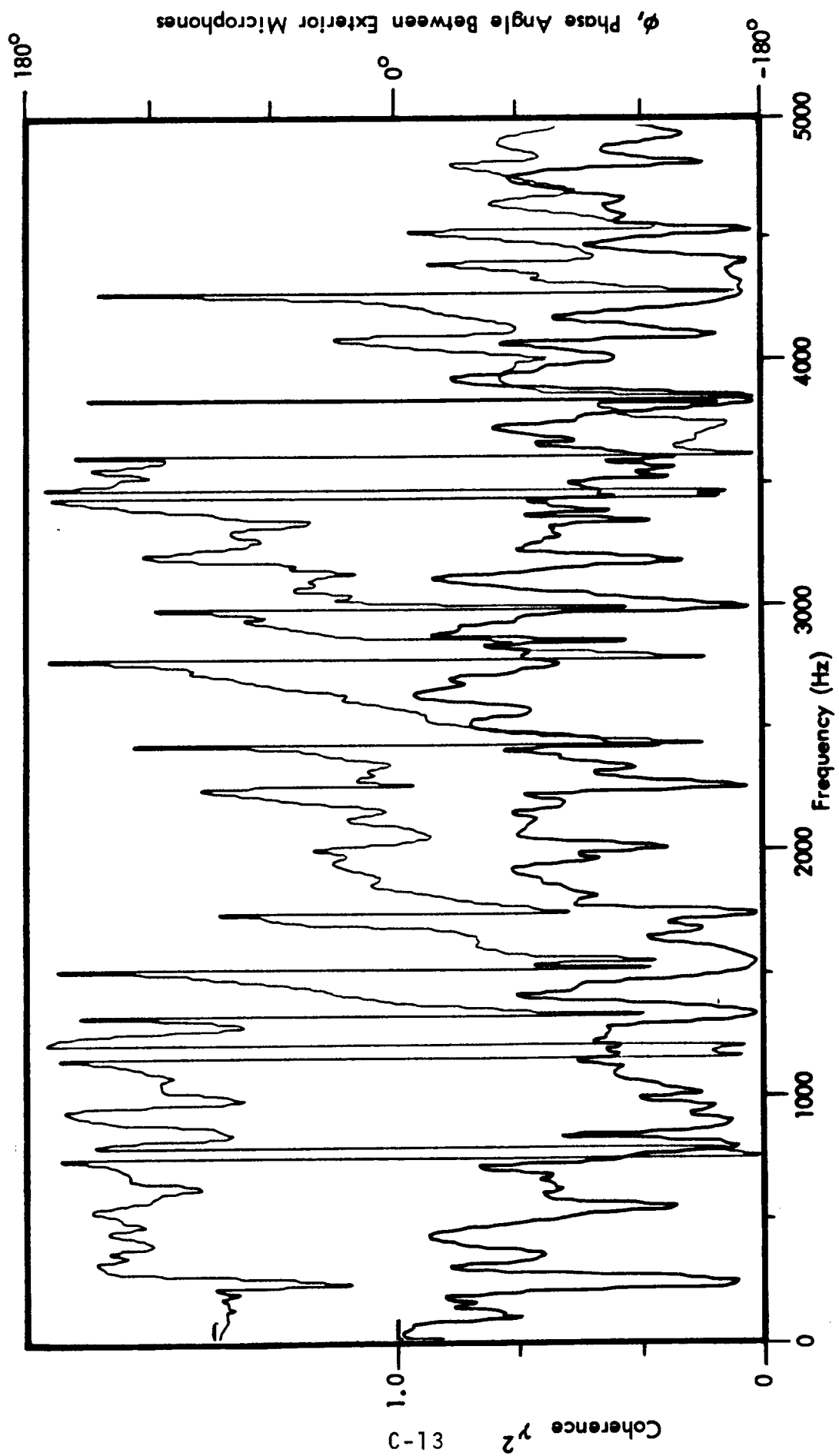
Record No. 211



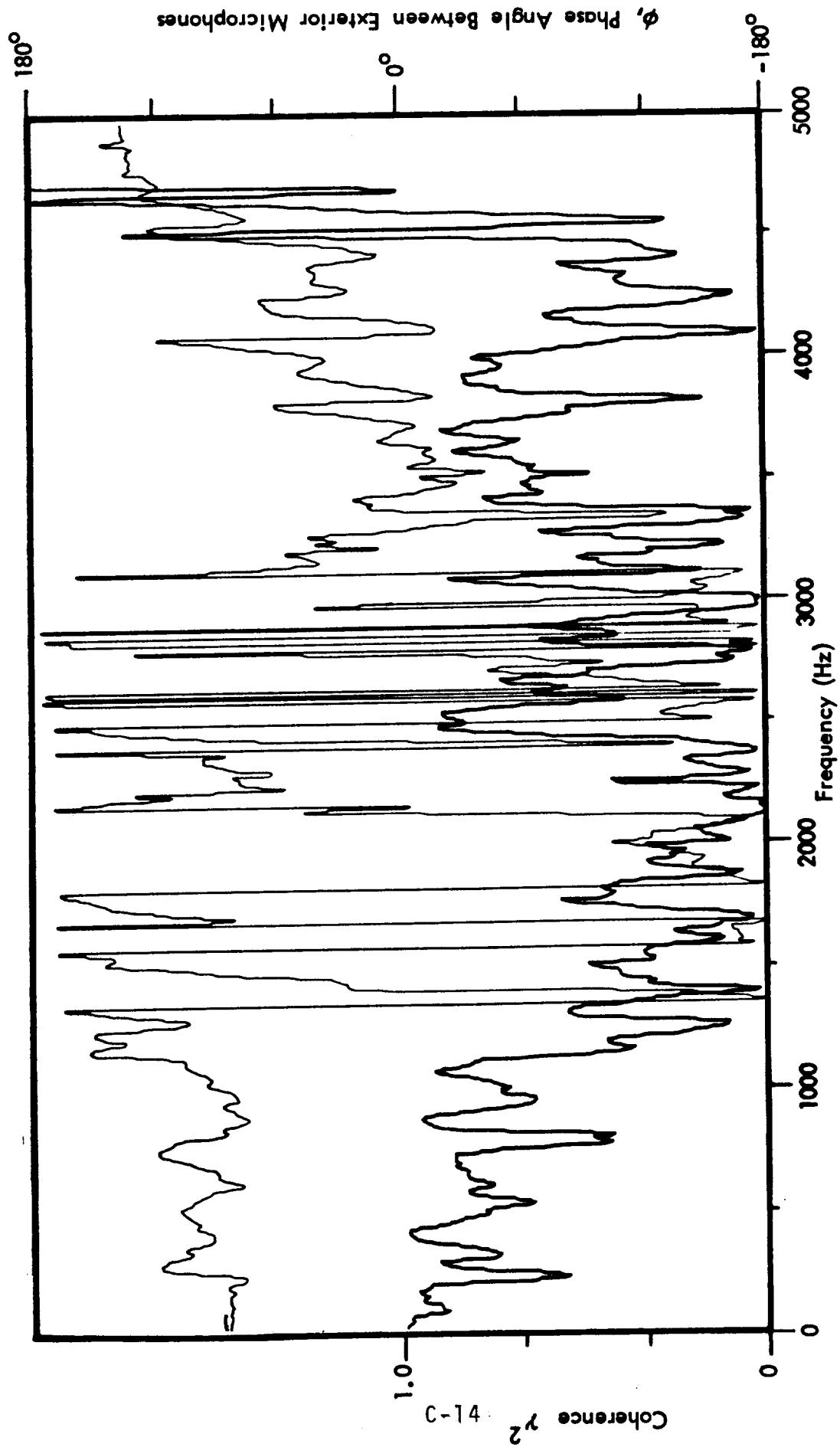
Record No. 212



Record No. 213



Record No. 215



Record No. 216

1. Report No. NASA CR-159363		2. Government Accession No.		3. Recipient's Catalog No.	
4. Title and Subtitle Analytical Prediction of the Interior Noise for Cylindrical Models of Aircraft Fuselages for Prescribed Exterior Noise Fields - Phase I (see 15. Supplementary Notes)				5. Report Date October 1980	
				6. Performing Organization Code	
7. Author(s) L. D. Pope, D. C. Rennison, and E. G. Wilby				8. Performing Organization Report No. 4420	
9. Performing Organization Name and Address Bolt Beranek and Newman Inc. 21120 Vanowen Street Canoga Park, CA 91303				10. Work Unit No.	
				11. Contract or Grant No. NAS1-15782	
12. Sponsoring Agency Name and Address National Aeronautics and Space Administration Langley Research Center Hampton, Virginia 23665				13. Type of Report and Period Covered Contractor Report	
				14. Sponsoring Agency Code	
15. Supplementary Notes Langley technical monitor: William H. Mayes BBN program manager: Larry D. Pope Phase I - Development and Validation of Preliminary Analytical Models					
16. Abstract As a part of a NASA Langley Research Center program to determine the important parameters associated with sound transmission into the interiors of airplanes and to identify appropriate noise control methods, an airplane interior noise prediction model is being developed. In Phase I, analytical modeling of the transmission problem (interaction of the structures with the exterior and interior acoustic fields) is undertaken and model validation studies completed using, as a test article, an unpressurized unstiffened cylinder. In this report, the basic theoretical work required to understand sound transmission into an enclosed space (that is, one closed by the transmitting structure) is developed for random pressure fields and for harmonic (tonal) excitation. The analysis is used to predict the noise reduction of the test article and, also, the interior response of the cylinder given a tonal (plane wave) excitation. Comparisons of predictions and measurements are made and a detailed analysis of the transmission is presented. In addition, results for tonal (harmonic) mechanical excitation are considered.					
17. Key Words (Suggested by Author(s)) Aircraft Interior Noise Cylinder Noise Reduction Band-Limited Response Predictions Power Balance				18. Distribution Statement Unclassified - Unlimited	
19. Security Classif. (of this report) Unclassified		20. Security Classif. (of this page) Unclassified		21. No. of Pages 175	
22. Price*					

NASA Contractor Report 159363

Distribution List

NAS1-15782

No.
Copies

NASA Langley Research Center
Hampton, VA 23665

Attn: Report and Manuscript Control Office, Mail Stop 180A
Technology Utilization Office, Mail Stop 139A
William H. Mayes, Mail Stop 463

1
1
20

NASA Ames Research Center
Moffett Field, CA 94035
Attn: Library, Mail Stop 202-3

1

NASA Dryden Flight Research Center
P.O. Box 273
Edwards, CA 93523
Attn: Library

1

NASA Goddard Space Flight Center
Greenbelt, MD 20771
Attn: Library

1

NASA Lyndon B. Johnson Space Center
2101 Webster Seabrook Road
Houston, TX 77058
Attn: JM5/Library

1

NASA Marshall Space Flight Center
Marshall Space Flight Center, AL 35812
Attn: Library, AS61L

1

Jet Propulsion Laboratory
4800 Oak Grove Drive
Pasadena, CA 91103
Attn: Library, Mail Code 111-113

1

NASA Lewis Research Center
21000 Brookpark Road
Cleveland, OH 44135
Attn: Library, Mail Stop

1

NASA John F. Kennedy Space Center
Kennedy Space Center, FL 32899
Attn: Library, NWSI-D

1

National Aeronautics and Space Administration
Washington, DC 20546
Attn: RTE-6

1

No.
Copies

Dr. Rimas Vaicaitis
Columbia University
Dept. of Civil Engineering
and Engineering Mechanics
New York, NY 10027

1

Prof. Earl H. Dowell
2 Aero Lab
School of Eng. & Applied Science
Dept. of Aerospace Mechanical Science
James Forestal Campus
Princeton, NJ 08540

1

Dr. Frank D. Hart
North Carolina State University
Director, Center for Acoustical
Studies
Box 5801
Raleigh, NC 27607

1

Dr. Malcolm Crocker
Purdue University
The Ray W. Herrick Laboratories
West Lafayette, IN 47907

1

Dr. Jan Roskam
Dept. of Aerospace Engineering
University of Kansas
Lawrence, KA 66044

1

Dr. James Unruh
Southwest Research Inst.
8500 Culebra Road
San Antonio, TX 78284

1

Dr. Jim D. Revell
Dept. 75-40
Bldg. 63
Lockheed-California Company
P.O. Box 551
Burbank, CA 91520

1

Mr. Robert E. Pendley
Douglas Aircraft Company
Dept. 251
Mail Code 123-11
3855 Lakewood Boulevard
Long Beach, CA 90846

1

Jack V. O'Keefe
Acoustics Group
Boeing Commercial Airplane Company
P. O. Box 3707
Seattle, WA 98124

1

NASA Scientific and Technical Information Facility
6571 Elkridge Landing Road
Linthicum Heights, MD 21090

No.
Copies

30 plus
original

